ABSTRACT

Title of Dissertation: MATHEMATICS OF THE DYNAMICS AND CONTROL OF THE SARS-COV-2 PANDEMIC

Binod Pant
Doctor of Philosophy, 2024

Dissertation Directed by: Professor Abba B. Gumel
Department of Mathematics

The pneumonia-like illness that emerged late in 2019, caused by SARS-CoV-2 (and coined COVID-19), became the greatest public health challenge humans have faced since the 1918/1919 influenza pandemic, causing over 670 million confirmed cases and 7 million fatalities globally. This dissertation contributes in providing deep qualitative insights and understanding on the transmission dynamics and control of the pandemic, using mathematical modeling approaches together with data analytics and computation. Specifically, it addresses some of the pertinent challenges associated with modeling the dynamics of the disease, notably the disproportionate effect of the disease on certain (risk and demographic) populations (inducing various heterogeneities) and behavior changes with respect to adherence or lack thereof to interventions. An $m-$group model, which monitors the temporal dynamics of the disease

in m heterogeneous populations, was designed and used to study the impact of age heterogeneity and vaccination on the spread of the disease in the United States. For instance, the disease-free equilibrium for the case of the model with $m = 1$ (i.e., the model with a homogeneous population) was shown to be globally-asymptotically stable for two special cases (when vaccine is perfect or when disease-induced mortality is negligible) whenever the associated reproduction number of the homogeneous model is less than one. The homogeneous model has a unique endemic equilibrium whenever the reproduction threshold exceeds unity (this equilibrium was shown to be globally-asymptotically stable for a special case, using a nonlinear Lyapunov function of Goh-Volterra type). The homogeneous model was fitted to the observed cumulative mortality data for the SARS-CoV-2 pandemic in the United States during the period from January to May of 2022 (when Omicron was the predominant variant). It was shown that vaccine-derived herd immunity (needed to eliminate the disease) cannot be attained using the homogeneous model regardless of the proportion of individuals fully vaccinated. Such vaccine-derived immunity can, however, be achieved using the m-group heterogeneous model, with $m = 2$ (where the total population is split into two groups: those under 65 years of age, and those 65 years and older), if at least 61% of the susceptible population is fully vaccinated. Thus, this dissertation shows that heterogeneity reduces the level of vaccine coverage needed to eliminate the pandemic (and models that do not account for heterogeneity may be over-estimating the vaccination coverage needed to achieve herd immunity in the community). To

quantify the impact of human behavior changes on the spread and control of the pandemic, we designed a novel behavior-epidemiology model which considers numerous metrics for inducing human behavior changes (such as current level of disease burden and intervention adherence fatigue). Unlike the equivalent model without human behavior explicitly incorporated, the behavior-epidemiology model fits the observed cumulative mortality and predicts the observed daily mortality data very well. It was also shown that the behavior metrics related to the level of SARS-CoV-2 mortality and symptomatic transmission were more influential in inducing positive behavior changes than all other behavior metrics considered. Finally, a model was developed to assess the utility of wastewater surveillance to study the transmission dynamics and control of SARS-CoV-2 in a community. Specifically, we developed and calibrated a wastewater-based epidemiology model using wastewater data from Miami-Dade county, Florida, during the third wave of the SARS-CoV-2 pandemic. The model showed a strong correlation between the observed (detected) weekly case data and the corresponding weekly data predicted by the calibrated model. The model's prediction of the week when maximum number of SARS-CoV-2 cases will be recorded in the county during the simulation period precisely matched the time when the maximum observed/reported cases were recorded (August 14, 2021). Furthermore, the model's projection of the maximum number of cases for the week of August 14, 2021 was about 15 times higher than the maximum observed weekly case count for the county on that day (i.e., the maximum case count estimated by the

model was 15 times higher than the actual/observed count for confirmed cases). In addition to being in line with other modeling studies, this result is consistent with the CDC estimate that the reported confirmed case data may be 10 times lower than the actual (since the confirmed data did not account for asymptomatic and presymptomatic transmission). Furthermore, the model accurately predicted a one-week lag between the peak in weekly COVID-19 case and hospitalization data during the time period of the study in Miami-Dade, with the model-predicted hospitalizations peaking on August 21, 2021. Detailed time-varying global sensitivity analysis was carried out to determine the parameters (wastewater-based, epidemiological and biological) that have the most influence on the chosen response function (namely, the cumulative viral load in the wastewater). This analysis identified key parameters that significantly affect the value of the response function (hence, they should be targeted for intervention). This dissertation conclusively showed that wastewater surveillance data can be a very powerful indicator for measuring (i.e., providing early-warning signal and current burden) and predicting the future trajectory and burden (e.g., number of cases and hospitalizations) of emerging and re-emerging infectious diseases, such as SARS-CoV-2, in a community.

MATHEMATICS OF THE DYNAMICS AND CONTROL OF THE SARS-COV-2 PANDEMIC

by

Binod Pant

Dissertation submitted to the Faculty of the Graduate School of the
University of Maryland, College Park in partial fulfillment
of the requirements for the degree of
Doctor of Philosophy
2024

Advisory Committee:
Professor Abba B. Gumel, Chair
Professor Radu Balan
Professor William Fagan
Professor Doron Levy
Professor Amir Sapkota

DEDICATION

To my children (Aditya and Aarya) thank you for providing endless distractions and being a source of my joy (thus far). To my dear wife, your unwavering support, encouragement, and occasional eye roll at my jokes have kept me grounded and focused throughout this journey. And to my wonderful parents, your guidance, sacrifices and encouragement have shaped me into the person I am today. Thank you, Nirpal and Jagannath for your blessings.

ACKNOWLEDGEMENT

I would like to express my deepest gratitude to my advisor, Professor Abba Gumel, for his invaluable guidance, unwavering support, and encouragement throughout the journey of completing my dissertation. His expertise, patience, and dedication have been instrumental in shaping the direction of my research and refining my ideas. I am truly grateful for his insightful feedback, constructive criticism, and mentorship, which have significantly contributed to my projects. I would like to thank my dissertation committee members: Professor Radu Balan, Professor William Fagan, Professor Doron Levy and Professor Amir Sapkota for their support and guidance.

I would like to thank Professor Calistus N. Ngonghala, Professor Mauricio Santillana and Dr. Salman Safdar for their help and support. I would like to thank AMSC Program Manager, Jessica Sadler, for her help and support during my graduate studies. I must extend my gratitude to many more people, ranging from friends and teachers from previous institutions to the individual who made being a mathematician 'cool' for me, and even my eighth and fifth-grade teachers. I would not be able to do this without the foundation laid by these individuals. I also thank my wife and parents, without whom this journey would not be possible.

TABLE OF CONTENTS

CHAPTER Page

CHAPTER Page

CHAPTER Page

APPENDIX Page

CHAPTER Page

CHAPTER Page

APPENDIX Page

LIST OF TABLES

Table Page

LIST OF FIGURES

Figure Page

Figure Page

Chapter 1

INTRODUCTION

1.1 Introduction

Throughout history, human civilization has repeatedly faced devastating disease pandemics, ranging from the bubonic plague (which caused 200 million deaths from 1347 to 1351), Smallpox (which caused 56 million deaths in 1520 alone), the plague of Justinian (which caused 30 to 50 million deaths from the year 541 to 542 AD), the third plague (which caused 12 million deaths in 1855 alone), the 1919 influenza pandemic (which claimed 40 million to 50 million lives), the HIV/AIDS epidemic (which resulted in 25 to 35 million deaths since its inception in 1981) [1, 2, 3] to the 2019 novel coronavirus pandemic (COVID-19). COVID-19, caused by the SARS-CoV-2, was first identified in the Wuhan province of China in December of 2019 and rapidly spread around the world causing the greatest public health challenge humans have faced since the 1918 influenza pandemic [1, 4, 5, 6]. Figure 1.1 presents a visual comparison of the death tolls attributed to various infectious diseases throughout human history (up to March 1, 2023), arranged from highest to lowest death toll.

Since infectious diseases present a heavy burden to humanity, understanding how these diseases originate in humans may help curtail their spread. Jones *et al.* [7] analyzed a database of 335 emerging infectious disease (EID) 'events' (origins of EIDs) between 1940 and 2004 and found that over 70% of these EID events originate in wildlife (for example, severe acute respiratory virus and Ebola virus). Figure 1.2 shows the transmission path for various bat-borne viral diseases such as Middle East

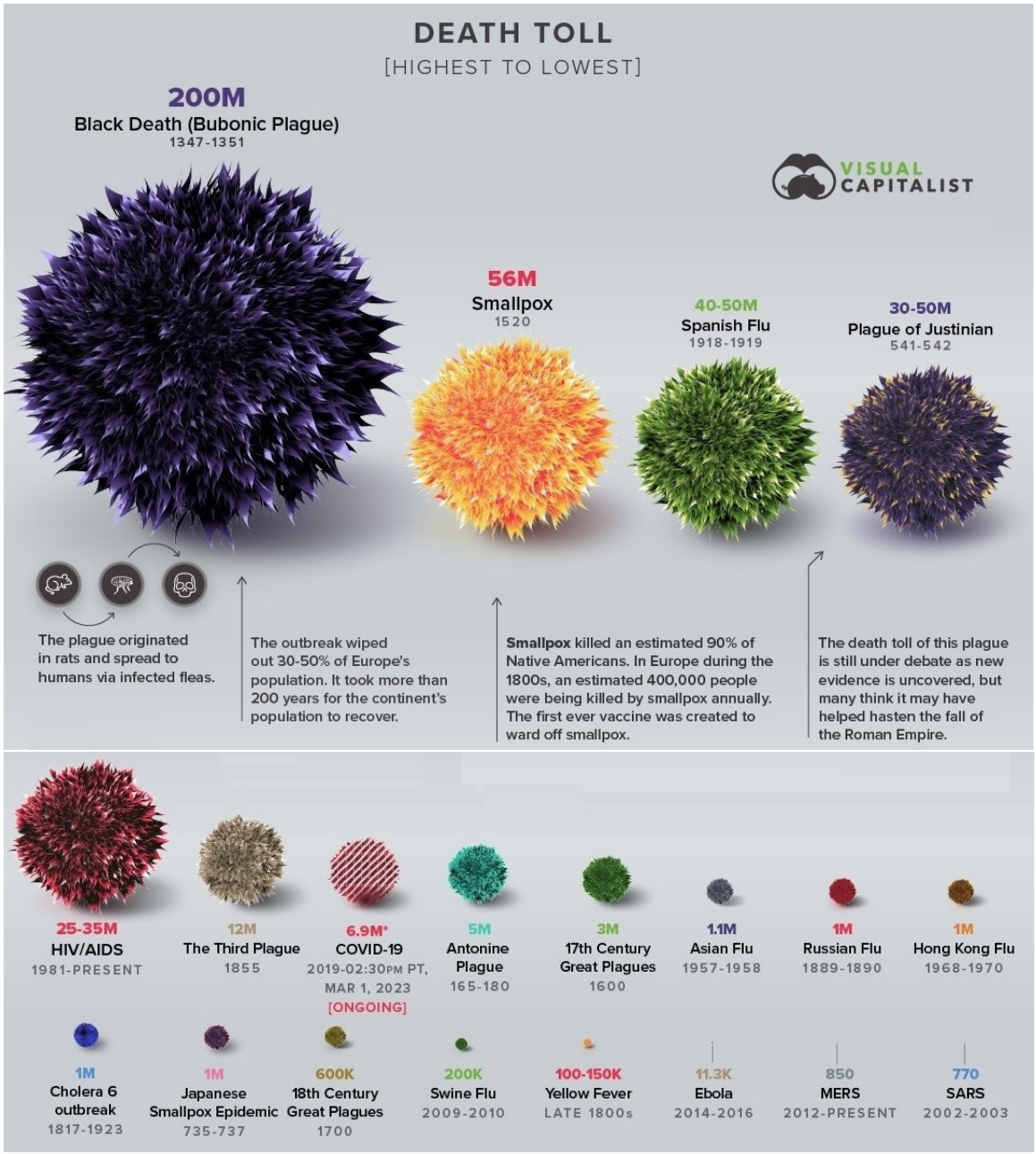

Figure 1.1: Death toll due to various infectious diseases. The figure is generated by Visual Capitalist and is based on various data sets including that from Johns Hopkins University, CDC, WHO, and BBC [1]. The data presented in the above figure represents the latest death toll due to various infectious diseases until March 1, 2023.

respiratory syndrome (MERS), severe acute respiratory syndrome (SARS), Ebola and SARS-CoV-2. Land-use change, agricultural industry change, and international travel and commerce have been attributed as the global top three drivers of zoonoses [7, 8]. Other primary drivers of diseases include medical industry changes, war and famine, climate and weather, human demography and behavior, breakdown of public health, bushmeat, and food industry change [7, 8]. As evident by the emerging disease outbreaks through wildlife trade, including monkeypox virus [9] SARS-CoV-1 [9], and probably SARS-CoV-2 [9, 10, 11], shutdown or strictly regulating wildlife market may help slowdown the pathogens spillover in humans. Since the above-listed top three contributors to zoonotic spillover, namely land-use change, agricultural industry change, and international travel and commerce, are recurring phenomena in various parts of the world, new infectious diseases can originate from any city (and thus from any country), however, their effect may be felt globally. Figure 1.3 highlights the first detection area and spatial spread of some animal-origin diseases affecting human health. As evident from this figure, the emergence of a new disease can have a global impact. Specifically, COVID-19, which was first detected in Wuhan, China in late 2019, quickly spread throughout the globe.

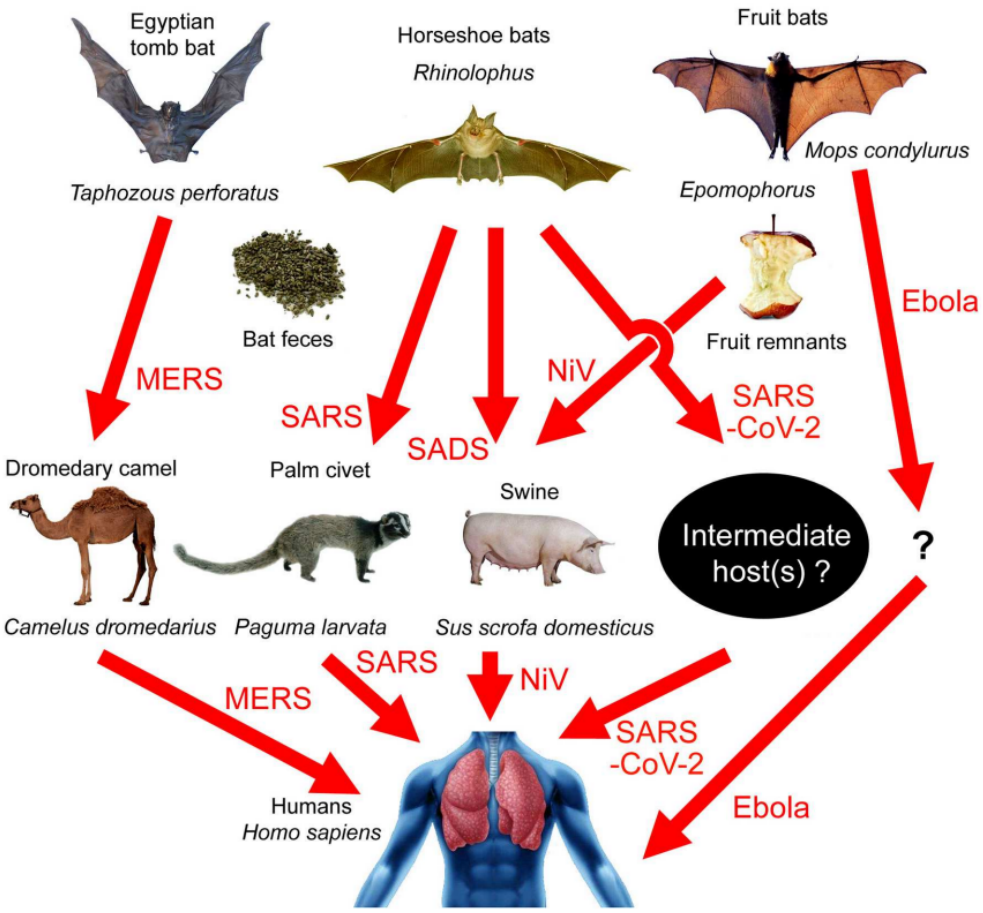

Figure 1.2: Transmission paths of bat-borne viral diseases [12].

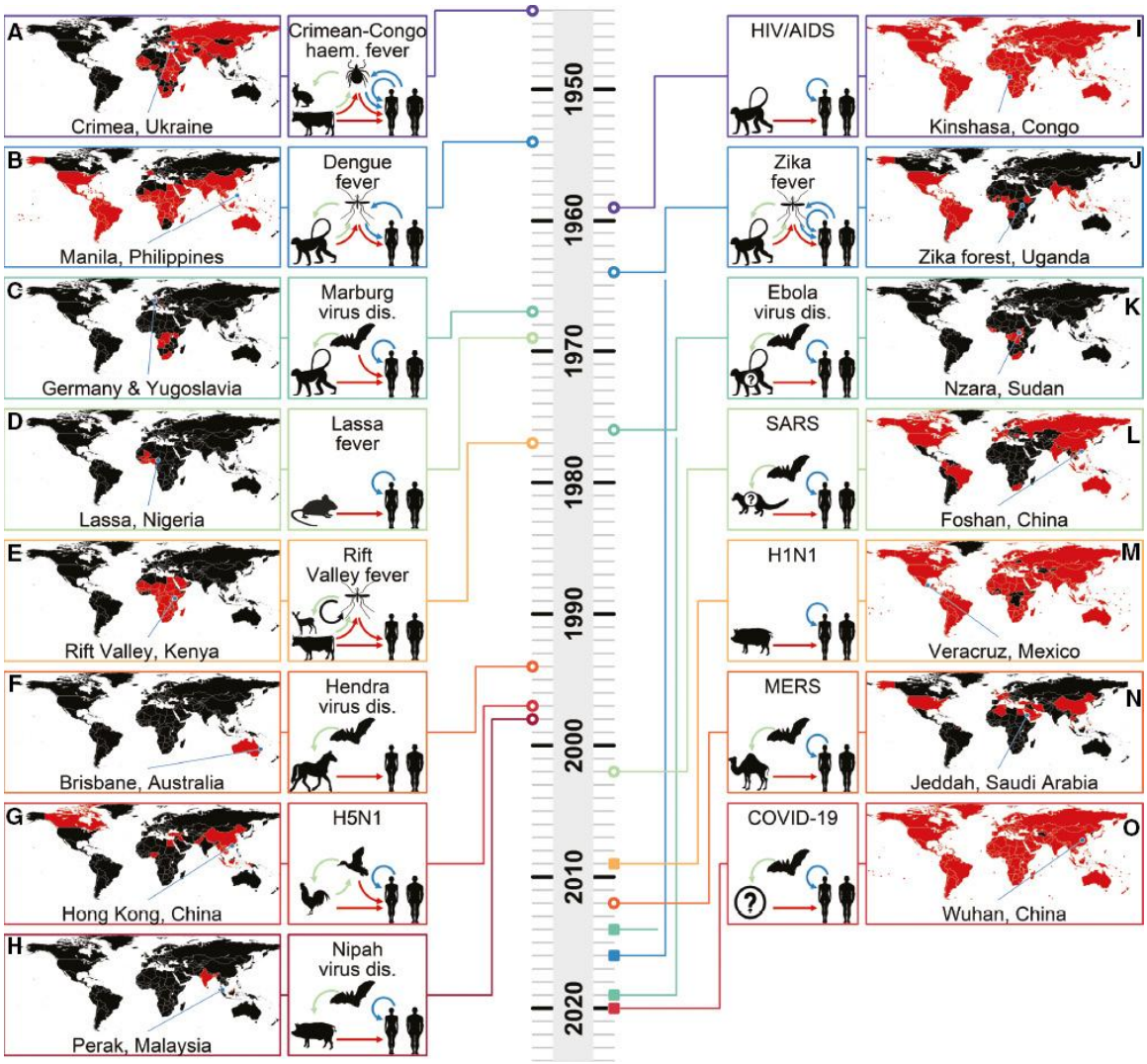

Figure 1.3: Some diseases of animal-origin affecting human health [13]. The local where the pathogen was first reported is denoted with a blue symbol on the map while the spatial spread of the disease is highlighted in red. The major routes of transmission in the zoonotic source population, primary zoonotic event and mode of maintenance in the human population are depicted with blue, red and green arrows, respectively. [13]. For each disease, the year of initial identification (round symbols on the timeline) or declaration of a public health emergency of international concern (square symbols on the timeline) are shown [13].

On March 11, 2020, after more than 118,000 cases in 114 countries and 4,291 deaths, the WHO declared COVID-19 a pandemic [14, 15]. It has caused over 670 million confirmed cases and 7 million deaths globally during the first three years since its

emergence [16]. In addition, COVID-19 has induced a severe socio-economic burden (with an estimated $12.5 trillion cost to the global economy projected through 2024 [17]). Figure 1.4 shows the world map with confirmed cumulative mortality due to COVID-19 since the beginning of the pandemic till February 4, 2024.

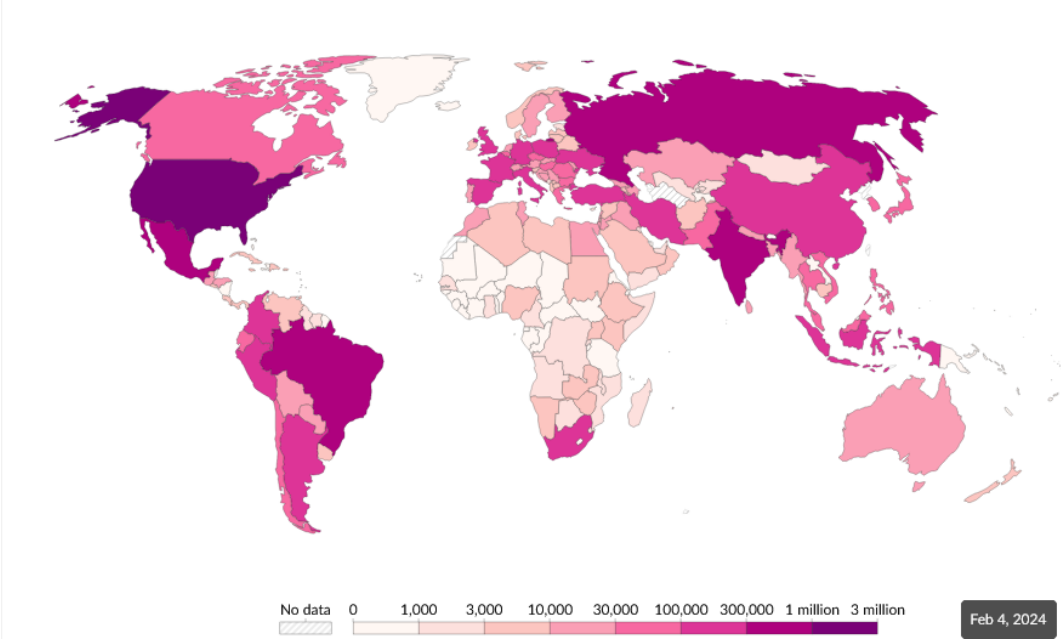

Figure 1.4: Global map of confirmed cumulative mortality due to COVID-19 since the beginning of the pandemic till February 4, 2024 [18].

Curtailing a pandemic of such scale requires the utmost attention from not only policymakers, scientists and healthcare workers but also modelers. Specifically, models can help support policy-makers in making the most informed decisions. Models can be used to make scenario-based predictions to better inform not only the policy-makers but also the general public. Numerous modeling efforts have been undertaken to answer various questions related to the COVID-19 pandemic. Numerous mathematical models, of varying types, have been developed and used to gain insight into the transmission dynamics and control of the pandemic. For instance, models that take the form of deterministic systems of nonlinear differential equations have been

used to assess the impacts of non-pharmaceutical interventions (such as face-masks usage, social-distancing, quarantine and self-isolation) [19, 6, 20, 21], pharmaceutical interventions (such as vaccination and the use of antiviral drugs) [21, 22, 23, 24, 25] and human mobility between neighboring countries [26] on the transmission dynamics and control of the COVID-19 pandemic. Similarly, agents-based (or individual-based) models have been used to study various aspects of the pandemic, such as the impact of contract tracing [27, 28] and the impact of pharmaceutical and non-pharmaceutical interventions against COVID-19 [29, 30, 31]. Network models have been used to study the impact of testing and contact tracing [32] and social-distancing etc. [33, 34, 35, 36]. Rahimi *et al.* reviewed various statistical models used to forecast the outbreak of COVID-19 [37].

1.1.1 Outline of the Dissertation

This dissertation began with an introductory chapter, which will then be followed by three technical chapters, each of which model an important research question pertaining to COVID-19.

The primary objective of Chapter 2 is to assess the population-level impact of age heterogeneity and vaccination on the transmission dynamics and control of the SARS-CoV-2 pandemic in the United States. In order to achieve this objective, Chapter 2 begins by introducing a general heterogeneous model, which stratifies the total population into m subgroups and incorporates the use of FDA-EUA administered vaccines in the United States. The basic theoretical results for the general $m-$group model are also presented. The corresponding homogeneous version of the model (i.e., the general model with $m = 1$) is rigorously analysed. In addition to fitting the homo-

geneous model to observed data, detailed global sensitivity analysis, with respect to the parameters of the model, is also carried out in Chapter 2. It is shown that intervention strategies that target presymptomatic and asymptomatic individuals, such as contact tracing and mass random testing (implemented with the required coverage and level of effectiveness), are consistently very effective in combating and mitigating the SARS-CoV-2 pandemic in the United States. Another special case of the general heterogeneous model with $m = 2$ is considered and qualitatively analysed, with respect to the asymptotic stability of its associated disease-free equilibrium. It is shown that adding age heterogeneity into a SARS-CoV-2 vaccination model with homogeneous mixing significantly reduces the level of vaccination coverage needed to achieve vaccine-derived herd immunity. The consequence of this result is that vaccination models for SARS-CoV-2 that do not explicitly account for age heterogeneity may be overestimating the level of vaccine-derived herd immunity threshold needed to eliminate the SARS-CoV-2 pandemic.

Chapter 3 is based on the use of mathematical modeling approaches to assess the extent to which SARS-CoV-2 transmission dynamics is impacted by population-level changes of human behavior due to factors such as (a) the severity of transmission (such as disease-induced mortality and level of symptomatic transmission), (b) fatigue due to the implementation of mitigation interventions measures (e.g., lockdowns) over a long (extended) period of time, (c) social peer-pressure, among others. A novel behavior-epidemiology model, which takes the form of a deterministic system of nonlinear differential equations, is developed and fitted using observed cumulative SARS-CoV-2 mortality data during the first wave (March 2020 -June 2020) in the United States. The model fits the observed data, as well as makes a more accurate prediction of the observed daily SARS-CoV-2 mortality during the first wave, in

comparison to the equivalent model which does not explicitly account for changes in human behavior. Furthermore, it is shown that an increase in the proportion of exposed individuals who become asymptomatically-infectious at the end of the exposed period can lead to an increase (decrease) in the control reproduction number ($\mathcal{R}_C$) if the effective contact rate of asymptomatic individuals is higher (lower) than that of symptomatic individuals. Overall, the findings of the Chapter 3 suggest that, as more newly-infected individuals become asymptomatically-infectious, the level of positive behavior change, as well as disease severity, hospitalizations and disease-induced mortality in the community can be expected to significantly decrease (while new cases may rise, particularly if asymptomatic individuals have higher contact rate, in comparison to symptomatic individuals).

Finally, Chapter 4 presents a wastewater-based mathematical model for assessing the transmission dynamics of the SARS-CoV-2 pandemic in Miami-Dade County, Florida. The model, which takes the form of a deterministic system of nonlinear differential equations, monitors the temporal dynamics of the disease, as well as changes in viral RNA concentration in the county's wastewater system (which consists of three sewage treatment plants). The model was calibrated using the wastewater data during the third wave of the SARS-CoV-2 pandemic in Miami-Dade (specifically, the time period from July 3, 2021 to October 9, 2021). The calibrated model was used to predict SARS-CoV-2 case and hospitalization trends in the county during the aforementioned time period, showing a strong correlation (with a correlation coefficient $r = 0.99$) between the observed (detected) weekly case data and the corresponding weekly data predicted by the calibrated model. The model's prediction of the week when maximum number of SARS-CoV-2 cases will be recorded in the county during the simulation period precisely matches the time when the maximum ob-

served/reported cases were recorded (which was August 14, 2021). Furthermore, the model's projection of the maximum number of cases for the week of August 14, 2021 is about 15 times higher than the observed weekly case count for the county on that day (i.e., the maximum case count estimated by the model was 15 times higher than the actual/observed count for confirmed cases). Furthermore, the model accurately predicts a one-week lag between the peak in weekly COVID-19 case and hospitalization data during the time period of the study in Miami-Dade, with the model-predicted hospitalizations peaking on August 21, 2021. This chapter shows, conclusively, that wastewater surveillance data can be a very powerful indicator for measuring (i.e., providing early-warning signal and current burden) and predicting the future trajectory and burden (e.g., number of cases and hospitalizations) of emerging and re-emerging infectious diseases, such as SARS-CoV-2, in a community.

Chapter 2

AGE HETEROGENEITY AND VACCINATION MODEL

2.1 Introduction

As mentioned before, the COVID-19 pandemic, which was first detected in Wuhan province of China in December of 2019, and was caused by SARS-CoV-2, became the greatest public health challenge humans have faced since the 1918 influenza pandemic [1]. It has, within the three years of its emergence, caused over 670 million confirmed cases and 7 million deaths globally [16]. When compared to other nations, the United States has the highest death toll from COVID-19 [38], with over 1.17 million deaths as of January 27, 2024 [39]. Until the Emergency Use Authorization (EUA) of effective anti-COVID vaccines, such as Pfizer and Moderna, in December 2020 by the United States Food and Drug Administration (FDA), control and mitigation strategies against COVID-19 primarily relied on nonpharmaceutical interventions (NPIs) like social distancing, community lockdowns, face-covering usage, quarantine, isolation, and contact tracing [40, 41, 6].

The significance of heterogeneity in the transmission of the disease has been underscored by the pandemic COVID-19 as certain individuals became more prone to acquiring the infection, experiencing severe illness and/or dying of the disease. Specifically, heterogeneities arise in numerous forms, such as heterogeneities in mortality (where individuals with underlying health conditions, such as diabetes and hypertension, are more likely to die of COVID-19 than those without those co-morbidities [42, 43, 44, 45, 46]), age (where humans of age 65 and older are more likely to suffer

severe COVID-19 infection and mortality, in comparison to those who are younger [47, 48]), risk (where some humans, such as health care workers or other essential workers (e.g., grocery workers, law enforcement agents etc.) are more at risk of acquiring infection than others)[49, 50, 51, 52, 53, 54] and adherence to interventions (where some individuals are more likely to adhere to interventions than others) [55, 56, 57]. Therefore, it is crucial for models describing the transmission dynamics of COVID-19 to explicitly integrate the influences of various heterogeneities. However, only a limited number of models addressing the transmission dynamics of COVID-19 explicitly include the effects of these heterogeneities in their modeling procedures. Age-structured models were developed and used to study the impact of social-distancing [58] and non-pharmaceutical interventions [59] on the spread of COVID-19. Elbasha and Gumel [60] used a generalized multigroup vaccination model to analyze the impact of heterogeneities on vaccine-induced herd immunity threshold.

The chapter is organized as follows. The general heterogeneous model, which stratifies the total population into m subgroups, is formulated in Section 2.2. The model incorporates the use of FDA-EUA administered vaccines in the United States. The basic theoretical results for the general $m-$group model are also presented. The corresponding homogeneous version of the model (i.e., the general model with $m = 1$) is rigorously analysed in Section 2.3. In addition to fitting the homogeneous model to observed data, detailed global sensitivity analysis, with respect to the parameters of the model, is also carried out in this section. Another special case of the general heterogeneous model with $m = 2$ is considered and qualitatively analysed, with respect to the asymptotic stability of its associated disease-free equilibrium, in Section 2.4. The main conclusions of the chapter are presented in Section 2.5.

2.2 Formulation of the Heterogeneous Model

The general m group heterogeneous model (henceforth called *heterogeneous model*), with k distinct subgroups ($k = \{1, 2, \cdots m\}$) is formulated by dividing subgroup k into the mutually-exclusive compartments of unvaccinated susceptible ($S_k(t)$), fully-vaccinated susceptible ($V_k(t)$), exposed/latent ($E_k(t)$), pre-symptomatic infectious ($P_k(t)$), symptomatic infectious ($I_k(t)$), asymptomatically-infectious ($A_k(t)$), hospitalized ($H_k(t)$), and recovered ($R_k(t)$) individuals. Hence, the total number of individuals in any of the k subgroup at time t, denoted by $N_k(t)$, is given by [61]:

$$N_k(t) = S_k(t) + V_k(t) + E_k(t) + P_k(t) + A_k + I_k(t) + H_k(t) + R_k(t).$$

Thus, the total population (in all k subgroups) at time t, denoted by $N(t)$, is given by [61]:

$$N(t) = \sum_{k=1}^{m} N_k(t). \tag{2.1}$$

It is assumed that the population of unvaccinated susceptible individuals in subgroup k (S_k) are fully-vaccinated using an FDA-EUA vaccine with protective efficacy $\varepsilon_{v,k}$ at a *per capita* rate $\xi_{v,k}$. Additionally, the unvaccinated susceptible population is increased by the recruitment of individuals into the population (either by birth or by immigration) at a rate Π_k, and by the waning of vaccine-derived protective immunity in fully-vaccinated individuals (at a rate $\omega_{v,k}$). Individuals in the S_k class acquire COVID-19 infection at a rate λ_k (*force of infection*), given by [61]:

$$\lambda_k = \sum_{l=1}^{m} a_k c_{kl}, \left[\frac{\mathcal{P}_{P,l} P_l(t) + \mathcal{P}_{I,l} I_l(t) + \mathcal{P}_{A,l} A_l(t) + \mathcal{P}_{H,l} H_l(t)}{N_l(t)} \right], \tag{2.2}$$

where a_k is the average number of contacts made by individuals in group k during a time period and c_{kl} is the proportion of contacts that individuals in group k have with individuals in group l [60]. Furthermore, the parameters $\mathcal{P}_{P,l}$, $\mathcal{P}_{I,l}$, $\mathcal{P}_{A,l}$, and $\mathcal{P}_{H,l}$ represent the *per* contact transmission probability of infectious individuals (in group l) that are pre-symptomatic (P_l), symptomatic (I_l), asymptomatic (A_l), and hospitalized (H_l), respectively. Mixing should meet the closure relation $a_k c_{kl} N_k = a_l c_{lk} N_l$ [62]. In other words, the total number of contacts individuals in group k have with individuals in group l must balance the total number of contacts individuals in group l have with individuals in group k. Exposed (or latent) individuals in the k^{th} sub-population progress to pre-symptomatic class in the k^{th} sub-population at a rate σ_k, and a proportion r_k of these individuals progress to the I_k class (at the rate $r_k\psi_k$), while the remaining proportion, $1 - r_k$, progress to the A_k class (at the rate $(1 - r_k)\psi_k$). Symptomatic individuals in the k^{th} sub-population are hospitalized at a rate ϕ_k, recover at a rate $\gamma_{I,k}$ or die due to the disease at a rate $\delta_{I,k}$. Asymptomatic infectious individuals recover naturally at a rate $\gamma_{A,k}$. It is assumed that recovered individuals obtain permanent immunity (i.e., no reinfection) from COVID-19. It is assumed that recovered individuals lose their infection-acquired (natural) immunity at a rate $\omega_{n,k}$. Furthermore, natural death occurs in all sub-populations at a rate μ_k.

Based on the above derivations and assumptions, the general m-group heterogeneous model for the spread of COVID-19 in a population that uses an FDA-EUA vaccine, is given by the following deterministic system of nonlinear differential equations (where a dot represents differentiation with respect to time t) [61]:

$$
\begin{cases}
\dot{S}_k(t) = \Pi_k + \omega_{v,k} V_k(t) + \omega_{n,k} R_k(t) - \lambda_k(t) S_k(t) - (\xi_{v,k} + \mu_k) S_k(t), \\
\dot{V}_k(t) = \xi_{v,k} S_k(t) - (1 - \varepsilon_{v,k}) \lambda_k(t) V_k(t) - (\omega_{v,k} + \mu_k) V_k(t), \\
\dot{E}_k(t) = \lambda_k(t) S_k(t) + (1 - \varepsilon_{v,k}) \lambda_k(t) V_k(t) - (\sigma_k + \mu_k) E_k(t), \\
\dot{P}_k(t) = \sigma_k E_k(t) - (\psi_k + \mu_k) P_k(t), \\
\dot{I}_k(t) = r_k \psi_k P_k(t) - (\phi_k + \gamma_{I,k} + \mu_k + \delta_{I,k}) I_k(t), \\
\dot{A}_k(t) = (1 - r_k) \psi_k P_k(t) - (\gamma_{A,k} + \mu_k) A_k(t), \\
\dot{H}_k(t) = \phi_k I_k(t) - (\gamma_{H,k} + \mu_k + \delta_{H,k}) H_k(t), \\
\dot{R}_k(t) = \gamma_{I,k} I_k(t) + \gamma_{A,k} A_k(t) + \gamma_{H,k} H_k(t) - (\omega_{n,k} + \mu_k) R_k(t),
\end{cases}
\tag{2.3}
$$

where, λ_k (the *force of infection*) is given by Equation (2.2). A flow diagram of the model (2.3) is depicted in Figure 2.1 and the state variables and parameters of the model are described in Tables 2.1 and 2.2, respectively.

Some of the main assumptions made in the formulation of the model (2.3) are [61]:

1. Individuals in the vaccinated compartment (V_k) are fully-vaccinated. That is, in line with the CDC definition of being fully-vaccinated, individuals in the V_k class are those that have received the single dose of the Janssen/Johnson & Johnson COVID-19 vaccine or the two doses of any of the approved mRNA COVID-19 vaccines at least 14 days earlier [63].

2. Only unvaccinated susceptible individuals are vaccinated. Although the CDC recommends people with COVID-19 symptoms to wait to be vaccinated until the completion of the isolation period [64], this still opens the possibility for exposed (i.e., infected but not infectious), pre-symptomatic, and asymptomatic individuals receiving the SARS-CoV-2 vaccine. Furthermore, although recovered individuals can choose to get vaccinated, our model does not allow for this

possibility.

The model (2.3) extends the heterogeneous $S_kV_kE_kI_kR_k$ model in [60] by adding compartments for pre-symptomatic (P_k), asymptomatic (A_k) and hospitalized (H_k) infectious individuals and also accounting for the waning of natural immunity (ω_{nk}). The chapter also contributes by providing detailed asymptotic stability of the model (including completed global asymptotic stability analysis of the disease-free and endemic equilibria of the homogeneous version of the original heterogeneous model).

State variables	**Description**
S_k	Number of non-vaccinated susceptible individuals in subgroup k
V_k	Number of fully-vaccinated susceptible individuals in subgroup k
E_k	Number of exposed (newly-infected but not yet infectious) individuals in subgroup k
P_k	Number of pre-symptomatically-infectious individuals in subgroup k
I_k	Number of symptomatically-infectious individuals in subgroup k
A_k	Number of asymptomatically-infectious individuals in subgroup k
H_k	Number of hospitalized individuals in subgroup k
R_k	Number of recovered individuals in subgroup k

Table 2.1: Description of the state variables of the m-group heterogeneous model (2.3), with $k = \{1, 2, \cdots, m\}$ [61].

2.2.1 Basic qualitative properties

In this section, the basic qualitative property of the m-group model (2.3) will be explored. In particular, the invariance properties of the solutions of the model will be rigorously analysed.

Consider the following biologically-feasible region for the model (2.3), with $k = \{1, 2, \cdots, m\}$:

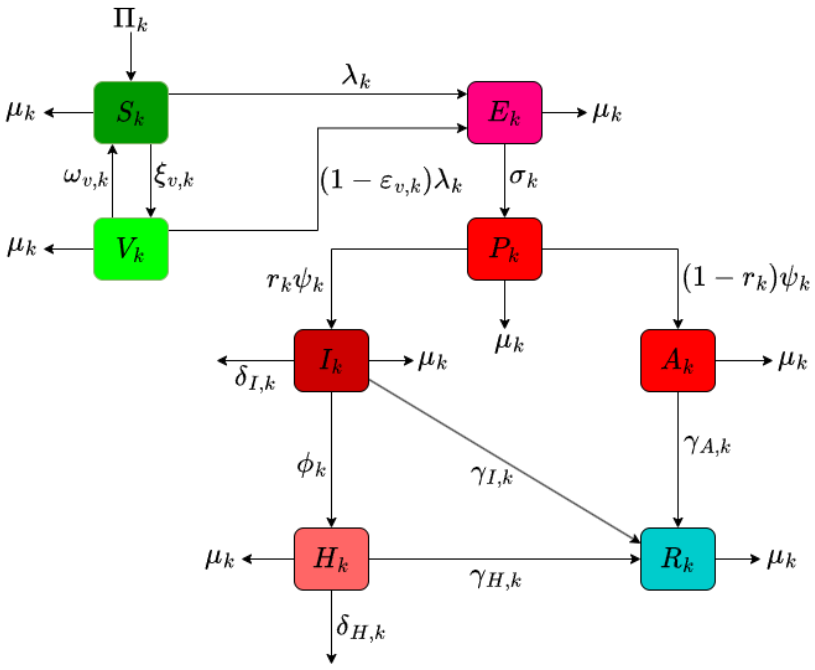

Figure 2.1: The flow diagram describing the m-group heterogeneous model (2.3), with $k = \{1, 2, \cdots, m\}$ and the infection rate, λ_k, defined in (2.2) [61].

$$\Omega = \left\{ (S_k, V_k, E_k, P_k, I_k, A_k, H_k, R_k) \in \mathbb{R}_+^{8m} : \sum_{k=1}^{m} (S_k + V_k + E_k + P_k + I_k + A_k + H_k + R_k) \leq N(0) \right\},$$

where $N(0)$ is the total initial size of the population. We claim the following result:

Theorem 2.2.1. *The region Ω is positively-invariant and attracts all solutions of the model* (2.3).

Proof. Adding all equations of the heterogeneous model (2.3) gives:

$$\dot{N} = \sum_{k=1}^{m} \Big(\Pi_k - \mu_k N_k - \delta_{I,k} I_k - \delta_{H,k} H_k \Big). \tag{2.4}$$

It is convenient to define $\Pi = \sum_{k=1}^{m} \Pi_k$. Then, Equation (2.4) can be rewritten as:

Parameter	Description
Π_k	Recruitment rate into subgroup k
μ_k	Natural death rate for individuals in subgroup k
a_k	Average number of contacts *per* unit time made by individuals in subgroup k
$c_{k,l}$	Proportion of contacts individuals in subgroup k have with individuals in subgroup l
$\mathcal{P}_{P,k}(\mathcal{P}_{I,k})(\mathcal{P}_{A,k})(\mathcal{P}_{H,k})$	Transmission probability *per* contact for individuals in the $P_k(I_k)(A_k)(H_k)$ class
$\xi_{v,k}$	Rate at which susceptible individuals in subgroup k are fully-vaccinated
$\varepsilon_{v,k}$	Vaccine efficacy for vaccinated individuals in subgroup k
$\omega_{v,k}$	Waning rate of vaccine for individuals in subgroup k
$\omega_{n,k}$	Waning rate of natural immunity for recovered individuals in subgroup k
σ_k	Progression rate from E_k to P_k class
r_k	Proportion of presymptomatic individuals in subgroup k who show clinical symptoms of the disease at the end of the presymptomatic period
$r_k\psi_k$	Progression rate from the P_k to the I_k class
$(1-r_k)\psi_k$	Progression rate from the P_k to the A_k class
ϕ_k	Hospitalization rate for symptomatically-infectious individuals in subgroup k
$\gamma_{I,k}(\gamma_{A,k})(\gamma_{H,k})$	Recovery rate for individuals in the $I_k(A_k)(H_k)$ class
$\delta_{I,k}(\delta_{H,k})$	Disease-induced mortality rate for individuals in the $I_k(H_k)$ compartment

Table 2.2: Description of the parameters of the m-group heterogeneous model (2.3), with $k = \{1, 2, \cdots, m\}$ [61].

$$\dot{N} \leq \Pi - \sum_{k=1}^{m} \Big(\mu_k N_k\Big). \tag{2.5}$$

Let, $\mu_g = \min\{\mu_1, \mu_2, \cdots, \mu_m\}$, then it follows from (2.5) (and the definition of $N(t)$ in (2.1)) that:

$$\dot{N} \leq \Pi - \mu_g N(t). \tag{2.6}$$

Hence, if $N \geq \Pi/\mu_g$, then $\dot{N} \leq 0$. Furthermore, it follows, by applying a standard

comparison theorem [65] on (2.6), that:

$$N(t) \leq N(0)e^{-\mu_g t} + \frac{\Pi}{\mu_g}\left(1 - e^{-\mu_g t}\right). \tag{2.7}$$

In particular, $N(t) \leq \Pi/\mu_g$ if $N(0) \leq \dfrac{\Pi}{\mu_g}$. If $N(0) > \dfrac{\Pi}{\mu_g}$ (i.e., if the initial size of the population exceeds the carrying capacity, Π/μ_g, and the initial solutions are outside the region Ω), then $N(t) > \dfrac{\Pi}{\mu_g}$ for all $t > 0$ but with $\lim_{t\to\infty} N(t) = \dfrac{\Pi}{\mu_g}$ (and this initial solution trajectory eventually enters the region Ω [66]). Thus, every solution of the model (2.3), with $\mu_g = \min\{\mu_1, \mu_2, \cdots, \mu_m\}$ and initial conditions in Ω, remains in Ω for all time $t > 0$, and all initial solutions outside Ω are eventually attracted into Ω. In other words, the region Ω is positively-invariant and attracts all initial solutions of the model (2.3).

□

The epidemiological implication of Theorem 2.2.1 is that the model (2.3) is well-posed mathematically and epidemiologically in the positively-invariant region Ω [67]. Hence, it is sufficient to consider the dynamics of the flow generated by the heterogeneous model in Ω. Before analysing a two-group model, it is instructive to study the dynamics of the model for the case where the population is assumed to be homogeneous (i.e., it is instructive to consider, first of all, the model (2.3) with $m = 1$). The objective is to determine whether the homogeneous model has certain qualitative features that may not be present in a heterogeneous model or *vice versa*.

2.3 Model with Homogeneous Population

Before introducing a two-group heterogeneous model, a homogeneous model, obtained by setting $m = 1$ in the heterogeneous model (2.3), is rigorously analyzed. The

aforementioned homogeneous model is given by [61]:

$$\begin{cases} \dot{S}(t) = \Pi + \omega_v V(t) + \omega_n R(t) - \lambda S(t) - (\xi_v + \mu)S(t), \\ \dot{V}(t) = \xi_v S(t) - (1-\varepsilon_v)\lambda(t)V(t) - (\omega_v + \mu)V(t), \\ \dot{E}(t) = \lambda(t)S(t) + (1-\varepsilon_v)\lambda(t)V(t) - (\sigma + \mu)E(t), \\ \dot{P}(t) = \sigma E(t) - (\psi + \mu)P(t), \\ \dot{I}(t) = r\psi P(t) - (\phi + \gamma_I + \mu + \delta_I)I(t), \\ \dot{A}(t) = (1-r)\psi P(t) - (\gamma_A + \mu)A(t), \\ \dot{H}(t) = \phi I(t) - (\gamma_H + \mu + \delta_H)H(t), \\ \dot{R}(t) = \gamma_I I(t) + \gamma_A A + \gamma_H H - (\omega_n + \mu)R(t), \end{cases} \tag{2.8}$$

where λ is the *force of infection* of the homogeneous model (2.8), given by [61]:

$$\lambda = \left(\frac{\beta_P P + \beta_I I + \beta_A A + \beta_H H}{N} \right), \tag{2.9}$$

and β_P, β_I, β_A, and β_H are effective contact rates (i.e., the product of number of contacts during a given time period and the probability of transmission *per* contact) associated with disease transmission by individuals in the pre-symptomatic (P), symptomatic (I), asymptomatic (A), and the hospitalized (H) compartment, respectively. Let $D(t)$ represent the total number of individuals who have died from the disease by time t. Hence, it follows from the homogeneous model (2.8) that the rate of change of this population is given by [61]:

$$\dot{D}(t) = \delta_I I + \delta_H H. \tag{2.10}$$

It is convenient to define the following feasible region for the homogeneous model (2.8) [61]:

$$\Omega_1 = \left\{ (S, V, E, P, I, A, H, R) \in \mathbb{R}_+^8 : N(t) \leq \frac{\Pi}{\mu} \right\}, \tag{2.11}$$

where $N(t)$ is the total population at time t. It can be shown that the region Ω_1 is positively-invariant and attracts all solutions of the homogeneous model (2.8).

2.3.1 Fixed and estimated parameters of the homogeneous model

The homogeneous model (2.8) contains eighteen parameters. The values of twelve of these parameters are well-known from the literature (these parameters are defined as *fixed parameters*), while the values of the remaining six parameters (namely β_P, β_I, β_A, β_H, δ_I, and δ_H) are unknown, and will be estimated from observed COVID-19 data for the United States (these unknown parameters to be estimated from data are termed as *estimated parameters*). For data-fitting purposes, we will consider the following three time periods, corresponding to the major three waves of the COVID-19 pandemic in the United States, namely [61]:

1. **Wave A:** time period from October 15, 2020 to April 5, 2021 (Alpha was the predominant variant in the United States during most of this period [68, 69]).
2. **Wave B:** time period from July 9, 2021 to November 7, 2021 (Delta was the dominant variant in the United States during this period [70, 71, 72]).
3. **Wave C:** time period from January 1, 2022 to May 7, 2022 (Omicron was the dominant variant during this period [70, 71, 72]).

The homogeneous model (2.8) was fitted with observed cumulative COVID-19 mortality data for the United States to obtain the best values of the six unknown parameters of the model, namely the effective contact rates (β_P, β_I, β_A, and β_H) and disease-induced death rates (δ_I and δ_H). The model fitting was done using a standard nonlinear least squares approach, which involved using the inbuilt MATLAB

minimization function "lsqcurvefit" to minimize the sum of the squared differences between each observed cumulative mortality data point (obtained from Johns Hopkins University COVID-19 repository [73]), and the corresponding cumulative mortality projection obtained from the simulation of the homogeneous model (2.8). The result of the fitting for Waves A, B, and C are depicted in Figures 2.2(a), 2.2(b), and 2.2(c), respectively (and the estimated values of these parameters, corresponding to each of the three waves, are tabulated in Table 2.3). The goodness of fit (for each of the figures) was assessed by plotting the predicted daily mortality and the predicted 7-day rolling averages against the observed daily mortality data and the observed 7-day rolling average data, respectively. The 7-day rolling average of day t_n is calculated by dividing the sum of the daily mortality on days $t_{n-6}, \cdots, t_n$ by 7.

Parameter	**Estimated (fitted) Value**		
	Wave A	**Wave B**	**Wave C**
β_P	$0.201\ \text{day}^{-1}$	$0.448\ \text{day}^{-1}$	$0.724\ \text{day}^{-1}$
β_I	$0.110\ \text{day}^{-1}$	$0.394\ \text{day}^{-1}$	$0.448\ \text{day}^{-1}$
β_A	$0.363\ \text{day}^{-1}$	$0.604\ \text{day}^{-1}$	$0.846\ \text{day}^{-1}$
β_H	$2.468 \times 10^{-8}\ \text{day}^{-1}$	$8.889 \times 10^{-3}\ \text{day}^{-1}$	$1.950 \times 10^{-3}\ \text{day}^{-1}$
δ_I	$1.998 \times 10^{-4}\ \text{day}^{-1}$	$1.001 \times 10^{-4}\ \text{day}^{-1}$	$1.014 \times 10^{-5}\ \text{day}^{-1}$
δ_H	$5.472 \times 10^{-4}\ \text{day}^{-1}$	$3.088 \times 10^{-4}\ \text{day}^{-1}$	$1.015 \times 10^{-3}\ \text{day}^{-1}$

Table 2.3: Table of estimated (fitted) parameters of the homogeneous model (2.8) generated by fitting the model with the observed cumulative mortality data for the United States during Waves A, B, and C [61].

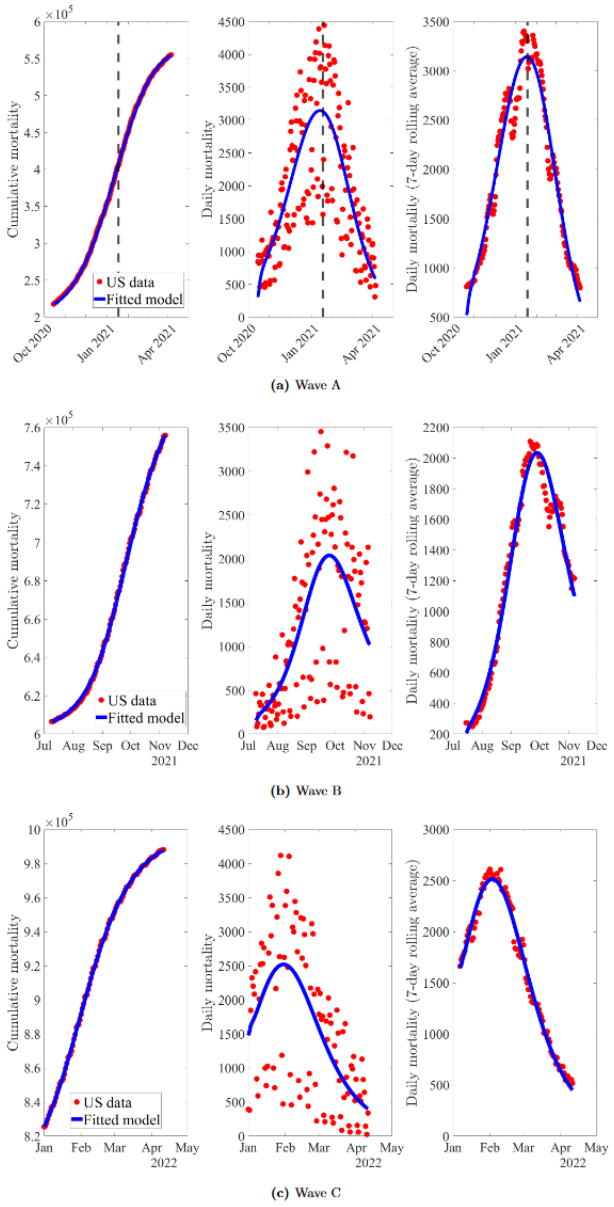

Figure 2.2: The left figures are time series illustrations of the least square fit of the model (2.8), showing the model's output for the cumulative COVID-19 mortality compared to the observed cumulative mortality for the United States during the time periods associated with (a) Wave A, (b) Wave B, and (c) Wave (c) [61]. The middle figures are simulation result of the model (2.8), showing the daily COVID-19 mortality cases for the United States as a function of time, using the fixed (see Table 2.3) and estimated parameter (see Table 2.4) associated with (a) Wave A, (b) Wave B, and (c) Wave C. The right figures are a seven-day rolling average of daily mortality for (a) Wave A, (b) Wave B, and (c) Wave C. Red dots indicate data points, while the solid blue line represents output from the model. The dashed vertical line in Figure 2.2 (a) marks the first day of susceptible individuals (S) entering the fully-vaccinated compartment (V). The initial conditions used to generate these figures are given in Table A1 of Appendix A [61].

Parameter	Value			Source
	Wave A	**Wave B**	**Wave C**	
Π	$11,670$ day^{-1}	$11,670$ day^{-1}	$11,670$ day^{-1}	[74, 75]
μ	$1/(77.8\times365)$ day^{-1}	$1/(77.8\times365)$ day^{-1}	$1/(77.8\times365)$ day^{-1}	[75]
r	0.6 (dimensionless)	0.6 (dimensionless)	0.6 (dimensionless)	[76, 77, 78]
$1-r$	0.4 (dimensionless)	0.4 (dimensionless)	0.4 (dimensionless)	[26, 78]
ϕ	$1/5$ day^{-1}	$1/5$ day^{-1}	$1/5$ day^{-1}	[24]
γ_I	$1/10$ day^{-1}	$1/10$ day^{-1}	$1/10$ day^{-1}	[79]
γ_A	$1/5$ day^{-1}	$1/5$ day^{-1}	$1/5$ day^{-1}	[80]
ω_v	$1/(9\times30)$ day^{-1}	$1/(9\times30)$ day^{-1}	$1/(9\times30)$ day^{-1}	[24]
ξ_v	2.356×10^{-3} day^{-1}	8.029×10^{-4} day^{-1}	2.702×10^{-4} day^{-1}	[81]
ε_v	0.90 (dimensionless)	0.86 (dimensionless)	0.70 (dimensionless)	[82, 83]
σ	$1/3.5$ day^{-1}	$1/2.91$ day^{-1}	$1/1.92$ day^{-1}	[84, 85]
ψ	$1/2$ day^{-1}	$1/1.5$ day^{-1}	$1/1.5$ day^{-1}	[76, 84, 86]
γ_H	$1/8$ day^{-1}	$1/7.6$ day^{-1}	$1/5.5$ day^{-1}	[87]

Table 2.4: Values of fixed parameters of the homogeneous model (2.8) for Waves A, B, and C. For Wave A, it should be noted that the rate at which susceptible (S) enter the fully-vaccinated compartment (V) from October 15, 2020 to January 3, 2021 is 0 [61].

2.3.2 Asymptotic stability of disease-free equilibrium (DFE) of homogeneous model

In this section, the asymptotic stability property of the DFE of the homogeneous model (2.8) is explored. The disease-free equilibrium of the homogeneous model (2.8) is given by [61]:

$$\mathbb{E}_0 : (S^*, V^*, E^*, P^*, I^*, A^*, H^*, R^*) = \left(\frac{\Pi(\omega_v + \mu)}{\mu(\omega_v + \xi_v + \mu)}, \frac{\Pi\xi_v}{\mu(\omega_v + \xi_v + \mu)}, 0, 0, 0, 0, 0, 0 \right). \tag{2.12}$$

2.3.2.1 Local asymptotic stability of the DFE of the homogeneous model

The local asymptotic stability of the DFE ($\mathbb{E}_0$) of the homogeneous model will be explored using the *next generation operator method* [88, 89]. Using the notation in [88], it follows that the associated non-negative matrix of new infection terms (F)

and the M-matrix of all linear transition terms (V) are given, respectively, by [61]

$$F = \begin{bmatrix} 0 & \beta_P f_{SV} & \beta_I f_{SV} & \beta_A f_{SV} & \beta_H f_{SV} \\ 0 & 0 & 0 & 0 & 0 \\ 0 & 0 & 0 & 0 & 0 \\ 0 & 0 & 0 & 0 & 0 \\ 0 & 0 & 0 & 0 & 0 \end{bmatrix}, \tag{2.13}$$

and,

$$V = \begin{bmatrix} \sigma + \mu & 0 & 0 & 0 & 0 \\ -\sigma & \psi + \mu & 0 & 0 & 0 \\ 0 & -r\psi & \phi + \gamma_I + \mu + \delta_I & 0 & 0 \\ 0 & -(1-r)\psi & 0 & \gamma_A + \mu & 0 \\ 0 & 0 & -\phi & 0 & \gamma_H + \mu + \delta_H \end{bmatrix}, \tag{2.14}$$

with $f_{SV} = \dfrac{S^* + (1-\varepsilon_v)V^*}{N^*}$.

It is also convenient to define the quantity (where ρ is the spectral radius) [88, 89]:

$$\mathcal{R}_v = \rho(FV^{-1}) = \mathcal{R}_{v,P} + \mathcal{R}_{v,I} + \mathcal{R}_{v,A} + \mathcal{R}_{v,H}, \tag{2.15}$$

where,

$$\begin{aligned} \mathcal{R}_{v,P} &= \beta_P \left(1 - \varepsilon_v v^*\right) \frac{\sigma}{(\sigma+\mu)(\psi+\mu)}, \\ \mathcal{R}_{v,I} &= \beta_I \left(1 - \varepsilon_v v^*\right) \frac{\sigma r \psi}{(\sigma+\mu)(\psi+\mu)(\phi+\gamma_I+\mu+\delta_I)}, \\ \mathcal{R}_{v,A} &= \beta_A \left(1 - \varepsilon_v v^*\right) \frac{\sigma(1-r)\psi}{(\sigma+\mu)(\psi+\mu)(\gamma_A+\mu)}, \\ \mathcal{R}_{v,H} &= \beta_H \left(1 - \varepsilon_v v^*\right) \frac{\sigma r \psi \phi}{(\sigma+\mu)(\psi+\mu)(\phi+\gamma_I+\mu+\delta_I)(\gamma_H+\mu+\delta_H)}, \end{aligned} \tag{2.16}$$

with v^* defined as the proportion of individuals vaccinated at the disease-free equilibrium, given by

$$v^* = \frac{V^*}{N^*} = \frac{\xi_v}{\omega_v + \xi_v + \mu}, \tag{2.17}$$

from which it follows that,

$$1 - \varepsilon_v v^* = \frac{S^* + (1 - \varepsilon_v)V^*}{N^*}. \tag{2.18}$$

The quantity $\mathcal{R}_v$ is the *vaccination reproduction number* of the model (2.8). It measures the average number of new cases generated by a typical infected individual if introduced into a population almost completely consisting of susceptible and vaccinated individuals. The quantities $\mathcal{R}_{v,P}$, $\mathcal{R}_{v,I}$, $\mathcal{R}_{v,A}$, and $\mathcal{R}_{v,H}$ are the constituent vaccination reproduction numbers for the pre-symptomatic, symptomatic, asymptomatic, and hospitalized individuals, respectively. The result below follows from Theorem 2 of [88].

Theorem 2.3.1. *The disease-free equilibrium ($\mathbb{E}_0$) of the homogeneous model* (2.8)*, is locally-asymptotically stable (LAS) if $\mathcal{R}_v < 1$, and unstable if $\mathcal{R}_v > 1$.*

The epidemiological implication of Theorem 2.3.1 is that a small influx of COVID-19 cases will not generate a large outbreak in the community if $\mathcal{R}_v < 1$. The community-level transmission of the disease can be controlled if the initial number of infected individuals is small enough (i.e., if the initial conditions are in the basin of attraction of the disease-free equilibrium) and the vaccinated reproduction number ($\mathcal{R}_v$) can be brought to (and maintained at) a value less than one. It is worth mentioning that, using the definitions (2.17) and (2.18), the vaccination reproduction number ($\mathcal{R}_v$), given by (2.21), can be re-written as [61]:

$$\mathcal{R}_v = (1 - \varepsilon_v v^*)\mathcal{R}_0, \tag{2.19}$$

where,

$$\mathcal{R}_0 = \beta_P \frac{\sigma}{k_3 k_4} + \beta_I \frac{\sigma r \psi}{k_3 k_4 k_5} + \beta_A \frac{\sigma(1-r)\psi}{k_3 k_4 k_6} + \beta_H \frac{\sigma r \psi \phi}{k_3 k_4 k_5 k_7}, \tag{2.20}$$

Reproduction Numbers	Wave A	Wave B	Wave C
$\mathcal{R}_v$	0.88	2.28	3.50
$\mathcal{R}_0$	1.35	2.69	3.68

Table 2.5: Values of vaccination ($\mathcal{R}_v$) and basic ($\mathcal{R}_0$) reproduction numbers of the homogeneous model (2.8) for Waves A, B, and C [61]. These values are obtained by substituting the fixed and estimated (fitted) parameters of the model, tabulated in Tables 2.4 and 2.3, respectively, into Equations (2.19) and (2.20), respectively [61].

with,

$$\begin{aligned} &k_1 = \xi_v + \mu, \quad k_2 = \omega_v + \mu, \quad k_3 = \sigma + \mu, \quad k_4 = \psi + \mu, \\ &k_5 = \phi + \gamma_I + \mu + \delta_I, \quad k_6 = \gamma_A + \mu, \quad k_7 = \gamma_H + \mu + \delta_H. \end{aligned} \tag{2.21}$$

The quantity $\mathcal{R}_0$ is the *basic reproduction number* of the homogeneous model (2.8) (which measures the average number of new cases generated by a typical infected individual if introduced into a completely susceptible population). The values of the vaccination ($\mathcal{R}_v$) and basic ($\mathcal{R}_0$) reproduction numbers of the homogeneous model corresponding to the three waves are tabulated in Table 2.5 (this table shows a more severe epidemic during Waves B and C, in comparison to during Wave A, in line with the observed data depicted in Figure 2.2). This is in agreement with the fact that the Delta and Omicron variants, circulating during Waves B and C, were more transmissible than the Alpha variant, which was the predominant variant during Wave A [90, 91].

The relative contributions of infectious individuals in the pre-symptomatic, symptomatic, asymptomatic and hospitalized compartments in the generation of new SARS-CoV-2 cases in the community are compared by computing the percent ratios of their associated constituent vaccination reproduction numbers, $(\mathcal{R}_{v,j}/\mathcal{R}_v) \times 100\%$ (with $j = \{P, I, A, H\}$) during each of the three waves. The percent contributions computed for the four infectious classes during each of the three waves are tabulated in Table 2.6, from which it follows that the main drivers of the pandemic (for all

three waves) are the pre-symptomatic and asymptomatic individuals (accounting for a combined total of approximately 84% of all new cases during Wave A, 70% of all new cases during Wave B, and 76% of all new cases during Wave C). This result is in line with those reported in [92, 93, 94], which also showed that the main drivers of the COVID-19 pandemic (during the time periods considered in their study) were the pre-symptomatic and asymptomatic individuals. It is worth noting from Table 2.6 that the relative contribution of new cases generated by hospitalized infectious individuals is very low across the three waves (i.e., the vast majority of new SARS-CoV-2 cases were generated in the community, and not in the hospital setting).

Transmission Source	**Percent Contribution for New Cases**		
	Wave A	**Wave B**	**Wave C**
Pre-symptomatic ($\mathcal{R}_{v,P}$)	29.82%	24.94%	29.53%
Symptomatic ($\mathcal{R}_{v,I}$)	16.31%	29.23%	24.36%
Asymptomatic ($\mathcal{R}_{v,A}$)	53.86%	44.82%	46%
Hospitalized ($\mathcal{R}_{v,H}$)	0%	1%	0.12%

Table 2.6: Percentage of new SARS-CoV-2 cases generated by infectious individuals in the pre-symptomatic (P), symptomatic (I), asymptomatic (A), and hospitalized (H) compartments during Waves A-C of the SARS-CoV-2 pandemic in the United States. The percentages presented in this table are calculated by considering the relative contribution of the constituent vaccination reproduction numbers for the pre-symptomatic, symptomatic, asymptomatic, and hospitalized individuals, given respectively by $\mathcal{R}_{v,P}$, $\mathcal{R}_{v,I}$, $\mathcal{R}_{v,A}$, and $\mathcal{R}_{v,H}$, and defined in (2.16), on $\mathcal{R}_v$, during Waves A-C [61].

2.3.2.2 Global asymptotic stability of DFE of the homogeneous model: special case

The local asymptotic stability result established in Theorem 2.3.1 implies that the effective control of the disease when the vaccination reproduction number of the homogeneous model (2.8) is less than one depends on the initial sizes of the sub-populations of the model (i.e., the initial sizes of the sub-populations must lie within

the basin of attraction of the disease-free equilibrium). For such effective control to be independent of the initial sizes of the sub-populations of the model, it is necessary that the disease-free equilibrium is proved to be globally-asymptotically stable when the vaccination reproduction number is less than one. This is explored for a special case below. Consider a special case of the homogeneous model with perfect protective efficacy of the vaccine (i.e., consider the homogeneous model (2.8) with $\varepsilon_v = 1$). It is convenient to define $\tilde{\mathcal{R}}_v = \mathcal{R}_v|_{\varepsilon_v=1}$. We claim the following result [61]:

Theorem 2.3.2. *The disease-free equilibrium of the special case of the homogeneous model* (2.8) *with perfect vaccine protective efficacy (i.e.,* $\varepsilon_v = 1$*) is globally-asymptotically stable in* Ω_1 *if* $\tilde{\mathcal{R}}_v \leq s^* < 1$*, where* $s^* = S^*/N^* = \dfrac{\omega_v + \mu}{\omega_v + \xi_v + \mu} < 1$.

The proof of Theorem 2.3.2, based on using Lyapunov function theory and LaSalle's Invariance Principle [95], is given in Appendix B. The epidemiological implication of Theorem 2.3.2 is that, for the special case of the homogeneous model with perfect vaccine-derived protection against acquisition of infection (i.e., $\varepsilon_v = 1$), the disease will be eliminated if $\tilde{\mathcal{R}}_v$ can be brought down to (and maintained at) a value less than $s^* < 1$. In other words, for the special case of the homogeneous model with $\varepsilon_v = 1$, the requirement $\tilde{\mathcal{R}}_v \leq s^* < 1$ is necessary and sufficient for the effective control or elimination of the SARS-CoV-2 pandemic. The results of Theorem 2.3.2 are numerically illustrated in Figure 2.3, where all initial conditions converged to the disease-free equilibrium when the associated reproduction number ($\tilde{\mathcal{R}}_v$) is less than s^*.

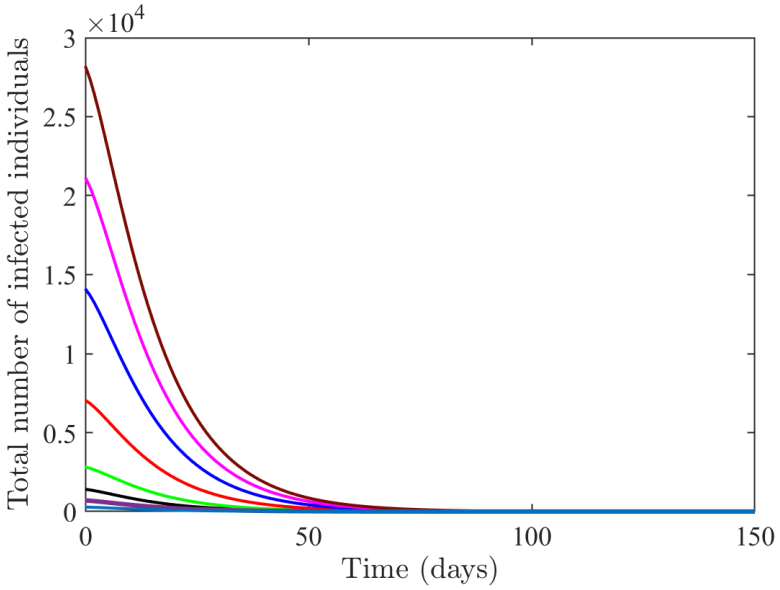

Figure 2.3: Simulations of a special case of the homogeneous model (2.8) with $\varepsilon_v = 1$, showing convergence of initial solutions to the disease-free equilibrium when $\tilde{\mathcal{R}}_v < 1$. Parameter values used in these simulations are those for Wave C, given in Tables 2.4 and 2.3, with $\varepsilon_v = 1$, $\beta_P = \beta_I = \beta_A = 0.1$ (so that, $\tilde{\mathcal{R}}_v = 0.55 < s^* = 0.93 < 1$) [61].

The global asymptotic stability of the DFE of the homogeneous model can also be established for another special case as follows. Consider a special case of the homogeneous model (2.8) with negligible disease-induced mortality (i.e., consider the model (2.8) with $\delta_I = \delta_H = 0$). Setting $\delta_I = \delta_H = 0$ in the model (2.8), and adding all the equations, gives the following equation for the rate of change of the total population:

$$\dot{N} = \Pi - \mu N, \tag{2.22}$$

from which it follows that $N(t) \to \dfrac{\Pi}{\mu}$ as $t \to \infty$. Thus, $\dfrac{\Pi}{\mu}$ is an upper bound of $N(t)$ provided that $N(0) \leq \dfrac{\Pi}{\mu}$. Furthermore, if $N(0) > \dfrac{\Pi}{\mu}$, then $N(t)$ will decrease to this value asymptotically. Consequently, we can replace $N(t)$ with its limiting value, $\dfrac{\Pi}{\mu}$. Substituting $\dfrac{\Pi}{\mu}$ for $N(t)$ in the expression for the force of infection (2.9) shows that λ reduces to:

$$\lambda^{\diamond} = \beta_P^{\diamond} P + \beta_I^{\diamond} I + \beta_A^{\diamond} A + \beta_H^{\diamond} H, \tag{2.23}$$

where,

$$\beta_j^{\diamond} = \frac{\beta_j \mu}{\Pi}, \quad \text{with } j = \{P, I, A, H\}. \tag{2.24}$$

Then, it follows from Equations (2.8), (2.12), and (2.23) that:

$$\begin{aligned}
\dot{S} &= \Pi + \omega_v V - \lambda^{\diamond} S - (\xi_v + \mu) S \\
&\leq \Pi + \omega_v V - (\xi_v + \mu) S \\
&\leq \Pi + \omega_v (\Pi/\mu - S - E - P - I - A - H - R) - (\xi_v + \mu) S \\
&\leq \frac{(\omega_v + \mu)\Pi}{\mu} - (\omega_v + \xi_v + \mu) S \\
&= (\omega_v + \xi_v + \mu)(S^* - S),
\end{aligned}$$

from which it follows that if $S > S^*$, then $\dot{S} < 0$. Hence, $S \leq S^*$ provided that $S(0) \leq S^*$. Similarly, it follows from the second equation of (2.8) that $\dot{V} \leq -(\omega_v + \mu)V + \xi_v S = (\omega_v + \mu)(V^* - V)$. If $V > V^*$, then $\dot{V} < 0$. Thus, $V \leq V^*$ provided $V(0) \leq V^*$. It follows from these bounds that the region

$$\Omega^{\diamond} = \{(S, V, E, P, I, A, H, R) \in \Omega_1 : S \leq S^*, V \leq V^*\},$$

is also positively invariant with respect to the flow generated by the homogeneous model (2.8), and attracts all solutions of the model in Ω_1.

It is convenient to define $\mathcal{R}_v^{\diamond} = \mathcal{R}_v|_{\delta_I = \delta_H = 0}$, the reproduction number of the special case of the homogeneous model with $\delta_I = \delta_H = 0$. It follows from the definition of $\mathcal{R}_v$ in (2.19), with (2.20), that:

$$\mathcal{R}_v^\diamond = (1-\varepsilon_v v^*)\left[\beta_P \frac{\sigma}{k_3 k_4} + \beta_I \frac{\sigma r \psi}{k_3 k_4 k_5^\diamond} + \beta_A \frac{\sigma(1-r)\psi}{k_3 k_4 k_6} + \beta_H \frac{\sigma r \psi \phi}{k_3 k_4 k_5^\diamond k_7^\diamond}\right], \tag{2.25}$$

where $k_5^\diamond = \phi + \gamma_I + \mu$ and $k_7^\diamond = \gamma_H + \mu$. We claim the following result [61].

Theorem 2.3.3. *Consider the homogeneous model* (2.8) *with negligible disease-induced mortality in the host population (i.e.,* $\delta_I = \delta_H = 0$*). The disease-free equilibrium of this special case of the homogeneous model* (2.8) *is globally-asymptotically stable in* $\Omega^\diamond$ *whenever* $\mathcal{R}_v^\diamond < 1$.

The proof of Theorem 2.3.3, based on using a comparison theorem [65], is given in Appendix C. The results of Theorem 2.3.3 are numerically illustrated in Figure 2.4, where all initial conditions converged to the disease-free equilibrium when the associated reproduction number ($\mathcal{R}_v^\diamond$) is less than one. Thus, based on the analyses above for the two special cases of the homogeneous model, we have identified two main mechanisms that could lead to the elimination of the pandemic (this is associated with bringing and maintaining the associated reproduction numbers of the homogeneous model to a value less than one). First, using highly efficacious vaccines, such that the vaccine protective efficacy (ε_v) approaches 100% could lead to SARS-CoV-2 elimination under the baseline parameter scenario (Theorem 2.3.2). Similarly, implementing effective therapeutic and other hospitalization measures that significantly reduce the disease-induced mortality for symptomatic and hospitalized individuals (e.g., the early detection and hospitalization of symptomatic individuals; use of highly effective drug therapies and ventilation systems etc.) can lead to the elimination of the pandemic (Theorem 2.3.3).

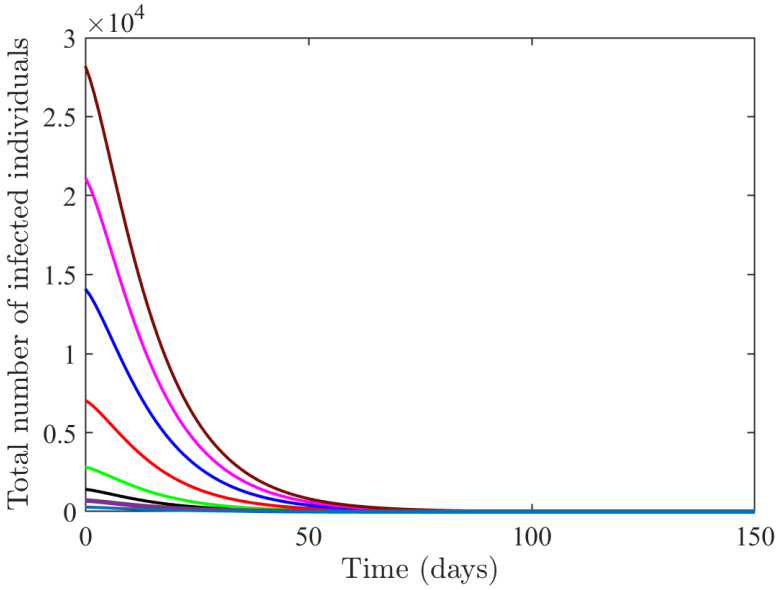

Figure 2.4: Simulations of a special case of the homogeneous model (2.8) with $\delta_I = \delta_H = 0$, showing convergence of initial solutions to the disease-free equilibrium when $\mathcal{R}_v^\diamond < 1$. Parameter values used are that of Wave C, given in Tables 2.4 and 2.3, with $\delta_I = \delta_H = 0$ and $\beta_P = \beta_I = \beta_A = 0.1$ (so that $\mathcal{R}_v^\diamond = 0.53 < 1$) [61].

2.3.3 Existence and asymptotic stability of endemic equilibria of the homogeneous model

In this section, conditions for the existence of endemic equilibria of the homogeneous model (i.e., equilibria where each of the state variable is nonzero) will be explored. Let $(S^{**}, V^{**}, E^{**}, P^{**}, I^{**}, A^{**}, H^{**}, R^{**})$ represent any arbitrary endemic equilibrium of the homogeneous model. It can be seen from (2.9) that the force of infection (λ) of the homogeneous model at an endemic equilibrium (denoted by λ^{**}) is given by [61]:

$$\lambda^{**} = \left(\frac{\beta_P P^{**} + \beta_I I^{**} + \beta_A A^{**} + \beta_H H^{**}}{N^{**}} \right). \tag{2.26}$$

$$
\begin{aligned}
S^{**} &= \frac{\Pi[(1-\varepsilon_v)\lambda^{**}+k_2]}{[(1-\varepsilon_v)\lambda^{**}+k_2](\lambda+k_1+\omega_n\tau\eta)-\omega_v\xi_v}, \quad V^{**} = \frac{\xi_v}{(1-\varepsilon_v)\lambda^{**}+k_2}S^{**},\\
E^{**} &= \eta S^{**}, \quad P^{**} = \frac{\sigma}{k_4}\eta S^{**}, \quad I^{**} = \frac{r\psi\sigma}{k_4k_5}\eta S^{**}, \quad A^{**} = \frac{(1-r)\psi\sigma}{k_4k_6}\eta S^{**},\\
H^{**} &= \frac{\phi r\psi\sigma}{k_4k_5k_7}\eta S^{**}, \quad R^{**} = \tau\eta S^{**},
\end{aligned}
\tag{2.27}
$$

where $\eta = \dfrac{\lambda^{**}\big[(1-\varepsilon_v)\lambda^{**}+k_2+(1-\varepsilon_v)\xi_v\big]}{k_3\big[(1-\varepsilon_v)\lambda^{**}+k_2\big]}$ and $\tau = \dfrac{\gamma_I}{\omega_n+\mu}\dfrac{r\psi\sigma}{k_4k_5}+\dfrac{\gamma_A}{\omega_n+\mu}\dfrac{(1-r)\psi\sigma}{k_4k_6}+\dfrac{\gamma_H}{\omega_n+\mu}\dfrac{\phi r\psi\sigma}{k_4k_5k_7}$. Substituting the expressions in (2.27) into (2.26) shows that the endemic equilibria of the homogeneous model satisfy the following quadratic equation (in terms of λ^{**}) [61]:

$$
a_2(\lambda^{**})^2 + a_1\lambda^{**} + a_0 = 0, \tag{2.28}
$$

where,

$$
\begin{aligned}
a_0 &= k_3(k_2+\xi_v)(1-\mathcal{R}_v),\\
a_1 &= [k_2+(1-\varepsilon_v)\xi_v]\rho - k_3(1-\varepsilon_v)(\mathcal{R}_0-1),\\
a_2 &= (1-\varepsilon_v)\rho,
\end{aligned}
\tag{2.29}
$$

with $\rho = 1+\dfrac{\sigma}{k_4}+\big(1+\dfrac{\gamma_I}{\mu+\omega_n}\big)\dfrac{r\psi\sigma}{k_4k_5}+\big(1+\dfrac{\gamma_A}{\mu+\omega_n}\big)\dfrac{(1-r)\psi\sigma}{k_4k_6}+\big(1+\dfrac{\gamma_H}{\mu+\omega_n}\big)\dfrac{\phi r\psi\sigma}{k_4k_5k_7} > 0$. The components of an endemic equilibrium of the homogeneous model can be obtained by solving for for λ^{**} in the quadratic equation (2.28) and substituting the result into the expressions in (2.29). Furthermore, it can be seen from (2.29) that the coefficient a_0 is positive (negative) whenever $\mathcal{R}_v < (>)1$. Similarly, the coefficient a_2 is always positive (since $0 < \varepsilon_v < 1$). The result below follows from the quadratic (2.28) with (2.29) [61].

Theorem 2.3.4. *The homogeneous model* (2.8) *has:*

(i) a unique endemic equilibrium if $a_0 < 0 \iff \mathcal{R}_v > 1$*;*

(ii) a unique endemic equilibrium if $a_1 < 0$ *and* $a_0 = 0$ *or* $a_1^2 - 4a_0a_2 = 0$*;*

(iii) two endemic equilibria if $a_2 > 0$, $a_1 < 0$, *and* $a_1^2 - 4a_0a_2 > 0$;

(iv) no endemic equilibrium otherwise.

While Case (i) of Theorem 2.3.4 implies the presence of a unique endemic equilibrium for the homogeneous model (2.8) whenever $\mathcal{R}_v > 1$, Case (iii) suggests the possibility of a *backward bifurcation*, a dynamic phenomenon characterized by the coexistence of the stable disease-free equilibrium (DFE) and a stable endemic equilibrium, when the associated vaccination reproduction number of the homogeneous model ($\mathcal{R}_v$) is less than one (see [96] for further details about the causes and consequences of backward bifurcation in the transmission dynamics of infectious diseases). It should be noted that in the case of a perfect vaccine ($\varepsilon_v = 1$), $a_2 = 0$, $a_1 > 0$ and the quadratic equation becomes linear in λ^{**} (with $\lambda^{**} = -a_0/a_1$). In this case, the homogeneous model (2.8) has a unique endemic equilibrium if and only if $a_0 > 0$ (i.e., $\mathcal{R}_v > 1$), ruling out backward bifurcation in this case (this is consistent with the result in Theorem 2.3.2, where it was shown that the disease-free equilibrium of the special case of the homogeneous model with $\varepsilon_v = 1$ is globally-asymptotically stable when the associated reproduction number is less than $s^* < 1$). It can be shown, following the approach in Section 2.3.3, that the special case of the homogeneous model (2.8) with $\delta_I = \delta_H = 0$ has a unique endemic equilibrium whenever $\mathcal{R}_v^\diamond > 1$. That is, the result below holds [61].

Theorem 2.3.5. *The special case of the homogeneous model* (2.8) *with* $\delta_I = \delta_H = 0$ *has a unique positive endemic equilibrium whenever* $\mathcal{R}_v^\diamond > 1$.

Furthermore, let $\hat{\mathcal{R}}_v = \mathcal{R}_v|_{\delta_I=\delta_H=\omega_v=\omega_n=0,\ \varepsilon=1}$. We claim the following result. We claim the following result [61].

Theorem 2.3.6. *Consider the special case of the homogeneous model* (2.8) *with negligible disease-induced mortality* (*i.e.,* $\delta_I = \delta_H = 0$)*, perfect vaccine* ($\varepsilon_v = 1$)*, and no waning* ($\omega_v = \omega_n = 0$)*. The associated unique endemic equilibrium of this special case of the homogeneous model is locally-asymptotically stable if* $\hat{\mathcal{R}}_v > 1$*.*

The proof of Theorem 2.3.6, based on using a Krasnoselskii sub-linearity argument (see [97, 98], and also [99, 100]), is given in Appendix D. The epidemiological implication of Theorem 2.3.6 is that the disease will persist in the population whenever $\mathcal{R}_v^{\diamond} > 1$. The local asymptotic stability result for the unique endemic equilibrium of the homogeneous model will be extended to global asymptotic stability for another special case as follows. It is, first of all, convenient to define the following region (the stable manifold of the disease-free equilibrium of the homogeneous model) [61]:

$$\Omega_0 = \left\{(S, V, E, P, I, A, H, R) \in \Omega_1 : E = P = I = A = H = R = 0\right\}.$$

Theorem 2.3.7. *Consider the special case of the homogeneous model* (2.8) *with negligible disease-induced mortality* (*i.e.,* $\delta_I = \delta_H = 0$)*, perfect vaccine* ($\varepsilon_v = 1$)*, and no waning* ($\omega_v \omega_n = 0$)*. The unique endemic equilibrium of this special case of the homogeneous model is globally-asymptotically stable in* $\Omega_1 \setminus \Omega_0$ *whenever* $\hat{\mathcal{R}}_v > 1$*.*

The proof of Theorem 2.3.7, based on using a nonlinear Lyapunov function of Goh-Volterra type, is given in Appendix E. The epidemiological implication of this result is that the disease will persist in the population whenever the associated reproduction threshold ($\hat{\mathcal{R}}_v$) exceeds unity. The results of Theorem 2.3.7 are numerically illustrated in Figure 2.5, where all initial conditions converged to the unique endemic equilibrium when the associated reproduction number ($\hat{\mathcal{R}}_v$) exceeds one. Although the global asymptotic stability property of the endemic equilibrium of the homogeneous model was only established for a special case, extensive numerical simulations suggest that

the endemic equilibrium of the full model is indeed globally-asymptotically stable whenever the reproduction number of the full model ($\mathcal{R}_v$) is greater than one. This suggests the following conjecture [61].

Conjecture 1. *The homogeneous model* (2.8) *has a unique and globally-asymptotically stable endemic equilibrium in* $\Omega_1 \setminus \Omega_0$ *whenever* $\mathcal{R}_v > 1$.

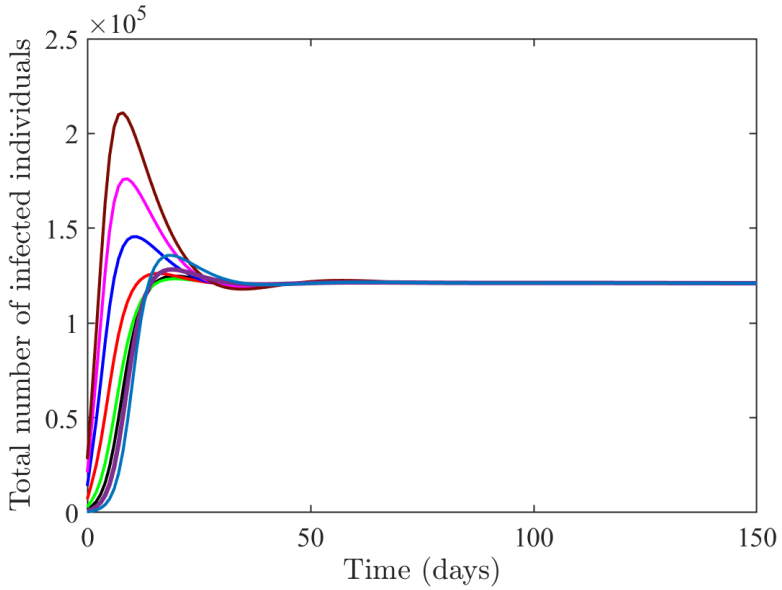

Figure 2.5: Simulations of a special case of the homogeneous model (2.8) with $\delta_I = \delta_H = \omega_v = 0$ and $\varepsilon_v = 1$, showing convergence of initial solutions to the unique endemic equilibrium when $\hat{\mathcal{R}}_v > 1$. Parameter values used are that of Wave B given in Tables 2.4 and 2.3, with $\varepsilon_v = 1$, $\delta_I = \delta_H = \omega_v = \omega_n = 0$, and $\beta_P = \beta_I = \beta_A = 2$ (so that $\hat{\mathcal{R}}_v = 1.27 > 1$) [61].

2.3.3.1 Computation of vaccine-derived herd immunity threshold for the homogeneous model

Herd immunity, also known as *mass immunity*, is a form of indirect protection from an infectious disease that occurs when a minimum percentage of the population is immune to the disease. The two main ways of achieving herd immunity are through vac-

cination and natural immunity developed through recovery from previous infection. Vaccination is the safest and fastest way to achieve herd immunity [101, 102, 103]. As noted in [21, 76], "for vaccine-preventable diseases, such as COVID-19, not every susceptible member of the community can be vaccinated. For instance people with underlying health conditions, or females who are pregnant or people who opt out of vaccination for various reasons (traditional or other reasons) may not be vaccinated". Hence, it is critical to determine the minimum proportion of susceptible individuals in the community that need to be vaccinated in order to protect the ones that cannot be vaccinated (i.e., achieve herd immunity). To obtain the herd immunity threshold, we set the vaccination reproduction number ($\mathcal{R}_v$), given by Equation (2.19), to one and solve for the proportion of individuals fully-vaccinated at steady-state (v^*) [22, 21]. Doing so gives (for $\mathcal{R}_0 > 1$ and $0 < \varepsilon_v \leq 1$):

$$v^* = \frac{1}{\varepsilon_v}\left(1 - \frac{1}{\mathcal{R}_0}\right) = v_c^*. \tag{2.30}$$

It follows from (2.19) and (2.30) that $\mathcal{R}_v < (>)1$ if $v^* > (<)v_c^*$. Further, $\mathcal{R}_v = 1$ whenever $v^* = v_c^*$. Hence, the result of Theorem 2.3.1 can be re-written in terms of the herd immunity threshold as follows:

Theorem 2.3.8. *The disease-free equilibrium ($\mathbb{E}_0$) of the homogeneous model* (2.8) *is locally-asymptotically stable if $v^* > v_c^*$ ($\mathcal{R}_v < 1$), and unstable if $v^* < v_c^*$ ($\mathcal{R}_v > 1$).*

The global asymptotic stability results for the disease-free equilibrium (given in Theorems 2.3.2 and 2.3.3) can be similarly re-written in terms of the above herd immunity threshold.

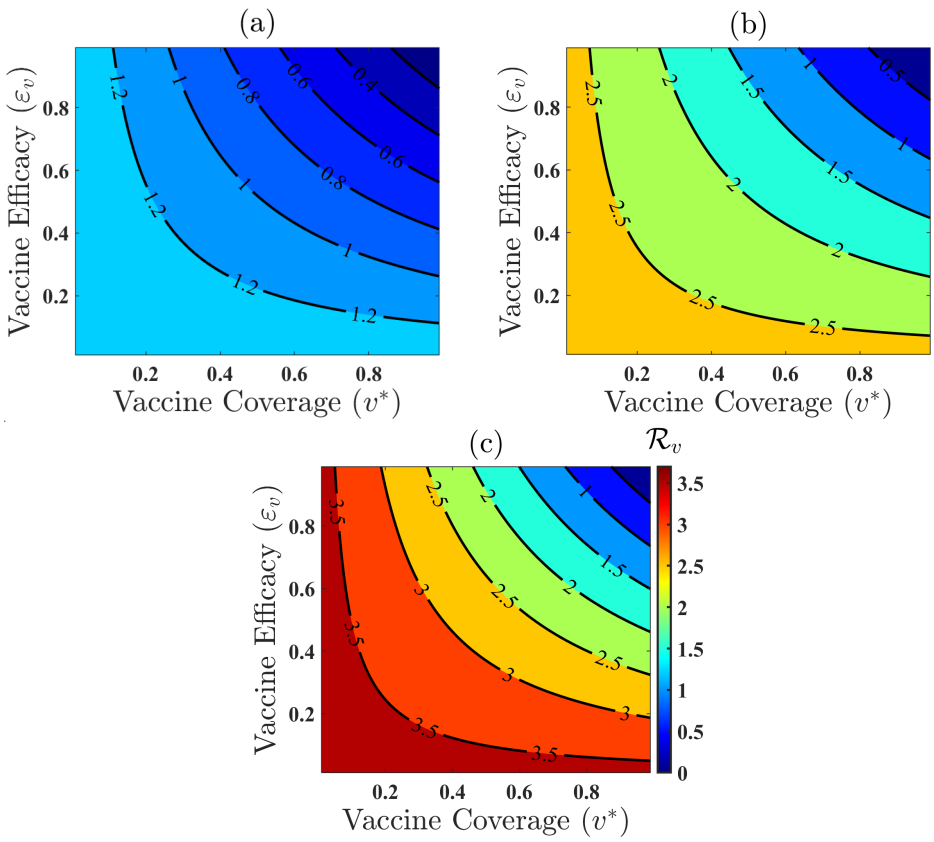

Figure 2.6: Contour plot of the vaccine reproduction number ($\mathcal{R}_v$) of the homogeneous model (2.8), as a function of vaccine coverage at steady-state (v^*) and vaccine efficacy (ε_v), for the United States during (a) Wave A, (b) Wave B, and (c) Wave C. Parameter values used to generate the contour plots for each wave are given by their respective values in Tables 2.4 and 2.3 [61]

Figure 2.6 depicts a contour plot of the vaccination reproduction number ($\mathcal{R}_v$), as a function of coverage of fully-vaccinated susceptible individuals at steady-state (v^*) and vaccine efficacy (ε_v), during Wave A-C COVID-19 wave considered in this chapter. This figure shows that using the two-dose Pfizer vaccine (with an estimated protective efficacy of 90% [82, 83]) during Wave A could lead to the effective control of the pandemic if at least 29% of the populace is fully-vaccinated (Figure 2.6(a)). The vaccine coverage required to achieve such effective control during Wave B (Figure 2.6(b)), using the same two-dose Pfizer vaccine (with an estimated efficacy of 85%

during Wave B [82, 83]), is 74%. However, these simulations show that using the same two-dose Pfizer vaccine during Wave C (with an estimated protective efficacy of 70% during this wave [82, 83]) could not reduce the control reproduction number to a value below one (which is needed for achieving the vaccine-derived herd immunity, and consequently, eliminating the disease) even if every unvaccinated susceptible individual is fully vaccinated (Figure 2.6(c)). This result can be attributed to the modest efficacy of the Pfizer vaccine (70% during Wave C [82, 83]) and a higher basic reproduction number ($\mathcal{R}_0 = 3.68$), in comparison to the reproduction numbers for Wave A ($\mathcal{R}_0 = 1.35$) and Wave B ($\mathcal{R}_0 = 2.69$).

Figure 2.6 also shows that if, on the other hand, a vaccine with moderate protective efficacy, such as the two-dose of AstraZeneca (with estimated protective efficacy of 67% [104] during Wave B) is prioritized, the coverage needed to achieve herd immunity (and, consequently, disease elimination) during Wave B (Figure 2.6(b)) is 94%. Likewise, the use of such a vaccine (with an estimated reduced efficacy of 49% during Wave C [105]) will also fail to reduce the control reproduction number below one even if the coverage in its usage is 100% during Wave C (Figure 2.6(c)).

2.3.4 Global sensitivity analysis for the homogeneous model

Global sensitivity analysis will be carried, using Latin Hypercube Sampling (LHS) and Partial Rank Correlation Coefficients (PRCCs) [106, 107, 108], on the homogeneous model (2.8) to determine the parameters that have the highest influence on the transmission dynamics of the disease (as measured by their impact on a chosen response function) during each of the three pandemic waves considered in this chapter. Specifically, the vaccination reproduction number ($\mathcal{R}_v$) is chosen as the response function. The application of this method entails using the baseline value of each of

the 18 parameters in the expression for the vaccination reproduction number (given by (2.15)), corresponding to each of the three pandemic waves, listed in Tables 2.3 and 2.4. The parameters are assumed to obey the uniform distribution, and the range of each parameter in the response function is chosen to be 40% to the left and 40% to the right of its respective baseline value [109]. The range of each parameter is subdivided into $1,000$ equal sub-intervals. Since the parameter set is drawn from this set without replacement, this leads to $1,000 \times 18$ parameter matrix (or hypercube) [109]. A parameter with a negative (positive) PRCC value is said to be negatively (positively) correlated with the response function (typically, PRCC values in the range (0.5,1) in absolute value are considered to be correlated [110], with values closer to -1 $(+1)$ signifying a much higher negative (positive) correlation).

The results obtained for the PRCC values, depicted in Figure 2.7 (see also Table 2.7), correlated with the response function (i.e., parameters with PRCC values higher than 0.5 in magnitude) during each of the three waves of the pandemic:

(a) The proportion of pre-symptomatic individuals that become symptomatic at the end of the pre-symptomatic period (r).

(b) The transmission rate of asymptomatically-infectious individuals (β_A).

(c) The recovery rate of asymptomatically-infectious individuals (γ_A).

(d) The rate at which pre-symptomatic individuals become symptomatic or asymptomatic (ψ).

(e) The transmission rate of pre-symptomatic individuals (β_P).

Hence, it follows that two parameters related to disease transmission dynamics by

asymptomatically-infectious individuals (namely, β_A and γ_A) and two parameters related to disease transmission dynamics by pre-symptomatically-infectious individuals (namely, β_P and ψ) are highly correlated with the response function ($\mathcal{R}_v$) during each of the three waves of the pandemic. Consequently, this chapter shows that intervention strategies that target pre-symptomatic and asymptomatically-infectious individuals, such as contact tracing and mass random testing (implemented with the required coverage and level of effectiveness), will consistently be very effective in combating and mitigating the SARS-CoV-2 pandemic in the United States.

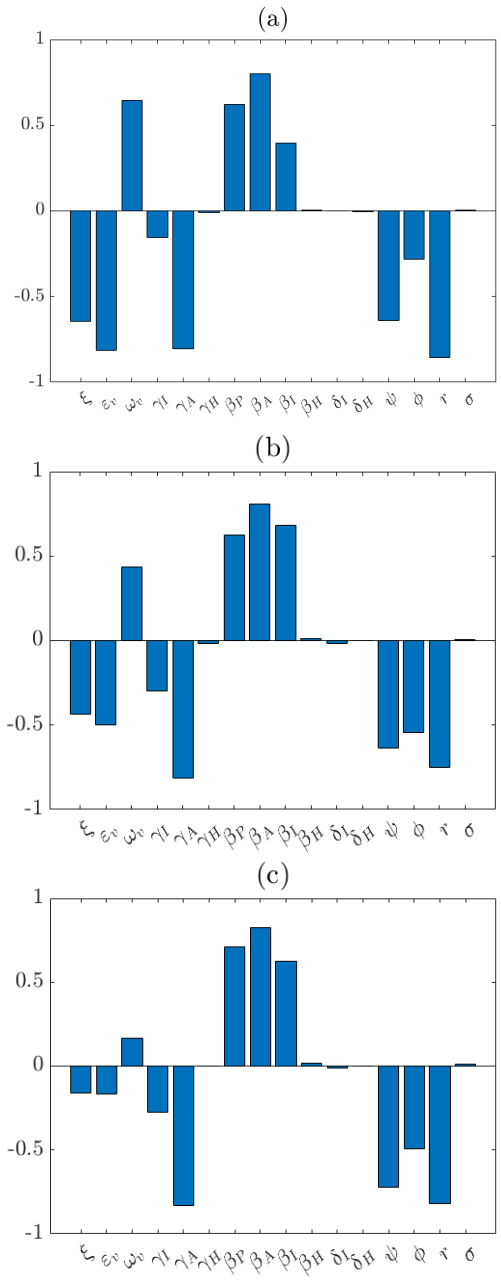

Figure 2.7: Simulations of the homogeneous model (2.8), showing the partial rank correlation coefficients (PRCCs) values of the parameters in the chosen response function ($\mathcal{R}_v$) for (a): Wave A; (b): Wave B; and (c): Wave C. Parameter values used in the simulations are as given by the baseline values in Tables 2.4 and 2.3, and their ranges are taken to be 40% to the left and 40% to the right of the respective baseline value. All parameters are assumed to follow a uniform distribution [61].

Parameter	PRCC Value		
	Wave A	**Wave B**	**Wave C**
ξ_v	$\mathbf{-0.65}$	-0.43	-0.16
ε_v	$\mathbf{-0.82}$	-0.50	-0.16
ω_v	$\mathbf{+0.65}$	$+0.43$	$+0.16$
γ_I	-0.16	-0.30	-0.27
γ_A	$\mathbf{-0.81}$	$\mathbf{-0.81}$	$\mathbf{-0.83}$
γ_H	-0.007	-0.17	-0.002
β_P	$\mathbf{+0.62}$	$\mathbf{+0.63}$	$\mathbf{+0.71}$
β_A	$\mathbf{+0.80}$	$\mathbf{+0.81}$	$\mathbf{+0.82}$
β_I	$+0.40$	$\mathbf{+0.68}$	$\mathbf{+0.62}$
β_H	$+0.007$	$+0.012$	$+0.018$
δ_I	-0.001	-0.016	-0.011
δ_H	-0.005	-0.0001	-0.001
ψ	$\mathbf{-0.64}$	$\mathbf{-0.63}$	$\mathbf{-0.72}$
ϕ	-0.28	$\mathbf{-0.54}$	-0.49
r	$\mathbf{-0.85}$	$\mathbf{-0.75}$	$\mathbf{-0.82}$
σ	$+0.005$	$+0.003$	$+0.012$

Table 2.7: PRCC values of the parameters of the homogeneous model (2.8) using the vaccination reproduction number ($\mathcal{R}_v$) as the response function for the three waves considered in this chapter. The baseline values used are the parameter values listed in Tables 2.4 and 2.3, and their ranges are taken to be 40% to the left and 40% to the right of the respective baseline value. The PRCC value of 0.5 or higher in magnitude is highlighted in bold face [61].

2.4 Two-Group Heterogeneous Model

In Section 2.3, the m-group heterogeneous model (2.3) was fitted and rigorously analyzed for the (homogeneous) case with $m = 1$. In this section, the heterogeneous model (2.3) will be used to assess the impact of age heterogeneity and variable mixing patterns on the dynamics and burden of the SARS-CoV-2 pandemic. The SARS-CoV-2 pandemic is well known to disproportionately affect the elderly population (in terms of severity of disease, hospitalization and death) [111, 112]. In particular, although the population of people 65 years and older represents less than 20% of

the total population of the United States [113], this population suffers the brunt of COVID-19 mortality (60.92%) and hospitalization (47.10%) in the United States (see Figure 2.8(a) and (b)). Specifically, it can be seen from Figure 2.8(a) that COVID-19-induced mortality *per* 100,000 people in this age group is 7.32 times higher than in the age group $0-64$. Similarly, Figure 2.8(b) shows that hospitalization *per* 100,000 in the age group 65 and older is 4.18 times that of the age group $0-64$. It is also well known that most COVID-19 cases occur among younger individuals [114, 115]. For example, data from the California Department of Public Health showed that, by May 9, 2023, 89.1% of the total reported cases of COVID-19 in California were among people 64 years of age or under [116]. This disproportionate effect of SARS-CoV-2 by age suggests the need to explicitly incorporate age structure (and the variable mixing patterns of the age groups considered) into mathematical models for the transmission dynamics and control of SARS-CoV-2 in a population. For this reason, we consider the heterogeneous model (2.3) for the case with two groups ($m = 2$) based on age. That is, we stratify the total population of the United States into those under 65 years of age (Group 1) and those 65 years and older (Group 2). Individuals in the two age groups also have variable mixing patterns with individuals in their age group, as well as with individuals in the other age group, and these variable mixing patterns need to also be incorporated into the model.

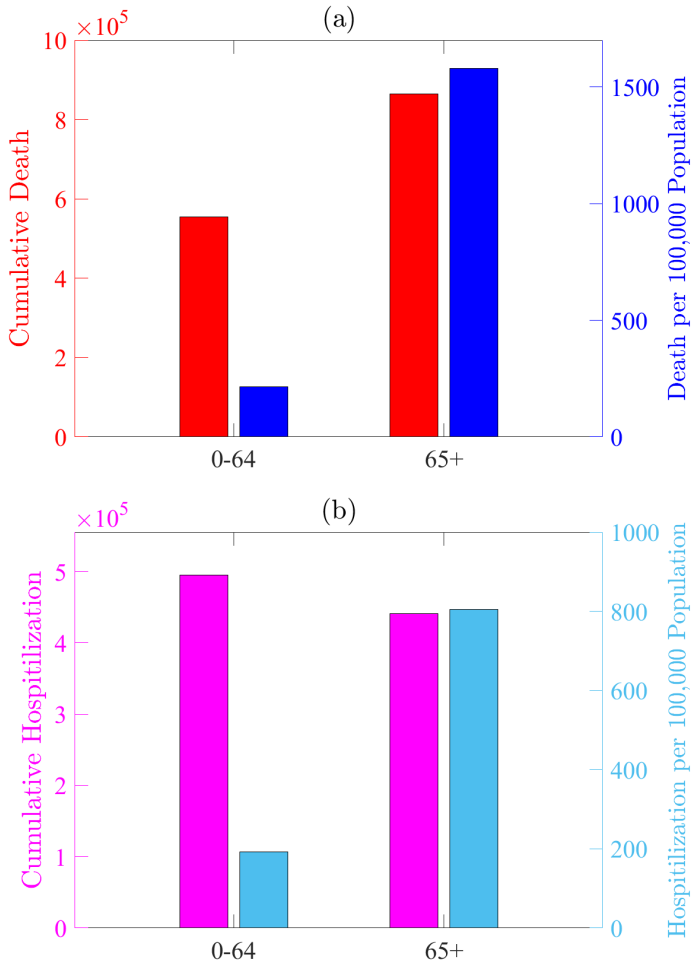

Figure 2.8: Heterogeneity of COVID-19 burden by age groups, for individuals $0-64$ years of age and those that are 65 years of age and older, in the United States until August 26, 2023. (a) Cumulative COVID-19 mortality (cumulative deaths shown in red, while cumulative deaths *per* 100,000 shown in blue) and (b) cumulative COVID-19 hospitalization (cumulative hospitalization shown in magenta, while cumulative hospitalization *per* 100,000 is shown in cyan color). The mortality data [111] used to generate this figure started in the first week of 2020, whereas the hospitalization data [112] begins in the tenth week of 2020 [61].

The main objective of this section is to determine whether or not adding these heterogeneities (age heterogeneity and the variable mixing patterns by age) significantly affects the level of the vaccine-derived herd immunity threshold needed to effectively control and mitigate the burden of the pandemic in the United States (i.e., we seek

to compare the level of herd immunity threshold generated using the heterogeneous model of two groups (2.3) with the value obtained from the homogeneous model 2.3). Let $N_k(t)$, with $k = \{1, 2\}$, be the total number of individuals in Group k at time t. This population is split into the sub-populations of susceptible ($S_k(t)$), vaccinated ($V_k(t)$), exposed ($E_k(t)$), pre-symptomatic ($P_k(t)$), symptomatic ($I_k(t)$), asymptomatic ($A_k(t)$), hospitalized ($H_k(t)$) and recovered ($R_k(t)$) individuals, so that:

$$N_k(t) = S_k(t) + V_k(t) + E_k(t) + P_k(t) + I_k(t) + A_k(t) + H_k(t) + R_k(t);\ k = \{1, 2\}.$$

The two-group age-structured model for the transmission dynamics of SARS-CoV-2 in the United States (obtained by setting $m = 2$ in (2.3)) is given by the following system of nonlinear differential equations:

$$
\begin{cases}
\dot{S}_1(t) = \Pi_1 + \omega_{v,1}V_1(t) + \omega_{n,1}R_1(t) - \lambda_1(t)S_1(t) - (\xi_{v,1} + \mu_1)S_1(t), \\
\dot{S}_2(t) = \Pi_2 + \omega_{v,2}V_2(t) + \omega_{n,2}R_2(t) - \lambda_2(t)S_2(t) - (\xi_{v,2} + \mu_2)S_2(t), \\
\dot{V}_1(t) = \xi_{v,1}S_1(t) - (1-\varepsilon_{v,1})\lambda_1(t)V_1(t) - (\omega_{v,1} + \mu_1)V_1(t), \\
\dot{V}_2(t) = \xi_{v,2}S_2(t) - (1-\varepsilon_{v,2})\lambda_2(t)V_2(t) - (\omega_{v,2} + \mu_2)V_2(t), \\
\dot{E}_1(t) = \lambda_1(t)S_1(t) + (1-\varepsilon_{v,1})\lambda_1(t)V_1(t) - (\sigma_1 + \mu_1)E_1(t), \\
\dot{E}_2(t) = \lambda_2(t)S_2(t) + (1-\varepsilon_{v,2})\lambda_2(t)V_2(t) - (\sigma_2 + \mu_2)E_2(t), \\
\dot{P}_1(t) = \sigma_1 E_1(t) - (\psi_1 + \mu_1)P_1(t), \\
\dot{P}_2(t) = \sigma_2 E_2(t) - (\psi_2 + \mu_2)P_2(t), \\
\dot{I}_1(t) = r_1\psi_1 P_1(t) - (\phi_1 + \gamma_{I,1} + \mu_1 + \delta_1)I_1(t), \\
\dot{I}_2(t) = r_2\psi_2 P_2(t) - (\phi_2 + \gamma_{I,2} + \mu_2 + \delta_2)I_2(t), \\
\dot{A}_1(t) = (1-r_1)\psi_1 P_1(t) - (\gamma_{A,1} + \mu_1)A_1(t), \\
\dot{A}_2(t) = (1-r_2)\psi_2 P_2(t) - (\gamma_{A,2} + \mu_2)A_2(t), \\
\dot{H}_1(t) = \phi_1 I_1(t) - (\gamma_{H,1} + \mu_1 + \delta_{H,1})H_1(t), \\
\dot{H}_2(t) = \phi_2 I_2(t) - (\gamma_{H,2} + \mu_2 + \delta_{H,2})H_2(t), \\
\dot{R}_1(t) = \gamma_{I,1}I_1(t) + \gamma_{A,1}A_1(t) + \gamma_{H,1}H_1(t) - (\omega_{n,1} + \mu_1)R_1(t), \\
\dot{R}_2(t) = \gamma_{I,2}I_2(t) + \gamma_{A,2}A_2(t) + \gamma_{H,2}H_2(t) - (\omega_{n,2} + \mu_2)R_2(t),
\end{cases}
\tag{2.31}
$$

where λ_k is the *force of infection* for group k, and is given by (the parameters in the model (2.31) and the expression 2.32 are as defined in Table 2.2 with $k = \{1, 2\}$):

$$
\lambda_k = \sum_{l=1}^{2} a_k c_{kl} \left[\frac{\beta_{P,l}P_l(t) + \beta_{I,l}I_l(t) + \beta_{A,l}A_l(t) + \beta_{H,l}H_l(t)}{N_l(t)} \right]; \quad k = \{1, 2\}. \tag{2.32}
$$

It can be shown (using the approach in Section 2.3.2.2) that the region:

$$\Omega_2 = \Bigg\{ \big(S_1, S_2, V_1, V_2, E_1, E_2, P_1, P_2, I_1, I_2, A_1, A_2, H_1, H_2, R_1, R_2\big) \in \mathbb{R}_+^{16} : \\ N_1(t) \leq \frac{\Pi_1}{\mu_2},\, N_2(t) \leq \frac{\Pi_2}{\mu_2} \Bigg\}, \tag{2.33}$$

is positively-invariant and attracting with respect to the two-group model (2.31). Thus, it is sufficient to study the dynamics of the model in Ω_2 (where it is well-posed mathematically and epidemiological).

2.4.1 Contact matrix and parameterization for the two-group model

Before analyzing the qualitative dynamics of the two-group model, with respect to the existence and asymptotic stability of its equilibria, we will first discuss the derivation of the associated contact matrix as well as the values of the fixed and estimated parameters of the model, as follows.

2.4.1.1 Contact matrix

Using a large cross-sectional survey in eight European countries from 2005 to 2006 (as part of the EU-funded POLYMOD project [117]), Mossong *et al.* [118] showed that "contact patterns were highly assortative with age" (specifically, "schoolchildren and young adults, in particular, tended to mix with people of the same age"). Prem *et al.* [119] used the data from [118], together with a Bayesian hierarchical model (using Markov chain Monte Carlo simulation), to estimate the age-and-location-specific contact patterns in 144 other countries across the globe, including the United States. Furthermore, the Prem *et al.* [119] study provided a 16×16 contact matrix that accounts for the general mixing patterns between sixteen age groups in the United

States. Since this chapter considers two age-groups only (under 65 and 65 and older), we will use the data in the 16×16 contact matrix (given in Prem *et al.* [119]) and adapt it to the 2×2 contact matrix for the variable mixing patterns between our two age groups. Specifically, In order to accomplish this reduction, the total population of each of the 16 age groups will be used as a "weight", and weighted averages of the number of contacts made by individuals in this age group are computed and used to generate the entries of the reduced 2×2 contact matrix. The resulting contact matrix, E, is depicted in Figure 2.9, where the entries e_{ij}, with $i \neq j$, represents the number of contacts *per* day an individual in age group i make with individuals in age group j, while e_{ii} ($i = \{1, 2\}$) represents the number of contacts *per* day an individual in age group i make with individuals in the same age group).

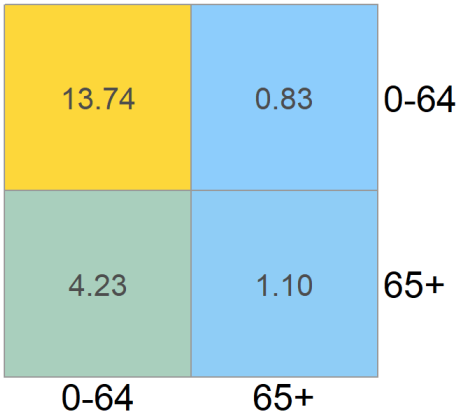

Figure 2.9: Contact matrix accounting for the number of contacts made by individuals in Group 1 (age group 0 to 64 years of age) and Group 2 (age group 65 years of age and older) *per* day.

It is worth noting that the contact-related term $a_k c_{k,l}$ in the equation for the force of infection, λ, given by (2.32) (with a_k and $c_{k,l}$ as defined in Table 2.2) can be expressed in terms of the entries of the contact matrix E as:

$$a_k c_{kl} = e_{kl}, \quad k, l = \{1, 2\}. \tag{2.34}$$

Hence, Equation 2.34 allows for the computation of the force of infection, λ, using the entries of the age-stratified mixing matrix, E.

2.4.1.2 Estimated (fitted) and fixed parameters

In this section, the derivation of the values of the estimated (fitted) and fixed parameters of the two-group model (2.31) will be discussed. For convenience, we only fit the two-group model with the cumulative mortality data corresponding to wave C of the SARS-CoV-2 pandemic in the United States (and not data during previous waves A and B; we choose wave C for illustrative purposes). It should be recalled from Section 2.3.1 that we fitted six parameters for the homogeneous model (2.8), namely the disease-induced mortality rates (δ_I and δ_H) and the effective contact rates (β_P, β_I, β_A and β_H). For the two-group model (2.31), we will also fit the parameters related to the disease-induced mortality (i.e., $\delta_{I,1}$, $\delta_{I,2}$, $\delta_{H,1}$, and $\delta_{H,2}$) and those related to the effective contact rates. Since the effective contact rate parameters for the two-group model (2.31) are defined in terms of the product of the inter- and extra-group contact rates of individuals in the two age groups *per* day (a_1c_{11}, a_1c_{12}, a_2c_{21} and a_2c_{22}) and the probability of transmission *per* contact for the infectious compartments ($\mathcal{P}_{P,1}$, $\mathcal{P}_{P,2}$, $\mathcal{P}_{I,1}$, $\mathcal{P}_{I,2}$, $\mathcal{P}_{A,1}$, $\mathcal{P}_{A,2}$, $\mathcal{P}_{H,1}$ and $\mathcal{P}_{H,2}$), and the contact rates are known from the contact matrix E (Figure 2.9), we only need to fit the aforementioned transmission probabilities. Furthermore, since it is reasonable to assume that no significant SARS-CoV-2 transmission (if at all) occurs in hospitals during wave C of the pandemic in the United States, the transmission probabilities $\mathcal{P}_{H,1}$ and $\mathcal{P}_{H,2}$ can be set to zero (it is worth recalling that the estimated value of the effective contact rate for

SARS-CoV-2 transmission in hospital for the homogeneous model, given in Table 2.3, was very low. This justifies the assumption to set the transmission probabilities for SARS-CoV-2 in the hospital to zero for the two-group model). Furthermore, we make the simplifying assumption that the probability of transmission for presymptomatic and asymptomatic individuals, for both age groups, *per* contact is the same. That is, we assume $\tilde{\mathcal{P}} := \mathcal{P}_{P,1} = \mathcal{P}_{P,2} = \mathcal{P}_{A,1} = \mathcal{P}_{A,2}$ (hence, we only need to fit three transmission probabilities). Thus, in summary, we are fitting seven parameters of the two-group model (namely, $\delta_{I,1}$, $\delta_{I,2}$, $\delta_{H,1}$, $\delta_{H,2}$, $\tilde{\mathcal{P}}$, $\mathcal{P}_{I,1}$, and $\mathcal{P}_{I,2}$).

The two-group model (2.31) is used to fit the cumulative mortality of COVID-19 in the United States during wave C. The same data source [73] and fitting procedure used for the homogeneous model (see Section 2.3.1 for details on the fitting of the homogeneous model to the data) are used here as well. Figure 2.10(a) depicts the result obtained for fitting the two-group model with the cumulative mortality data for SARS-CoV-2 during wave C in the United States, and the estimated values of the seven fitted parameters are tabulated in Table 2.9. The goodness of fit of Figure 2.10(a) is assessed by plotting the predicted daily mortality and the predicted 7-day rolling averages, against the observed daily SARS-CoV-2 mortality data and the observed 7-day rolling average data (shown in Figure 2.10(b) and Figure 2.10(c), respectively), showing a reasonably good fit, particularly the 7-day rolling average Figure 2.10(c). In fact, the predicted 7-day rolling average appears to capture the peaks of the pandemic better than the predicted daily mortality for both the homogeneous and the two-group models (see Figures 2.2 and 2.10, respectively). This may be due to the delay in reporting of SARS-CoV-2 mortality over the weekend (Bergman *et al.* [120] noted that the inclusion of previously unaccounted mortality data from weekends into weekday mortality data can result in an increase in reported deaths

on weekdays.) Consequently, this result suggests that the goodness of fit of models to cumulative SARS-CoV-2 mortality data (and, consequently, improved parameter estimation) can be improved by using 7-day rolling average mortality data, rather than daily mortality data (in other words, 7-day daily mortality data should be used to improve the goodness of fit of models for the next pandemic of COVID-like respiratory pathogen). This suggestion is in line with [121] which proposes that a 7-day average approach can help smooth out daily fluctuation in data and thus "prevent major events (such as a change in reporting methods) from skewing the data".

Parameter	**Value**		**Source**
	Group 1	**Group 2**	
Π_k	$9,622$ day^{-1}	$2,048$ day^{-1}	[113]
μ_k	$1/(64 \times 365)$ day^{-1}	$1/(18.4 \times 365)$ day^{-1}	[75, 122]
r_k	0.56 (dimensionless)	0.803 (dimensionless)	[123, 76, 77, 78]
$1 - r_k$	0.44 (dimensionless)	0.197 (dimensionless)	[123, 26, 78]
ϕ_k	$1/6.69$ day^{-1}	$1/3.78$ day^{-1}	[124]
$\gamma_{I,i}$	$1/10$ day^{-1}	$1/10$ day^{-1}	[79]
$\gamma_{A,k}$	$1/5$ day^{-1}	$1/5$ day^{-1}	[80]
$\omega_{v,k}$	$1/(9 \times 30)$ day^{-1}	$1/(9 \times 30)$ day^{-1}	[24]
$\omega_{n,k}$	$1/(9 \times 30)$ day^{-1}	$1/(9 \times 30)$ day^{-1}	[24]
$\xi_{v,k}$	0.000418 day^{-1}	0.000102 day^{-1}	[81]
$\varepsilon_{v,k}$	0.70 (dimensionless)	0.70 (dimensionless)	[82, 83]
σ_k	$1/1.92$ day^{-1}	$1/1.92$ day^{-1}	[84, 85]
ψ_k	$1/1.5$ day^{-1}	$1/1.5$ day^{-1}	[76, 84, 86, 85]
$\gamma_{H,k}$	$1/3.9$ day^{-1}	$1/6.2$ day^{-1}	[87]

Table 2.8: Values of the fixed parameters of the two-group model (2.31) for Waves C. Group 1 ($k = 1$) corresponds to individuals age 0 to 64 while group 2 ($k = 2$) corresponds to individuals age 65 and older [61].

Parameter	Value
$\mathcal{P}_{P,1}$, $\mathcal{P}_{P,2}$, $\mathcal{P}_{A,1}$, $\mathcal{P}_{A,2}$	0.092 (dimensionless)
$\mathcal{P}_{I,1}$	0.062 (dimensionless)
$\mathcal{P}_{I,2}$	0.054 (dimensionless)
$\delta_{I,1}$	2.806×10^{-4} day^{-1}
$\delta_{I,2}$	2.836×10^{-4} day^{-1}
$\delta_{H,1}$	4.015×10^{-4} day^{-1}
$\delta_{H,2}$	5.281×10^{-4} day^{-1}

Table 2.9: Table of estimated (fitted) parameters of the two-group heterogeneous model (2.31) generated by fitting the model with the observed cumulative mortality data for the United States during Waves C [61].

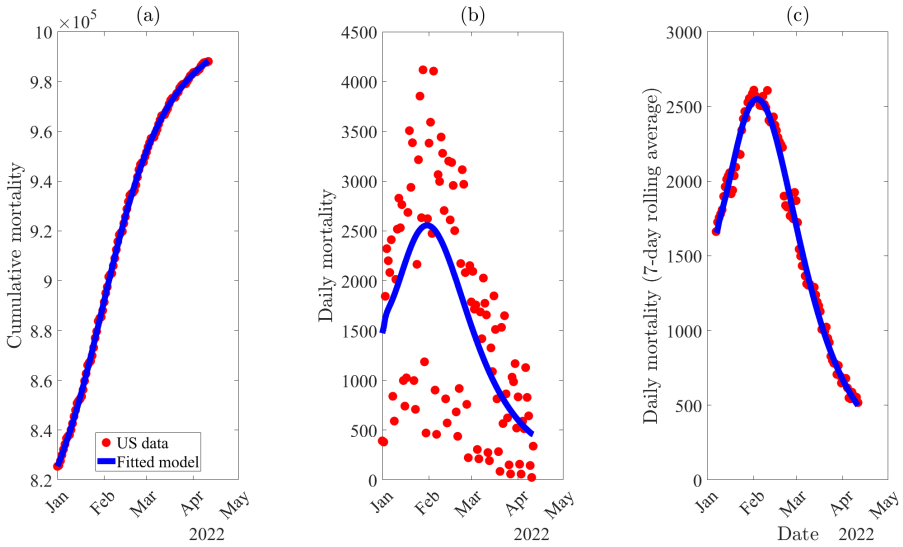

Figure 2.10: (a) Time series illustrations of the least square fit of the two-group model (2.31), showing the model's output for the cumulative COVID-19 mortality compared to the observed cumulative mortality for the United States during the time periods associated with Wave C. (b) The simulation result of the model (2.31), showing the daily COVID-19 mortality cases for the United States as a function of time, using the fixed (see Table 2.8) and estimated parameter (see Table 2.9) associated with Wave C. (c) The simulation result displaying seven-day rolling average of daily mortality for Wave C. Red dots indicate data points, while the solid blue line represents output from the model [61].

2.4.2 Asymptotic stability of the DFE of the two-group model

The two-group model (2.31) has a unique disease-free equilibrium given by:

$$\begin{aligned}(S_1^*, S_2^*, V_1^*, V_2^*, E_1^*, E_2^*, P_1^*, P_2^*, A_1^*, A_2^*, I_1^*, I_2^*, H_1^*, H_2^*, R_1^*, R_2^*)\\ = (S_1^*, S_2^*, V_1^*, V_2^*, 0, 0, 0, 0, 0, 0, 0, 0, 0, 0, 0, 0),\end{aligned} \tag{2.35}$$

where,

$$S_k^* = \frac{\Pi_k(\omega_{v,k} + \mu_k)}{\mu_k(\omega_{v,k} + \mu_k + \xi_{v,k})} \quad \text{and} \quad V_k^* = \frac{\Pi_k \xi_{v,k}}{\mu_k(\omega_{v,k} + \mu_k + \xi_{v,k})}, \text{ with } k = \{1, 2\}.$$

The asymptotic stability of the DFE will be explored using the next generation operator method [88, 89](as in Section 2.3.2). Following Elbasha and Gumel [60], we make the simplifying assumption that the population in each of the two groups (N_k, with $k = \{1, 2\}$) has reached an equilibrium state. That is, we assume that:

$$N_k^* = N_k(0) = \frac{\Pi_k}{\mu_k}, \quad k = \{1, 2\}.$$

Furthermore, following Elbasha and Gumel [60], it is convenient to express the proportion of vaccinated individuals in group k (with respect to the total population), denoted by v_k^*. That is,

$$v_k^* = \frac{V_k^*}{N_1^* + N_2^*} = \frac{N_k^*}{N_1^* + N_2^*} \times \frac{V_k^*}{N_k^*} = n_k^* \times \frac{\xi_{v,k}}{\omega_{v,k} + \mu_k + \xi_{v,k}}, \ k = \{1, 2\} \tag{2.36}$$

where,

$$n_k^* = \frac{N_k^*}{N_1^* + N_2^*} \tag{2.37}$$

is the fraction of individuals in group k.

The derivation of the vaccination reproduction number of the two-group model (denoted by $\mathcal{R}_v^\dagger$), using the next generation operator method, is presented in Appendix

F. It follows from Equation F.1 that the vaccination reproduction number for the two-group model (2.31) is given by

$$\mathcal{R}_v^\dagger = \frac{1}{2}\left(\Delta_1 + \sqrt{\Delta_1^2 - 4\Delta_2}\right), \tag{2.38}$$

where,

$$\begin{aligned}\Delta_1 &= (1 - v_1^*\varepsilon_{v,1})\mathcal{R}_{11}^\dagger + (1 - v_2^*\varepsilon_{v,2})\mathcal{R}_{22}^\dagger,\\ \Delta_2 &= (1 - v_1^*\varepsilon_{v,1})(1 - v_2^*\varepsilon_{v,2})(\mathcal{R}_{12}^\dagger\mathcal{R}_{21}^\dagger - \mathcal{R}_{11}^\dagger\mathcal{R}_{22}^\dagger),\end{aligned} \tag{2.39}$$

with $\mathcal{R}_{11}^\dagger$, $\mathcal{R}_{12}^\dagger$, $\mathcal{R}_{21}^\dagger$, and $\mathcal{R}_{22}^\dagger$ defined by

$$\mathcal{R}_{kl}^\dagger = \mathcal{R}_{kl,P}^\dagger + \mathcal{R}_{kl,I}^\dagger + \mathcal{R}_{kl,A}^\dagger + \mathcal{R}_{kl,H}^\dagger, \quad k,l = \{1,2\}, \tag{2.40}$$

where,

$$\begin{aligned}\mathcal{R}_{kl,P}^\dagger &= a_k c_{kl}\beta_{k,P}\frac{\sigma_l}{(\sigma_l+\mu_l)(\psi_l+\mu_l)},\\ \mathcal{R}_{kl,I}^\dagger &= a_k c_{kl}\beta_{k,I}\frac{\sigma_l r_l\psi_l}{(\sigma_l+\mu_l)(\psi_l+\mu_l)(\phi_l+\gamma_{l,I}+\delta_{l,I}+\mu_l)},\\ \mathcal{R}_{kl,A}^\dagger &= a_k c_{kl}\beta_{k,A}\frac{\sigma_l(1-r_l)\psi_l}{(\sigma_l+\mu_l)(\psi_l+\mu_l)(\gamma_A+\mu)},\\ \mathcal{R}_{kl,H}^\dagger &= a_k c_{kl}\beta_{k,H}\frac{\sigma_l r\psi_l\phi_l}{(\sigma_l+\mu_l)(\psi_l+\mu_l)(\phi_l+\gamma_{l,I}+\delta_{l,I}+\mu_l)(\gamma_{l,H}+\delta_{l,H}+\mu_l)}.\end{aligned} \tag{2.41}$$

The quantity $\mathcal{R}_{kl}^\dagger$, defined in (2.40), is the *constituent reproduction number* associated with disease transmission by individuals in group k to those in group l, while the quantities $\mathcal{R}_{kl,P}^\dagger, \mathcal{R}_{kl,I}^\dagger, \mathcal{R}_{kl,A}^\dagger$, and $\mathcal{R}_{kl,H}^\dagger$, given in (2.41), represent the constituent reproduction numbers associated with disease transmission between groups k and l by infectious individuals in the P, I, A and H compartments.

The result below follows from Theorem 2 of [88].

Theorem 2.4.1. *The disease-free equilibrium, given by* (2.31)*, of the two-group model* (2.31) *is locally-asymptotically stable (LAS) in* Ω_2 *whenever* $\mathcal{R}_v^\dagger < 1$*, and unstable if* $\mathcal{R}_v^\dagger > 1$*.*

Using Equation (2.38), the vaccination reproduction number for the two-group model (2.31) during Wave C is calculated to be 2.96.

It should be mentioned that the *basic reproduction number* ($\mathcal{R}_0$) associated with the two-group model (2.31) can be obtained by setting the vaccination-related parameters in Equation (2.38) to zero (i.e., $v_1^* = v_2^* = 0$) [60]:

$$\mathcal{R}_0^\dagger = \frac{1}{2}\left[\mathcal{R}_{11}^\dagger + \mathcal{R}_{22}^\dagger + \sqrt{(\mathcal{R}_{11}^\dagger + \mathcal{R}_{22}^\dagger)^2 - 4\mathcal{R}_{12}^\dagger \mathcal{R}_{21}^\dagger}\right]. \tag{2.42}$$

The local asymptotic stability result (Theorem 2.4.1) can be extended to global asymptotic stability for a special case of the two-group model, as follows. Consider a special case of the two-group model (2.31) with negligible disease-induced mortality (i.e., set $\delta_{I,1} = \delta_{I,2} = \delta_{H,1} = \delta_{H,2} = 0$). Using the approach in Section 2.3.2.2, it can be shown that the feasible region

$$\Omega_2^\Delta = \left\{ \begin{array}{l} (S_1, S_2, V_1, V_2, E_1, E_2, P_1, P_2, I_1, I_2, A_1, A_2, H_1, H_2, R_1, R_2) \\ \in \mathbb{R}_+^{16} : S_1 < S_1^*, S_2 < S_2^*, V_1 < V_1^*, V_2 < V_2^* \end{array} \right\},$$

is positively-invariant with respect to the flow generated by the two-group model (2.31), and attracts all solutions of the model that reside in the region Ω_2. It is convenient to define $\mathcal{R}_v^\Delta = \mathcal{R}_v^\dagger|_{\delta_{I,k}=\delta_{H,k}=0}$ (with $k = \{1, 2\}$), the reproduction number of the special case of the two-group model (2.31) with $\delta_{I,k} = \delta_{H,k} = 0$ (with $k = \{1, 2\}$). We claim the following result.

Theorem 2.4.2. *The disease-free equilibrium of the special case of the two-group model* (2.31) *with negligible disease-induced mortality (i.e.,* $\delta_{I,k} = \delta_{H,k} = 0$*, with* $k = \{1, 2\}$*), given by* (2.35)*, is globally-asymptotically stable in* Ω_2^Δ *whenever* $\mathcal{R}_v^\Delta < 1$.

The proof of Theorem 2.3.3, based on using a comparison theorem [65], is given in Appendix G. Like in the case of Theorem 2.3.3 for the special case of the homogeneous

model without disease-induced mortality, the epidemiological implication of Theorem 2.4.2 is that, for the special case of the two-group model without disease-induced mortality, bringing (and maintaining) the reproduction threshold ($\mathcal{R}_v^{\Delta}$) to a value less than one is necessary and sufficient for the elimination of the pandemic in the population. Therefore, this result shows that the implementation of a vaccination program that can bring (and maintain) the reproduction threshold, $\mathcal{R}_v^{\Delta}$, to a value below one will lead to the elimination of the pandemic in the United States.

Owing to the assortative mixing pattern shown by the data used to generate Figure 2.9, it can be seen, using the expressions for the constituent reproduction numbers (2.40), that the transmission of COVID-19 occurs more due to mixing within each group than mixing between groups. That is, the following inequality holds (as a natural consequence of the assortative mixing in favor of within-group mixing):

$$\mathcal{R}_{11}^{\dagger}\mathcal{R}_{22}^{\dagger} > \mathcal{R}_{12}^{\dagger}\mathcal{R}_{21}^{\dagger}.$$

It should also be noted from Equations (2.40) and (2.41) that the mixing terms (a_k and c_{kl}) determine the sign of the expression of $\mathcal{R}_{11}^{\dagger}\mathcal{R}_{22}^{\dagger} - \mathcal{R}_{12}^{\dagger}\mathcal{R}_{21}^{\dagger}$. Specifically, as shown by Elbasha and Gumel [60],

$$\operatorname{sign}\big(\mathcal{R}_{11}^{\dagger}\mathcal{R}_{22}^{\dagger} - \mathcal{R}_{12}^{\dagger}\mathcal{R}_{21}^{\dagger}\big) = \operatorname{sign}\big(a_1c_{11}a_2c_{22} - a_1c_{12}a_2c_{21}\big), \tag{2.43}$$

from which, using (2.34), it follows that

$$\operatorname{sign}\big(\mathcal{R}_{11}^{\dagger}\mathcal{R}_{22}^{\dagger} - \mathcal{R}_{12}^{\dagger}\mathcal{R}_{21}^{\dagger}\big) = \operatorname{sign}\big(e_{11}e_{12} - e_{12}e_{21}\big). \tag{2.44}$$

Thus, the entries of the mixing matrix (Figure 2.9) determine the biased assortative

nature of the mixing patterns (in favor of within-group mixing) in the population.

2.4.3 Vaccine-derived herd immunity threshold for the two-group model

In this section, the result of Theorem 2.4.2 will be used to compute an expression for the vaccine-derived herd immunity threshold (HIT) needed to eliminate the pandemic using the two-group model. The objective is to determine whether the level of vaccine-derived HIT obtained using the two-group model differs from the HIT value obtained for the homogeneous model (given in Section 2.3.3.1). The approach here follows closely the approach introduced by Elbasha and Gumel [60]. Specifically, in order to compute the HIT for the two-group model, it is convenient to re-write the proportion of vaccinated individuals at steady-state as [60]:

$$\frac{V_1^* + V_2^*}{N_1^* + N_2^*} = \left(\frac{N_1^*}{N_1^* + N_2^*}\right)\frac{V_1^*}{N_1^*} + \left(\frac{N_2^*}{N_1^* + N_2^*}\right)\frac{V_2^*}{N_2^*} = n_1^* v_1^* + n_2^* v_2^*, \tag{2.45}$$

where n_k^* and v_k^* are defined by Equations (2.37) and (2.36), respectively. Hence, following Elbasha and Gumel [60], the computation of the vaccine-derived HIT for the two-group model (2.31) entails solving the following optimization problem [60]:

$$\text{minimize}(n_1^* v_1^* + n_2^* v_2^*) \quad \text{subject to,} \quad 0 \leq v_1^*, v_2^* \leq 1, \mathcal{R}_v^\dagger \leq 1. \tag{2.46}$$

Since individuals in each of the two age groups continued to receive SARS-CoV-2 vaccines in the United States during wave C of the pandemic (i.e., $0 \leq v_1^*, v_2^* \leq 1$), and considering the fact that contact matrix 2.9 produces biased assortative mixing (i.e., $\mathcal{R}_{11}^\dagger \mathcal{R}_{22}^\dagger > \mathcal{R}_{12}^\dagger \mathcal{R}_{21}^\dagger$), the HIT for Wave C is given by (the derivation of this expression is given in [60], and not repeated here):

$$n_1^* v_1^* + n_2^* v_2^* = \frac{\varepsilon_1 n_2^* (\mathcal{R}_{11}^\dagger + \mathcal{R}_{12}^\dagger \mathcal{R}_{21}^\dagger - \mathcal{R}_{22}^\dagger \mathcal{R}_{11}^\dagger) + \varepsilon_2 n_1^* (\mathcal{R}_{22}^\dagger + \mathcal{R}_{12}^\dagger \mathcal{R}_{21}^\dagger - \mathcal{R}_{22}^\dagger \mathcal{R}_{11}^\dagger) - 2\sqrt{\varepsilon_1 n_2^* \varepsilon_2 n_1^* \mathcal{R}_{12}^\dagger \mathcal{R}_{21}^\dagger}}{\varepsilon_1 \varepsilon_2 (\mathcal{R}_{12}^\dagger \mathcal{R}_{21}^\dagger - \mathcal{R}_{11}^\dagger \mathcal{R}_{22}^\dagger)}. \quad (2.47)$$

Substituting the values of constituent reproduction numbers ($\mathcal{R}_{11}^\dagger$, $\mathcal{R}_{12}^\dagger$, $\mathcal{R}_{21}^\dagger$ and $\mathcal{R}_{22}^\dagger$), vaccine efficacy (ε_1 and ε_2) and the fraction of the total population that belongs to a group (n_1^* and n_2^*) into the right-hand side of Equation 2.47 shows that the value of HIT for the two-group model is $n_1^* v_1^* + n_2^* v_2^* = 0.61$. That is, the computation in this section shows that, using the two-group model (2.31), vaccine-derived herd immunity can be achieved in the United States if at least 61% of the population is fully vaccinated. It should be recalled that, for the homogeneous model (2.8), it was shown that vaccine-derived herd immunity could not be achieved during Wave C even if all unvaccinated susceptible individuals were fully vaccinated during that wave. Thus, this chapter shows that adding age-related heterogeneity into a homogeneous model for SARS-CoV-2 pandemic that includes a vaccination significantly reduces the vaccination coverage needed to eliminate the disease. This result is consistent with [60] where it was theoretically shown that the value of the herd immunity threshold obtained using the (two-group) heterogeneous model was smaller than that obtained using the (one-group) homogeneous model.

2.5 Discussion and Conclusions

This chapter is based on using mathematical modeling approaches, together with data analytics and computation, to unravel the combined population-level impacts of the disproportionate effect of the SARS-CoV-2 pandemic on the elderly (i.e., age heterogeneity and associated mixing patterns), which represents the highest risk group [125], and vaccination on the transmission dynamics and control of the SARS-CoV-2 pandemic in the United States. The objective of this chapter was achieved *via* the

design of a generalized multigroup mathematical model, which takes the form of a deterministic system of nonlinear differential equations for the temporal dynamics of the disease within a population with m heterogeneous subgroups (the m heterogeneous sub-populations could represent various heterogeneities, such as heterogeneities with respect to age, risk of acquiring infection, mixing patterns, socioeconomic status etc.). The m-group model was shown to be well-posed mathematically and epidemiologically, by rigorously establishing the boundedness and invariance of its solutions. A special case of the model with homogeneous mixing (i.e., the model with $m = 1$) was considered first of all. The disease-free equilibrium of this (*homogeneous*) model was shown to be locally-asymptotically stable whenever a certain epidemiological threshold, known as the *vaccination reproduction number*, is less than one. The implication of this result is that the vaccination program implemented in the United States could lead to the elimination of the pandemic if the reproduction number could be brought to (and maintained at) a value less than one, provided the initial number of infected individuals is small enough.

The homogeneous model was fitted using the observed cumulative mortality data for the United States during three waves of the pandemic. The three waves (denoted Wave A, B and C) correspond to the time periods when the pandemic was mostly dominated by the Alpha, Delta and Omicron variants, respectively. The calibrated model was used to estimate the unknown parameters of the homogeneous model and to compute the level of vaccine-derived herd immunity threshold needed to eliminate the pandemic. Our simulations showed that, for the one-group homogeneous model, vaccine-derived herd immunity cannot be achieved during Wave C even if all the unvaccinated susceptible individuals in the population are fully vaccinated during Wave C. We conducted a detailed global sensitivity analysis to determine the parameters

of the model that have the highest impact on the vaccination reproduction number (hence, the burden of the pandemic). A number of parameters (such as parameters related to asymptomatically-infectious individuals) were identified as the most influential in driving the disease dynamics during the three waves considered in this chapter. We used these parameters to suggest the most effective control and mitigation interventions to be implemented during each of the three waves of the pandemic. This chapter shows that some interventions that may be very effective during one of the three waves may not always be as effective during the other wave or waves. However, we showed that interventions related to targeting asymptomatic infectious individuals is always very effective across the three waves. Therefore, another novel finding in this chapter is that strategies that focus on rapidly detecting and isolating asymptomatic infectious individuals (such as wide-scale random testing, rapid detection, and contact tracing of contacts of identified asymptomatic individuals) will be very effective in controlling and mitigating the spread of respiratory pathogens, such as SARS-CoV-2, where asymptomatic transmission is a major feature of its transmission dynamics.

To account for the disproportionate effect of SARS-CoV-2 on the elderly, we considered another special case of the generalized m-group model where the total population of the United States is stratified into two sub-groups of individuals under 65 years of age (Group 1) and those that are 65 and older (Group 2). The resulting two-group model (i.e., the heterogeneous model with $m = 2$) was rigorously analysed and fitted with the cumulative mortality data for Wave C (as in the case of the aforementioned homogeneous model). The main objective is to determine whether age heterogeneity (together with the associated variability in mixing patterns by age) affects the size of the vaccination coverage needed to achieve vaccine-derived herd immunity in the United States (in comparison to the case where the model assumes a homogeneous

population). Our results showed that, for the two-group model, vaccine-derived herd immunity can be achieved in the United States during wave C of the pandemic (for example) if at least 61% of the population is fully vaccinated. Thus, this chapter shows that adding age heterogeneity to a vaccination model for SARS-CoV-2 that assumes a homogeneous population dramatically decreases the size of the herd immunity threshold needed to eliminate the pandemic (it should be recalled that, for the case where the homogeneous model was used, such vaccine-derived herd immunity was not attainable during Wave C even if all unvaccinated susceptible members of the community are fully vaccinated). Thus, adding the realism of the well-known heterogeneities associated with the SARS-CoV-2 pandemic makes the likelihood of its elimination using a vaccine more realistically achievable (because it requires vaccination coverage that can perhaps be readily and realistically achieved). This finding strongly supports the study by Britton *et al.* [126] (which shows, via numerical simulations, that the herd immunity threshold obtained through a heterogeneous model is "substantially less" than one obtained through a homogeneous model) and the theoretical study by Elbasha and Gumel [60] (which used a geometric approach to rigorously show that the herd immunity threshold of a vaccination model for an infectious disease that uses heterogeneous populations is lower than that of an equivalent model with a homogeneous population).

In summary, in addition to highlighting the importance of adding heterogeneities to mathematical models for the transmission dynamics and control of diseases such as SARS-CoV-2 and showing that control and mitigation strategies that are very effective during one wave may not always be very effective during other waves, this chapter shows that the prospect for the elimination of SARS-CoV-2 using a vaccination program is highly promising, provided the coverage level is high enough to

achieve herd immunity (adding heterogeneity reduces the coverage level of the herd immunity threshold needed to achieve herd immunity; hence, makes the elimination of the pandemic more likely).

Chapter 3

MATHEMATICAL ASSESSMENT OF THE ROLE OF HUMAN BEHAVIOR CHANGES ON SARS-COV-2 TRANSMISSION DYNAMICS

3.1 Introduction

A pandemic of COVID-19's devastating magnitude naturally invokes fear, unprecedented chaos, pandemonium, spread of mis(dis)information, mistrust, polarization resulting in both positive and negative behavior changes with respect to adherence (or lack thereof) of public health intervention and mitigation measures [127, 128, 129, 130, 131, 132]. Numerous mathematical models, of varying types (such as compartmental, agents-based, social network, statistical, and machine learning models) have been developed and used in an attempt to study the impact of human behavior changes on the trajectory, transmission dynamics and overall burden of the pandemic. Specifically, some of these models have accounted for the behavior change due to the transmission of information through contacts between humans [133, 134, 135, 136, 137] or due to the prevalence of the pandemic [134, 133, 138]. For instance, using data collected through a contact diary-based survey, Kummer *et al.* [139] showed the impact of the seasonal change in the number of contacts made between individuals on the spread of the disease. Furthermore, d'Onofrio *et al.* used a deterministic compartmental model to study vaccination uptake behavior as a function of prevalence [140, 141]. Coelho and Codeco [142] used Bayesian inference to model vaccination behavior as a function of individual perception of vaccine safety [142]. Mooij *et al.* [143] developed a large-scale agent-based epidemic model that uses mobility data to

calibrate the behavior of agents. Similarly, Del Valle *et al.* [144, 141] used an agent-based model to showcase the impact of school closure and fear-based home isolation during a pandemic.

Some studies have shown that a key factor that affects both COVID-19 transmission dynamics and human behavior changes with respect to the SARS-CoV-2 pandemic is the level of asymptomatic transmission in the community (i.e., disease transmission by infectious individuals who do not display clinical symptoms of the SARS-CoV-2 pandemic) [92, 93, 94, 145]. Additionally, it is possible that for various reasons, such as repeated exposures and partial cross-immunity, the proportion of exposed individuals who become asymptomatic (as opposed to symptomatic) at the end of the exposed period may increase. Hence, it is important to assess the impact of the proportion of exposed individuals who become asymptomatic at the end of the exposed period on the spread of the disease and human behavior. Furthermore, numerous studies have shown that mathematical models for disease transmission that did not explicitly incorporate human behavior and heterogeneities failed to accurately capture the correct trajectory and burden of the pandemic [146, 141, 147]. For example, although some mathematical models have correctly captured the trajectory and burden of the ongoing COVID-19 pandemic [148, 26, 94, 149], numerous others that did not explicitly account for social and human behavior aspects have failed to correctly capture current and/or future course/trajectory of the pandemic (the agents-based model developed by the United Kingdom's Scientific Advisory Group on Emergencies overestimated the burden of the SARS-CoV-2 Omicron at its peak by a factor of 20; and this discrepancy is attributed, in part, by the lack of explicit incorporation of human behavior elements into the model [150]).

This chapter focuses on developing and using a novel mathematical model, which

takes the form of a compartmental deterministic system of nonlinear differential equations, to assess the impact of human behavior changes on the transmission dynamics and control of infectious diseases. The proposed model specifically considers human behavior changes in two distinct population groups, one which strictly adheres to mitigation measures, and another one which ignores them. We assume that changes of human behavior in these two groups may occur due to a number of key (epidemiological) factors, such as (a) disease-related information received from members of the other group, (b) the level of symptomatic transmission in the community (c) proportion of non-symptomatic (susceptible, exposed, asymptomatic infectious and recovered) individuals in the community, (d) the level of publicly-available disease-induced mortality information and (e) fatigue to adherence to control and mitigation interventions in the community. Another notable feature of the model to be developed is the inclusion of the impact of asymptomatic transmission on the disease dynamics as well as on human behavior changes with respect to the spread and burden of the SARS-CoV-2 pandemic. The chapter is organized as follows. The human behavior model is formulated in Section 3.2 with the functional form of behavior change functions derived in Section 3.2.1. A behavior-free model is also considered, which is a special case of the model with behavior changes. Both the behavior and behavior-free version of the model are fitted with observed data in Section 3.2.2. Numerical simulations are carried out in Section 3.3. The behavior change functions considered in this chapter are visualized in Section 3.3.1 and their impact on cumulative mortality and infection is also assessed through simulation. The impact of change in the proportion of exposed individuals who become asymptomatic on the reproduction number, mortality and behavior change is simulated in Section 3.3.2. Finally, the main results of this chapter are discussed and summarized in Section 3.4.

3.2 Formulation of the Mathematical Model

The SARS-CoV-2 transmission model that incorporates human behavior in the disease dynamics to be developed in this chapter is based on splitting the total human population at time t, denoted by $N(t)$, into two groups based on adherence or lack thereof to public health interventions implemented to combat or mitigate the burden of the pandemic. Specifically, we define the following groups [151]:

- **Group 1:** Individuals who do not adhere to public health interventions and mitigation measures (also defined as the *non-adherent* group).
- **Group 2:** Individuals who strictly adhere to public health interventions and mitigation measures (also defined as the *adherent* group).

The total population of individuals in group 1 at time t, denoted by $N_1(t)$, is subdivided into the mutually-exclusive compartments of non-adherent susceptible ($S_1(t)$), exposed/latent ($E_1(t)$), symptomatically-infectious ($I_1(t)$), asymptomatically-infectious ($A_1(t)$) and recovered ($R_1(t)$) individuals, so that [151]

$$N_1(t) = S_1(t) + E_1(t) + I_1(t) + A_1(t) + R_1(t). \tag{3.1}$$

Similarly, the total population in group 2 at time t, denoted by $N_2(t)$, is subdivided into the mutually-exclusive compartments of adherent susceptible ($S_2(t)$), exposed/latent ($E_2(t)$), symptomatically-infectious ($I_2(t)$), asymptomatically-infectious ($A_2(t)$) and recovered ($R_2(t)$) individuals, so that [151]

$$N_2(t) = S_2(t) + E_2(t) + I_2(t) + A_2(t) + R_2(t). \tag{3.2}$$

Thus, the total population at time t, $N(t)$, is given by $N(t) = N_1(t) + N_2(t)$. Some

of the main behavior-related assumptions made in the formulation of the model are [151]:

(i) Individuals change their behavior during disease outbreaks based on the following epidemiological and social factors:
(a) disease-related information members of one group received from members of the other group, (b) the level of symptomatic transmission in the community (c) the proportion of non-symptomatic (susceptible, exposed, asymptomatic infectious and recovered) individuals in the community, (d) the level of publicly-available disease-induced mortality information and (e) due to fatigue factor associated with adherence to interventions over a long-term period.

(ii) Symptomatic individuals in group 2 do not change their behavior (i.e., they do not move to group 1) for the entire duration of their symptomatic status.

(iii) The proportion of new recruited individuals into the community recruitment who are adherent to public health interventions depends on the proportion of symptomatic individuals in the community.

We define the following behavior-related transition rates [151]:

(a) ψ_{ij}^{c}: the rate at which individuals in group i change their behavior, and move to the other group j (with $i, j = \{1, 2\}$ and $i \neq j$), due to transmission of disease-related information received from contact with individuals in group j.

(b) ψ_{12}^{i}: the rate at which individuals in group 1 positively change their non-adherent behavior and move to group 2 due to the level of symptomatic transmission in the community.

(c) ψ_{21}^{ns}: the rate at which individuals in group 2 negatively change their behavior and move to the non-adherent group 1 due to the proportion of non-symptomatic individuals in the community.

(d) ψ_{12}^{m}: the rate at which individuals in group 1 positively change their behavior and move to the adherent group 2 due to the level of publicly-available disease-induced mortality information.

(e) ψ_{21}^{f}: the rate at which individuals in group 2 negatively change their behavior and move to the non-adherent group 1 due to fatigue to adherence to intervention measures.

The functional forms of the aforementioned behavior-related rates will be derived in Section 3.2.1. In the formulation of the human behavior SARS-CoV-2 model, we let Π represent the recruitment rate of individuals into the population or community (and all recruited individuals are assumed to be susceptible). It is further assumed that a proportion, p, of these individuals strictly adhere to public health intervention and mitigation measures (i.e., $p\Pi$ is the recruitment rate into the susceptible population of group 2), while the remaining proportion, $1-p$, are assumed to not adhere to interventions (i.e., $(1-p)\Pi$ is the recruitment rate of individuals into the susceptible population in group 1). Individuals in all epidemiological compartments suffer natural death or removal at a rate μ. Individuals in group 1 (i.e., non-adherent individuals) acquire infection at a rate λ (*force of infection*), given by [151]:

$$\lambda = (\beta)\left[\frac{I_1 + \eta_a A_1 + (1-\varepsilon_m)(I_2 + \eta_a A_2)}{N}\right], \tag{3.3}$$

where β is the effective contact rate associated with disease transmission by symptomatically-infectious individuals, η_a is a modification parameter accounting for the variability

in disease transmission by asymptomatically-infectious individuals, in comparison to symptomatically-infectious individuals and $0 \leq \varepsilon_m < 1$ is the *outward* efficacy of the public health intervention and mitigation measures (e.g., face mask) to prevent the transmission of infection by infectious adherent individuals (group 2) to susceptible individuals [19, 94]. For simplicity, it is assumed that the *inward* efficacy of the public health intervention measures to prevent susceptible individuals in group from acquiring infection, following contact with infectious individuals, is the same as the outward efficacy, and denoted by ε_m.

Individuals in group 1 (non-adherents) positively change their behavior and become adherents due to the positive information they received about the disease from individuals in group 2 (due to contact at a rate ψ_{12}^c). They also change their behavior positively and move to group 2 due to the level of symptomatic transmission in the community (at a rate ψ_{12}^i) and due to the level of disease-induced mortality in the community, obtained from publicly-available sources (at a rate ψ_{12}^m). Similarly, individuals in group 2 negatively change their behavior and move to group 1 due to: the contact-related information received from individuals in group 1 (at a rate ψ_{21}^c), the proportion of non-symptomatic individuals in the community (at a rate ψ_{21}^{ns}) and due to fatigue to adherence of intervention (at a rate ψ_{21}^f). Adherents susceptible individuals acquire infection at a reduced rate $(1 - \varepsilon_m)\lambda$, where $0 < \varepsilon_m < 1$ is the efficacy of public health intervention and mitigation measures implemented in the community to prevent the acquisition of infection. Let σ represents the rate at which exposed (i.e., newly-infected) individuals progress to to either the asymptomatically-infectious class (at a rate $r\sigma$, where $0 \leq r \leq 1$ is the proportion of these individuals that become asymptomatically-infectious at the end of the exposed period) or develop clinical symptoms of the disease (at a rate $(1 - r)\sigma$, where the complement, $1 - r$, is

the proportion of exposed individuals who display clinical symptoms of the disease at the end of the exposed period). Symptomatic (asymptomatic) infectious individuals are assumed to recover at a rate $\gamma_i(\gamma_a)$, and symptomatic-infectious individuals in group 1 (group 2) suffer disease-induced mortality at a rate $\delta_1(\delta_2)$. It follows, based on the above assumptions and derivations, that the endemic model for the SARS-CoV-2 pandemic, that explicitly incorporates elements of human behavior during the outbreaks of the disease, is given by the following deterministic system of nonlinear differential equations (where a dot represents differentiation with respect to time t) [151]:

$$
\begin{cases}
\dot{S}_1(t) = \Pi(1-p) + (\psi_{21}^c + \psi_{21}^{ns} + \psi_{21}^f)S_2 - \lambda S_1 - (\psi_{12}^c + \psi_{12}^i + \psi_{12}^m)S_1 - \mu S_1, \\
\dot{S}_2(t) = \Pi p + (\psi_{12}^c + \psi_{12}^i + \psi_{12}^m)S_1 - (1-\varepsilon_m)\lambda S_2 - (\psi_{21}^c + \psi_{21}^{ns} + \psi_{21}^f)S_2 - \mu S_2, \\
\dot{E}_1(t) = \lambda S_1 + (\psi_{21}^c + \psi_{21}^{ns} + \psi_{21}^f)E_2 - (\psi_{12}^c + \psi_{12}^i + \psi_{12}^m)E_1 - (\sigma+\mu)E_1, \\
\dot{E}_2(t) = (1-\varepsilon_m)\lambda S_2 + (\psi_{12}^c + \psi_{12}^i + \psi_{12}^m)E_1 - (\psi_{21}^c + \psi_{21}^{ns} + \psi_{21}^f)E_2 - (\sigma+\mu)E_2, \\
\dot{I}_1(t) = (1-r)\sigma E_1 - (\psi_{12}^c + \psi_{12}^i + \psi_{12}^m)I_1 - (\gamma_i + \mu + \delta_1)I_1, \\
\dot{I}_2(t) = (1-r)\sigma E_2 + (\psi_{12}^c + \psi_{12}^i + \psi_{12}^m)I_1 - (\gamma_i + \mu + \delta_2)I_2, \\
\dot{A}_1(t) = r\sigma E_1 + (\psi_{21}^c + \psi_{21}^{ns} + \psi_{21}^f)A_2 - (\psi_{12}^c + \psi_{12}^i + \psi_{12}^m)A_1 - (\gamma_a + \mu)A_1, \\
\dot{A}_2(t) = r\sigma E_2 + (\psi_{12}^c + \psi_{12}^i + \psi_{12}^m)A_1 - (\psi_{21}^c + \psi_{21}^{ns} + \psi_{21}^f)A_2 - (\gamma_a + \mu)A_2, \\
\dot{R}_1(t) = \gamma_i I_1 + \gamma_a A_1 + (\psi_{21}^c + \psi_{21}^{ns} + \psi_{21}^f)R_2 - (\psi_{12}^c + \psi_{12}^i + \psi_{12}^m)R_1 - \mu R_1, \\
\dot{R}_2(t) = \gamma_i I_2 + \gamma_a A_2 + (\psi_{12}^c + \psi_{12}^i + \psi_{12}^m)R_1 - (\psi_{21}^c + \psi_{21}^{ns} + \psi_{21}^f)R_2 - \mu R_2.
\end{cases}
\tag{3.4}
$$

In the behavior-epidemiology model (3.4), the proportion p of individuals recruited into the community who adhere to public health interventions is assumed to defend on the proportion of individuals who are symptomatic at time t, and is defined as [151]:

$$p = \widetilde{p}\,\left(\frac{I_1 + I_2}{N}\right), \tag{3.5}$$

where $\widetilde{p}$ is the maximum proportion of recruited individuals who are adherent. The proportion p is behavior-related, since it is a function of the total proportion of symptomatic individuals in the community. It is zero if there are no symptomatic individuals in the community, and it rises to its maximum ($\widetilde{p}$) if the proportion of symptomatic individuals in the community tend towards one; in other words, newly-recruited individuals choose to remain in group 1 if the proportion of symptomatic individuals in the community is small, and opt to move to group 2 if the proportion of symptomatic individuals is large).

It is convenient to define the rate of change of cumulative mortality due to the disease as [151]

$$\dot{D}(t) = \delta[I_1(t) + I_2(t)], \tag{3.6}$$

from which it follows that the daily mortality on day k (denoted by M_k) is given by [151]:

$$M_k = \int_{k-1}^{k} \dot{D}(t)\, dt. \tag{3.7}$$

Figure 3.1 depicts the flow diagram of the model, and the state variables and parameters are described in Tables 3.1 and 3.2, respectively.

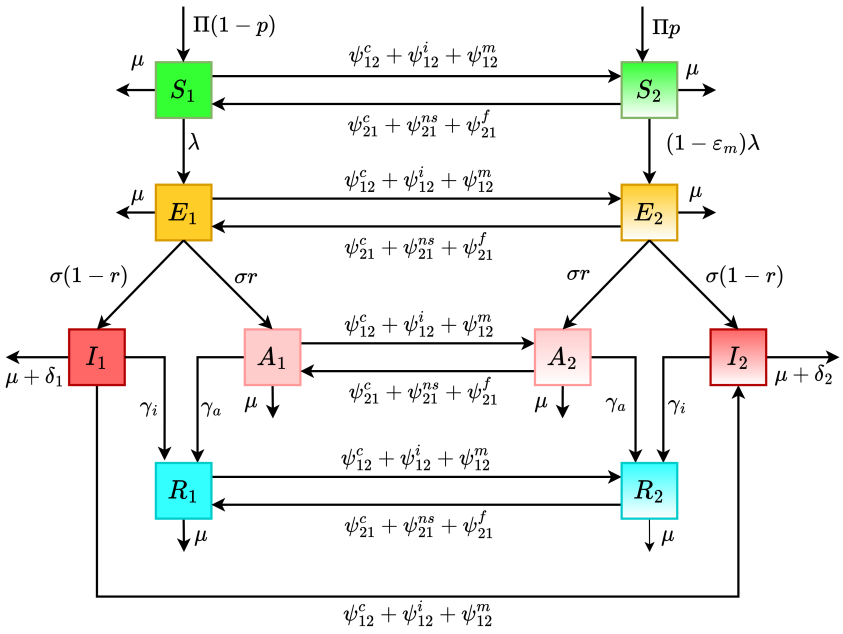

Figure 3.1: Flow diagram of the behavior-epidemiology model (3.4), where λ and p are defined in Equations (3.3) and (3.5), respectively [151]. The state variables and parameters of the model are described in Tables 3.1 and 3.2, respectively [151].

3.2.1 Derivation of the functional forms of behavior-related parameters of the model

The behavior-related transition rates of the behavior-epidemiology model (3.4) are described and derived below [151].

3.2.1.1 Behavior change due to information received from contact with members of the other group ($\psi_{ij}^c(t)$)

Since the behavior-epidemiology model to be developed in this chapter stratifies the total population into two subgroups, namely group 1 of individuals who do not adhere to public health control and mitigation interventions and group 2 consisting of individuals who strictly adhere to such interventions, contacts between individuals

of one group with those of the other could induce behavior change with respect to the adherence (or lack thereof) to interventions (due, for instance, to *peer influence or pressure*). It is intuitive to assume that the probability of such contact-induced behavior change depends on the capacity of (or degree or extent to which) members of one group to influence members of the other and the relative size of the other group [133, 134, 135, 136, 137]. Recall that $\psi_{12}^{c}(t)\,(\psi_{21}^{c}(t))$ represents the rate at which non-adherent (adherent) individuals become adherents (non-adherents), at time t, following contacts with adherent (non-adherent) individuals in the community. The rate $\psi_{12}^{c}(t)$ can then be defined as the product of the maximum rate of behavior change of non-adherent individuals to become adherents due to contacts with adherent individuals (denoted by α_{12}^{c}), the probability of influence adherent individuals have on non-adherent individuals to become adherent due to transmission of disease-related information by contact (denoted by $0 < q_{12}^{c} < 1$) and the current proportion of adherent individuals in the community $\left(\frac{N_2(t)}{N(t)}\right)$. Thus, the rate $\psi_{12}^{c}(t)$ is given by [151]:

$$\psi_{12}^{c}(t) = \left(\alpha_{12}^{c}\right) \times \left(q_{12}^{c}\right) \times \left[\frac{N_2(t)}{N(t)}\right]. \tag{3.8}$$

Similarly, the rate at which adherent individuals in the community become non-adherent due to contacts with non-adherent individuals at time t (ψ_{21}^{c}(t)) is defined as the product of the maximum rate of behavior change of adherent individuals due to contacts with non-adherent individuals (denoted by α_{21}^{c}), the probability of influence non-adherent individuals have on adherent individuals to become non-adherents due to transmission of disease-related information by contacts (denoted by $0 < q_{21}^{c} < 1$) and the current proportion of non-adherent individuals in the community $\left(\frac{N_1(t)}{N(t)}\right)$, so that [151]:

$$\psi_{21}^{c}(t) = \left(\alpha_{21}^{c}\right) \times \left(q_{21}^{c}\right) \times \left[\frac{N_1(t)}{N(t)}\right]. \tag{3.9}$$

3.2.1.2 Behavior change due to the level of symptomatic transmission ($\psi_{12}^{i}(t)$) in community

Individuals can also change their behavior with respect to adherence to interventions based on the current relative level of symptomatic transmission in the community [133]. Let $\psi_{12}^{i}(t)$ represent the rate at which non-adherent individuals become adherent due to the level of symptomatic transmission in the community. The rate $\psi_{12}^{i}(t)$ is defined as the product of the maximum behavior change of non-adherent individuals due to the level of symptomatic transmission in the community (α_{12}^{i}), the probability of influence on non-adherent individuals due to the level of symptomatic transmission in the community (q_{12}^{i}) and the relative level of symptomatic transmission in the community (given by the Holling Type-II saturation incidence function $(I_1(t) + I_2(t))/(K + I_1(t) + I_2(t))$, where $K > 0$ is the saturation constant). That is [151],

$$\psi_{12}^{i}(t) = \left(\alpha_{12}^{i}\right) \times \left(q_{12}^{i}\right) \times \left[\frac{I_1(t) + I_2(t)}{K + I_1(t) + I_2(t)}\right]. \tag{3.10}$$

3.2.1.3 Behavior change due to the proportion of non-symptomatic ($\psi_{21}^{ns}(t)$) pool in community

Individuals can also change their behavior due to the proportion of non-symptomatic (i.e., susceptible, exposed, asymptomatic, and recovered) individuals in the com-

munity [134]. Let $\psi_{21}^{ns}(t)$ represent the rate at which adherent individuals become non-adherent due to the current proportion of non-symptomatic individuals in the community. The parameter for the rate of behavior change of adherent individuals to become non-adherent due to the proportion of non-symptomatic individuals in the community (ψ_{21}^{ns}) is given by the product of the maximum rate of behavior change of adherent individuals due to the proportion of non-symptomatic individuals in the community (α_{21}^{ns}), the probability of influence on adherent individuals due to the current size of the non-symptomatic pool in the community (q_{21}^{ns}) and the proportion of the non-symptomatic pool in the community (given by $(S_1(t) + S_2(t) + E_1(t) + E_2(t) + A_1(t) + A_2(t) + R_1(t) + R_2(t))/N(t)$). Hence [151],

$$\psi_{21}^{ns}(t) = \left(\alpha_{21}^{ns}\right) \times \left(q_{21}^{ns}\right) \times \left[\frac{S_1(t) + S_2(t) + E_1(t) + E_2(t) + A_1(t) + A_2(t) + R_1(t) + R_2(t)}{N(t)}\right]. \tag{3.11}$$

3.2.1.4 Behavior change due to level of daily reported disease-induced mortality ($\psi_{12}^{m}(t)$)

Individuals can also change their behavior due to the level of daily reported disease-induced mortality (obtained from publicly-available information sources, such as the print/audio/visual/social and the internet) [133]. To model the rate of behavior change due to such access to information on the level of daily disease-induced mortality in the community, we first assume that the level of disease-induced mortality in the community only causes behavior change in group 1, and not in group 2 (i.e., only the non-adherent individuals can change their behavior to become adherent in fear of succumbing to the disease; whereas those that are strictly adherent, in group

2, are not expected to negatively change their behavior, when daily disease-induced mortality is on the rise, and move to group 1). The rate $\psi_{12}^m(t)$ can then be expressed as a product of the maximum rate of behavior change of non-adherent individuals due to the level of daily reported disease-induced mortality in the community (denoted by α_{12}^m), the probability of influence adherent individuals have on non-adherent individuals due to the size of the reported daily disease-induced mortality in the community (denoted by q_{12}^m) and the current level of disease-induced mortality (modeled by the Ivlev function [152], $\left(1 - e^{-\zeta M(t)}\right)$, where $M(t)$ is the daily mortality on day t of the pandemic, as defined by Equation (3.7) and $1/\zeta$ (with $0 < \zeta \leq 1$) could be thought of as the threshold number of reported daily disease-induced mortality above which fear or *panic wave* begin to rapidly spread in the community [133]). Thus [151],

$$\psi_{12}^m(t) = \left(\alpha_{12}^m\right) \times \left(q_{12}^m\right) \times \left(1 - e^{-\zeta M(t)}\right). \tag{3.12}$$

3.2.1.5 Behavior change due to high level of fatigue to interventions in the community (ψ_{21}^f)

Behavior change "requires a person to disrupt a current habit while simultaneously fostering a new, possibly unfamiliar, set of actions" [153]. Thus, perhaps for that reason, behavior change, even if it is triggered by health-related reasons (i.e., triggered by the need to adhere to public health intervention and mitigation measures to minimize the risk of acquiring infection, severe disease, hospitalization or even death), can often be quite difficult to sustain. To model behavior change due to fatigue to adherence to public health intervention and mitigation measures, it is plausible to, first of all, assume that only individuals in group 2 (the adherent group) can develop in-

tervention fatigue (due to being strictly adherent for an extended period of time) and potentially negatively change their behavior to become non-adherents. For simplicity, it is assumed that adherent individuals begin to experience fatigue of adherence to intervention after a certain fatigue time threshold (denoted by t_f) has been met. This factor can be modeled using a Heaviside-like function (H^f), given by [151]:

$$\mathcal{H}^f = \begin{cases} 1 & \text{if } t \geq t_{\text{f}} \\ 0 & \text{if } t < t_{\text{f}}, \end{cases} \tag{3.13}$$

with H^f set to 1 if the fatigue time threshold has been met or exceeded (i.e., $t \geq t_f$) and $H^f = 0$ if the threshold has not been met, and adherents are not experiencing intervention fatigue (i.e., $t < t_f$). The rate at which adherent individuals become non-adherent due to fatigue (ψ_{21}^f) can then be expressed as a product of the maximum rate of behavior change of adherent individuals due to fatigue (denoted by α_{21}^f), the probability of influence non-adherent individuals have on adherent individuals due to high fatigue level to intervention (denoted by q_{21}^f) and the fatigue threshold time (given by the function $\mathcal{H}^f$) [151].

$$\psi_{21}^f(t) = \left(\alpha_{21}^f\right) \times \left(q_{21}^f\right) \times \left(\mathcal{H}^f\right). \tag{3.14}$$

State variable	Description
S_1	Number of non-adherent susceptible individuals
S_2	Number of adherent susceptible individuals
E_1	Number of non-adherent exposed individuals
E_2	Number of adherent exposed individuals
I_1	Number of non-adherent symptomatically-infectious individuals
I_2	Number of adherent symptomatically-infectious individuals
A_1	Number of non-adherent asymptomatically-infectious individuals
A_2	Number of adherent asymptomatically-infectious individuals
R_1	Number of non-adherent recovered individuals
R_2	Number of adherent recovered individuals

Table 3.1: Description of the state variables of the behavior-epidemiology model (3.4) [151].

3.2.2 Data-fitting and parameter estimation of behavior-epidemiology model (3.4)

The behavior-epidemiology model (3.4) consists of many parameters, the values of many of which (at least 16) are known from the literature. The values of a few of the parameters, particularly the disease-induced mortality rate (δ_1 and δ_2; although, for simplicity, we assume that $\delta = \delta_1 = \delta_2$ since it is reasonable to assume that both adherent and non-adherent infected individuals die at the same rate due to, for example having access to the same quality of disease-induced mortality prevention treatment), the effective contact rate of symptomatic individuals (β), the modification parameter for the effective contact rate of asymptomatic individuals (η_a) and the product of the maximum rate of behavior change from one group to another and the associated parameter of influence ($\alpha^i_{12}q^i_{12}$, $\alpha^{ns}_{21}q^{ns}_{21}$, $\alpha^m_{12}q^m_{12}$ and $\alpha^f_{21}q^f_{21}$) are unknown and will be estimated through fitting. Furthermore, behavior-related functions are computed using the fixed and fitted parameters as well as the associated state variables at time t. The model (3.4) will be fitted and cross-validated using the cumulative mortality data for the COVID-19 pandemic in the United States for the period from March 1st,

State variable	Description
p	Proportion of new recruitment that is adherent
$\Pi(1-p)$	Recruitment rate into non-adherent susceptible population
Πp	Recruitment rate into adherent susceptible population
μ	Natural death rate
ε_m	Average efficacy of an intervention (such as masking or social distancing)
β	Effective contact rate associated with individuals in I_1 compartment
η_a	Modification parameter for the infectiousness of the individuals in asymptomatic class
r	Proportion of exposed individuals who become asymptomatically-infectious at the end of the exposed period
$1-r$	Proportion of exposed individuals who show clinical symptoms of the disease at the end of the exposed period
$r\sigma$	Progression rate from exposed to asymptomatically-infectious class
$(1-r)\sigma$	Progression rate from exposed to symptomatically-infectious class
$\gamma_i(\gamma_a)$	Recovery rate for individuals in the symptomatically-(asymptomatically-) infectious class
δ_1	Disease-induced mortality rate for individuals in the I_1 compartment
δ_2	Disease-induced mortality rate for individuals in the I_2 compartment
ψ_{12}^c	Rate at which non-adherent individuals become adherent due to contact with adherents
ψ_{21}^c	Rate at which adherent individuals become non-adherent due to contact with non-adherents
ψ_{12}^i	Rate at which non-adherent individuals become adherent due to the level of symptomatic transmission in the community
ψ_{21}^{ns}	Rate at which adherent individuals become non-adherent due to the proportion of non-symptomatic individuals in the community
ψ_{12}^m	Rate at which non-adherent individuals become adherent due to disease-induced mortality
ψ_{21}^f	Rate at which adherent individuals become non-adherent due to high fatigue level

Table 3.2: Description of the parameters of the model (3.4) [151].

2020 to June 18th, 2020, which corresponds to the first wave of the pandemic in the United States. Specifically, the model will be fitted using a segment of this data, for the period between March 1, 2020, to May 29, 2020, and the remaining data is used to cross-validate the model. Additionally, some of the initial conditions will be fitted from the data as well.

Parameter	**Value**	**Source**
Π	$11,670$ day^{-1}	[74, 75]
$\widetilde{p}$	0.80 (dimensionless)	[154]
μ	$1/(77.8 \times 365)$ day^{-1}	[75]
ε_m	0.5 (dimensionless)	[94, 19]
r	0.4 (dimensionless)	[77]
σ	$1/3.6$ day^{-1}	[155]
γ_i	$1/5$ day^{-1}	[156]
γ_a	$1/5$ day^{-1}	[80]
t_f	0 (day)	Assumed
ζ	$1/1500$ (human^{-1})	Assumed
K	$5,000,000$ (dimensionless)	Assumed

Table 3.3: Values of the fixed parameters of the behavior-epidemiology ((3.4)) and behavior-free ((H.1)) models [151].

Parameter	**Estimated (fitted) Value**
$\alpha_{12}^c q_{12}^c$	9.337×10^{-3} day^{-1}
$\alpha_{21}^c q_{21}^c$	9.223×10^{-3} day^{-1}
$\alpha_{12}^i q_{12}^i$	0.110 day^{-1}
$\alpha_{21}^{ns} q_{21}^{ns}$	2.597×10^{-3} day^{-1}
$\alpha_{12}^m q_{12}^m$	0.305 day^{-1}
$\alpha_{21}^f q_{21}^f$	5.682×10^{-5} day^{-1}
β	0.661 day^{-1}
η_a	2.275 (dimensionless)
$\delta = \delta_1 = \delta_2$	2.505×10^{-4} day^{-1}

Table 3.4: Values of the fitted (estimated) parameters of the behavior-epidemiology model (3.4) [151].

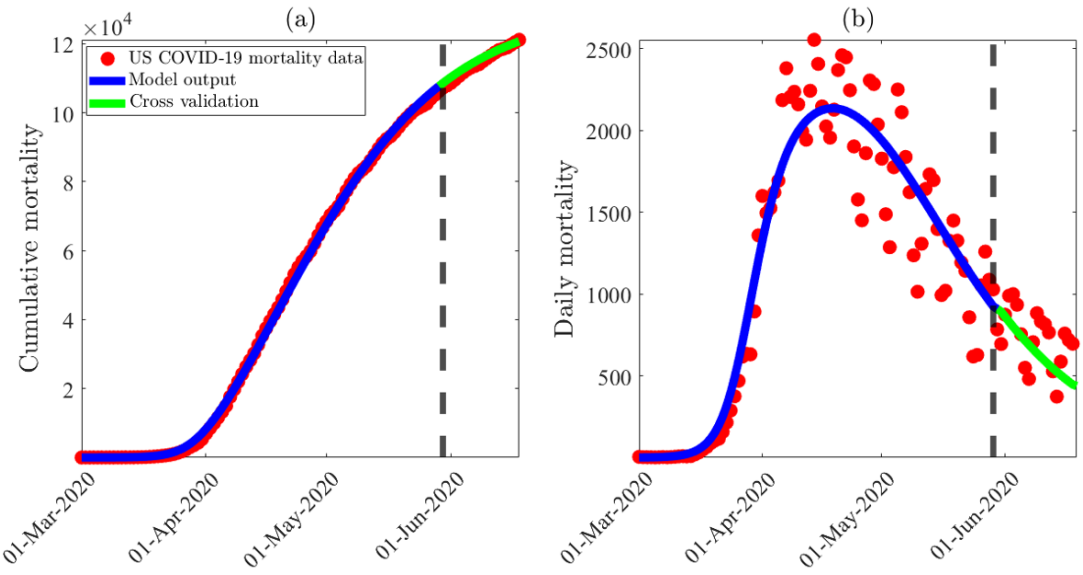

Figure 3.2: Data fitting, parameter estimation and cross-validation of the behavior-epidemiology model (3.4), using SARS-CoV-2 cumulative mortality data for the United States during the first wave of the pandemic (corresponding to the period from March 1st, 2020 to June 18th, 2020). (a) Least-squares fitting of the behavior-epidemiology model (3.4), showing the cumulative COVID-19 mortality generated from the model, compared to the observed cumulative mortality data for the United States during the first wave (obtained from the Johns Hopkins University COVID-19 repository [73]). (b) Simulation results of the behavior-epidemiology model (3.4), depicting the daily COVID-19 mortality for the United States, as a function of time, predicted by the behavior-epidemiology model using the fixed and estimated parameters tabulated in Tables 3.3 and 3.4, respectively, in comparison to the observed daily mortality data for the United States during the first wave (obtained from the Johns Hopkins University COVID-19 repository [73]). The behavior-epidemiology model was fitted to the data from March 1st, 2020 until May 29th, 2020 (depicted by a dashed black line in the figure), and cross-validated by comparing the model output with the observed mortality data for the remaining 20 days (depicted with a green curve). Three of the initial conditions of the behavior-epidemiology model (namely $E_1(0), I_1(0)$ and $A_1(0)$) were estimated from fitting the model with the aforementioned cumulative mortality data. The estimated values were $E_1(0) = 5,754$, $I_1(0) = 2,338$ and $A_1(0) = 2,501$, respectively. The remaining initial conditions were set to (using US census data near the disease-free equilibrium): $N(0) = 3.314 \times 10^8, S_2(0) = 1, E_2(0) = 0, I_2(0) = 0, A_2(0) = 0, R_1(0) = 0, R_2(0) = 0, D(0) = 1$, and $S_1(0) = N(0) - E_1(0) - I_1(0) - A_1(0) - S_2(0)$ [151].

3.2.2.1 Insight from fitting the behavior-epidemiology model

The numerical values or sizes of the estimated parameters of the behavior-epidemiology model (3.4), tabulated in Table 3.4, can provide important insight into the impact of human behavior changes on the trajectory and burden of the disease during the simulation/fitting period (i.e., during the first wave of the pandemic in the United States). In particular, since the estimated value of the modification parameter accounting for the variability in disease transmission by asymptomatically-infectious individuals, in comparison to symptomatically-infectious individuals, is $\eta_a = 2.275$, it follows that the transmission rate for asymptomatic infectious individuals ($\beta\eta_a$) is at least twice the size of the transmission rate for symptomatic infected individuals (β). Furthermore, asymptomatic infectious individuals accounted for at least 70% of all new SARS-CoV-2 cases in the United States during the first wave of the pandemic (this is computed from the ratio: $\eta_a\,\beta/(\eta_a\,\beta + \beta) \times 100\%$). Thus, it follows from the parameter estimation associated with fitting the behavior-epidemiology model with the cumulative SARS-CoV-2 mortality data, that this chapter confirms that asymptomatic infectious individuals were the main drivers of the SARS-CoV-2 pandemic in the United States during the first wave [92, 93, 94]. Table 3.4 also shows that the estimated value for the product of the maximum rate of behavior change attributed to fatigue to adherence to the public health interventions implemented in the United States during the first wave (α_{21}^f), and its associated probability of influence (q_{21}^f), given by $\alpha_{21}^f q_{21}^f = 5.681 \times 10^{-5}$ *per* day, is exceptionally small. Hence, it can be inferred (from the very small value of the product $\alpha_{21}^f q_{21}^f$) that behavior change due to fatigue to adherence to interventions was negligible (if at all) during the first wave of the pandemic in the United States. Similarly, the estimated values for the product of parameters associated with behavior change attributed to contact (i.e.,

$\alpha_{12}^c q_{12}^c = 9.337 \times 10^{-3}$ *per* day and $\alpha_{21}^c q_{21}^c = 9.223 \times 10^{-3}$ *per* day), as well as those for the parameters associated with the proportion of non-symptomatic individuals in the community (i.e., $\alpha_{21}^{ns} q_{21}^{ns} = 2.597 \times 10^{-3}$ *per* day) were relatively small, suggesting behavior changes due to these metrics (contacts and size of non-symptomatic pools) were of marginal impact on the trajectory or burden of the pandemic during the first wave in the United States. On the other hand, Table 3.4 shows that the value of the product of the parameters associated with behavior change due to the level of symptomatic transmission in the community (i.e., $\alpha_{12}^i q_{12}^i = 0.110$ *per* day) and disease-induced mortality (i.e., $\alpha_{12}^m q_{12}^m = 0.305$ *per* day) were relatively large (in comparison to the sizes of the other estimated parameters). Hence, behavior change due to these metrics (level of symptomatic transmission and disease-induced mortality) play significant role in driving the pandemic during the first wave in the United States (i.e., the most influential forms of behavior change were linked to mortality followed by the level of symptomatic transmission during the first wave of the SARS-CoV-2 pandemic in the United States). The behavior change functions will be further analysed in Section 3.3.1 (and their impact on disease transmission and disease-induced mortality will also be discussed there).

3.2.3 Fitting the behavior-free model with data

In order to fully understand the impact of explicitly accounting for human behavior elements in the model, it is instructive to also consider the version of the behavior-epidemiology model (3.4) without the behavior elements (known as the *behavior-free model*. The equations for the behavior-free model, obtained by setting all the behavior-related parameters of the behavior-epidemiology model (3.4) to zero (i.e., we consider the model (3.4) with $p = \psi_{12}^c = \psi_{21}^c = \psi_{12}^i = \psi_{21}^{ns} = \psi_{12}^m = \psi_{21}^f = 0$), are given

by Equation (H.1) in Appendix H. The resulting behavior-free model (H.1) will also be fitted using the same cumulative mortality data used to fit the behavior-epidemiology model and fixed parameters given in Table 3.3. Here, too, some parameters of the behavior-free model (namely, β, η_a and δ), as well as initial conditions (namely $E_1(0)$, $I_1(0)$ and $A_1(0)$) will be estimated from the data fitting.

3.2.3.1 Insights from fitting the behavior-free model (H.1) with data

First of all, since the estimated value of the modification parameter accounting for the variability in disease transmission by asymptomatically-infectious individuals (η_a), for the behavior-free model, is $\eta_a = 5.41$, it follows that, for the behavior-free model (H.1), the transmission rate for asymptomatic infectious individuals ($\beta\eta_a$) is at least five times as much as that of symptomatic infected individuals (β). Thus, the behavior-free model shows that asymptomatic infectious individuals are a lot more influential (in generating more new cases), in comparison to the model with human behavior (in other words, adding heterogeneity due to human behavior changes during an epidemic significantly reduces the relative infectiousness or influence of asymptomatic transmission). Furthermore, specifically for this model, the fitting shows that asymptomatic infectious individuals accounted for about 84% ($\eta_a\beta/(\eta_a\beta+\beta)\times 100\%$) of all new cases during the first wave of the pandemic in the United States (recall that asymptomatic individuals accounted for 70% of new cases using the behavior-epidemiology model (3.4)). Since most of the modeling and empirical studies suggest that asymptomatic individuals accounted for between 50% to 70% of new cases [157, 158, 159], this chapter shows that the model without human behavior (unlike with human behavior) over-estimated the influence of asymptotic transmission in the United States.

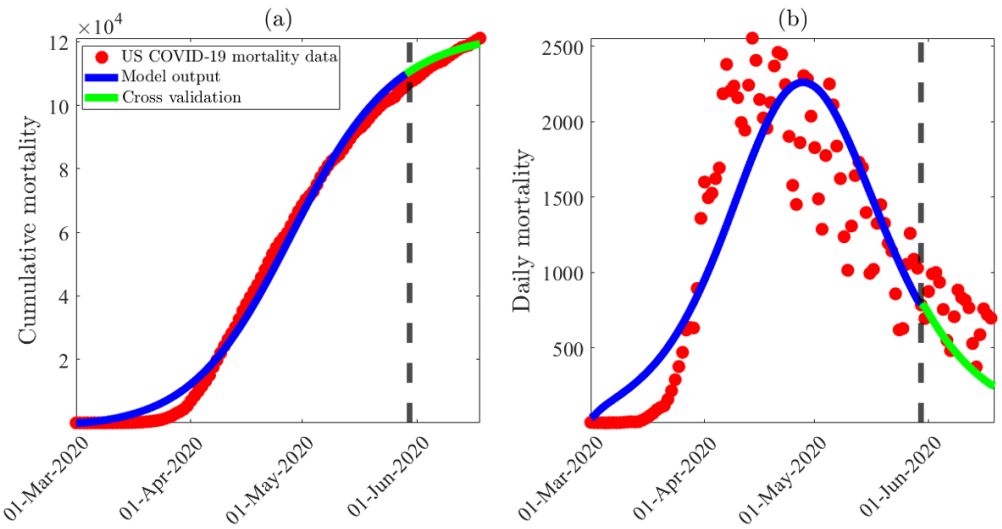

Figure 3.3: Data fitting, parameter estimation and cross-validation of the behavior-free model (H.1), using SARS-CoV-2 cumulative mortality data for the United States during the first wave of the pandemic (corresponding to the period from March 1st, 2020 to June 18th, 2020). (a) Least-squares fitting of the behavior-free model (H.1), showing the cumulative COVID-19 mortality generated from the model, compared to the observed cumulative mortality data for the United States during the first wave (obtained from the Johns Hopkins University COVID-19 repository [73]). (b) Simulation results of the behavior-free model (H.1), depicting the daily COVID-19 mortality for the United States, as a function of time, predicted by the behavior-free model using the fixed parameters tabulated in Table 3.3 and estimated parameters obtained through fitting (i.e., $\beta = 0.132$ *per* day, $\eta_a = 5.349$ and $\delta = 1.611 \times 10^{-4}$ *per day*), in comparison to the observed daily mortality data for the United States during the first wave (obtained from the Johns Hopkins University COVID-19 repository [73]). The behavior-free model was fitted to the data from March 1st, 2020 until May 29th, 2020 (depicted by a dashed black line in the figure), and cross-validated by comparing the model output with the observed mortality data for the remaining 20 days (depicted with a green curve). Three of the initial conditions of the behavior-free model (namely $E_1(0), I_1(0)$ and $A_1(0)$) were estimated from fitting the model with the aforementioned cumulative mortality data. The estimated values were $E_1(0) = 1,388,568$, $I_1(0) = 10,3571$ and $A_1(0) = 350,357$, respectively. The remaining initial conditions were set to (using US census data near the disease-free equilibrium): $S_2(0) = 1, E_2(0) = 0, I_2(0) = 0, A_2(0) = 0, R_1(0) = 0, R_2(0) = 0, D(0) = 1, N(0) = 3.314 \times 10^8$, and $S_1(0) = N(0) - E_1(0) - I_1(0) - A_1(0) - R_1(0), R_1(0) = 0$ [151].

3.2.4 Basic qualitative properties of the behavior-epidemiology model

Before analysing the asymptotic properties of the behavior-epidemiology model (3.4), it is instructive to analyse its basic qualitative properties first of all. This is done below [151]. We define the following biologically-feasible region for the model:

$$\Omega = \left\{ \left(S_1, S_2, E_1, E_2, I_1, I_2, A_1, A_2, R_1, R_2\right) \in \mathbb{R}_+^{10} : N(t) \leq \frac{\Pi}{\mu} \right\}. \tag{3.15}$$

Theorem 3.2.1. *Suppose that the initial values* $S_1(0), S_2(0), E_1(0), E_2(0), I_1(0), I_2(0), A_1(0), A_2(0), R_1(0), R_2(0)$ *of the model* (3.4) *are non-negative. The region* Ω *is positively-invariant and bounded with respect to the model* (3.4).

Proof. The equation for the rate of change of the total human population, obtained by adding all equations in (3.4), is given by:

$$\dot{N}(t) = \Pi - \mu N - \delta_1 I_1 - \delta_2 I_2. \tag{3.16}$$

By the non-negativity of the parameters and state variables of the model (3.4), it follows from (3.16) that

$$\dot{N}(t) \leq \Pi - \mu N. \tag{3.17}$$

Hence, if $N > \frac{\Pi}{\mu}$, then $\dot{N} \leq 0$. Thus, it can be shown using a standard comparison theorem [65] on (3.17) that

$$N(t) \leq \frac{\Pi}{\mu} + \left(N(0) - \frac{\Pi}{\mu} \right) e^{-\mu t}, \tag{3.18}$$

where $N(0)$ represents the initial population (i.e., the population at time $t = 0$). Hence, $N(t) \leq \dfrac{\Pi}{\mu}$ if $N(0) \leq \dfrac{\Pi}{\mu}$. If the initial population exceeds the carrying capacity $\left(\text{i.e., } N(0) > \dfrac{\Pi}{\mu}\right)$ then the solutions are initially outside the region Ω but the solution

trajectory will eventually enter the region Ω since $\lim_{t\to\infty} N(t) = \dfrac{\Pi}{\mu}$. Thus, every solution of the model (3.4) with initial conditions in Ω remains in Ω for all time $t > 0$, and those outside Ω are eventually attracted into Ω. In other words, the region Ω is positively-invariant and attracts all initial solutions of the model (3.4).

□

3.2.5 Asymptotic stability of disease-free equilibria

The model (3.4) has two disease-free equilibria (DFE), namely a trivial *adherents-free* DFE (denoted by $\mathbb{E}_1$) and a non-trivial *adherents-present* DFE (denoted by $\mathbb{E}_2$), given, respectively, by [151]:

$$\begin{aligned}
&\mathbb{E}_1 := (S_1^*, S_2^*, E_1^*, E_2^*, I_1^*, I_2^*, A_1^*, A_2^*, R_1^*, R_2^*) = (N^*, 0, 0, 0, 0, 0, 0, 0, 0, 0) \text{ and} \\
&\mathbb{E}_2 := (S_1^*, S_2^*, E_1^*, E_2^*, I_1^*, I_2^*, A_1^*, A_2^*, R_1^*, R_2^*) = (S_1^*, N^* - S_1^*, 0, 0, 0, 0, 0, 0, 0, 0),
\end{aligned} \tag{3.19}$$

where (for $\alpha_{21}^c q_{21}^c \neq 0$ and $r_0 \neq 1$),

$$S_1^* = \frac{N^*\left(\alpha_{21}^{ns} q_{21}^{ns} + \psi_{21}^f + \mu\right)}{\alpha_{21}^c q_{21}^c (r_0 - 1)} \quad \text{and} \quad N^* = \frac{\Pi}{\mu}, \tag{3.20}$$

with $r_0 = \dfrac{\alpha_{12}^c q_{12}^c}{\alpha_{21}^c q_{21}^c}$ (for $\alpha_{21}^c q_{21}^c \neq 0$). It follows from (3.20) that the DFE $\mathbb{E}_2$ exists if and only if $r_0 > 1$. This result is summarized below [151].

Theorem 3.2.2. *The behavior-epidemiology model* (3.4) *has a trivial disease-free equilibrium ($\mathbb{E}_1$, which always exists) and a non-trivial disease-free equilibrium ($\mathbb{E}_2$), which exists whenever $r_0 > 1$.*

The quantity r_0 is the ratio of the *contact-mediated* capacity of non-adherent individu-

als to become adherents (at the rate $\alpha_{12}^c q_{12}^c$) to that of adherent individuals becoming non-adherents (at the rate $\alpha_{21}^c q_{21}^c$). In other words, $r_0 > 1$ implies that non-adherent individuals adhere to interventions and move to the adherents group at a rate faster than that at which adherent individuals become non-adherent and move to the non-adherent group (i.e., $r_0 > 1$ means the overall rate of transition from group 1 to group 2 exceeds that for group 2 to group 1). The trivial disease-free equilibrium ($\mathbb{E}_1$) is not epidemiologically realistic, since it does not have any individuals in group 2 (hence, it will not be considered or analysed in this chapter).

3.2.5.1 Local asymptotic stability of the non-trivial DFE of the behavior-epidemiology model

In this section, the *next generation operator method* [88, 89] will be used to analyse the local asymptotic stability property of the non-trivial disease-free equilibrium ($\mathbb{E}_2$) of the behavior-epidemiology model (3.4). The implementation of the next generation operator method requires the computation of two matrices, one that keeps track of new infection terms (denoted by F) and the other that tracks the linear transition terms (denoted by V). It can be shown, using the notation in [88], that the matrices F and V, corresponding to the behavior-epidemiology model (3.4), are given, respectively, by [151]:

$$F = \begin{bmatrix} 0 & 0 & \beta\frac{S_1^*}{N^*} & \beta(1-\varepsilon_m)\frac{S_1^*}{N^*} & \beta\eta_a\frac{S_1^*}{N^*} & \beta\eta_a(1-\varepsilon_m)\frac{S_1^*}{N^*} \\ 0 & 0 & \beta(1-\varepsilon_m)\frac{S_2^*}{N^*} & \beta(1-\varepsilon_m)^2\frac{S_2^*}{N^*} & \beta\eta_a(1-\varepsilon_m)\frac{S_2^*}{N^*} & \beta\eta_a(1-\varepsilon_m)^2\frac{S_2^*}{N^*} \\ 0 & 0 & 0 & 0 & 0 & 0 \\ 0 & 0 & 0 & 0 & 0 & 0 \\ 0 & 0 & 0 & 0 & 0 & 0 \\ 0 & 0 & 0 & 0 & 0 & 0 \end{bmatrix}, \tag{3.21}$$

and,

$$V = \begin{bmatrix} W+\sigma+\mu & -U & 0 & 0 & 0 & 0 \\ -W & U+\sigma+\mu & 0 & 0 & 0 & 0 \\ -(1-r)\sigma & 0 & W+\gamma_i+\mu+\delta_1 & 0 & 0 & 0 \\ 0 & -(1-r)\sigma & -W & \gamma_i+\mu+\delta_2 & 0 & 0 \\ -r\sigma & 0 & 0 & 0 & W+\gamma_a+\mu & -U \\ 0 & -r\sigma & 0 & 0 & -W & U+\gamma_a+\mu \end{bmatrix}, \tag{3.22}$$

where,

$$U = \alpha_{21}^c q_{21}^c \frac{S_1^*}{N^*} + \alpha_{21}^{ns} q_{21}^{ns} + \psi_{21}^f \quad \text{and} \quad W = \alpha_{12}^c q_{12}^c \frac{S_2^*}{N^*}. \tag{3.23}$$

It is convenient to define the following quantity (where ρ is the spectral radius) [151]:

$$\mathcal{R}_C = \rho(FV^{-1}). \tag{3.24}$$

The result below follows from Theorem 2 of [88] (note that closed form expression for $\mathcal{R}_C$ is not readily available, due to the high dimensionality of the associated next

generation matrices, and has to be computed numerically) [151].

Theorem 3.2.3. *The non-trivial disease-free equilibrium of the behavior-epidemiology model* (3.4) *(which exists only if* $r_0 > 1$*) is locally-asymptotically stable if* $\mathcal{R}_C < 1$*, and unstable whenever* $\mathcal{R}_C > 1$*.*

The quantity $\mathcal{R}_C$ is the *control reproduction number* of the behavior-epidemiology model (3.4). It measures the average number of new cases generated by a typical infectious individuals if introduced in a population where some public health intervention measures (notably nonpharmaceutical interventions, such as the use of face mask in public) are implemented. The epidemiological implication of Theorem 3.2.3 is that a small influx of infected individuals into the community will not generate a large outbreak in the community if the control interventions can bring (and maintain) the threshold quantity $\mathcal{R}_C$ to a value less than one. Using the baseline values of the fixed and estimated parameters in Tables 3.3 and 3.4 in Equation (3.24) shows that the value of $\mathcal{R}_C$ during the first wave of the SARS-CoV-2 pandemic in the United States was $\mathcal{R}_C \approx 2.42$ (showing that the non-trivial equilibrium is unstable, and suggesting significant outbreak of the disease). It is worth stating that the value of the control reproduction number associated with the behavior-free model (H.1), denoted by $\widetilde{\mathcal{R}}_C$ and computed by substituting the parameters in Table 3.3 and the estimated parameters for the behavior-free model (namely $\beta = 0.132$ *per* day, $\eta_a = 5.349$ and $\delta = 1.611 \times 10^{-4}$ *per* day) into the corresponding expression for its associated control reproduction number, is $\widetilde{\mathcal{R}}_C = 1.81$. Most modeling studies have suggested a control reproduction number for the first wave of SARS-CoV-2 in the United States in the range [2-4] [21, 160]. Thus, the behavior-free model, unlike the behavior-epidemiology model, may have under-estimated the burden (or severity) of the first wave in the United States.

3.3 Numerical Simulations of Behavior-Epidemiology Model

The behavior-epidemiology model (3.4) will now be simulated, using the baseline values of the fixed and estimated parameters of the model tabulated in Tables 3.3 and 3.4, to assess the impacts of disease-related metrics (namely, contacts with individuals from another group, level of disease-induced mortality, level of symptomatic transmission, proportion of non-symptomatic individuals and intervention fatigue in the community) on inducing behavior change (as measured in terms of the back-and-forth transitions between the two behavior groups considered in this chapter) during the first wave of the SARS-CoV-2 pandemic in the United States. Simulations will also be carried to assess the impact of the various behavior change functions and changes in the value of parameter that accounts for the proportion of exposed individuals who become asymptomatically-infectious at the end of the exposed period (r) on disease burden (specifically, cumulative mortality) during the first wave.

3.3.1 Relative influence of disease metrics on inducing behavior change in the community

In this chapter, behavior change is measured in terms of the transition from the adherent (non-adherent) to the non-adherent (adherent) group. These transitions, or associated behavior change functions ($\psi_{ij}; i, j = \{1, 2\}; i \neq j$), are influenced by the following disease metrics: contacts with individuals from another group (captured by the functions ψ_{12}^{c}, ψ_{21}^{c}; given by Equations (3.8), (3.9), respectively), the level of disease transmission by symptomatic individuals (represented by ψ_{12}^{i}, given by (3.10)), the level of non-symptomatic individuals in the community (represented by ψ_{21}^{ns}, given by (3.11)), the level of disease-induced mortality (ψ_{12}^{m}, given by (3.12)) and the level of

intervention fatigue (ψ_{21}^{f}, defined in (3.13)) in the community. The behavior change functions (ψ_{12}^{c}, ψ_{21}^{c}, ψ_{12}^{i}, ψ_{21}^{ns}, ψ_{12}^{m} and ψ_{21}^{f}) are depicted in Figure 3.4, from which it follows that behavior change (as measured in terms of transition from group 1 to group 2 or vice versa) is most influenced by two disease metrics: the level of disease-induced mortality in the community (red curve in Figure 3.4(a)) followed by the level of symptomatic transmission (blue curve in Figure 3.4(a)). As shown in Figure 3.4(b)), behavior change from group 2 to group 1 due to contact is more influential during the very early stage of the first wave (brown curve in Figure 3.4(b)). As the outbreak progresses, however, this mechanism of behavior change loses influence to, for example, behavior change due to contact with individuals in group 2 (light blue curve in Figure 3.4(b)). Additionally, it is also observed that behavior change due to the presence of non-symptomatic individuals in the community (gold curve in Figure 3.4(b)) is slightly lower when the number of symptomatic cases significantly increase but otherwise remains nearly constant throughout the first wave). Behavior change due to intervention fatigue was of very marginal (or no) influence during the first wave (dark blue curve in Figure 3.4(b)). In summary, the simulations in Figure 3.4 show that the level of disease-induced mortality and disease transmission by symptomatic individuals were the main drivers for positive behavior change from group 1 (non-adherent) to group 2 (adherent) during the first wave of the SARS-CoV-2 pandemic in the United States. The disease metric related to contact and the proportion of non-symptomatic individuals in the community were largely of marginal impact while the metric related to fatigue being inconsequential in inducing significant behavior change during the first wave of COVID-19 in the United States.

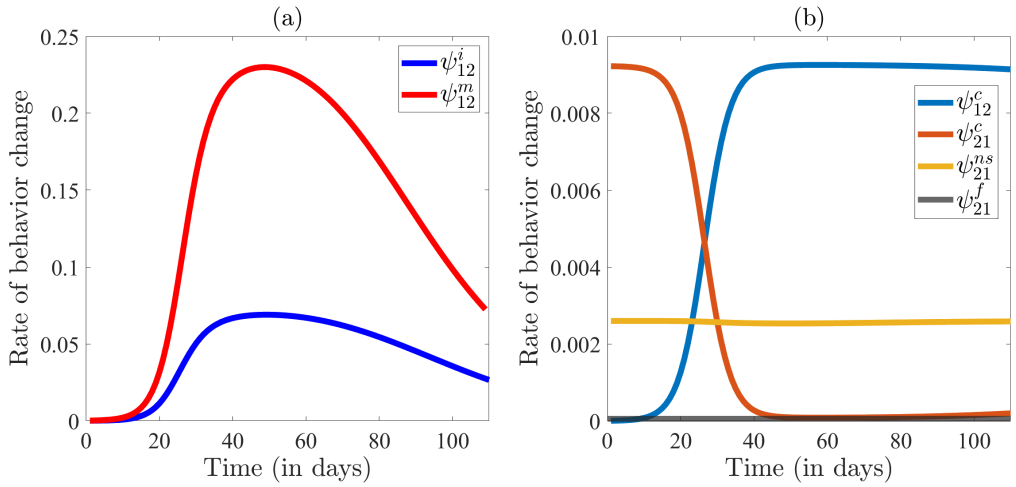

Figure 3.4: Simulations of the behavior-epidemiology model (3.4) assessing the impact of disease-related metric on behavior change during the first wave of COVID-19 in the United States. The rate of behavior change (a) due to infection (ψ_{12}^i) and mortality (ψ_{12}^m) and (b) due to contact with individuals in group 2 (ψ_{12}^c), contact with individuals in group 1 (ψ_{21}^c), presence of non-symptomatic individuals in the community (ψ_{21}^{ns}) and fatigue (ψ_{21}^f) plotted as a function of time. The figure is generated using baseline parameter values from Tables 3.3 and 3.4 [151].

3.3.2 Impact of size of proportion of exposed individuals who become asymptomatically-infectious at the end of exposed period (r)

Asymptomatic infectious individuals were shown, in Section 3.2.2.1, to account for a sizable proportion of new SARS-CoV-2 cases during the first wave in the United States [92, 93, 94]. In this section, the impact of the parameter accounting for the proportion of exposed individuals that become asymptomatic after the exposed period (r) on disease burden and inducing behavior change will be assessed [151].

3.3.2.1 Impact of the proportion of exposed individuals who become asymptomatically-infectious at the end of exposed period (r) on control reproduction number ($\mathcal{R}_C$)

The objective here is to quantify the impact of changes in the proportion of exposed individuals who become asymptomatic at the end of the exposed period (r) on disease burden (as measured in terms of the value of the control reproduction number, $\mathcal{R}_C$ of the behavior-epidemiology model (3.4)), (given by Equation (3.24)). Figure 3.5(a) depicts a profile of $\mathcal{R}_C$, as a function of r, generated by using the baseline values of the parameters in Tables 3.3 and 3.4, from which it follows that the control reproduction number (hence, disease burden) increases with increasing values of the proportion of exposed individuals who become asymptomatically-infectious at the end of the exposed period (r). This is intuitive, since asymptomatic infectious individuals are expected to have more contacts in the community, thereby generating more new cases (in comparison to symptomatic individuals, who may be bed-ridden or in self-isolation; thereby having limited or no contact with the public). However, when the value of the parameter for the relative infectiousness of asymptomatic individuals, in relation to symptomatic infectious individuals (η_a) is reduced from its estimated baseline value of $\eta_a = 2.275$ to $\eta_a = 0.85$, for example, while all other parameters are kept at their baseline values in Tables 3.3 and 3.4, the result obtained show that the control reproduction number ($\mathcal{R}_C$) decreases with increasing values of r (Figure 3.5(b)). Hence, this result shows that if the relative infectiousness of asymptomatic infectious individuals is lower than that of symptomatic individuals (for example if asymptomatic individuals have lower contacts or lower viral load and transmission capacity, in comparison to symptomatic individuals), then an increase in the proportion of exposed individuals who are asymptomatic can reduce disease burden. In

other words, this chapter shows that the size of asymptomatic infectious individuals (as measured by the parameter r) could lead to an increase or a decrease in disease burden in the community, depending on whether or not the relative infectiousness of asymptomatic infectious individuals is larger or lower than the relative infectiousness of symptomatic infectious individuals (i.e., this depends on whether $r > 1$ or $r < 1$).

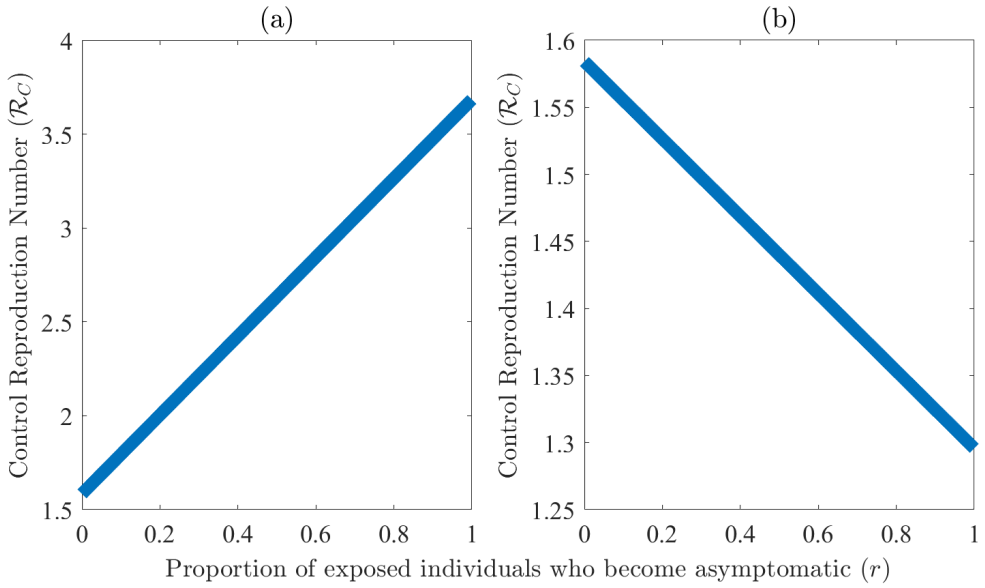

Figure 3.5: Simulations of the behavior-epidemiology model (3.4) assessing the impact of change of the proportion of exposed individuals who become asymptomatic at the end of the exposed period (r) on the control reproduction number ($\mathcal{R}_C$). An increase in r can (a) increase or (b) decrease $\mathcal{R}_C$. Figure (a) is generated by calculating $\mathcal{R}_C$, given by Equation (3.24), for varying values of r between 0 and 1, with remaining parameter values as in Tables 3.3 and 3.4. Figure (b) is similarly generated by varying r between 0 and 1, $\eta_a = 0.8$ and remaining parameter values as in Tables 3.3 and 3.4 [151].

3.3.2.2 Impact of the proportion of exposed individuals who become asymptomatically-infectious at the end of exposed period (r) on mortality

The objective here is to quantify the impact of changes in the proportion of exposed individuals who become asymptomatic at the end of the exposed period (r) on SARS-CoV-2 mortality during the first wave in the United States. Here, too, the behavior-epidemiology model (3.4) is simulated using the baseline parameter values given in Tables 3.3 and 3.4, with varying values of r. The results obtained are depicted in Figure 3.6. The profile of the cumulative SARS-CoV-2 mortality in the United States during the first wave, as a function of r is depicted in Figure 3.6(a). This figure show that the cumulative mortality increases with increasing values of r until a peak is reached (at about $r = 0.46$), above which the cumulative mortality decreases, reaching zero at $r = 1$ (this is intuitive since $r = 1$ corresponds to the case that all exposed individuals become asymptomatic at the end of the exposed period, and, in the formulation of the behavior-epidemiology model, it was assumed that asymptomatic infectious individuals do not suffer disease-induced mortality). Thus, this chapter shows the existence of a critical threshold for the proportion of exposed individuals who become asymptomatic at the end of the exposed period that maximizes the cumulative SARS-CoV-2 mortality during the first wave in the United States. Specifically, if $r = 0.46$ (i.e., 46% of exposed individuals do not show clinical symptoms of SARS-CoV-2 at the end of the exposed period, while the remaining 54% do so), cumulative SARS-CoV-2 mortality in the United States is maximized. Above this threshold value, the cumulative SARS-CoV-2 mortality significantly decreases (reaching zero when all exposed individuals do not show symptoms of the disease at the end of the exposed period). This result shows that a strategy that significantly

increases the proportion of exposed individuals who become asymptomatic at the end of the exposed period (e.g., rapid testing, detection and treatment of exposed (i.e., newly-infected but not yet infectious) individuals) will significantly reduce the cumulative mortality of SARS-CoV-2 during the first wave in the United States. Furthermore, the behavior-epidemiology model is further simulated using the baseline parameter values in Tables 3.3 and 3.4 to generate the profile of the maximum daily SARS-CoV-2 mortality during the first wave of the pandemic in the United States, as a function of the proportion of exposed individuals who become asymptomatic at the end of the exposed period (r). The results obtained, depicted in Figure 3.6(b), also show an increase in the maximum daily mortality with increasing values of r until a peak is reached at $r = 0.64$, and the maximum daily mortality decreases thereafter (in other words, simulating the behavior-epidemiology model with $r = 0.64$, and all other parameters as given in Tables 3.3 and 3.4, resulted in the highest peak in the daily SARS-CoV-2 mortality during the first wave). Thus, based on the parameter values used in the simulations in this section, this chapter identifies two distinct threshold values of the parameter r (for the proportion of exposed individuals that become asymptomatic at the end of the exposed period) that maximize cumulative and daily mortality, respectively. While the daily SARS-CoV-2 mortality is maximized during the first wave when the proportion of exposed individuals who become asymptomatic at the end of the exposed period is 64% (this is equivalent to maximizing the mortality burden on the healthcare system if measured on a daily basis), the cumulative mortality is maximized when the proportion is 46% (this is equivalent to maximizing the overall mortality burden on the healthcare burden from the beginning of the pandemic until the end of the first wave). The profiles of the cumulative and daily SARS-CoV-2 mortality, as functions of time, for the two threshold values of r (i.e., $r = 0.46$ and $r = 0.64$) are depicted in Figure I.1 (in Appendix I).

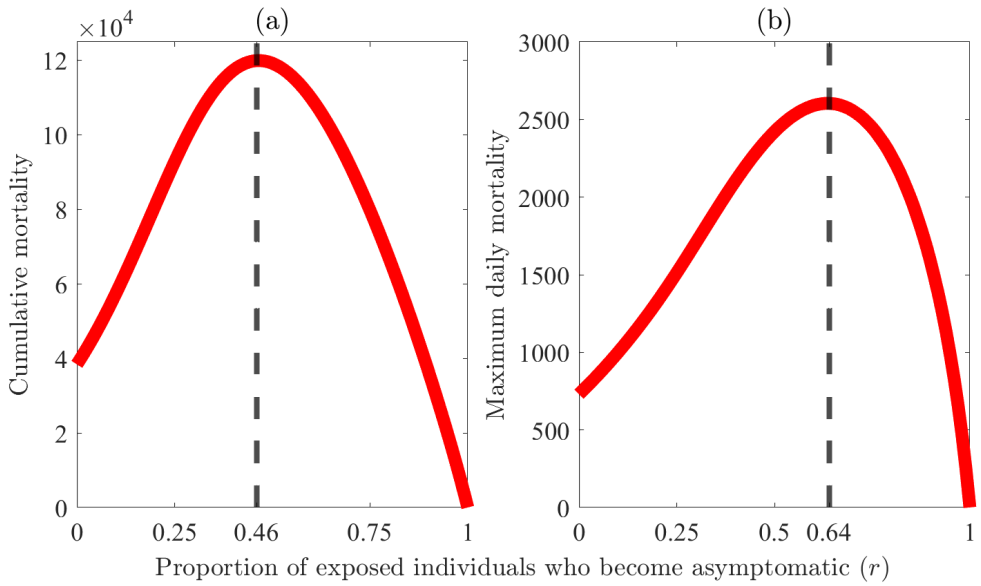

Figure 3.6: Simulations of the behavior-epidemiology model (3.4) assessing the impact of change in the proportion of exposed individuals who become asymptomatic at the end of the exposed period (r) on mortality. The change in (a) cumulative mortality and (b) maximum daily death is displayed for varying values of r. The vertical dashed line in (a) depicts the value of r that maximizes cumulative mortality while in (b) it depicts a value of r that maximizes daily mortality. The figures are generated by varying the value of r between 0 and 1 in the behavior-epidemiology model (3.4) while taking the remaining parameter values from Tables 3.3 and 3.4 [151].

3.4 Discussion and Conclusion

This chapter presents a novel mathematical model for the transmission dynamics and control of the SARS-CoV-2 pandemic in the United States that explicitly incorporates the impacts of changing human behavior. Specifically, the model was formulated by stratifying the total population into two groups based on their adherence or lack thereof to public health interventions, and considered five metrics for human behavior, namely behavior change due to: (a) information received by members of one group from members of the other group (b) the level of symptomatic transmission in the community (c) the size of the proportion of non-symptomatic individuals in

the community, (d) the level of disease-induced mortality in the community and (e) the degree of fatigue to adherence to intervention and mitigation measures (such as wearing a face mask in public, observing social distancing and community lockdowns etc).

The resulting two-group behavior-epidemiology model, which takes the form of a relatively large deterministic system of nonlinear differential equations, was parameterized using observed cumulative SARS-CoV-2 mortality data, at the national level, for the United States during the first wave of the pandemic (March to June, 2020). The model was then rigorously analysed to gain qualitative insights into its dynamical features. Such analyses revealed that the disease-free equilibrium of the model is locally-asymptotically stable whenever a certain epidemiological quantity (known as the *control reproduction number*, denoted by $\mathcal{R}_C$) is less than one, and unstable when the quantity exceeds one. The epidemiological consequence of this result is that the disease can be effectively controlled in the community (when $\mathcal{R}_C < 1$) if the initial number of infected individuals introduced into the community is small enough. In other words, significant outbreaks will not occur if the intervention and mitigation measures implemented can bring (and maintain) this threshold quantity to a value less than one. The model was then simulated to quantify the impact of behavior changes on the trajectory and burden of the disease, in addition to assessing the population-level impact of public health intervention and mitigation measures (specifically, basic nonpharmaceutical interventions, such as the use of face mask by individuals in the adherent group).

As stated above, the two-group behavior-epidemiology model was fitted and cross-validated using the observed cumulative mortality data for the United States during the first wave of the SARS-CoV-2 pandemic (which corresponds to the period from

March 1, 2020, to June 18, 2020; we used the segment of the data from March 1, 2020 to May 29, 2020 for fitting the model, and the data for the remaining segment, from May 30, 2020 to June 20, 2020, for cross-validation). We showed very good fit for the cumulative mortality data (and we used the estimated parameters, together with the fixed parameters of the behavior-epidemiology model, to predict the observed daily mortality for the SARS-CoV-2 pandemic during the first wave in the United States, showing a very good prediction). We showed that, unlike for the case of the behavior-epidemiology, the behavior-free analog of the behavior-epidemiology model (i.e., the two-group model without human behavior changes explicitly incorporated into the model) did not do as well in correctly capturing the observed trajectory and burden of the pandemic during the first wave.

Extensive numerical simulations of the behavior-epidemiology model is carried out to determine which of the five behavior metrics considered in this chapter were more influential in inducing positive behavior changes (to minimize risk of acquisition and/or transmission of infection) during the first wave of the SARS-CoV-2 pandemic in the United States. The results obtained showed that the behavior change metric that induces the greatest positive behavior change (as measured in terms of the transition from the non-adherent group to the adherent group) is the behavior change due to the level of disease-induced mortality in the community, followed by behavior change due to the level of symptomatic individuals in the community (in other words, this chapter shows that, during the first wave, people are more likely to change behavior, and begin to strictly adhere to public health intervention and mitigation measures implemented, if they see a significant increase in mortality due to the disease in addition to a significant increase in the number of people with symptoms of the disease in the community). Simulations also showed that behavior change induced by fatigue

to interventions (i.e., wearing a mask, in this case) had only a very marginal (or essentially no) effect in inducing a negative behavior change (from adherent to non-adherent group) during the first wave of the pandemic in the United States. In other words, this chapter shows that the overwhelming proportion of individuals in the adherent group did not experience significant level of fatigue to intervention during the first wave of COVID-19 pandemic in the United States.

Extensive numerical simulations were also carried out to assess the impact of the the proportion of exposed individuals who become asymptomatically-infectious at the end of the exposed period (denoted by the parameter r) on the burden of the SARS-CoV-2 pandemic, in addition to inducing behavior change to interventions, during the first wave in the United States. We showed that, using the baseline values of the parameters of the behavior-epidemiology model in the simulations (where asymptomatic infectious individuals were at least twice more infectious than symptomatic infectious individuals), the control reproduction number ($\mathcal{R}_C$) of the behavior-epidemiology model increases with increasing values of r. Thus, in this case, an increase in the proportion of exposed individuals who eventually become asymptomatically-infectious resulted in an increase in the burden of the pandemic (since an increase in $\mathcal{R}_C$ implies increase in average number of new cases and, potentially, increase in number of hospitalizations and deaths). On the other hand, if asymptomatic infectious were not as infectious as symptomatic infectious individuals (i.e., if the parameter η_a for the relative infectiousness of asymptomatic individuals is less than one), while all other parameters of the model are kept at their baseline values, the control reproduction number decreases with increasing values of r. In other words, this chapter shows that the ability of asymptomatic infectious individuals to significantly increase the burden of the pandemic depends on the relative infectiousness of asymptomatic in-

fectious individuals, in comparison to the infectiousness of symptomatic individuals. Nonetheless, this result highlights the importance of reducing the level of asymptomatic transmission in the community (through strategies such as widespread testing and rapid isolation and treatment of asymptomatic individuals).

Chapter 4

MATHEMATICAL ASSESSMENT OF WASTEWATER-BASED EPIDEMIOLOGY TO PREDICT SARS-COV-2 CASES AND HOSPITALIZATIONS IN MIAMI-DADE COUNTY

4.1 Introduction

The use of wastewater to study the spread of infectious disease (based on isolating pathogens from the stool of some individuals infected with the disease) has a long history, dating back to the pioneering work of John Snow (considered the *"Founding Father"* of modern epidemiology) in 1854, which showed that cholera-contaminated water from a Broad Street pump was the source of the cholera transmission in the Soho district of London [161, 162]. In the late 1930s and early 1940s, a Yale Poliomyelitis Study Unit led by John Paul and James Trask detected *poliomyelitis* (polio) virus in sewage collected in multiple cities in the United States with active polio epidemics, including Charleston, South Carolina; Detroit, Michigan; and Buffalo, New York, by injecting wastewater in the endemic regions into monkeys and observing to see if the monkeys acquire the polio infection [163, 164, 165]. Their experiment showed that wastewater could potentially be used as an indicator of disease activity in a community. However, their method involving monkeys was costly, slow, and inefficient as the monkeys died from other chemicals or pathogens that were present in the wastewater injected into them [166]. In the modern times, the availability of efficient and safe methods for detecting viral RNA in wastewater (such as *reverse transcription–polymerase chain reaction* (RT-PCR)), wastewater-based surveillance

of disease activity has become an effective and resource-efficient tool for gathering crucial/important community-level public health information during outbreaks of infectious diseases [167, 168]. For instance, the United States Centers for Disease Control and Prevention (CDC) launched the National Wastewater Surveillance System (NWSS) in September of 2020, in response to the novel 2019 coronavirus pandemic (coined COVID-19, caused by SARS-CoV-2) [169].

Wastewater-based surveillance epidemiology has numerous benefits. It, for instance, is a less invasive disease surveillance mechanism, in comparison to conducting mass testing to detect the level of spread of a pathogen in the community [170]. Furthermore, in the context of COVID-19, while a kit for rapid antigen tests can cost as little as 2 dollars to manufacture, bidding wars between health systems, state governments and employers can contribute to much higher prices [171]. For example, during the year 2021, a spokesperson for the state of South Carolina claimed that the state paid as high as 130 for some of its rapid test kits [171]. Ngwira *et al.* [172] estimated the economic costs of conducting wastewater-based environmental surveillance for SARS-CoV-2 in Blantyre, Malawi and Kathmandu, Nepal, estimating monthly costs of approximately $6,175$ to $8,272$ dollars for Blantyre and $16,756$ to $30,050$ dollars for Kathmandu, respectively. It is further estimated that the cost *per* person in the catchment area annually ranged from dollar 0.07 to 0.10 in Blantyre and dollar 0.07 to 0.13 in Kathmandu [172], respectively. Wastewater surveillance, when combined with other forms of public health surveillance and interventions, can result in a very effective control and mitigation of infectious diseases spreading in communities [173, 174]. For instance, during the SARS-CoV-2 pandemic, in 2020, researchers from the University of Arizona, Tucson, used wastewater samples from campus dorms to identify which dorms are infected (i.e., wastewater from which student dormitory contained

viral RNA), subsequently leading to mass testing of students in the infected dorm (and the detection and quarantine of two asymptomatic cases) [175, 176]. It has also been suggested that wastewater could potentially act as a "leading indicator" or an "early warning signal" for a disease outbreak [177, 178, 179, 180, 181]. Olesen *et al.* state that the biological principle behind wastewater as a leading indicator is that many infected individuals shed the virus in stool before they develop symptoms and thus also before they seek medical care [178]. Finally, wastewater genomic surveillance can provide insight into disease variants (or strains) co-circulating in the community [182, 183]. Wastewater surveillance in airports and on aircraft has been proposed as a low-cost mechanism to monitor SARS-CoV-2 variants entering a region [184, 185, 186]. All of these reasons not only highlight the importance of using wastewater surveillance to detect or mitigate disease activity, but also hint at the high utility of incorporating wastewater data into mathematical models for the spread of emerging and re-emerging infectious diseases in a community to enhance their prediction capacity.

Numerous mathematical models that use wastewater surveillance data have been developed and used to study the transmission dynamics and control of numerous emerging and re-emerging infectious diseases in communities. Before specifically discussing some of the COVID-19 mathematical models that used wastewater data, it is intuitive to highlight the fact that numerous models for cholera epidemics have already accounted for the concentration of the bacterium that causes the disease (*V. cholerae*) in water [187, 188, 189, 190, 191, 192]. The key difference between the COVID-19 wastewater models to be discussed and the cholera models is that, while in the latter contaminated water is a source of infection, in the former, the data collected from the wastewater (sewage) is used as an indicator of the level of spread

of the disease in the community. The state of Israel was certified as polio-free by the World Health Organization in June 2002 [193]. About 11 years later, wild-type *poliovirus 1* (WPV1) was detected during routine sewage samples collected between the 7th to the 13th of April 2013 [193, 194]. Oral polio vaccine (OPV), a weakened poliovirus given in the form of oral drops [195], was discontinued and replaced by inactivated poliovirus vaccine (IPV) only policy in Israel in 2005 [194, 196]. This change in policy was due to the risk of the emergence of circulating vaccine-derived poliovirus (cVDPV) and vaccine-associated paralytic poliomyelitis [196]. Although both types of the polio vaccine provide excellent protection against the disease, only OPV is able to prevent transmission (by inducing "strong gut immunity that blocks transmission of the virus, which is shed in the stool and spread largely through fecal-oral contamination" [196]). In response to the sudden reappearance of polio, in early August 2013, Israel launched a supplementary OPV vaccination program, by September 20, 2023 and 60% of the targeted Israeli children had been vaccinated with bivalent OPV [194]. The last two positive samples detected in Israel were on October 2013 and February 2014 [197], thus effectively ending the outbreak in less than a year's time. The silent spread of polio in Israel in 2013-2014 and its subsequent suppression before the detection/development of a single paralytic polio case highlights the importance of sewage-based surveillance.

In the context of the COVID-19 pandemic, several statistical methods have also been used to show a correlation between SARS-CoV-2 RNA levels in wastewater and COVID-19 cases in the community [198, 199, 200]. Statistical models have used wastewater data to predict COVID-19 cases [201], hospital admission [202, 203, 204] and the effective reproduction number [205]. Furthermore, compartmental models that incorporate wastewater data have also been used to achieve the same objective.

For instance, McMahan *et al.* [206] used an $SEIR$ model and wastewater surveillance data to show that the number of model predicted COVID-19 cases in Clemson University, South Carolina, between the time period from May 27, 2020 to August 25, 2020, was 11 (95% CI 4.2–17.5) times higher than the confirmed (i.e., observed) cases. Phan *et al.* [207] proposed an SEIR-V (where V is the viral load in wastewater) model that uses wastewater data to also show that the model predicted COVID-19 cases in the Greater Boston area, during the period from October 2, 2020 to January 25, 2021, were 8.3 to 10.2-fold higher than confirmed cases in Greater Boston area from October 2, 2020 to January 25, 2021. Nourbakhsh *et al.* [208] extended the standard $SEIR$ model to explicitly account for various classes of infectious individuals (symptomatic, asymptomatic and hospitalized) and recovered individuals who are still shedding the virus in feces. The authors also accounted for the delay and degradation of RNA from shedding to sampling.

This chapter is based on using a relatively simple SEIR epidemiology-wastewater model to predict the burden of the SARS-CoV-2 and disease-related hospitalizations in a population. Specifically, the model will be used to predict the case and hospitalization trends for Miami-Dade County, Florida. Although various compartmental models have been used to predict the burden of COVID-19 at a county and state level using SARS-CoV-2 case and mortality [151, 26, 109] and case data [23, 149], the utility of these models is affected by decisions to halt the collection of such data, as was the case with SARS-CoV-2 (when the Federal COVID-19 Public Health Emergency (PHE) Declaration expired on May 11, 2023; and the CDC's authorization to collect certain types of public health data (most notably COVID-19 cases) also expired) [209, 210]. Furthermore, the confirmed case data reported by the CDC does not include asymptomatic COVID-19 cases (i.e., the confirmed case count does not

accurately reflect the true burden of the disease) [211]. Additionally, the widespread availability of free at-home COVID-19 test kits since January 2022 [212] impacted the accuracy of the official testing count (due to under-reporting of positive at-home test results) [213]. These factors, taken in totality, suggest that compartmental models for the spread and control of the SARS-CoV-2 used after the halting of data collection in May 2023 may benefit from alternative data source, such as wastewater surveillance data.

Finally, the number of SARS-CoV-2-related deaths occurring at a county level may be low enough (or may occur infrequently enough) that fitting an ODE model to daily or weekly mortality data may pose additional challenges. This also potentially limits the utility of using mortality data (after May 2023) to fit compartmental models for the SARS-CoV-2 pandemic. Wastewater surveillance at the county level provides a cost-effective alternative to remedy the unavailability of reliable epidemiological (case and mortality) data for use to predict the transmission dynamics and control of the disease at the county level. The use of wastewater surveillance data (as an indicator for disease activity) is the main focus of this chapter. The chapter is organized as follows. The wastewater-based epidemiology (WBE) model will be formulated in Section 4.2. Specifically, while the equations describing the disease transmission dynamics in humans are described in Section 4.2.1, the equations for the dynamics of SARS-CoV-2 RNA concentration in the wastewater are described in Section 4.2.2. Asymptotic stability results for the associated disease-free equilibrium of the model are given in Section 4.2.3. The model is fitted, using weekly wastewater data for the county, in Section 4.3. Predictions for the number of weekly hospitalizations in the county are also made in this section. Detailed time-varying global sensitivity analysis is carried out in Section 4.4 to determine the parameters (wastewater-based, epidemi-

ological and biological) that have the most influence on the chosen response function (namely, the cumulative viral load in the wastewater). Numerical simulations are carried out in Section 4.5. The main results of the chapter, along with its limitations, are discussed and summarized in Section 4.6.

4.2 Wastewater-based Epidemiology (WBE) Model

In order to design the SARS-CoV-2 transmission model that incorporates wastewater data, the total human population at time t, denoted by $N(t)$, is split into mutually-exclusive compartments of susceptible ($S(t)$), exposed (i.e., newly infected but not infectious and not shedding virus into the wastewater system; $E(t)$), infectious and shedding viral RNA into the wastewater ($I(t)$), hospitalized and shedding viral RNA into the wastewater ($H(t)$), recovered and shedding viral RNA into the wastewater ($J(t)$) and recovered but not shedding viral RNA into the wastewater ($R(t)$), individuals, so that [214]:

$$N(t) = S(t) + E(t) + I(t) + H(t) + J(t) + R(t).$$

Let $V(t)$ represent the concentration of viral RNA (shed through feces) in the wastewater at time t. Furthermore, let $W(t)$ represents the cumulative amount of measured SARS-CoV-2 concentration in the wastewater at time t, after accounting for decay and delay of RNA from excretion to arrival, and other factors such as uncertainty in measurement. The equations for the rate of change of the various compartments are derived below.

4.2.1 *Equations for SARS-CoV-2 dynamics between humans*

Susceptible individuals acquire infection, following effective contact with infectious individuals (in the I and H classes), at a rate $\lambda(t)$ (*force of infection*), given by [214]:

$$\lambda(t) = \left(\frac{\beta_I I(t) + \beta_H H(t)}{N(t)} \right), \tag{4.1}$$

where β_I and β_H represent the effective contact rate of infectious individuals in the symptomatic (I) and hospitalized (H) compartments. Newly-infected individuals in the exposed class (E) progress to develop clinical symptoms of SARS-CoV-2 at a rate σ. Symptomatic individuals are hospitalized at a rate ϕ. Symptomatic and hospitalized individuals recover (while also shedding viral RNA into the wastewater) at a rate γ_I and γ_H, respectively (i.e., γ_I and γ_H, represent the rates at which individuals in the I and H classes progress to the J class, respectively, upon recovery from SARS-CoV-2 infection). Finally, recovered individuals who shed viral RNA into the wastewater (i.e., individuals in the J class) move to the no-viral-shedding recovered class (R) at a rate γ_R. It follows, based on the above assumptions and derivations, that the wastewater-epidemiology (WBE) epidemic model for the transmission of SARS-CoV-2 in a community is given by the following deterministic system of nonlinear differential equations (where a dot represents differentiation with respect to time t) [214]:

$$
\begin{cases}
\dot{S}(t) = -\lambda(t)S(t), \\
\dot{E}(t) = \lambda(t)S(t) - \sigma E(t), \\
\dot{I}(t) = \sigma E(t) - (\gamma_I + \phi)I(t), \\
\dot{H}(t) = \phi I(t) - \gamma_H H(t), \\
\dot{J}(t) = \gamma_I I(t) + \gamma_H H(t) - \gamma_J J(t), \\
\dot{R}(t) = \gamma_J J(t).
\end{cases}
\tag{4.2}
$$

4.2.2 Equations for dynamics of viral concentration in the wastewater

To derive the equations for the dynamics of viral concentration in the wastewater system, we assume, first of all, that the quantity of viral shedding (through feces) into the wastewater at time t, denoted by $V(t)$, increases by the viral shedding of individuals in the symptomatic (I), hospitalized (H) and recovered but shedding (J) classes. Let $\alpha\zeta_I$, $\alpha\zeta_H$ and $\alpha\zeta_J$ represent the rate at which individuals in the I, H and J compartments shed viral RNA into the wastewater system in the community. Here, α is the average fecal load (gram *per* unit time *per* person) and ζ_j (with $j = \{I,\ H,\ J\}$) is the average viral shedding rate of an individual in j compartment (RNA copies *per* gram) [207]. The quantity V is reduced at a rate d_V (where $1/d_V$ is the average time from excretion of feces to collection of a sample at the wastewater treatment plant). Furthermore, only a certain proportion of the viral RNA shed into the wastewater is measurable (denoted by a parameter η) due to a number of complex processes that affect RNA (for example, due to temperature-related decay) [215, 216]. Hence, the cumulative amount of the viral RNA measured in (or collected from) the wastewater, denoted by $W(t)$, is increased at a rate ηd_V. Thus, based on the above assumptions and derivations, the equations for the rate of change of the viral concentrations V

and W are given, respectively, by [214]:

$$\begin{cases} \dot{V}(t) = [\zeta_I I(t) + \zeta_H H(t) + \zeta_J J(t)]\, \alpha - d_V V(t), \\ \dot{W}(t) = \eta d_V V(t). \end{cases} \tag{4.3}$$

Let $\widetilde{W}(N)$ represents the amount of wastewater collected at time N. Hence, $\widetilde{W}(N)$ can be obtained from the integral [214]:

$$\widetilde{W}(N) = \int_{N-1}^{N} \dot{W}(l) dl. \tag{4.4}$$

The WBE model, defined based on coupling the equations for the dynamics of SARS-CoV-2 in humans with those for the viral dynamics within the wastewater system, is given by the system of equations {(4.2),(4.3)}. Figure 4.1 depicts the flow diagram of the WBE model, and the state variables and parameters are described in Tables 4.1 and 4.2, respectively. The WBE model (4.2),(4.3)} is an extension of various epidemiological models that incorporate wastewater dynamics [206, 207]. In particular, it extended the model in [207] by, *inter alia* [214]:

(i) Adding compartment of (and viral shedding by) hospitalized individuals (hospitalized individuals are not explicitly accounted for in [207]).

(ii) Adding the compartment J of recovered individuals who still shed viral RNA into the wastewater (this compartment was not accounted for in [207]).

(iii) Using standard incidence to model the infection rate (mass action incidence was used in [207]).

(iv) Modeling viral dynamics in the wastewater system using two equations, accounting for (a) the viral RNA shed by individuals in the community and (b) the viral RNA measured at the wastewater treatment plant (only one equation was used to model the wastewater component in [207]).

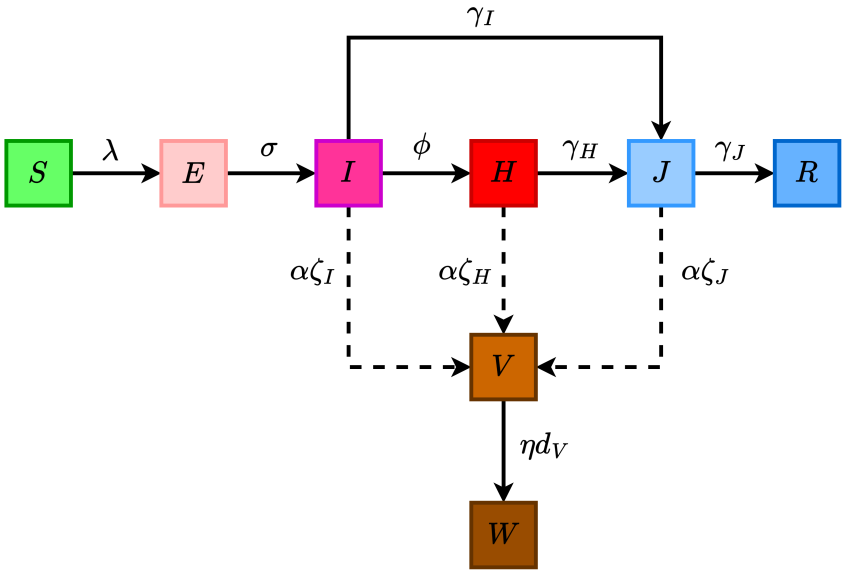

Figure 4.1: Flow diagram of the wastewater-based epidemiology (WBE) model {(4.2),(4.3)}, where λ is defined in Equation (4.1). The dashed lines represent the rate of fecal viral RNA shedding by individuals in the symptomatic (I), hospitalized (H) and recovered (J) compartments. The state variables and parameters of the model are described in Tables 4.1 and 4.2, respectively [214].

4.2.3 Asymptotic stability of disease-free equilibria

In this section, the local asymptotic stability of the disease-free solutions of the WBE model will be analysed to determine conditions, in parameter space, for the control or possible persistence of a SARS-CoV-2 outbreak in the community. It should, first of all, be noted that the sub-model describing the disease dynamics in humans (i.e.,Equation (4.2)) is decoupled from the equation for the wastewater dynamics

State variable	Description
S	Number of susceptible individuals
E	Number of exposed (newly infected but not infectious or shedding) individuals
I	Number of infectious (and shedding) individuals
H	Number of hospitalized (and shedding) individuals
J	Number of recovered (i.e., not infectious) individuals who are still shedding virus through feces
R	Number of recovered (i.e., not infectious) individuals who are shedding virus through feces
V	Quantity of viral RNA shed through feces
W	Cumulative measurement of viral RNA in wastewater

Table 4.1: Description of the state variables of the WBE model {(4.2),(4.3)} [214].

Parameter	Description
$\beta_I(\beta_H)$	Effective contact rate of individuals in the $I(H)$ compartment
σ	Progression rate from exposed (E) to I class
γ_I $(j = \{I, H, J\})$	Recovery rate for individuals in j class
ϕ	Rate of at which individuals in I class get hospitalized
α	Average fecal load *per* person *per* unit time
ζ_j $(j = \{I, H, J\})$	Average viral shedding *per* gram from individuals in j compartment
$\alpha\zeta_j$ $(j = \{I, H, J\})$	Rate at which individuals in j class shed
$1/d_v$	Average time from excretion of feces to collection at the treatment plant
η	Proportion of shed viral RNA that is not lost in sewage by measurement time
ηd_V	Rate at which viral RNA goes from V to W class

Table 4.2: Description of the parameters of the WBE model {(4.2),(4.3)} [214].

(Equation (4.3)). Thus, the asymptotic dynamics of the WBE model reduces to the analysis of the disease-free equilibria of the sub-model (4.2).

It can be seen that the model (4.2) has a continuum of disease-free equilibria (DFE), given by [21, 26]:

$$\mathbb{E}_0 = (S^*, E^*, I^*, H^*, J^*, R^*) = (N(0) - R^*, 0, 0, 0, 0, R^*),$$

where $N(0)$ is the initial total population, $0 < S^* \leq N(0)$, $0 \leq R^* \leq N(0)$ and $0 < S^* + R^* \leq N(0)$. It is convenient to define the total population at the DFE as $N^* =$

S^*+R^*. Since our epidemic model does not account for disease-induced mortality (i.e., the population is asymptotically constant), $N^* = N(0)$. The asymptotic stability of the DFE of the model (4.2) can be analysed using the *next generation operator method* [88, 89]. Using the notation in [88], it can be seen that the non-negative matrix of new infection terms (denoted by F) and the M-Matrix of linear transition terms in the infected compartments of the model (denoted by V) are given, respectively, by [214]:

$$F = \begin{bmatrix} 0 & \beta_I \dfrac{S^*}{N^*} & \beta_H \dfrac{S^*}{N^*} \\ 0 & 0 & 0 \\ 0 & 0 & 0 \end{bmatrix} \quad \text{and} \quad V = \begin{bmatrix} \sigma & 0 & 0 \\ -\sigma & \gamma_I + \phi & 0 \\ 0 & -\phi & \gamma_H \end{bmatrix}. \tag{4.5}$$

It is also convenient to define the quantity (where ρ is the spectral radius) [88, 89]:

$$\mathcal{R}_v = \rho(FV^{-1}) = \mathcal{R}_{0,I} + \mathcal{R}_{0,H}, \tag{4.6}$$

where,

$$\mathcal{R}_{0,I} = \beta_I \left(\frac{S^*}{N^*}\right)\left(\frac{1}{\gamma_I + \phi}\right), \quad \mathcal{R}_{v,H} = \beta_H \left(\frac{S^*}{N^*}\right)\left(\frac{\phi}{\gamma_I + \phi}\right)\left(\frac{1}{\gamma_H}\right). \tag{4.7}$$

The quantity $\mathcal{R}_0$ is the *basic reproduction number* of the model (4.2) (and, hence, of the WBE model {(4.2),(4.3)}). It is a measure of the average number of new cases generated by a typical infected individual if introduced into a population that is completely susceptible. The quantities $\mathcal{R}_{0,I}$ and $\mathcal{R}_{0,H}$ are the constituent basic reproduction numbers for the average number of new cases generated by symptomatic and hospitalized individuals, respectively. The result below follows from Theorem 2 of [88].

Theorem 4.2.1. *The continuum of disease-free equilibria* ($\mathbb{E}_0$) *of the model* (4.2) *is locally-asymptomatically stable (LAS) if* $\mathcal{R}_0 < 1$.

The epidemiological implication of Theorem 4.2.1 is that a small influx of COVID-19 cases will not generate a large outbreak in the community if $\mathcal{R}_0 < 1$. In the case of epidemic models, such as the sub-model (4.2), the epidemiological requirement of having $\mathcal{R}_0 < 1$, while sufficient, is not necessary for the elimination of the disease from the community [26, 21]. In other words, unlike in an endemic model (with demographic birth and death processes, guaranteeing an influx of new susceptible individuals into the population), the disease will die out (with time) under the assumptions of an epidemic model regardless of the value of the reproduction number (it should be noted that models for new epidemics, such as (4.2), always assume a large, closed population, with no influx of people into or out of the population, in addition to the assumption that the timescale of the epidemic is smaller than the demographic timescale [217]. Consequently, the susceptible population can decrease as more people acquire the infection but is not replenished, thus eventually leading to the elimination of the disease even if the reproduction number exceeds unity.

Remark 4.2.1. *In the case that $\mathcal{R}_0 > 1$, the epidemic will grow to a peak and then eventually decline to zero [26, 22, 21].*

4.3 Data-fitting and Parameter Estimation

The wastewater-based epidemiology (WBE) model {(4.2),(4.3)} has 13 parameters. While the values of 8 parameters is known from literature, the values of the remaining 5 parameters (namely the the parameters for the effective contact rate of infectious (β_I) and hospitalized (β_H) individuals, the rate of hospitalization (ϕ), the average fecal load *per* person (α) and the proportion of shed viral RNA that arrives at the treatment plant (η) will be obtained by fitting the model with the wastewater data from the community. Specifically, the WBE model {(4.2),(4.3)} will be fitted using

the weekly-measured wastewater data (obtained from Biobot Analytics [218]) for the COVID-19 pandemic in the Miami-Dade county, Florida, for the period from July 3, 2021 to October 9, 2021. Additionally, some of the initial values of the state variables of the model (namely, $E(0)$, $I(0)$, $J(0)$ and $R(0)$) will be fitted from the data as well (see the details in the caption of Figure 4.3). Miami-Dade county has three wastewater treatment plants (WWTPs): the north district WWTP, the central district WWTP and south district WWTP, servicing approximately 780,000, 830,000 and 920,000 people, respectively [219]. U.S. Census Bureau estimates the total population of Miami-Dade county for July 1, 2022 to be 2,673,837 [220]. Hence, these wastewater treatment plants serve about 95% of the total population of Miami-Dade county. The map of the service area corresponding to each of the three treatment plants is given in Figure 4.2. The wastewater data used to fit the model is processed by Biobot Analytics. This company gives the average weekly data collected from each of the three treatment plants in the county [218]. Consequently, to convert this to total weekly wastewater data (which is what we really need for fitting the model), we multiply the average weekly data by 7.

Before describing the data fitting of the WBE model {(4.2),(4.3)}, the values of the 8 known parameters (also known as *fixed parameters*) of the model are described below.

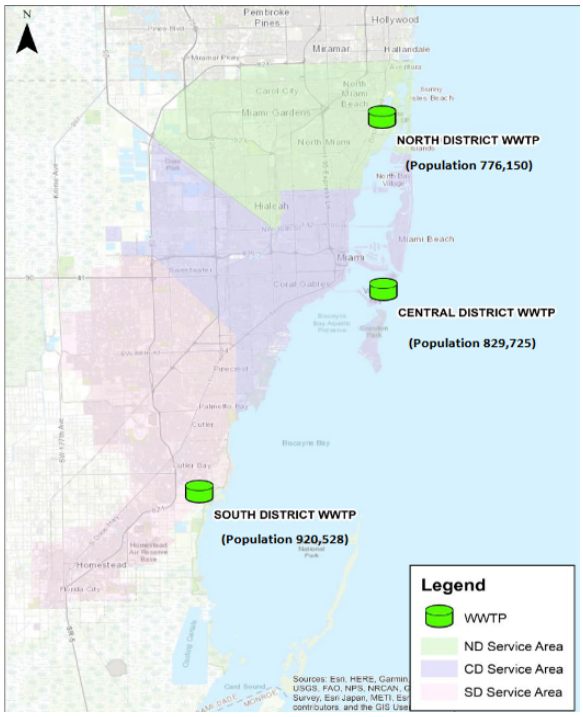

Figure 4.2: Map showing the three wastewater treatment plants (WWTP) in Miami-Dade county in Florida and their service area. The three treatment plants, namely the north district treatment plant, central district treatment plant and south district treatment plant, are marked in the map with green cylinder icons and their service area is depicted with green, violet and red shaded color in the map. The north district, central district and south district treatment plants respectively service approximately 0.78, 0.83 and 0.92 million individuals, respectively. The map is taken from the January 30, 2023 report by Miami-Dade County [219].

4.3.1 Values of the fixed (known) parameters of the WBE model

The values of the 8 known parameters of the WBE model {(4.2),(4.3)} (tabulated in Table 4.3) are described as follows: the incubation period for COVID-19 is estimated to be 3 days [84], so we set the transition parameter (σ) from exposed to infectious class to be $\sigma = 1/3$ *per* day. The recovery time for infectious individuals ($1/\gamma_I$) and hospitalized individuals ($1/\gamma_H$) is 8 days [221, 87], hence $\gamma_I = \gamma_H = 1/8$ *per* day. Upon recovery, newly recovered individuals (i.e., individuals in J compartment) continue

to shed for 24 days, hence $\gamma_R = 1/24$ *per* day. The viral shedding in hospitalized patients' stool data in [221] (given in $\log_{10}$ viral RNA copies *per* gram) was fitted by Phan *et al.* [207] to obtain a function, $f(t)$, that describes the temporal fecal viral shedding profile, and is given by:

$$f(t) = \frac{71.97t}{16 + t^2}. \tag{4.8}$$

As shown in [207], taking the average of this function from average time of entering the infectious I class (i.e., 3 days) to the average time of recovery in this class (i.e., 8 days) gives an average fecal viral shedding rate for an infectious individual (here, individuals in compartment I) to be 7.65 $\log_{10}$ viral RNA per gram, which is equivalent to 4.49×10^7 viral RNA per gram. Thus, $\zeta_I = 4.49 \times 10^7$ viral RNA per gram. It is assumed that the average fecal viral shedding rate for hospitalized individuals (who have an average recovery period of 8 days [87]) is the same (i.e., $\zeta_H = \zeta_I = 4.49 \times 10^7$ viral RNA per gram). Admittedly, it is an extremely crude way of approximating ζ_H, however since the proportion of individuals who are in H class is a small fraction of that in I [222], the impact of this crude assumption is negligible on the overall viral concentration in wastewater. Similarly, the average fecal viral shedding rate for recovered individuals who are still shedding (i.e., individuals in J compartment), denoted as ζ_J, is [214]:

$$\zeta_J = \frac{1}{24 - 8} \int_8^{24} \frac{71.97\ t}{16 + t^2} dt = 4.50 \log_{10} \text{viral RNA per gram} = 3.17 \times 10^4 \text{ viral RNA per gram}. \tag{4.9}$$

The average time from excretion of feces to collection at the treatment plant is assumed to be 1 day, hence $d_v = 1$ *per* day or 7 *per* week. This is a reasonable estimate based on references providing 18 to 36 hour travel time for wastewater treatment

plants serving similar sized population[207, 223]. Finally, like in [207], to compute the total viral load in sewershed, the weekly wastewater data is multiplied by the total influent flow rate *per* week, (the influent flow rate is estimated to be 300 million gallons *per* day for Miami-Dade County [224, 225]).

4.3.2 Estimated (fitted) parameters of the WBE model

In this section, the values of the 5 unknown parameters (also known as *estimated parameters*) of the WBE model {(4.2),(4.3)}, obtained by fitting the model with the measured wastewater data for the SARS-CoV-2 pandemic for the period from July 3rd, 2021 to October 9th, 2021, is discussed. Nonlinear least-squares optimization method was used to fit the model. MATLAB's minimization function "lsqcurvefit" is specifically used to minimize the sum of the squared differences between each weekly wastewater data point (data obtained from Biobot Analytics [218] and Miami-Dade County [224]), and the value of the corresponding wastewater data generated by solving the WBE model {(4.2),(4.3)}. The results obtained, for the model fitting is depicted in Figure 4.3(a) with a blue curve (with data points marked with brown dots). Furthermore, the values of unknown parameters obtained from the data fitting are tabulated in Table 4.4. The projection of the number of weekly hospitalized individuals, using fixed and fitted parameters in Table 4.3 and 4.4, respectively, is depicted with a cyan curve in Figure 4.3(b), alongside observed hospitalization data points marked in red dots (data obtained from The New York Times [226]). It can be observed in Figure 4.3 that weekly hospitalization data peaks a week later than weekly wastewater data (the time when wastewater and hospitalization data peaks are marked by dashed orange and violet lines in Figures 4.3(a) and (b), respectively). As seen in Figure 4.3(b), the model projection captures the week in which hospitalization

peaks as well as the overall trend of hospitalization during the wave. The cumulative wastewater and hospitalization curves was then simulated (using fixed and fitted parameter values in Tables 4.3 and 4.4, respectively) and compared with the observed cumulative wastewater and hospitalization data in Figures 4.3(c) and (d). It can be observed that a model with parameters estimated using the weekly case data can explain the aggregated data.

The parameter values obtained through data fitting are briefly discussed. The transmission rate associated with individuals in H class is $\beta_H = 0.00847$ *per* week, which suggests that the level of transmission at hospitals is relatively low. The rate of hospitalization is $\phi = 0.0066$ *per* week, which suggests that a relatively small proportion of individuals who get COVID-19 get hospitalized. Plugging the value of γ_I and ϕ from Tables 4.3 and 4.4, the proportion of individuals in I class that get hospitalized, defined as infection-to-hospitalization ratio (IHR), is obtained as [214]

$$\text{IHR} = \frac{\phi}{\gamma_I + \phi} \times 100\% = 0.58\%.$$

This suggests, that an estimate of 0.58% of the infected individuals were hospitalized in Miami-Dade County during the time period of our study. This is in line with the finding in [227], which suggests a range of IHR from 0.4% for those younger than 40 years to 9.2% for those older than 60 years. The media age of individuals in Miami-Dade County is 41.0 years [228], hence the obtained 0.58% IHR is reasonable.

The proportion of shed viral RNA that makes it to treatment plant is obtained to be $\eta = 0.956$, which suggests that in Miami-Dade, during the time period considered in this chapter, only a small portion of viral RNA is lost due to factors such as degradation due to temperature. Lastly, the average fecal load *per* person *per* week is $\alpha = 3283.5$ grams *per* week, which is equivalent to 469.1 grams *per* day. This is

a reasonable result since Rose *et al.* [229] estimate daily fecal load to be 51 to 796 grams *per* day. Additionally, an average person of 70 kilograms (154.32 pounds) is estimated to excrete about 500 grams of stool *per* day [230]. The average weight of male and female residents in Miami-Dade is 188 pounds and 154 pounds, respectively [231], hence assuming an equal sex ratio (i.e., an equal number of male and female in the population), the average weight of Miami-Dade residents can be estimated to be 171 pounds, so an average fecal load of 469.1 grams *per* person *per* day is not too far off.

The basic reproduction number, obtained by substituting values of parameters of model from Tables 4.3 and 4.4 in Equation 4.6, is 2.02.

Parameter	**Value**	**Source**
σ	7/3 week^{-1}	[84]
γ_I	7/8 week^{-1}	[221]
γ_H	7/8 week^{-1}	[87]
γ_R	7/24 week^{-1}	[208, 232, 233]
ζ_I	4.49×10^7 viral RNA *per* gram	[207]
ζ_H	4.49×10^7 viral RNA *per* gram	Assumed
ζ_J	3.17×10^4 viral RNA *per* gram	Calculated (see (4.9))
d_v	7 week^{-1}	Assumed

Table 4.3: Values of the fixed parameters of the WBE model {(4.2),(4.3)} [214].

Parameter	**Estimated (fitted) Value**
β_I	1.770 week^{-1}
β_H	0.00847 week^{-1}
ϕ	0.00512 week^{-1}
η	0.956 (dimensionless)
α	3283.5 grams week^{-1}

Table 4.4: Values of the fitted (estimated) parameters of the WBE model {(4.2),(4.3)} [214].

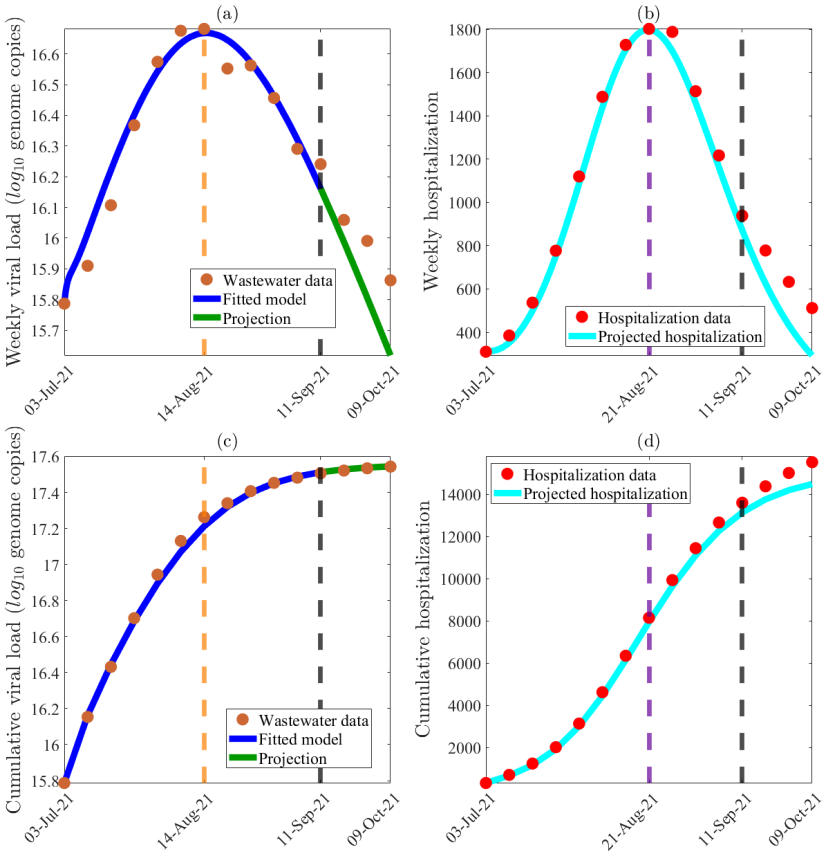

Figure 4.3: Data fitting, parameter estimation and projection of the model {(4.2), (4.3)} using weekly wastewater data for Miami-Dade County, Florida from July 3rd, 2021 to October 9th, 2021. (a) Least-squares fitting of the WBE model {(4.2), (4.3)}, showing weekly viral load in wastewater generated from the model, compared to the observed wastewater data (obtained from Biobot Analytics [218] and Miami-Dade County [224]). (b) Simulation results of the WBE model {(4.2), (4.3)}, depicting the weekly COVID-19 hospitalization for Miami-Dade County, as a function of time, predicted by the WBE model using the fixed and estimated parameters tabulated in Tables 4.3 and 4.4, respectively, in comparison to the observed weekly hospitalization data for Miami-Dade County from July 3rd, 2021 to October 9th, 2021 (obtained from The New York Times [226]). (c) Cumulative viral load in wastewater (depicted with a blue curve) is compared with the observed cumulative wastewater data for Miami-Dade County from July 3rd, 2021 to October 9th, 2021 (obtained from Biobot Analytics [218] and Miami-Dade County [224]; depicted with brown dots). (d) Cumulative COVID-19 hospitalization (depicted with the cyan curve) is compared to the observed cumulative hospitalization data (depicted with red dots) for Miami-Dade County from July 3rd, 2021 to October 9th, 2021 (obtained from The New York Times [226]). The WBE model was fitted to the data from July 1st, 2021 until September 11th, 2021 (depicted by a dashed black line in the figure), and the projection of the model output is compared with the observed wastewater data till October 9, 2021 (the projection period is depicted with a green curve). The vertical dashed orange and violet lines in Figures (a) and (b) respectively correspond to the time when weekly wastewater and hospitalization data peaks (i.e., August 14, 2021, and August 21, 2021, respectively). Four of the initial conditions of the WBE model (namely $E(0), I(0), J(0)$ and $R(0)$) were estimated by fitting the model with the aforementioned wastewater data. The estimated values were $E(0) = 17,377$, $I(0) = 55,592$, $J(0) = 3,058$ and $R(0) = 2,077$, respectively. The initial condition for the number of hospitalized individuals (i.e., $H(0)$) is obtained from The New York Times to be 310 [226]. Using the U.S. Census data, the total initial population of Miami-Dade County is assumed to be $N(0) = 2,716,940$ [234, 235]. Hence, the initial susceptible population is obtained as $S(0) = N(0) - (E(0) + I(0) + H(0) + J(0) + R(0))$. The remaining initial conditions are $V(0) = 10^{14.96}$ (i.e., $\log_{10}(V(0)) = 14.96$) and $W(0) = 10^{15.79}$ (i.e., $\log_{10}(V(0)) = 15.79$) [214].

4.4 Global Sensitivity Analysis

Global sensitivity analysis will be carried out, using Latin Hypercube Sampling (LHS) and Partial Rank Correlation Coefficients (PRCCs) [106, 107, 108], on the WBE model {(4.2)(4.3)} to determine the parameters that have the most influence on a chosen response function. Various SARS-CoV-2 modeling studies have chosen the reproduction number of the models (a measure of the average number of new cases generated by a typical infectious individual over the duration of their infectiousness) as the response function [21, 109, 236, 237]. In this chapter, we will use the cumulative viral load in wastewater (W) as the response function. Choosing the state variable W as the response function allows us to assess the population-level impact of the epidemiological, biological and wastewater-related parameters on wastewater itself (it is worth noting that the expression for the reproduction number of the WBE model, given by Equation (4.6), does not contain wastewater-related parameters, such as ζ_I, ζ_H, ζ_J, α, d_V and η; hence, using it as a response function will not allow us to assess the impact of the wastewater-related parameters). An Increase in the rate of increase of the response function (i.e., an increase in the cumulative viral RNA concentration in the wastewater function, W) can signify an increase in disease burden (i.e., higher concentration of viral RNA in the wastewater means increases in the number of individuals who shed virus, and, consequently, increases in SARS-CoV-2 burden in the community). Thus, the epidemiological objective of the sensitivity analysis is to decrease the rate of increase of the response function (W). On the other hand, an increase in the rate of increase of the response function (W) can improve the precision with which wastewater surveillance can be used to accurately assess the trend, spread and burden of the disease in the community. Thus, the ecological objective is to identify the wastewater-related parameters that

can improve the accuracy of the method used to measure the viral RNA concentration in the wastewater. These (epidemiological and ecological) objectives will be assessed.

The baseline values of the 13 parameters of the WBE model, given in Tables 4.3 and 4.4, will be used in the sensitivity analysis. These parameters are assumed to obey uniform distribution, and the range of each of these parameters is assumed to be 20% to the left and 20% to the right of its baseline value (except η which is given a range of [0.8, 1]). The range of each parameter is subdivided into $1,000$ equal sub-intervals. Since the parameter set is drawn from this set without replacement, this leads to $1,000 \times 13$ parameter matrix (or hypercube) [109]. A parameter with a PRCC value greater than 0.5 in absolute value and corresponding small p-values ($p < 0.05$) is strongly correlated to the response function [110]. Since the response function (W) is a non-decreasing function, a PRCC larger than 0.5 (smaller than -0.5) indicates that a change in a parameter leads to a significant increase (decrease) in the rate of increase of the cumulative function W. Since the response function ($W(t)$) is time-dependent, the impact of the parameters of the WBE model on $W(t)$ may vary with time. Thus, the PRCCs associated with these parameters (with respect to the response function $W(t)$) may be time-dependent as well.

Figure 4.4 depicts the time-varying PRCCs of the parameters in the response function $W(t)$ [238] generated from the sensitivity analysis carried out in this section. This figure, which depicts the PRCC curves for parameters in the response function $W(t)$ that had a PRCC value of higher than 0.5 in absolute value during some time t, shows that, while six parameters of the WBE model {(4.2),(4.3)}, namely transmission rate of infectious individuals (β_I), average fecal load *per* person *per* unit time (α), average viral shedding *per* gram from individuals in I compartment (ζ_I), proportion of viral RNA in the wastewater that is not lost in sewage by measurement time

(η), progression rate from exposed to infectious class (σ) and rate at which excreted feces arrives at the sewage treatment plant (d_V), are strongly positively correlated with the response function (i.e., an increase in the values of these parameters result in a corresponding increase in the rate of increase the response function), one of the parameter (recovery rate of infectious individuals (γ_I)) is strongly negatively correlated with the response function (i.e., an increase in the value of this parameter will result in a corresponding decrease in the rate of increase of the response function). In other words, the sensitivity analysis carried out in this section identifies seven parameters of the WBE model {(4.2),(4.3)} that have the highest influence on the value of the response function, as summarized below:

(a) The parameter for the transmission rate of infectious individuals (β_I; with PRCC values lying in the range [0.72, 0.97]).

(b) The parameter for the average fecal load *per* person *per* unit time (α; with PRCC values in the range [0.87, 0.97]).

(c) The parameter for the average viral shedding *per* gram from individuals in I compartment (ζ_I; with PRCC values in the range [0.87, 0.97]).

(d) The parameter for the proportion of viral RNA in the wastewater that is not lost in sewage by measurement time (η; with PRCC values in the range [0.69,0.91]).

(e) The parameter for the progression rate from exposed to infectious class (σ; with PRCC values in the range [0.14, 0.80]).

(f) The parameter for the rate at which excreted feces arrives at the sewage treatment plant (d_V; with PRCC values in the range [0.04, 0.57]).

(g) The recovery rate of infectious individuals (γ_I; with PRCCs ranging in [-0.97, -0.79]).

It can be seen from Figure 4.4 that although the PRCC curves for the parameters β_I, η, α and ζ_I slightly oscillate (i.e., increase or decrease slightly) over time, their PRCC values remain consistently above +0.5. Hence, any increase in the values of these parameters will lead to a significant increase in the response function (i.e., an increase in the level of viral RNA in the wastewater) for all time t. For the remaining two positively-correlated parameters mentioned above (namely, σ and d_V), however, Figure 4.4 shows that the significance of these parameters (in increasing the response function) depends on time. In particular, this figure shows that while the PRCC curves for these two parameters take values greater than +0.5 initially, the values decrease significantly to positive values much lower than +0.5 as time increases. Thus, during the first few weeks of the wave, any increase in the values of the two parameters will cause a significant increase in the response function, and an increase in the values of these parameters much later during the wave (e.g., after week 7) will only cause a marginal increase in the value of the response function. For example, the black curve in Figure 4.4 shows that, while during the early stages of this pandemic wave (e.g., during the first eight weeks of the wave), an increase in the value of the parameter σ (for the progression rate from the exposed class to the infectious class) will cause a significant increase in the viral concentration in the wastewater, an increase in the value of this parameter afterwards (i.e., after the first eight weeks of the wave) will only cause a correspondingly small increase in the viral RNA concentration in the wastewater. A similar result holds for the parameter d_V, which is the reciprocal of the average time from excretion of feces to collection at the treatment plan.

Figure 4.4 shows that the only parameter that is negatively-correlated with the response function is the recovery rate parameter (γ_I; with PRCC values in the range [-0.97, -0.79]). This figure (blue curve) shows a very strong negative correlation for this parameter, with the PRCC values increasing (in absolute value) from -0.79 to around -1 as time increases. Thus, this figure shows that an increase in the value of this parameter will lead to a very significant decrease in the rate of increase of the response function, $W(t)$, for all time t. It is worth stating that the solid red vertical line in Figure 4.4 on Week 7 of the wave (corresponding to August 14, 2021) represents the time when both the weekly wastewater data (W(t)) and the model projection of weekly viral load in the wastewater peak (see Figure 4.3(a)). It should be mentioned that Figure 4.4 only depicts the time-varying PRCC curves for parameters that have PRCC value greater or equal to 0.5 in magnitude at some time t during the wave (the PRCC curves for the remaining six of the WBE model that have PRCC values never exceeding 0.5 in magnitude for all time t, namely, β_H, ϕ, γ_H, γ_J, ζ_H and ζ_J, are depicted in Figure 4.5.

The results of the sensitivity analysis suggest that the rate of increase of the response function (W) is highly correlated with increases in the transmission rate (β), the progression rate from exposed to infectious class (σ), the proportion of viral RNA that is not lost by measurement time (η), the rate at which excreted feces arrives at the sewage treatment plant (d_V), the fecal load parameter (α), the average viral shedding rate by infectious individuals (ζ_I) and the recovery rate (γ_I). The epidemiological objective of the sensitivity analysis is to decrease the viral RNA in the wastewater, which entails decreasing the rate of increase of the response function W. Hence, it follows from the sensitivity analysis that the implementation of targeted public health control and mitigation strategies that reduce the transmission rate (β), the progres-

sion rate (σ) and increase the recovery rate (γ_I) will significantly reduce the burden of the pandemic in the county. While the transmission rate parameter β_I can be reduced through nonpharmaceutical and pharmaceutical intervention measures, such as the use of high-impact face masks, social distancing, testing and isolation, progression rate parameter σ can be reduced by early detection and treatment of newly-infected individuals. Furthermore, the recovery rate parameter γ_I can be increased by using effective antiviral drugs, such as *remdesivir* [239]. The ecological objective of the sensitivity analysis is to accurately measure the viral RNA concentration in the wastewater, which entails increasing the rate of increase of the response function W. The results of the sensitivity analysis suggest that the implementation of strategies that increase the rate at which excreted feces arrives at the sewage treatment plant (d_V) and the proportion of viral RNA in the wastewater that is not lost in sewage by measurement time (η) can increase the precision with which the spread of the disease can be captured through wastewater surveillance. The parameter for the viral RNA in the wastewater that is not lost in the sewage by measurement time (η) can be increased by enhancing the accuracy of the measurement of viral RNA concentration in the wastewater data (e.g., by increasing measurement frequency or selecting sampling location that is closer (relative to the location of treatment plants) to the inhabitants of the county). The fecal arrival rate parameter (d_V) can also be increased by selecting sampling location that is closer to the inhabitants of the county. The remaining two top PRCC-ranked parameters, α (for the average fecal load *per* person) and ζ_I (for the average viral shedding rate for infectious individuals), are biological parameters that depend on the physiology of the infected individual, and there may not be specific strategies to target these processes. For instance, while having infectious individuals shed more virus into the wastewater (i.e., increase ζ_I) will increase the accuracy of the viral RNA measurement in the wastewater, such high shedding rate

increases the response function (since the parameter is highly positively-correlated with the response function), hence increasing the disease burden. In other words, more shedding increases both viral RNA measurement accuracy (a desirable feature) and disease burden (an undesirable feature). It is worth restating that while five of the seven top PRCC-ranked parameters ($\beta_I, \eta, \alpha, \zeta_I$ and γ_I) remain highly-correlated with the response function (i.e., they have PRCC value greater or equal to 0.5 in magnitude) throughout the duration of the pandemic wave considered in this chapter, the remaining two top PRCC-ranked parameters (σ and d_V) lose influence over time during the duration of the wave (by having PRCC values lower than 0.5 in magnitude). In summary, the sensitivity analysis conducted in this section suggests the targeted strategies that need to be implemented to ensure the effective control (or elimination) of the SARS-CoV-2 pandemic in the Miami-Dade County, as well as improving the accuracy of wastewater data in capturing the trend of the pandemic.

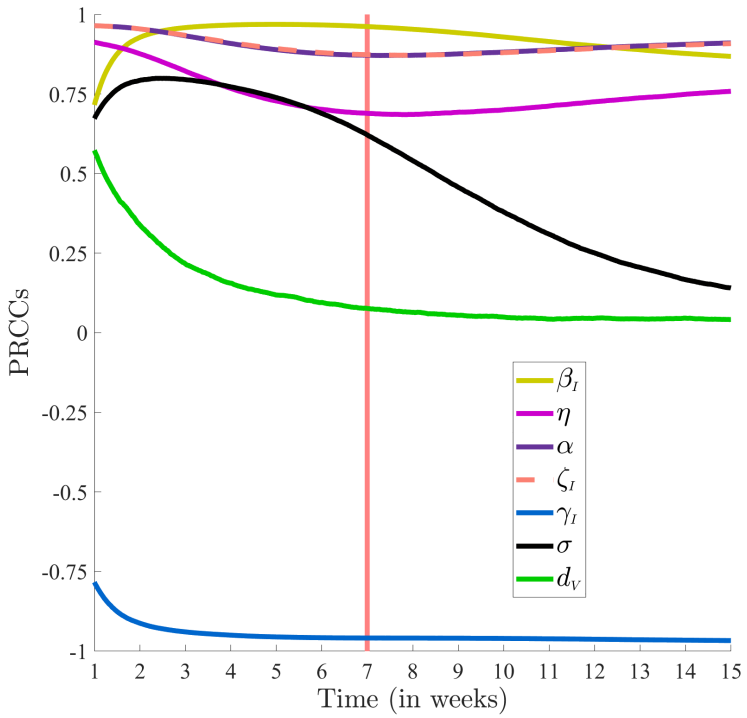

Figure 4.4: Time-varying partial rank correlation coefficients (PRCCs) of the parameters that are strongly correlated (i.e., PRCC greater than 0.5 in absolute value and corresponding small p-values ($p < 0.05$)) for the chosen response function (W) of the WBE model {(4.2),(4.3)} during some period of the study. Note that time-varying PRCCs of parameters ζ_I (depicted with a dashed orange line) and α (depicted with a dark violet curve) are nearly identical. Week 7 corresponds to the time when weekly wastewater data (and model projection of weekly viral load in wastewater) peaks (i.e., August 14, 2021; see Figure 4.3(a)) and is depicted by a vertical red line. Parameter values used in the simulations are given by the baseline values in Tables 4.3 and 4.4, and their ranges are taken to be 20% to the left and 20% to the right of the respective baseline value (except η which is given a range of [0.8, 1]). In this simulation p-value is less than 0.05 whenever PRCC is larger than 0.5 in magnitude.

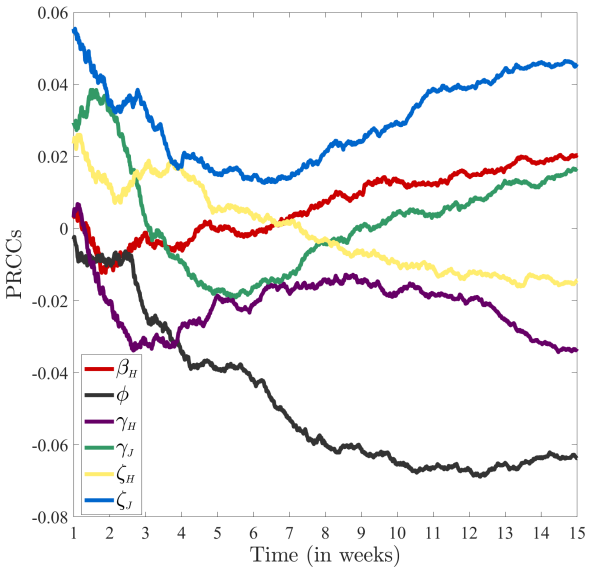

Figure 4.5: Time-varying partial rank correlation coefficients (PRCCs) of the parameters that are not strongly correlated with respect to the response function (W) of WBE model {(4.2),(4.3)}. Parameter values used in the simulations are given by the baseline values in Tables 4.3 and 4.4, and their ranges are taken to be 20% to the left and 20% to the right of the respective baseline value (except η which is given a range of [0.8, 1]) [214].

4.5 Numerical Simulations

In this section, the WBE model {(4.2),(4.3)} will be simulated, using the baseline values of the fixed and estimated parameters in Tables 4.3 and 4.4, to (a) predict the SARS-CoV-2 cases in Miami-Dade county, for the time period from July 3, 2021 to October 9, 2021 considered in this chapter and (b) quantify the contributions of recovered individuals in shedding viral RNA into the wastewater system in the county (i.e., we will quantify the contributions of viral RNA by individuals in the J compartment towards the weekly viral load in wastewater in the county). The simulations for the contribution of viral RNA into the wastewater by recovered individuals, which will be carried out by varying their viral shedding rate (ζ_J) and duration of shedding ($1/\gamma_J$),

allows us to further assess the impact of two parameters of the model that were not among the most highly-correlated ones (note that this two parameters are included in Figure 4.5, which depicts parameters of the WBE with weaker correlations with the response function). These simulations are further described below.

4.5.1 Projecting weekly cases

The weekly SARS-CoV-2 cases predicted by the WBE model {(4.2),(4.3)} for the county will be compared with the weekly reported case data for the county, obtained from [240]. The WBE model is now simulated using the baseline values of the parameters in Tables 4.3 and 4.4, and the results obtained are depicted in Figure 4.6. In particular, Figure 4.6(a) depicts a logarithmic plot of detected SARS-CoV-2 case data for the county (magenta dots) and the model prediction of weekly cases for the county (black curve), from which it follows that a clear correlation (or consistent unimodal pattern) emerges between the data (of the weekly detected cases) and the model prediction. This figure shows an increase in the number of cases with increasing time until a peak is reached (on August 14, 2021), and the number of cases decreases thereafter. This figure also shows that the week predicted by the model for the peak number of cases in the county matches the week the peak occurred in the reported data (namely, the week of August 14, 2021; it should also be recalled from Figures 4.3(a) and (b) that the WBE model also accurately captured the week when the wastewater and hospitalization data peaked). It is evident from Figure 4.6(a) that the model projection for the weekly case data during the week of August 14 is much higher than the observed weekly case count for the county. In fact, the model prediction is about 15.37 times higher than the observed weekly case count. This result is in line with the CDC's prediction of the true number of COVID-19-infected cases being

at least 10 times higher than the reported confirmed cases [241]. Furthermore, Wu *et al.* estimate that, in 33 states in the United States (including Florida), the number of COVID-19 infections was at least 10 times larger than the number of confirmed cases [242]. We plotted the model prediction of the weekly case data for the scenario where the reported weekly case data for the county is re-scaled (i.e., multiplied) by the 15.37 factor above. The results obtained, depicted in Figure 4.6(b), clearly shows that the model prediction perfectly captures the trend of the reported detected weekly cases. Figure 4.6(c) depicts a plot of the model-predicted number of weekly cases, as a function of the detected weekly cases, showing a strong linear relationship between the two (with a correlation coefficient of $r = 0.99$ and coefficient of determination $r^2 = 0.98$). This further confirms that the model captures the trend of the detected case data.

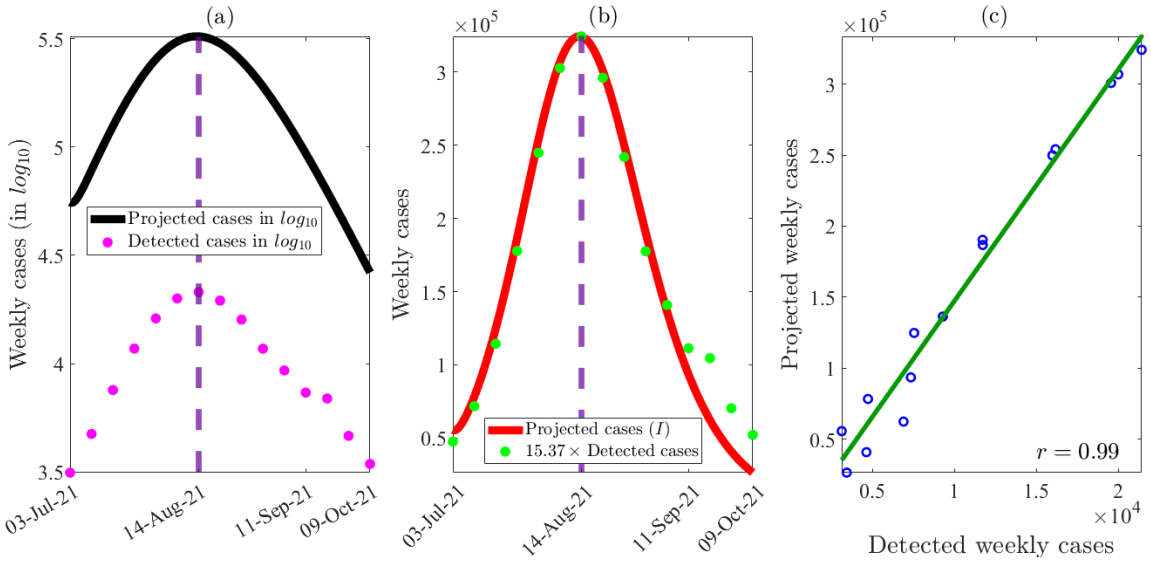

Figure 4.6: A comparison of model projected weekly cases with detected weekly cases for Miami-Dade county, Florida from July 3rd, 2021 to October 9th, 2021. (a) The log (base 10) of projected weekly cases (depicted with a black curve) along with the log of detected weekly cases obtained from Covid Act Now [240]) (depicted with red dots). (c) The model projected weekly cases (depicted with a red curve) along with 15.37-fold of the weekly detected cases (depicted with green dots). (c) The correlation of detected weekly cases with projected weekly cases (with a correlation coefficient of $r = 0.99$). The green line represents the best linear fit to the detected weekly cases versus projected weekly cases data [214] [214].

4.5.2 Quantifying viral RNA contributions by recovered individuals who shed virus

The WBE model will now be simulated to quantify the contributions of viral RNA into the wastewater by individuals who newly-recovered from SARS-CoV-2 infection but are still shedding virus (i.e., individuals in the J class). Natarajan *et al.* [243, 244] showed that fecal SARS-CoV-2 RNA shedding can occur even seven months after infection, *albeit* among a small group of individuals (3.8% of 113 patients considered in the study). Furthermore, the fecal shedding rate among individuals who have recovered but are still shedding the virus may be much higher than the baseline value used in this chapter (see Table 4.3). Hence, it is crucial to study the impact

of varying the parameters related to viral shedding by recovered individuals (namely the parameters ζ_J and $1/\gamma_J$, for the shedding rate and shedding duration in the post-infectious period, respectively) on the concentration of viral RNA in the wastewater. The contribution of viral shedding at time t, by individuals in K compartment (with K ={I,H,J}), is given by:

$$\left[\frac{\zeta_K K(t)}{\zeta_I I(t) + \zeta_H H(t) + \zeta_J J(t)}\right] \times 100\%\,, \quad \text{with } K(t) = \{I(t), H(t), J(t)\}. \tag{4.10}$$

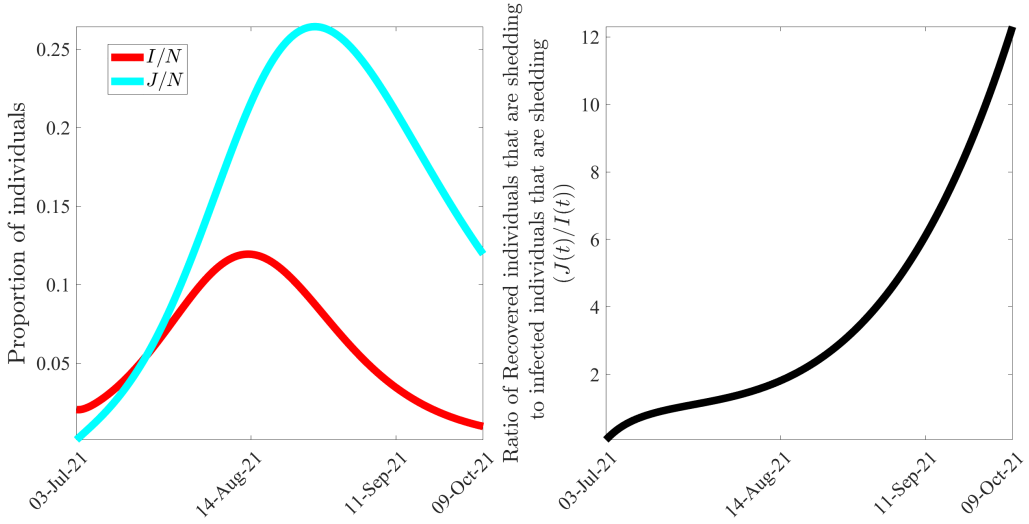

Figure 4.7: Comparison of WBE model {(4.2)(4.3)} projected profiles of the proportion of infected (I/N) and recovered individuals (J/N) who are shedding viral RNA in feces for Miami-Dade County, Florida, from July 3rd, 2021 to October 9th, 2021. (a) The profiles of the proportions of infectious (I/N) and recovered (J/N) who are shedding virus. (b) The ratio of the population of recovered individuals who are shedding to the proportion of infectious individuals (J/I), highlighting the relative increase in the number of recovered individuals who are shedding virus as the pandemic wave progresses. The figure is generated using the baseline values of the parameter given in Tables 4.3 and 4.4 [214].

The WBE model is simulated to generate the profiles of the proportions of individuals in the infectious (I) and the viral shedding recovered (J) compartments, as a function

of time. The results obtained, depicted in Figure 4.7(a), show that the proportions of individuals in the two viral shedding compartments increase with increasing time (i.e., as the pandemic wave progresses) until a peak is reached (which occur around August 14, 2021 for the infectious proportion and around August 28, 2021 for the recovered proportion, respectively), and decrease thereafter. This figure also shows that as the pandemic wave progresses (e.g., a month into the wave), the proportion of viral shedding recovered individuals in the community is much larger than that of the viral shedding infectious individuals. The model is further simulated to quantify the size of the population of the viral shedding recovered individuals (J), in relation to the population of the viral shedding infectious individuals (I), as a function of time (J/I). The results obtained, depicted in Figure 4.7(b), show a steady increase in this proportion with increasing time (into the pandemic wave being considered). It should be stated that, since the number of hospitalized individuals in the county is relatively small (see Figure 4.3(b)), we did not simulate the contribution of viral shedding by hospitalized infectious individuals.

It should be recalled that the simulations depicted in Figure 4.7 show that the profile (i.e., proportion) of viral shedding recovered individuals exceeds that of viral shedding infectious individuals about a month into the wave. Yet, the viral shedding contribution of recovered individuals who shed SARS-CoV-2 into the wastewater (computed using (4.10)), under the baseline scenario (with the baseline parameter values given in Tables 4.3 and 4.4) is negligible throughout the wave. This is because, under the baseline scenario, the viral shedding rate of recovered individuals (ζ_J) is disproportionately lower than the shedding rate of infectious individuals (ζ_I). It is, therefore, instructive (based on the simulations in Figure 4.7 and that fact that the baseline value of ζ_J is disproportionately lower than that of ζ_I) to explore the scenario where

the viral shedding rate by recovered individuals is much higher than its baseline value To check this scenario, we simulate the WBE model to generate contour plots of the percentage of viral contribution by viral shedding recovered individuals (computed using Equation (4.10)), as a function of the parameter for viral shedding by recovered individuals (ζ_J, but now expressed as a function of the proportion of the baseline value of the viral shedding rate of infectious individuals ζ_I; that is, $\zeta_J = c\zeta_I$; where $c \in [0.1, 1]$ and the parameter for the average shedding time by recovered individuals ($1/\gamma_J$). The results obtained, depicted in Figure 4.8, show that the percentage of viral contribution by recovered individuals increases with increasing values of the viral shedding rate by recovered individuals and the average shedding time by recovered individuals. Furthermore, this figure shows that if the viral shedding rate by recovered individuals is set at one-fifth that by infectious individuals (i.e., $\zeta_J = 0.2\zeta_I$), then the overall viral contribution by viral shedding recovered individuals during the second week of the wave in Miami-Dade County ranges from 8% to 12% (Figure 4.8(a)), depending on the average shedding duration of viral shedding recovered individuals. Similarly, for this scenario with $\zeta_J = 0.2\zeta_I$, the overall viral contribution by the viral shedding recovered individuals during week seven of the wave ranges from 15% to 40% (Figure 4.8(b)). Thus (by comparing Figures 4.8 (a) and (b)), the viral contribution by viral shedding recovered individuals during week seven exceed their shedding during week two of the wave. Finally, for this scenario with $\zeta_J = 0.2\zeta_I$, the simulations show that the overall viral contribution by viral shedding recovered individuals during week fifteen of the wave (i.e., at the end of the wave) ranges from 26% to 86% (Figure 4.8(c)). The simulation in Figure 4.8(c) also shows that if ζ_J and γ_J are large enough, then it is possible that the majority of the viral contribution at the end of a wave can be attributed to viral shedding recovered individuals. Hence, it can be concluded from the simulations in Figure 4.8 that, for the case where the

viral shedding rate by recovered individuals is not disproportionately lower than that by infectious individuals the overall viral contribution by viral shedding recovered individuals during the early stage of the epidemic was low, but grows (and can dominates the contribution by infectious individuals) as the epidemic progresses through the wave. Thus, the simulations depicted in Figures 4.7 and 4.8 strongly suggest the need to conduct further lab experiments to accurately measure or estimate the viral shedding rate and shedding duration for individuals in the viral shedding recovered compartment (our study may have under-estimated the values of these two parameters; hence, further experiments to obtain more accurate values of these parameters can enhance the accuracy of the utility of wastewater-based modeling to predict the trajectory and burden of infectious diseases in a population.

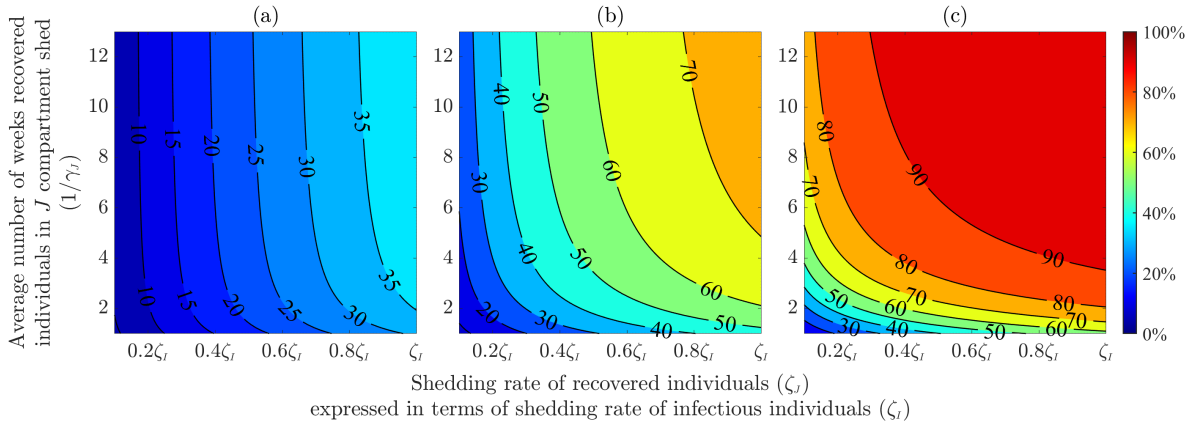

Figure 4.8: The contour plots of the percentage of viral contribution by viral shedding recovered individuals (computed using Equation (4.10)), as a function of shedding rate of viral shedding recovered individuals (ζ_J) and the average time of viral shedding by viral shedding recovered individuals ($1/\gamma_J$) during the (a) second week (b) seventh week and (c) fifteenth week of the study period. The x-axis of the contour plot is generated by varying ζ_J between $0.1\zeta_I$ to ζ_I (where ζ_I is the viral shedding rate of infectious individuals and its value is given in Table 4.3) while the y-axis (i.e., $1/\gamma_J$) is varied from 1 to 13 weeks. The remaining parameters are taken from Tables 4.3 and 4.4 [214].

4.6 Discussion and Conclusion

Although the use of wastewater to study the spread of infectious disease (based on isolating pathogens from the stool of some individuals infected with the disease) has a long history, perhaps dating back to the pioneering work of John Snow in the 1854s, it was only after the advent and widespread availability of efficient and safe methods for detecting viral RNA in wastewater (e.g., *reverse transcription–polymerase chain reaction*, invented in 1985 [245, 246]) that wastewater-based surveillance of disease activity has become an effective and resource-efficient tool for gathering crucial community-level public health information during outbreaks of infectious diseases [167, 168]. For example, the United States Centers for Disease Control (CDC) launched the National Wastewater Surveillance System (NWSS) in September of 2020 to "coordinate and build the nation's capacity to track the presence of SARS-CoV-2, the virus that causes COVID-19, in wastewater samples collected across the country" [169]. Some of the benefits of wastewater-based surveillance epidemiology includes the fact that it is a less invasive surveillance mechanism (unlike the use of mass testing or large scale genomic surveillance to detect disease activity in the community) and cost-effective (in comparison to the cost of testing kits, for instance) [170, 171]. In addition to being a "leading indicator" or an "early warning signal" for disease presence or activity in a community, it can provide important insight into the presence of disease variants or their entry into community (by monitoring wastewater in airports or on airplanes) [177, 178, 179, 180, 181]. All in all, it is generally believed that wastewater-based surveillance epidemiology (or implementing it in combination with other forms of public health surveillance and interventions) can be a very effective tool to detect disease activity, in addition to quanttifying the trajectory and burden of the disease (thereby leading to the development of effective control and mitigation strategies)

[173, 174].

Several mathematical models, of varying types (notably statistical and a few compartmental models) have been used to establish the correlation between SARS-CoV-2 RNA levels in wastewater and COVID-19 cases and burden in communities [198, 199, 200, 247, 201, 202, 203, 204, 248, 205]. The current study presents a wastewater-based epidemiology (WBE) model for the dynamics of SARS-CoV-2 viral RNA in wastewater treatment plants in Miami-Dade county of Florida. The model, which takes the form of an epidemic (no human demographic) deterministic system of nonlinear differential equations (obtained by coupling equations for the dynamics of SARS-CoV-2 in humans and in the wastewater system), was fitted to weekly wastewater data for the SARS-CoV-2 pandemic in Miami-Dade for the period from July 3, 2021 to October 9, 2021. The model has a continuum of disease-free equilibria, which was shown to be locally-asymptotically stable when a certain epidemiological threshold (denoted by $\mathcal{R}_0$; which depends on human parameters only) is less than one. The epidemiological implication of this result is that the outbreak will not grow in the county if the reproduction threshold is brought to (and maintained at) a value less than one.

Simulations of the calibrated WBE model showed that it accurately predicts both the trend for weekly SARS-CoV-2 hospitalizations in the county and the time when th weekly hospitalizations reached a peak. Specifically, these simulations showed that there was a one-week delay between when the weekly wastewater data peaked (i.e., showed a peak in the viral RNA concentration in the wastewater; which occurred on August 14, 2021) and when the weekly hospitalization data peaked (which occurred on August 21, 2021). The ability of the WBE model to capture both peaks demonstrates its robustness to accurately predict the time delay between the two peaks. Furthermore, the calibrated WBE model was simulated to predict the weekly

SARS-CoV-2 cases for the county, and the result obtained showed a very strong correlation between the predicted weekly case data and the observed weekly case data for the county. Here, too, our simulations showed that the predicted weekly case data peaked on August 14, 2021, which was exactly the same day the observed weekly case data for the county peaked. Furthermore, the maximum case count estimated by the calibrated WBE model was approximately 15 times higher than the maximum of the actual (observed or confirmed) weekly cases for the county. This result is consistent with those reported in numerous SARS-CoV-2 modeling studies (including other wastewater-based modeling, as well as statistical models) in the literature [242, 207, 206]. It is also consistent with the statement from the CDC, which estimated that their reported case count during the SARS-CoV-2 pandemic was at least 10 times lower than the actual number of infected individuals [241]. Thus, these simulations demonstrate the utility and robustness of the wastewater-based surveillance mechanism to not only detect the presence of disease in a community, but to reasonably (and, perhaps, accurately) estimate its trajectory and burden in the community.

Detailed time-varying global sensitivity analysis was carried out to determine the parameters (wastewater-based, epidemiological and biological) that have the most influence on the chosen response function (namely, the cumulative SARS-CoV-2 viral load in the wastewater system (denoted by $W(t)$)). These analyses revealed the five parameters of the WBE model that have the highest influence on the value of the response function ($W(t)$) for all time t during the duration of the SARS-CoV-2 wave considered in this chapter. Specifically, the identified parameters are the transmission rate of infectious individuals (β_I), the average fecal load *per* person *per* unit time (α), the average viral shedding *per* gram of infectious individuals compartment (ζ_I), the proportion of viral RNA in the wastewater system that is not lost in the sewage by

measurement time (η), and the recovery rate of infectious individuals (γ_I). Thus, strategies that target these parameters (e.g., the use of face masks, testing, isolation and social-distancing that reduce the transmission rate) can reduce the overall burden of the pandemic. Furthermore, the results of the sensitivity analysis revealed that enhancing the accuracy of the measurement of viral RNA concentration in the wastewater data can be increased by increasing the proportion of shed viral RNA that is not lost in sewage by measurement time. This can be achieved by increasing measurement frequency or selecting sampling location that is closer (relative to the location of treatment plants) to the inhabitants of the county.

The simulations of the WBE model further showed that, during the period of the simulations considered, the number of recovered individuals who shed virus into the wastewater in Miami-Dade during the simulation period (i.e., individuals in the J compartment) exceeds that of infectious individuals (i.e., individuals in the I compartment) about a month into the wave. In other words, this chapter showed that the majority of the people shedding the SARS-CoV-2 virus into the wastewater system in Miami-Dade, during the time period considered in this chapter, are the viral-shedding recovered individuals (and not the viral-shedding infectious individuals). This chapter also showed that the viral contribution by the viral-shedding recovered individuals during the early phase of the pandemic wave considered in this chapter was low. That is, the majority of the viral contribution during the early stage of the outbreak may be due primarily to the infectious individuals. However, our simulations showed that the viral RNA contribution by viral-shedding recovered individuals increases with increasing time during the wave (i.e., the contribution of viral shedding recovered individuals increases as the wave progresses). In particular, the simulations showed that, during the end of the pandemic wave considered (and depending on the value

of the shedding rate and the average shedding duration of viral shedding recovered individuals used in the simulations), viral-shedding recovered individuals may have accounted for the majority of the viral shedding in the Miami-Dade wastewater system. Thus, the result of this chapter strongly suggests the need to conduct further lab experiments to accurately measure or estimate the viral shedding rate and shedding duration for individuals in the viral shedding recovered compartment.

This chapter has several limitations, which we hope to account for in future studies. These include not explicitly differentiating between symptomatically-infectious individuals and asymptomatically-infectious individuals (we lumped all infectious individuals into one compartment for mathematical tractability, and owing to the fact that data to quantify viral shedding by asymptomatic infectious individuals appear to be missing at the current time). Moreover, the viral shedding rate of recovered individuals used for data-fitting purposes is significantly lower than that of infectious individuals. However, the actual rate of viral shedding of recovered individuals may be much larger. Thus, quantifying the value of this parameter based on data generated from relevant clinical (laboratory) studies will further enhance the effectiveness of wastewater-based epidemiological modeling to assess and predict the dynamics and burden of SARS-CoV-2 in a community. The study did not also include the impact of vaccination (it is intuitive to expect that viral shedding in breakthrough infections may be lower, in comparison to viral shedding by unvaccinated infected individuals; here, too, there is currently no precise data on viral shedding by vaccinated infected individuals). Furthermore, the lack of precise information about some of the dynamical aspects of the wastewater-related data also poses challenges in wastewater-based epidemiological modeling. For instance, data on average duration of fecal transportation from source to the treatment plant (i.e., data to estimate

the average time from excretion of feces to arrival at the sewage treatment plant) will be very useful in the modeling process. Similarly, having daily wastewater data (rather than weekly) will help improve the accuracy of model calibration with the wastewater data (thereby improving the accuracy of the estimate of the unknown parameters from the model fitting, as well as improving the overall predictive capacity of the WBE model). Overall, this chapter shows that the prospect of using wastewater-based surveillance to provide insight into the transmission dynamics and effective control (and elimination) of emerging, re-emerging and resurging infectious diseases of major public health significance in a community, such as SARS-CoV-2, is very promising, particularly if such data is collected with precision and timely (e.g., daily) basis, and made readily available to modelers. We emphasize the urgent need for more clinical studies/experiments to accurately quantify the level of viral shedding by asymptomatic, recovered and vaccinated infected individuals to further enhance the predictive capacity of wastewater-based epidemiology models.

APPENDIX A

INITIAL CONDITIONS FOR THE MODELS IN CHAPTER 2

A.1 Homogeneous Model

The initial conditions for the state variables of the homogeneous model (2.8), corresponding to Waves A, B and C, are given in Table A1.

A.2 Two-group Model (During Wave C)

For the two-group model (2.31), the initial conditions for the state variables for individuals in Group 1 (i.e., individuals 64 years and younger) during Wave C is denoted by X_{01}, where:

$$X_{01} = (S_{01}, V_{01}, P_{01}, I_{01}, A_{01}, H_{01}, R_{01}), \tag{A.1}$$

with,

$$\begin{aligned} &S_{01} = 54,168,536, V_{01} = 76,784,154, E_{01} = 73,596, P_{01} = 366,386, \\ &I_{01} = 4,126,977, A_{01} = 3,558,881, H_{01} = 42,140 \text{ and } R_{01} = 118,643,401. \end{aligned} \tag{A.2}$$

Similarly, the initial conditions for the state variables for individuals in Group 2 (i.e., individuals 65 and older), denoted by X_{02}, are computed from the relation:

$$X_{02} = X_0 - X_{01}, \quad \text{where} \quad X_i = \{S_i, V_i, E_i, P_i, I_i, A_i, H_i, R_i\}, \ \text{ with } i = \{0, 01\}, \tag{A.3}$$

where X_0 is the vector of the initial conditions for the state variables of the homogeneous model (given in Table A1) and X_{01} is the set of the initial conditions for the state variables of the individuals in Group 1 (as given in (A.1)).

Initial Condition	Value		
	Wave A	**Wave B**	**Wave C**
S_0	327,433,290	155,108,886	73,443,709
V_0	0	54,250,695	100,070,766
E_0	$800,109$	$300,105$	$97,860$
P_0	$800,032$	$400,302$	$388,859$
I_0	$1,091,821$	$1,293,500$	$4,169,424$
A_0	$311,949$	$748,501$	$3,586,032$
H_0	$32,604$	$14,085$	$84,281$
R_0	$1,009,051$	$118,974,149$	$149,030,355$

Table A1: The initial conditions of the state variables of the homogeneous model (2.8) used to generate Figure 2.2 (obtained by fitting the homogeneous model with the observed cumulative mortality data for the United States during Waves A, B, and C). The initial value of the susceptible population (S_0) was obtained by subtracting the initial values of remaining state variables of the homogeneous model ($V_0, E_0, P_0, I_0, A_0, H_0$ and R_0) and the observed cumulative mortality (recorded at the beginning of each of the three waves) from the total population of the United States (331.69 million [113]). The initial conditions for the hospitalized individuals and the cumulative mortality (at the beginning of each of the three waves) are obtained from data [73, 81] [61].

APPENDIX B

PROOF OF THEOREM 3.2.2

Proof. Consider the homogeneous model (2.8) with a perfect vaccine (i.e., $\varepsilon_v = 1$). Let $\tilde{\mathcal{R}}_v \leq s^* < 1$ (where $s^* = S^*/N^* = \dfrac{\omega_v + \mu}{\omega_v + \xi_v + \mu}$). Further, consider the following linear Lyapunov function:

$$\mathcal{L} = \alpha_0 E + \alpha_1 P + \alpha_2 I + \alpha_3 A + \alpha_4 H,$$

where,

$$\begin{aligned} \alpha_0 &= \frac{1}{\sigma + \mu},\ \alpha_1 = \frac{\alpha_0\beta_P + r\psi\alpha_2 + (1-r)\psi\alpha_3}{(\psi + \mu)},\ \alpha_2 = \frac{\alpha_0\beta_I + \phi\alpha_4}{\phi + \gamma_I + \delta_I + \mu}, \\ \alpha_3 &= \alpha_0\frac{\beta_A}{\gamma_A + \mu} \text{ and } \alpha_4 = \alpha_0\frac{\beta_H}{\gamma_H + \delta_H + \mu}. \end{aligned}$$

The Lyapunov derivative is given by (where a dot represents differentiation with respect to time t):

$$\dot{\mathcal{L}} = \alpha_0\dot{E} + \alpha_1\dot{P} + \alpha_2\dot{I} + \alpha_3\dot{A} + \alpha_4\dot{H},$$

which can be simplified to

$$\begin{aligned} \dot{\mathcal{L}} = &\left[\alpha_0\beta_P\frac{S}{N} - \alpha_1(\psi + \mu) + \alpha_2 r\psi + \alpha_3(1-r)\psi\right]P + \left[\alpha_0\beta_A\frac{S}{N} - \alpha_3(\gamma_A + \mu)\right]A \\ &+ \left[\alpha_0\beta_I\frac{S}{N} - \alpha_2(\phi + \gamma_I + \delta_I + \mu) + \alpha_4\phi\right]I + \left[\alpha_0\beta_H\frac{S}{N} - \alpha_4(\gamma_H + \delta_H + \mu)\right]H \\ &+ \left[-\alpha_0(\sigma + \mu) + \alpha_1\sigma\right]E, \end{aligned}$$

so that (noting $S(t) \leq N(t)$ for all t in Ω_1),

$$\begin{aligned} \dot{\mathcal{L}} &\leq \left[\frac{\sigma}{\sigma + \mu}\left\{\frac{\beta_P}{\psi + \mu} + \frac{r\psi\beta_I}{(\psi + \mu)(\phi + \gamma_I + \delta_I + \mu)} + \frac{r\psi\phi\beta_H}{(\gamma_H + \delta_H + \mu)(\phi + \gamma_I + \delta_I + \mu)}\right.\right. \\ &\quad \left.\left. + \frac{(1-r)\psi\beta_A}{(\psi + \mu)(\gamma_A + \mu)}\right\} - 1\right]E, \\ \dot{\mathcal{L}} &\leq (\mathcal{R}_0 - 1)E, \\ \dot{\mathcal{L}} &\leq \left[\left(\frac{1 - v^*}{1 - v^*}\right)\mathcal{R}_0 - 1\right]E, \\ \dot{\mathcal{L}} &= \left(\frac{\tilde{\mathcal{R}}_v}{1 - v^*} - 1\right)E. \end{aligned}$$

Thus, $\dot{\mathcal{L}} \leq \left(\frac{\tilde{\mathcal{R}}_v}{s^*} - 1 \right) E$, where $s^* = 1 - v^*$ (with v^* defined in Equation (2.18)). That is, the Lyapunov derivative $\dot{\mathcal{L}} \leq 0$ if $\tilde{\mathcal{R}}_v \leq s^* < 1$, and $\dot{\mathcal{L}} = 0$ if and only if $E(t) = 0$. Thus, $\mathcal{L}$ is a Lyapunov function in Ω_1 and it follows from LaSalle's Invariance Principle [95] that every solution to the model (2.8) (with $\varepsilon_v = 1$ and initial conditions in Ω_1) converges to DFE as $t \to \infty$. That is, $(S(t), V(t), E(t), P(t), I(t), A(t), H(t), R(t)) \to (S^*, V^*, 0, 0, 0, 0, 0, 0)$ as $t \to \infty$ for $\tilde{\mathcal{R}}_v \leq s^*$. Hence, the DFE is globally-asymptotically stable in Ω_1 if $\tilde{\mathcal{R}}_v \leq s^*$ for the special case of the model (2.8) with $\varepsilon_v = 1$. This completes the proof. $\square$

APPENDIX C

PROOF OF THEOREM 2.3.3

Proof. Consider a special case of the homogeneous model (2.8) with negligible disease-induced mortality (i.e., consider the model (2.8) with $\delta_I = \delta_H = 0$). Furthermore, let $\mathcal{R}_v^\diamond < 1$. The proof is based on using a comparison theorem [65].

It is convenient to define:

$$W = \frac{S + (1-\varepsilon_v)V}{\Pi/\mu} \quad \text{and} \qquad W^* = \frac{S^* + (1-\varepsilon_v)V^*}{N^*}. \tag{C.1}$$

The equations for the infected compartments of this special case of the model (2.8) can be re-written in terms of the next generation matrices F and $V^\diamond = V|_{\delta_I=\delta_H=0}$ (with F and V matrices given in Section 2.3.2.1) as:

$$\frac{d}{dt}\begin{bmatrix} E(t) \\ P(t) \\ I(t) \\ A(t) \\ H(t) \end{bmatrix} = (F - V^\diamond)\begin{bmatrix} E(t) \\ P(t) \\ I(t) \\ A(t) \\ H(t) \end{bmatrix} - M^\diamond \begin{bmatrix} E(t) \\ P(t) \\ I(t) \\ A(t) \\ H(t) \end{bmatrix}, \tag{C.2}$$

where,

$$F - V^\diamond = \begin{bmatrix} -(\sigma+\mu) & \beta_P W^* & \beta_I W^* & \beta_A W^* & \beta_H W^* \\ \sigma & -(\psi+\mu) & 0 & 0 & 0 \\ 0 & r\psi & -(\phi+\gamma_I+\mu) & 0 & 0 \\ 0 & (1-r)\psi & 0 & -(\gamma_A+\mu) & 0 \\ 0 & 0 & \phi & 0 & -(\gamma_H+\mu) \end{bmatrix}, \tag{C.3}$$

and,

$$M^{\diamond} = \begin{bmatrix} 0 & \beta_P(W^* - W) & \beta_I(W^* - W) & \beta_A(W^* - W) & \beta_H(W^* - W) \\ 0 & 0 & 0 & 0 & 0 \\ 0 & 0 & 0 & 0 & 0 \\ 0 & 0 & 0 & 0 & 0 \\ 0 & 0 & 0 & 0 & 0 \end{bmatrix}. \quad \text{(C.4)}$$

Since $S^* \geq S$ and $V^* \geq V$ in $\Omega^{\diamond}$ (so that $W^* > W$) and $N^* = \Pi/\mu$, it follows that the matrix $M^{\diamond}$, defined in (C.4), is non-negative. Thus, Equation (C.2) can be re-written as the following inequality:

$$\frac{d}{dt}\begin{bmatrix} E(t) \\ P(t) \\ I(t) \\ A(t) \\ H(t) \end{bmatrix} \leq (F - V^{\diamond}) \begin{bmatrix} E(t) \\ P(t) \\ I(t) \\ A(t) \\ H(t) \end{bmatrix}. \quad \text{(C.5)}$$

If $\mathcal{R}_v^{\diamond} < 1$, then $\rho(FV^{\diamond -1}) < 1$ (see Section 2.3.2.1), which is equivalent to all eigenvalues of $F - V^{\diamond}$ matrix being negative [88]. Hence, the linearized differential inequality (C.5) is stable whenever $\mathcal{R}_v^{\diamond} < 1$, so $(E(t), P(t), I(t), A(t), H(t)) \to (0, 0, 0, 0, 0)$ as $t \to \infty$ for this linear ODE system. It follows, using a standard comparison theorem [65], that: $(E(t), P(t), I(t), A(t), H(t)) \to (0, 0, 0, 0, 0)$. Substituting $E(t) = P(t) = I(t) = A(t) = H(t) = 0$, into the equations for $\dot{S}$, $\dot{V}$, and $\dot{R}$ of the homogeneous model (2.8) gives:

$$S(t) \to S^*, V(t) \to V^* \text{ and } R(t) \to 0, \text{ as } t \to \infty.$$

Hence, the disease-free equilibrium of the special case of the model (2.8) with negligible disease-induced mortality (i.e., model (2.8) with $\delta_I = \delta_H = 0$) is globally-asymptomatically stable in $\Omega^{\diamond}$, whenever $\mathcal{R}_v^{\diamond} < 1$. $\square$

APPENDIX D

PROOF OF THEOREM 2.3.6

Proof. Consider a special case of the homogeneous model (2.8) with negligible disease-induced mortality (i.e., consider the model (2.8) with $\delta_I = \delta_H = 0$), and no waning of immunity ($\omega_v = \omega_n = 0$). The proof of Theorem 2.3.6 is based on using a Krasnoselskii sub-linearity trick (see [97, 98], and also [99, 100]). The substitution $S = N^* - V - E - P - I - A - H - R$ (along with (2.21)) is used to rewrite this special case of model (2.8) as [61]:

$$\begin{aligned}
\dot{V}(t) &= \xi_v(N^* - V - E - P - I - A - H - R) - k_2 V,\\
\dot{E}(t) &= \lambda^\diamond(N^* - V - E - P - I - A - H - R) - k_3 E,\\
\dot{P}(t) &= \sigma E - k_4 P,\\
\dot{I}(t) &= r\psi P - k_5^\diamond I,\\
\dot{A}(t) &= (1-r)\psi P - k_6 A,\\
\dot{H}(t) &= \phi I - k_7^\diamond H,\\
\dot{R}(t) &= \gamma_I I + \gamma_A A + \gamma_H H - \mu R,
\end{aligned} \tag{D.1}$$

where $k_5^\diamond = \phi + \gamma_I + \mu$, $k_7^\diamond = \gamma_H + \mu$, and $\lambda^\diamond$, the force of infection obtained by substituting $N = N^*$ in (2.9), is given by [61]

$$\lambda^\diamond = \frac{\beta_P P + \beta_I I + \beta_A A + \beta_H H}{N^*}. \tag{D.2}$$

Linearizing the system (D.1) around the endemic equilibrium, $\mathbb{E}_1^{\diamond}$, gives [61]

$$\begin{aligned}
\dot{V}(t) &= -\xi_v(V+E+P+I+A+H+R) - k_2 V,\\
\dot{E}(t) &= -a_0 V - (a_0+k_3)E + (a_1-a_0)P + (a_2-a_0)I + (a_3-a_0)A + (a_4-a_0)H - a_0 R,\\
\dot{P}(t) &= \sigma E - k_4 P,\\
\dot{I}(t) &= r\psi P - k_5^{\diamond} I,\\
\dot{A}(t) &= (1-r)\psi P - k_6 A,\\
\dot{H}(t) &= \phi I - k_7^{\diamond} H,\\
\dot{R}(t) &= \gamma_I I + \gamma_A A + \gamma_H H - \mu R,
\end{aligned} \tag{D.3}$$

where, $a_0 = \dfrac{\beta_P P^{**} + \beta_I I^{**} + \beta_A A^{**} + \beta_H H^{**}}{N^*}$, $a_1 = \beta_P \dfrac{S^{**}}{N^*}$, $a_2 = \beta_I \dfrac{S^{**}}{N^*}$, $a_3 = \beta_A \dfrac{S^{**}}{N^*}$, and $a_4 = \beta_H \dfrac{S^{**}}{N^*}$.

It follows that the Jacobian of the system (D.3), evaluated at $\mathbb{E}_1^{\diamond}$, is given by [61]

$$J(\mathbb{E}_1^{\diamond}) = \begin{pmatrix}
-\xi_v - k_2 & -\xi_v & -\xi_v & -\xi_v & -\xi_v & -\xi_v & -\xi_v \\
-a_0 & -a_0 - k_3 & a_1 - a_0 & a_2 - a_0 & a_3 - a_0 & a_4 - a_0 & -a_0 \\
0 & \sigma & -k_4 & 0 & 0 & 0 & 0 \\
0 & 0 & r\psi & -k_5^{\diamond} & 0 & 0 & 0 \\
0 & 0 & (1-r)\psi & 0 & -k_6 & 0 & 0 \\
0 & 0 & 0 & \phi & 0 & -k_7^{\diamond} & 0 \\
0 & 0 & 0 & \gamma_I & \gamma_A & \gamma_H & -\mu
\end{pmatrix}.$$

Assume that the linearized system (D.3) has a solution of the form [61]

$$\mathbf{Z}(t) = \mathbf{Z}_0 e^{\omega t}, \tag{D.4}$$

with $\mathbf{Z}_0 = (Z_1, Z_2, Z_3, Z_4, Z_5, Z_6, Z_7)$, ω, $Z_i \in \mathbb{C}$ $(i = \{1, 2, \cdots, 7\})$. Substituting the

solution of the form (D.4) into the linearized system (D.3) gives [61]

$$\begin{aligned}
\omega Z_1 &= -\xi_v(Z_1 + Z_2 + Z_3 + Z_4 + Z_5 + Z_6 + Z_7) - k_2 Z_1,\\
\omega Z_2 &= -a_0 Z_1 - (a_0 + k_3)Z_2 + (a_1 - a_0)Z_3 + (a_2 - a_0)Z_4 + (a_3 - a_0)Z_5 + (a_4 - a_0)Z_6 - a_0 Z_7,\\
\omega Z_3 &= \sigma Z_2 - k_4 Z_3,\\
\omega Z_4 &= r\psi Z_3 - k_5^{\diamond} Z_4,\\
\omega Z_5 &= (1 - r)\psi Z_3 - k_6 Z_5,\\
\omega Z_6 &= \phi Z_4 - k_7^{\diamond} Z_6,\\
\omega Z_7 &= \gamma_I Z_4 + \gamma_A Z_5 + \gamma_H Z_6 - \mu Z_7.
\end{aligned} \tag{D.5}$$

The third to the seventh equation in system (D.5) can be rewritten by moving negative terms to their respective left-hand side as [61]

$$\begin{aligned}
\left(1 + \frac{\omega}{k_4}\right) Z_3 &= \frac{\sigma}{k_4} Z_2,\\
\left(1 + \frac{\omega}{k_5^{\diamond}}\right) Z_4 &= \frac{r\psi}{k_5^{\diamond}} Z_3,\\
\left(1 + \frac{\omega}{k_6}\right) Z_5 &= \frac{(1 - r)\psi}{k_6} Z_3,\\
\left(1 + \frac{\omega}{k_7^{\diamond}}\right) Z_6 &= \frac{\phi}{k_7^{\diamond}} Z_4,\\
\left(1 + \frac{\omega}{\mu}\right) Z_7 &= \frac{\gamma_I}{\mu} Z_4 + \frac{\gamma_A}{\mu} Z_5 + \frac{\gamma_H}{\mu} Z_6.
\end{aligned} \tag{D.6}$$

To get a similar expression from first and second equations in system (D.5), we first

rewrite all equations in system (D.6) in terms of Z_2 as [61]

$$\begin{aligned}
Z_3 &= \frac{\sigma}{\omega + k_4} Z_2 = A_1 Z_2, \\
Z_4 &= \frac{r\psi\sigma}{(\omega + k_4)(\omega + k_5^{\diamond})} Z_2 = A_2 Z_2, \\
Z_5 &= \frac{\sigma(1-r)\psi}{(\omega + k_4)(\omega + k_6)} = A_3 Z_2, \\
Z_6 &= \frac{\phi r\psi\sigma}{(\omega + k_4)(\omega + k_6)(\omega + k_7^{\diamond})} Z_2 = A_4 Z_2, \\
Z_7 &= \frac{1}{\mu}(\gamma_I A_4 + \gamma_A A_5 + \gamma_H A_6) Z_2 = A_5 Z_2.
\end{aligned} \tag{D.7}$$

Then, using the first two equations of (D.5) and expressions in (D.7), we obtain [61]

$$\begin{aligned}
\left(1 + \frac{\omega + \xi_v}{k_2}\right) Z_1 + \left[1 + \frac{\omega + a_0}{k_3} + \frac{\xi_v}{k_2} + \left(\frac{\xi_v}{k_2} + \frac{a_0}{k_3}\right)(A_3 + A_4 + A_5 + A_6 + A_7)\right] Z_2 \\
= \frac{a_1}{k_3} Z_3 + \frac{a_2}{k_3} Z_4 + \frac{a_3}{k_3} Z_5 + \frac{a_4}{k_3} Z_6.
\end{aligned} \tag{D.8}$$

System (D.6) along with (D.8) can be rewritten as [61]

$$\begin{aligned}
[1 + F_1(\omega)] Z_1 + [1 + F_2(\omega)] Z_2 &= \frac{a_1}{k_3} Z_3 + \frac{a_2}{k_3} Z_4 + \frac{a_3}{k_3} Z_5 + \frac{a_4}{k_3} Z_6, \\
[(1 + F_3(\omega)] Z_3 &= \frac{\sigma}{k_4} Z_2 = (MZ)_3, \\
[1 + F_4(\omega)] Z_4 &= \frac{r\psi}{k_5^{\diamond}} Z_3 = (MZ)_5, \\
[1 + F_5(\omega)] Z_5 &= \frac{(1-r)\psi}{k_6} Z_3 = (MZ)_5, \\
[1 + F_6(\omega)] Z_6 &= \frac{\phi}{k_7^{\diamond}} Z_4 = (MZ)_6, \\
[1 + F_7(\omega)] Z_7 &= \frac{\gamma_I}{\mu} Z_4 + \frac{\gamma_A}{\mu} Z_5 + \frac{\gamma_H}{\mu} Z_6 = (MZ)_7,
\end{aligned} \tag{D.9}$$

where,

$$\begin{aligned}
F_1(\omega) &= \frac{\omega + \xi_v}{k_2} + \frac{a_0}{k_3}, \\
F_2(\omega) &= \frac{\omega + a_0}{k_3} + \frac{\xi_v}{k_2} + \left(\frac{\xi_v}{k_2} + \frac{a_0}{k_3}\right)(A_1 + A_2 + A_3 + A_4 + A_5), \\
F_3(\omega) &= \frac{\omega}{k_4}, \quad F_4(\omega) = \frac{\omega}{k_5^{\diamond}}, \quad F_5(\omega) = \frac{\omega}{k_6}, \quad F_6(\omega) = \frac{\omega}{k_7^{\diamond}}, \text{ and } F_7(\omega) = \frac{\omega}{\mu},
\end{aligned} \tag{D.10}$$

with,

$$M = \begin{pmatrix} 0 & 0 & 0 & 0 & 0 & 0 & 0 \\ 0 & 0 & \frac{a_1}{k_3} & \frac{a_2}{k_3} & \frac{a_3}{k_3} & \frac{a_4}{k_4} & 0 \\ 0 & \frac{\sigma}{k_4} & 0 & 0 & 0 & 0 & 0 \\ 0 & 0 & \frac{r\psi}{k_5^\diamond} & 0 & 0 & 0 & 0 \\ 0 & 0 & \frac{(1-r)\psi}{k_6} & 0 & 0 & 0 & 0 \\ 0 & 0 & 0 & \frac{\phi}{k_7^\diamond} & 0 & 0 & 0 \\ 0 & 0 & 0 & \frac{\gamma_I}{\mu} & \frac{\gamma_A}{\mu} & \frac{\gamma_H}{\mu} & 0 \end{pmatrix}.$$

In the above expressions, the notation $(M\mathbf{Z})_i$ (with $i = 1, \cdots, 7$) denotes the i^{th} coordinate of the vector MZ. Furthermore, note that the matrix M has non-negative entries and the endemic equilibrium $\mathbb{E}_1^\diamond$ satisfies $\mathbb{E}_1^\diamond = M\mathbb{E}_1^\diamond$. Hence, if $\mathbf{Z}$ is a solution of (D.9), then it is possible to find a minimal positive real number b such that [99, 100]

$$||\mathbf{Z}|| \leq b\mathbb{E}_1^\diamond, \tag{D.11}$$

where, $||\mathbf{Z}|| = (||Z_1||, ||Z_2||, ||Z_3||, ||Z_4||, ||Z_5||, ||Z_6||, ||Z_7||)$ with lexicographic order, and $||.||$ is a norm in $\mathbb{C}$. Now it is sufficient to show that $Re(\omega) < 0$. Assume the contrary (i.e., $Re(\omega) \geq 0$) and consider the following two cases [61].

Case 1: $\omega = 0$.

In this case, (D.5) is the homogeneous linear system in the variables Z_i (with $i =$

$1, \cdots, 7$). The determinant of this system is given by

$$\Delta = -A + \left(\frac{S^{**}\mathcal{R}_v^{\diamond}}{N^*} - 1\right)\mu(\xi_v + k_2)k_3k_4k_5^{\diamond}k_6k_7^{\diamond}, \tag{D.12}$$

where,

$$\begin{aligned} A =& \mu\sigma k_2k_5^{\diamond}k_6k_7^{\diamond} + \mu k_2k_4k_5^{\diamond}k_6k_7^{\diamond} + r\mu\sigma\phi\psi k_2k_6 + r\mu\sigma\psi k_2k_6k_7^{\diamond} + (1-r)\mu\sigma\psi k_2k_5^{\diamond}k_7^{\diamond} \\ &+ r\sigma\psi\gamma_I k_2k_6k_7^{\diamond} + (1-r)\sigma\psi\gamma_A k_2k_5^{\diamond}k_7^{\diamond} + r\sigma\phi\psi\gamma_H k_2k_5^{\diamond} > 0. \end{aligned}$$

To determine the sign of Δ it is enough to determine that of $\dfrac{S^{**}\mathcal{R}_v^{\diamond}}{N^*}$. To do this, we first solve the system (D.1) at the endemic steady-state ($\mathbb{E}_1^{\diamond}$) as

$$\frac{S^{**}}{N^*} = \frac{k_3E^{**}}{\beta_P P + \beta_I I^{**} + \beta_A A^{**} + \beta_H H^{**}}, \tag{D.13}$$

$$P^{**} = \frac{\sigma}{k_4}E^{**}, \quad I^{**} = \frac{r\psi\sigma}{k_5^{\diamond}}E^{**}, \quad A^{**} = \frac{(1-r)\psi\sigma}{k_4k_6}E^{**}, \quad H^{**} = \frac{r\psi\sigma\phi}{k_4k_5k_7^{\diamond}}E^{**}. \tag{D.14}$$

Then, we observe that

$$\beta_P P^{**} + \beta_I I^{**} + \beta_A A^{**} + \beta_H H^{**} = \left[\beta_P\frac{\sigma}{k_4} + \beta_I\frac{r\psi\sigma}{k_4k_5^{\diamond}} + \beta_A\frac{(1-r)\psi\sigma}{k_4k_6} + \beta_H\frac{r\psi\sigma\phi}{k_4k_5^{\diamond}k_7^{\diamond}}\right]E^{**} = k_3\mathcal{R}_v^{\diamond}E^{**}, \tag{D.15}$$

and substitute the expression from equation (D.15) into (D.13) to get

$$\frac{S^{**}}{N^*} = \frac{1}{\mathcal{R}_v^{\diamond}}. \tag{D.16}$$

This implies that $\dfrac{S^{**}\mathcal{R}_v^{\diamond}}{N^*} - 1 = 0$, which means (D.12) can be simplified as

$$\Delta = -A < 0. \tag{D.17}$$

Since the determinant Δ is negative, it follows that the system (D.5) has a unique solution, given by $\mathbf{Z} = 0$ (which corresponds to the DFE ($\mathbb{E}_0$)).

Case 2: $\omega \neq 0$.

In this case, since by assumption $Re(\omega) > 0$, so $|1 + F_i(\omega)| > 1$ for all $i = 1, \cdots, 7$. Define $F(\omega) = \min|1 + F_i(\omega)|$ for $i = 1, \cdots, 7$. Then, $F(\omega) > 1$, and $\dfrac{b}{F(\omega)} < b$. Since b is a minimal positive real number such that $||\mathbf{Z}|| \leq b\mathbb{E}_1^{\diamond}$, then [249]

$$||\mathbf{Z}|| > \frac{b}{F(\omega)}\mathbb{E}_1^{\diamond}. \tag{D.18}$$

On the other hand, by taking the norm of both sides of the second equation in (D.9) and noting that M is a non-negative matrix, we have [249]

$$F(\omega)||Z_2|| \leq |1 + F_2(\omega)||Z_2|| = ||(MZ)_2|| \leq M||Z_2|| \leq bM(\mathbb{E}_1^{\diamond})_2 = b(\mathbb{E}_1^{\diamond})_2 = bI^{**}. \tag{D.19}$$

It follows from (D.19) that $||Z_2|| \leq \dfrac{b}{F(\omega)}I^{**}$, which contradicts (D.18). Hence, $Re(\omega) < 0$. Thus, all eigenvalues of the characteristic equation associated with the linearized system (D.3) will have a negative real part, so that the unique endemic equilibrium, $\mathbb{E}_1^{\diamond}$, is LAS whenever $\mathcal{R}_v^{\diamond} > 1$. This completes the proof. □

APPENDIX E

PROOF OF THEOREM 2.3.7

Proof. Consider a special case of the homogeneous model (2.8) with negligible disease-induced mortality (i.e., $\delta_I = \delta_H = 0$), perfect vaccine ($\varepsilon_v = 1$) and no waning of immunity ($\omega_v = 0$). For this special case of the model, the fully-vaccinated (V) and recovered (R) terms are not featured in the remaining equations of model (2.8), so it is enough to consider the following non-linear Lyapunov function (non-linear functions of this type have been used in ecology and epidemiology literature, such as in [250, 251, 252]):

$$\begin{aligned}\mathcal{F} =& S - S^{**} - S^{**}\ln\left(\frac{S}{S^{**}}\right) + E - E^{**} - E^{**}\ln\left(\frac{E}{E^{**}}\right) + a_1\left[P - P^{**} - P^{**}\ln\left(\frac{S}{S^{**}}\right)\right] \\ &+ a_2\left[I - I^{**} - I^{**}\ln\left(\frac{I}{I^{**}}\right)\right] + a_3\left[A - A^{**} - A^{**}\ln\left(\frac{A}{A^{**}}\right)\right] \\ &+ a_4\left[H - H^{**} - H^{**}\ln\left(\frac{H}{H^{**}}\right)\right],\end{aligned} \tag{E.1}$$

where,

$$a_1 = \frac{k_3}{\sigma}, \quad a_2 = \frac{\beta_I k_7 + \beta_H \phi}{k_5 k_7} S^{**}, \quad a_3 = \frac{\beta_A}{k_6} S^{**}, \quad a_4 = \frac{\beta_H}{k_7} S^{**}. \tag{E.2}$$

Taking the time derivative of (E.1) gives

$$\begin{aligned}\dot{\mathcal{F}} &= \dot{S} - \frac{S^{**}}{S}\dot{S} + \dot{E} - \frac{E^*}{E}\dot{E} + a_1\left(\dot{P} - \frac{P^{**}}{P}\dot{P}\right) + a_2\left(\dot{I} - \frac{I^{**}}{I}\dot{I}\right) + a_3\left(\dot{A} - \frac{A^{**}}{A}\dot{A}\right) \\ &\quad + a_4\left(\dot{H} - \frac{H^{**}}{H}\dot{H}\right) \\ &= \Pi - k_1 S - \frac{S^{**}}{S}[\Pi - (\beta_P + \beta_I I + \beta_A A + \beta_H H)S - k_1 S] - k_3 E \\ &\quad - \frac{E^{**}}{E}[(\beta_P P + \beta_I I + \beta_A A + \beta_H H)S - k_3 E] \\ &\quad + a_1\left[\sigma E - k_4 P - \frac{P^{**}}{P}(\sigma E - k_4 P)\right] + a_2\left[r\psi P - k_5 I - \frac{I^{**}}{I}(r\psi P - k_5 I)\right] \\ &\quad + a_3\left[(1-r)\psi P - k_6 A - \frac{A^{**}}{A}((1-r)\psi P - k_6 A\right] + a_4\left[\phi I - k_7 H - \frac{H^{**}}{H}(\phi I - k_7 H)\right].\end{aligned} \tag{E.3}$$

It can be shown from this special case of the model (2.8) that, at endemic steady-state,

$$\begin{aligned}\Pi &= (\beta_P P^{**} + \beta_I I^{**} + \beta_A A^{**} + \beta_H H^{**})S^{**} - k_1 S^{**}, \\ a_2\sigma = \frac{k_3 k_4 P^{**}}{\sigma E^{**}}, &\quad a_3 r\psi = \frac{\beta_I S^* S^*}{P^*} + \beta_H \frac{S^* H^*}{P^*}, \\ a_4(1-r)\psi = \frac{\beta_A S^{**} A^{**}}{P^{**}}, &\quad a_5\phi = \frac{\beta_H S^{**} H^{**}}{I^{**}}.\end{aligned} \tag{E.4}$$

Plugging in the first equation from (E.4) into (E.3) and simplifying, gives

$$\begin{aligned}\dot{\mathcal{F}} =& k_1 S^{**}\left[2 - \frac{S^{**}}{S} - \frac{S}{S^{**}}\right] + (\beta_P P^{**} + \beta_I I^{**} + \beta_A A^{**} + \beta_H H^{**})S^{**} + k_3 E^{**} + a_1 k_4 P^{**} \\ &+ a_2 k_5 I^{**} + a_3 k_6 A^{**} + a_4 k_7 H^{**} - (\beta_P P^{**} + \beta_I I^{**} + \beta_A A^{**} + \beta_H H^{**})\frac{{S^{**}}^2}{S} \\ &- (\beta_P P + \beta_I I + \beta_A A + \beta_H H)\frac{SE^{**}}{E} \\ &- a_1\sigma\frac{EP^{**}}{P} - a_3 r\psi\frac{PI^{**}}{I} - a_4(1-r)\psi\frac{PA^{**}}{A} - a_5\phi\frac{IH^{**}}{H}.\end{aligned} \tag{E.5}$$

Then, making use of the remaining equations in (E.4), the equation (E.5) can be re-written as

$$\begin{aligned}
\dot{\mathcal{F}} =& k_1 S^{**}\left[2-\frac{S^{**}}{S}-\frac{S}{S^{**}}\right]+4(\beta_P P^{**}+\beta_I I^{**}+\beta_A A^{**}+\beta_H H^{**})S^{**} \\
&-(\beta_P P^{**}+\beta_I I^{**}+\beta_A A^{**}+\beta_H H^{**})\frac{S^{**^2}}{S}-(\beta_P P+\beta_I I+\beta_A A+\beta_H H)\frac{SE^{**}}{E} \\
&-(\beta_P P^{**}+\beta_I^{**}+\beta_A A^{**}+\beta_H H^{**})\frac{S^{**}EP^{**}}{E^{**}P}-\beta_I\frac{S^{**}I^{**^2}P}{IP^{**}}-\beta_H\frac{S^{**}PI^{**}H^{**}}{P^{**}I} \\
&-\beta_A\frac{S^{**}A^{**^2}P}{AP^{**}}-\beta_H\frac{S^{**}IH^{**^2}}{I^{**}H}, \\
\dot{\mathcal{F}} =& k_1 S^{**}\left[2-\frac{S^{**}}{S}-\frac{S}{S^{**}}\right]+\beta_P S^{**}P^{**}\left[3-\frac{S^{**}}{S}-\frac{SPE^{**}}{S^{**}P^{**}E}-\frac{EP^{**}}{E^{**}P}\right] \\
&+\beta_I S^{**}I^{**}\left[4-\frac{S^{**}}{S}-\frac{SIE^{**}}{S^{**}I^{**}E}-\frac{EP^{**}}{E^{**}P}-\frac{I^{**}P}{IP^{**}}\right] \\
&+\beta_A S^{**}A^{**}\left[4-\frac{S^{**}}{S}-\frac{SAE^{**}}{S^{**}A^{**}E}-\frac{EP^{**}}{E^{**}P}-\frac{A^{**}P}{AP^{**}}\right] \\
&+\beta_H S^{**}H^{**}\left[5-\frac{S^{**}}{S}-\frac{SHE^{**}}{S^{**}H^{**}E}-\frac{EP^{**}}{E^{**}P}-\frac{PI^{**}}{P^{**}I}-\frac{IH^{**}}{I^{**}H}\right].
\end{aligned} \tag{E.6}$$

Since the arithmetic mean exceed the geometric mean, it implies that

$$\begin{aligned}
k_1 S^{**}\left[2-\frac{S^{**}}{S}-\frac{S}{S^{**}}\right] &\leq 0, \\
\beta_P S^{**}P^{**}\left[3-\frac{S^{**}}{S}-\frac{SPE^{**}}{S^{**}P^{**}E}-\frac{EP^{**}}{E^{**}P}\right] &\leq 0, \\
\beta_I S^{**}I^{**}\left[4-\frac{S^{**}}{S}-\frac{SIE^{**}}{S^{**}I^{**}E}-\frac{EP^{**}}{E^{**}P}-\frac{I^{**}P}{IP^{**}}\right] &\leq 0, \\
\beta_A S^{**}A^{**}\left[4-\frac{S^{**}}{S}-\frac{SAE^{**}}{S^{**}A^{**}E}-\frac{EP^{**}}{E^{**}P}-\frac{A^{**}P}{AP^{**}}\right] &\leq 0, \\
\beta_H S^{**}H^{**}\left[5-\frac{S^{**}}{S}-\frac{SHE^{**}}{S^{**}H^{**}E}-\frac{EP^{**}}{E^{**}P}-\frac{PI^{**}}{P^{**}I}-\frac{IH^{**}}{I^{**}H}.\right] &\leq 0
\end{aligned} \tag{E.7}$$

Thus $\dot{\mathcal{F}} \leq 0$ for $\hat{\mathcal{R}}_v > 1$. Hence, $\mathcal{F}$ is a Lyapunov function for the aforementioned special case of the model (2.8) on Ω_1/Ω_0. Therefore, it follows, by LaSalle's Invariance

Principle [95], that

$$\lim_{x\to\infty} S(x) = S^{**}, \quad \lim_{x\to\infty} E(x) = E^{**}, \quad \lim_{x\to\infty} P(x) = P^{**},$$
$$\lim_{x\to\infty} I(x) = I^{**}, \quad \lim_{x\to\infty} A(x) = A^{**}, \quad \lim_{x\to\infty} H(x) = H^{**}.$$

Thus, $\liminf_{t\to\infty} S = \limsup_{t\to\infty} S = S^{**}$. Since, $\limsup_{t\to\infty} S = S^{**}$, it follows that, for sufficiently small $\zeta > 0$, there exists a $T_1 > 0$ such that $\limsup_{t\to\infty} S \leq S^{**} + \zeta$ for all $t > T_1$. It follows from (2.21) and the $\dot{V}$ equation of the special case of the model (2.8) that, for $t > T_1$,

$$\dot{V} \leq \xi_v(S^{**} + \zeta) - k_2 V.$$

So, by comparison theorem [65],

$$V^{\infty} = \limsup_{t\to\infty} V \leq \frac{\xi_v(S^{**} + \zeta)}{k_2} \to \frac{\xi_v S^{**}}{k_2} \quad \text{as } \zeta \to 0. \tag{E.8}$$

Similarly, by using $\liminf_{t\to\infty} S = S^{**}$, we can show that

$$V_{\infty} = \liminf_{t\to\infty} V \geq \frac{\xi_v(S^{**} + \zeta)}{k_2} \to \frac{\xi_v S^{**}}{k_2} \quad \text{as } \zeta \to 0. \tag{E.9}$$

Then, it follows from (E.8) and (E.9) that

$$V_{\infty} \geq \frac{\xi_v S^{**}}{k_2} \geq V^{\infty}. \tag{E.10}$$

Hence, $\lim_{t\to\infty} V = \frac{\xi_v S^{**}}{k_2} = V^{**}$. Similarly, it can be shown that $\lim_{t\to\infty} R = R^{**}$. Thus, for $\hat{\mathcal{R}}_v > 1$, every solution of the system (2.8), with initial conditions in Ω_1/Ω_0, approaches the unique endemic equilibrium for $t \to \infty$. □

APPENDIX F

COMPUTATION OF REPRODUCTION NUMBER OF THE TWO-GROUP MODEL

Using the *next generation operator method* [88, 89], the non-negative matrix of new infection terms (F_2) and M-Matrix (V_2) of linear transition term in the infected compartments corresponding to two-group heterogeneous model (2.31) are given respectively by [61]:

$$F_2 = \begin{bmatrix} 0 & 0 & f_{1,3} & f_{1,4} & f_{1,5} & f_{1,6} & f_{1,7} & f_{1,8} & f_{1,9} & f_{1,10} \\ 0 & 0 & f_{2,3} & f_{2,4} & f_{2,5} & f_{2,6} & f_{2,7} & f_{2,8} & f_{2,9} & f_{2,10} \\ 0 & 0 & 0 & 0 & 0 & 0 & 0 & 0 & 0 & 0 \\ 0 & 0 & 0 & 0 & 0 & 0 & 0 & 0 & 0 & 0 \\ 0 & 0 & 0 & 0 & 0 & 0 & 0 & 0 & 0 & 0 \\ 0 & 0 & 0 & 0 & 0 & 0 & 0 & 0 & 0 & 0 \\ 0 & 0 & 0 & 0 & 0 & 0 & 0 & 0 & 0 & 0 \\ 0 & 0 & 0 & 0 & 0 & 0 & 0 & 0 & 0 & 0 \\ 0 & 0 & 0 & 0 & 0 & 0 & 0 & 0 & 0 & 0 \\ 0 & 0 & 0 & 0 & 0 & 0 & 0 & 0 & 0 & 0 \end{bmatrix},$$

and

$$V_2 = \begin{bmatrix} \sigma_1+\mu_1 & 0 & 0 & 0 & 0 & 0 & 0 & 0 & 0 & 0 \\ 0 & \sigma_2+\mu_2 & 0 & 0 & 0 & 0 & 0 & 0 & 0 & 0 \\ -\sigma_1 & 0 & \psi_1+\mu_1 & 0 & 0 & 0 & 0 & 0 & 0 & 0 \\ 0 & -\sigma_2 & 0 & \psi_2+\mu_2 & 0 & 0 & 0 & 0 & 0 & 0 \\ 0 & 0 & -r_1\psi_1 & 0 & v_{55} & 0 & 0 & 0 & 0 & 0 \\ 0 & 0 & 0 & -r_2\psi_2 & 0 & v_{66} & 0 & 0 & 0 & 0 \\ 0 & 0 & -(1-r_1)\psi_1 & 0 & 0 & 0 & \gamma_{A,1}+\mu_1 & 0 & 0 & 0 \\ 0 & 0 & 0 & -(1-r_2)\psi_2 & 0 & 0 & 0 & \gamma_{A,2}+\mu_2 & 0 & 0 \\ 0 & 0 & 0 & 0 & -\phi_1 & 0 & 0 & 0 & \gamma_{H,1}+\delta_{H,1}+\mu_1 & 0 \\ 0 & 0 & 0 & 0 & 0 & -\phi_2 & 0 & 0 & 0 & \gamma_{H,2}+\delta_{H,2}+\mu_2 \end{bmatrix},$$

where,

$$\begin{aligned} f_{1,3} &= a_1c_{11}\mathcal{P}_{P,1}\frac{S_1^*+(1-\varepsilon_v)V_1^*}{N_1^*}, & f_{1,4} &= a_1c_{12}\mathcal{P}_{P,2}\frac{S_1^*+(1-\varepsilon_v)V_1^*}{N_2^*}, \\ f_{1,5} &= a_1c_{11}\mathcal{P}_{I,1}\frac{S_1^*+(1-\varepsilon_v)V_1^*}{N_1^*}, & f_{1,6} &= a_1c_{12}\mathcal{P}_{I,2}\frac{S_1^*+(1-\varepsilon_v)V_1^*}{N_2^*}, \\ f_{1,7} &= a_1c_{11}\mathcal{P}_{A,1}\frac{S_1^*+(1-\varepsilon_v)V_1^*}{N_1^*}, & f_{1,8} &= a_1c_{12}\mathcal{P}_{A,2}\frac{S_1^*+(1-\varepsilon_v)V_1^*}{N_2^*}, \\ f_{1,9} &= a_1c_{11}\mathcal{P}_{H,1}\frac{S_1^*+(1-\varepsilon_v)V_1^*}{N_1^*}, & f_{1,10} &= a_1c_{12}\mathcal{P}_{H,2}\frac{S_1^*+(1-\varepsilon_v)V_1^*}{N_2^*}, \\ f_{2,3} &= a_2c_{21}\mathcal{P}_{P,1}\frac{S_2^*+(1-\varepsilon_v)V_2^*}{N_1^*}, & f_{2,4} &= a_2c_{22}\mathcal{P}_{P,2}\frac{S_2^*+(1-\varepsilon_v)V_2^*}{N_2^*}, \\ f_{2,5} &= a_2c_{21}\mathcal{P}_{I,1}\frac{S_2^*+(1-\varepsilon_v)V_2^*}{N_1^*}, & f_{2,6} &= a_2c_{22}\mathcal{P}_{I,2}\frac{S_2^*+(1-\varepsilon_v)V_2^*}{N_2^*}, \\ f_{2,7} &= a_2c_{21}\mathcal{P}_{A,1}\frac{S_2^*+(1-\varepsilon_v)V_2^*}{N_1^*}, & f_{2,8} &= a_2c_{22}\mathcal{P}_{A,2}\frac{S_2^*+(1-\varepsilon_v)V_2^*}{N_2^*}, \\ f_{2,9} &= a_2c_{21}\mathcal{P}_{H,1}\frac{S_2^*+(1-\varepsilon_v)V_2^*}{N_1^*}, & f_{2,10} &= a_2c_{22}\mathcal{P}_{H,2}\frac{S_2^*+(1-\varepsilon_v)V_2^*}{N_2^*}, \\ v_{55} &= \phi_1+\gamma_{I,1}+\delta_1+\mu_1, & v_{66} &= \phi_2+\gamma_{I,2}+\delta_2+\mu_2. \end{aligned}$$

Hence, it follows from [60] that the vaccination reproduction number for the two-group

model (2.31) is given by [88, 89]:

$$\mathcal{R}_v^{\dagger} = \rho(F_2 V_2^{-1}) \tag{F.1}$$

APPENDIX G

PROOF OF THEOREM 2.4.2

Proof. Let $k, l = \{1, 2\}$. Consider a special case of the two-group model (2.31) with negligible disease-induced mortality (i.e., $\delta_{I,k} = \delta_{H,k} = 0$). Furthermore, let $\mathcal{R}_v^{\Delta} < 1$. Summing equations with indices k in (2.3) gives

$$\dot{N}_k = \Pi_k - \mu_k N_k - \mu_{k,I} I_k - \mu_{1,k} H_k.$$

In the absence of disease-included mortality (i.e., set $\delta_{k,I} = \delta_{k,H} = 0$), we get $N_k \to \dfrac{\Pi_k}{\mu_k}$ as $t \to \infty$ and $\dfrac{\Pi_k}{\mu_k}$ is an upper bound of $N_k(t)$ provided that $N_k(0) \leq \dfrac{\Pi_k}{\mu_k}$. If $N_k(0) > \dfrac{\Pi_k}{\mu_k}$, then N_k will decrease to that level. Hence, in Ω_2, $N_k \leq \dfrac{\Pi_k}{\mu_k}$. Then, it follows from first equation in (2.3) and (2.2) that

$$\begin{aligned}
\dot{S}_k &= \Pi_k + \omega_{v,k} V_k - \lambda_k S_k - (\xi_{v,k} + \mu_k) S_k \\
&\leq \Pi_k + \omega_{v,k} V_k - (\xi_{v,k} + \mu_k) S_k \\
&\leq \Pi_k + \omega_{v,k} (\Pi_k/\mu_k - S_k - E_k - P_k - I_k - A_k - H_k - R_k) - (\xi_{v,k} + \mu_k) S_k \\
&\leq \frac{(\omega_{v,k} + \mu_k)\Pi_k}{\mu_k} - (\omega_{v,k} + \xi_{v,k} + \mu_k) S_k = (\omega_{v,k} + \xi_{v,k} + \mu_k)(S_k^* - S_k).
\end{aligned}$$

So, if $S_k > S_k^*$, then $\dot{S}_k < 0$; hence $S_k \leq S_k^*$ given $S_k(0) \leq S_k^*$ is true. Following a similar argument, one can show that $\dot{V}_k \leq -(\omega_{v,k} + \mu_k) V_k + \xi_{v,k} S_k = (\omega_{v,k} + \mu_k)(V_k^* - V_k)$. If $V_k > V_k^*$ then $\dot{V}_k < 0$; hence $V_k \leq V_k^*$ given $V_k(0) \leq V_k^*$ is true.

It follows from these bounds that the region

$$\tilde{\Omega}_2^{\Delta} = \Big\{(S_1, S_2, V_1, V_2, E_1, E_2, P_1, P_2, I_1, I_2, A_1, A_2, H_1, H_2, R_1, R_2) \in \Omega_2 : S_k \leq S_k^*, V_k \leq V_k^*\Big\},$$

is also positively invariant and attracts all solutions in Ω_2. It is convenient to define

the following

$$\begin{aligned}
&\bar{a}_k = \sigma_k + \mu_k, \quad \bar{b}_k = \psi_k + \mu_k, \quad \bar{c}_k = \psi_k + \gamma_{I,k} + \mu_k + \delta_{I,k}, \\
&\bar{d}_k = \gamma_{A,k} + \mu_k, \quad \bar{e}_k = \gamma_{H,k} + \mu_k + \delta_{H,k}, \\
&W_{kl} = \frac{S_k + (1-\varepsilon_{v,k})V_k}{\Pi_l/\mu_l}, \quad W^*_{kl} = \frac{S^*_k + (1-\varepsilon_{v,k})V^*_k}{N^*_l},
\end{aligned} \tag{G.1}$$

Since $S^*_k \geq S_k$, $V^*_k \geq V_k$, observe that

$$W^*_{kl} \geq W_{kl}. \tag{G.2}$$

The equations of the infected component of this special case of the model (2.31) can be re-written in terms of the next generation matrices F_2 and $V_2^\Delta = V_2|_{\delta_{I,k}=\delta_{H,k}=0}$, given in Appendix F as:

$$\frac{d}{dt}\begin{pmatrix} E_1(t) \\ E_2(t) \\ P_1(t) \\ P_2(t) \\ I_1(t) \\ I_2(t) \\ A_1(t) \\ A_2(t) \\ H_1(t) \\ H_2(t) \end{pmatrix} = (F_2 - V_2^\Delta)\begin{pmatrix} E_1(t) \\ E_2(t) \\ P_1(t) \\ P_2(t) \\ I_1(t) \\ I_2(t) \\ A_1(t) \\ A_2(t) \\ H_1(t) \\ H_2(t) \end{pmatrix} - J_2\begin{pmatrix} E_1(t) \\ E_2(t) \\ P_1(t) \\ P_2(t) \\ I_1(t) \\ I_2(t) \\ A_1(t) \\ A_2(t) \\ H(t) \\ H_2(t) \end{pmatrix}, \tag{G.3}$$

where,

$$F_2 - V_2^{\Delta} = \begin{bmatrix} -\bar{a}_1 & 0 & f_{1,3} & f_{1,4} & f_{1,5} & f_{1,6} & f_{1,7} & f_{1,8} & f_{1,9} & f_{1,10} \\ 0 & -\bar{a}_2 & f_{2,3} & f_{2,4} & f_{2,5} & f_{2,6} & f_{2,7} & f_{2,8} & f_{2,9} & f_{2,10} \\ \sigma_1 & 0 & -\bar{b}_1 & 0 & 0 & 0 & 0 & 0 & 0 & 0 \\ 0 & \sigma_2 & 0 & -\bar{b}_2 & 0 & 0 & 0 & 0 & 0 & 0 \\ 0 & 0 & r_1\psi_1 & 0 & -\bar{c}_1 & 0 & 0 & 0 & 0 & 0 \\ 0 & 0 & 0 & r_2\psi_2 & 0 & -\bar{c}_2 & 0 & 0 & 0 & 0 \\ 0 & 0 & (1-r_1)\psi_1 & 0 & 0 & 0 & -\bar{d}_1 & 0 & 0 & 0 \\ 0 & 0 & 0 & (1-r_2)\psi_2 & 0 & 0 & 0 & -\bar{d}_2 & 0 & 0 \\ 0 & 0 & 0 & 0 & \phi_1 & 0 & 0 & 0 & -\bar{e}_1 & 0 \\ 0 & 0 & 0 & 0 & 0 & \phi_2 & 0 & 0 & 0 & -\bar{e}_2 \end{bmatrix}, \tag{G.4}$$

and,

$$J_2 = \begin{pmatrix} 0 & 0 & J_{1,3} & J_{1,4} & J_{1,5} & J_{1,6} & J_{1,7} & J_{1,8} & J_{1,9} & J_{1,10} \\ 0 & 0 & J_{2,3} & J_{2,4} & J_{2,5} & J_{2,6} & J_{2,7} & J_{2,8} & J_{2,9} & J_{2,10} \\ 0 & 0 & 0 & 0 & 0 & 0 & 0 & 0 & 0 & 0 \\ 0 & 0 & 0 & 0 & 0 & 0 & 0 & 0 & 0 & 0 \\ 0 & 0 & 0 & 0 & 0 & 0 & 0 & 0 & 0 & 0 \\ 0 & 0 & 0 & 0 & 0 & 0 & 0 & 0 & 0 & 0 \\ 0 & 0 & 0 & 0 & 0 & 0 & 0 & 0 & 0 & 0 \\ 0 & 0 & 0 & 0 & 0 & 0 & 0 & 0 & 0 & 0 \\ 0 & 0 & 0 & 0 & 0 & 0 & 0 & 0 & 0 & 0 \\ 0 & 0 & 0 & 0 & 0 & 0 & 0 & 0 & 0 & 0 \end{pmatrix}, \tag{G.5}$$

with

$$
\begin{aligned}
J_{1,3} &= a_1 c_{11} \mathcal{P}_{P,1}(W_{11}^* - W_{11}), & J_{1,4} &= a_1 c_{12} \mathcal{P}_{P,2}(W_{12}^* - W_{12}),\\
J_{1,5} &= a_1 c_{11} \mathcal{P}_{I,1}(W_{11}^* - W_{11}), & J_{1,6} &= a_1 c_{12} \mathcal{P}_{I,2}(W_{12}^* - W_{12}),\\
J_{1,7} &= a_1 c_{11} \mathcal{P}_{A,1}(W_{11}^* - W_{11}), & J_{1,8} &= a_1 c_{12} \mathcal{P}_{A,2}(W_{12}^* - W_{12}),\\
J_{1,9} &= a_1 c_{11} \mathcal{P}_{H,1}(W_{11}^* - W_{11}), & J_{1,10} &= a_1 c_{12} \mathcal{P}_{H,2}(W_{12}^* - W_{12}),\\
J_{2,3} &= a_2 c_{21} \mathcal{P}_{P,1}(W_{21}^* - W_{21}), & J_{2,4} &= a_2 c_{22} \mathcal{P}_{P,2}(W_{22}^* - W_{22}),\\
J_{2,5} &= a_2 c_{21} \mathcal{P}_{I,1}(W_{21}^* - W_{21}), & J_{2,6} &= a_2 c_{22} \mathcal{P}_{I,2}(W_{22}^* - W_{22}),\\
J_{2,7} &= a_2 c_{21} \mathcal{P}_{A,1}(W_{21}^* - W_{21}), & J_{2,8} &= a_2 c_{22} \mathcal{P}_{A,2}(W_{22}^* - W_{22}),\\
J_{2,9} &= a_2 c_{21} \mathcal{P}_{H,1}(W_{21}^* - W_{21}), & J_{2,10} &= a_2 c_{22} \mathcal{P}_{H,2}(W_{22}^* - W_{22}).
\end{aligned}
\tag{G.6}
$$

Since (G.2) holds, J_2 is a non-negative matrix. Thus, Equation (G.3) can be re-written as the following inequality:

$$
\frac{d}{dt}\begin{pmatrix} E_1(t)\\ E_2(t)\\ P_1(t)\\ P_2(t)\\ I_1(t)\\ I_2(t)\\ A_1(t)\\ A_2(t)\\ H_1(t)\\ H_2(t) \end{pmatrix} \leq (F - V)\begin{pmatrix} E_1(t)\\ E_2(t)\\ P_1(t)\\ P_2(t)\\ I_1(t)\\ I_2(t)\\ A_1(t)\\ A_2(t)\\ H_1(t)\\ H_2(t) \end{pmatrix}. \tag{G.7}
$$

If $\mathcal{R}_v^{\Delta} < 1$, then $\rho(F_2 V_2^{\Delta^{-1}}) < 1$, which is equivalent to all eigenvalues of $F - V^{\diamond}$ matrix being negative [88]. Hence, the linearized differential inequality (C.5) is stable whenever $\mathcal{R}_v^{\Diamond} < 1$, so

$(E_1(t), E_2(t), P_1(t), P_2(t), I_1(t), I_2(t), A_1(t), A_2(t), H_1(t), H_2(t)) \to (0,0,0,0,0,0,0,0,0,0)$ as $t \to \infty$ for this linear ODE system. It follows, using a standard comparison theorem [65], that:
$(E_1(t), E_2(t), P_1(t), P_2(t), I_1(t), I_2(t), A_1(t), A_2(t), H_1(t), H_2(t)) \to (0,0,0,0,0,0,0,0,0,0)$.
Substituting $E_k(t) = P_k(t) = I_k(t) = A_k(t) = H_k(t) = 0$, into the equations for $\dot{S}$, $\dot{V}$, and $\dot{R}$ of the homogeneous model (2.8) gives:

$$S_k(t) \to S_k^*, V_k(t) \to V_k^* \text{ and } R_k(t) \to 0, \text{ as } t \to \infty.$$

Hence, the disease-free equilibrium of the special case of the two-group model (2.31) with negligible disease-induced mortality (i.e, (2.31) with $\delta_I = \delta_H = 0$) is globally-asymptomatically stable in Ω_2^{Δ}, whenever $\mathcal{R}_v^{\Delta} < 1$. □

APPENDIX H

EQUATIONS FOR THE BEHAVIOR-FREE MODEL

The behavior-free model, discussed in Section 3.2.3 and obtained by setting behavior-related parameters of the model (3.4) to zero (i.e., consider the model (3.4) with $p = \psi_{12}^c = \psi_{21}^c = \psi_{12}^i = \psi_{21}^{ns} = \psi_{12}^m = \psi_{21}^f = 0$), is given by the following system of nonlinear differential equations [151]:

$$\begin{cases} \dot{S}_1(t) = \Pi - \lambda S_1 - \mu S_1, \\ \dot{S}_2(t) = -(1-\varepsilon_m)\lambda S_2 - \mu S_2, \\ \dot{E}_1(t) = \lambda S_1 - (\sigma+\mu)E_1, \\ \dot{E}_2(t) = (1-\varepsilon_m)\lambda S_2 - (\sigma+\mu)E_2, \\ \dot{I}_1(t) = (1-r)\sigma E_1 - (\gamma_i+\mu+\delta_1)I_1, \\ \dot{I}_2(t) = (1-r)\sigma E_2 - (\gamma_i+\mu+\delta_2)I_2, \\ \dot{A}_1(t) = r\sigma E_1 - (\gamma_a+\mu)A_1, \\ \dot{A}_2(t) = r\sigma E_2 - (\gamma_a+\mu)A_2, \\ \dot{R}_1(t) = \gamma_i I_1 + \gamma_a A_1 - \mu R_1, \\ \dot{R}_2(t) = \gamma_i I_2 + \gamma_a A_2 - \mu R_2, \end{cases} \tag{H.1}$$

where λ (i.e., the *force of infection*) for the behavior-free model (H.1) is as given in (3.3)). Furthermore, like for the case of the behavior-epidemiology model, the state variables and parameters of the behavior-free model are described in Tables 2.1 and 2.2.

APPENDIX I

MISCELLANEOUS FIGURE FOR CHAPTER 3

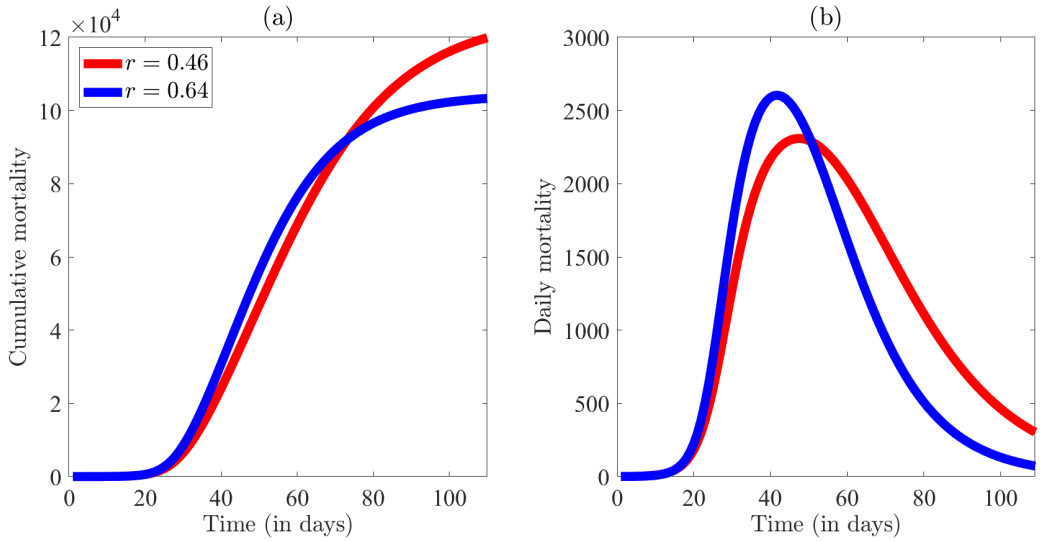

Figure I.1: Simulation of the behavior-epidemiology model (3.4) depicting the impact of two specific values of the proportion of newly infected individuals who become asymptomatically-infectious at the end of the exposed period (r) on mortality. The (a) cumulative mortality and (b) daily mortality figures are generated for values of $r = 0.46$ and $r = 0.64$ with remaining parameters as in Tables 3.3 and 3.4 [151].

APPENDIX J

PROFILE OF INFECTED AND RECOVERED INDIVIDUALS WHO ARE SHEDDING

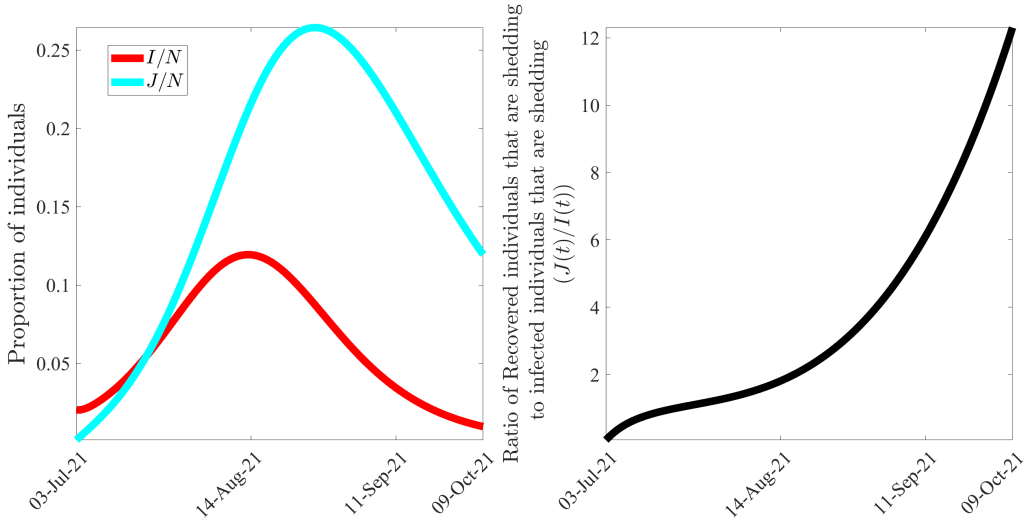

Figure J.1: Comparison of WBE model {(4.2), (4.3)} projected profiles of infected (I) and recovered individuals (J) who are shedding viral RNA in feces for Maimi-Dade County, Florida from July 3rd, 2021 to October 9th, 2021. (a) The profile of the proportion of the population in I and J compartments over time. (b) The ratio of J and I compartments highlights a relative increase in individuals in the J compartment during a wave. The figure is generated using parameter values in Tables 4.3 and 4.4 [214].

REFERENCES

[1] N. LePan, N. Routley, and H. Schell, "Visualizing the history of pandemics." `https://www.visualcapitalist.com/history-of-pandemics-deadliest/`, 2020. Accessed September 18, 2023.

[2] D. Huremović, "Brief history of pandemics (pandemics throughout history)," *Psychiatry of Pandemics: a Mental Health Response to Infection Outbreak*, pp. 7–35, 2019.

[3] J. Piret and G. Boivin, "Pandemics throughout history," *Frontiers in Microbiology*, vol. 11, p. 631736, 2021.

[4] D. M. Morens and A. S. Fauci, "The 1918 influenza pandemic: insights for the 21st century," *The Journal of Infectious Diseases*, vol. 195, no. 7, pp. 1018–1028, 2007.

[5] J. S. Faust, Z. Lin, and C. Del Rio, "Comparison of estimated excess deaths in New York City during the COVID-19 and 1918 influenza pandemics," *JAMA Network Open*, vol. 3, no. 8, pp. e2017527–e2017527, 2020.

[6] C. N. Ngonghala, E. Iboi, S. Eikenberry, M. Scotch, C. R. MacIntyre, M. H. Bonds, and A. B. Gumel, "Mathematical assessment of the impact of non-pharmaceutical interventions on curtailing the 2019 novel coronavirus," *Mathematical Biosciences*, vol. 325, p. 108364, 2020.

[7] K. E. Jones, N. G. Patel, M. A. Levy, A. Storeygard, D. Balk, J. L. Gittleman, and P. Daszak, "Global trends in emerging infectious diseases," *Nature*, vol. 451, no. 7181, pp. 990–993, 2008.

[8] E. H. Loh, C. Zambrana-Torrelio, K. J. Olival, T. L. Bogich, C. K. Johnson, J. A. Mazet, W. Karesh, and P. Daszak, "Targeting transmission pathways for emerging zoonotic disease surveillance and control," *Vector-Borne and Zoonotic Diseases*, vol. 15, no. 7, pp. 432–437, 2015.

[9] Y. Alimi, A. Bernstein, J. Epstein, M. Espinal, M. Kakkar, D. Kochevar, and G. Werneck, "Report of the scientific task force on preventing pandemics." `https://www.hsph.harvard.edu/wp-content/uploads/sites/2343/2021/08/PreventingPandemicsAug2021.pdf`, 2021. Accessed Feburary 26, 2024.

[10] M. Worobey, J. I. Levy, L. Malpica Serrano, A. Crits-Christoph, J. E. Pekar, S. A. Goldstein, A. L. Rasmussen, M. U. Kraemer, C. Newman, M. P. Koopmans, *et al.*, "The huanan seafood wholesale market in wuhan was the early epicenter of the covid-19 pandemic," *Science*, vol. 377, no. 6609, pp. 951–959, 2022.

[11] S. Lytras, W. Xia, J. Hughes, X. Jiang, and D. L. Robertson, "The animal origin of sars-cov-2," *Science*, vol. 373, no. 6558, pp. 968–970, 2021.

[12] S. Yuan, S.-C. Jiang, and Z.-L. Li, "Analysis of possible intermediate hosts of the new coronavirus sars-cov-2," *Frontiers in Veterinary Science*, vol. 7, p. 379, 2020.

[13] G. Dharmarajan, R. Li, E. Chanda, K. R. Dean, R. Dirzo, K. S. Jakobsen, I. Khan, H. Leirs, Z.-L. Shi, N. D. Wolfe, *et al.*, "The animal origin of major human infectious diseases: what can past epidemics teach us about preventing the next pandemic?," *Zoonoses*, vol. 2, no. 1, 2022.

[14] CDC, "CDC Museum COVID-19 timeline." https://www.cdc.gov/museum/timeline/covid19.html#. Accessed February, 2024.

[15] D. Cucinotta and M. Vanelli, "WHO declares COVID-19 a pandemic," *Acta Biomedica: Atenei Parmensis*, vol. 91, no. 1, p. 157, 2020.

[16] World Health Organization, "WHO coronavirus disease (COVID-19) dashboard." https://covid19.who.int. Accessed September 17, 2023.

[17] A. Shalal, "IMF sees cost of covid pandemic rising beyond $12.5 trillion estimate." https://www.reuters.com/business/imf-sees-cost-covid-pandemic-rising-beyond-125-trillion-estimate-2022-01-20/, 2022.

[18] O. W. in Data, "Cumulative confirmed COVID-19 deaths, feb 4, 2024." https://ourworldindata.org/explorers/coronavirus-data-explorer?tab=map&time=latest&facet=none&country=~OWID_WRL&Interval=Cumulative&Relative+to+Population=false&Color+by+test+positivity=false&Metric=Confirmed+deaths, 2024.

[19] S. E. Eikenberry, M. Mancuso, E. Iboi, T. Phan, K. Eikenberry, Y. Kuang, E. Kostelich, and A. B. Gumel, "To mask or not to mask: Modeling the potential for face mask use by the general public to curtail the COVID-19 pandemic," *Infectious Disease Modelling*, vol. 5, pp. 293–308, 2020.

[20] C. N. Ngonghala, J. R. Knitter, L. Marinacci, M. H. Bonds, and A. B. Gumel, "Assessing the impact of widespread respirator use in curtailing COVID-19 transmission in the USA," *Royal Society Open Science*, vol. 8, no. 9, p. 210699, 2021.

[21] A. B. Gumel, E. A. Iboi, C. N. Ngonghala, and E. H. Elbasha, "A primer on

using mathematics to understand COVID-19 dynamics: Modeling, analysis and simulations," *Infectious Disease Modelling*, vol. 6, pp. 148–168, 2021.

[22] E. A. Iboi, C. N. Ngonghala, and A. B. Gumel, "Will an imperfect vaccine curtail the COVID-19 pandemic in the US?," *Infectious Disease Modelling*, vol. 5, pp. 510–524, 2020.

[23] S. Safdar, C. N. Ngonghala, and A. Gumel, "Mathematical assessment of the role of waning and boosting immunity against the BA. 1 Omicron variant in the United States," *medRxiv*, 2022.

[24] C. N. Ngonghala, H. B. Taboe, and A. B. Gumel, "Dynamics of the Delta and Omicron variants of SARS-CoV-2 in the United States: the battle of supremacy in the presence of vaccination, mask usage and antiviral treatment," *medRxiv*, 2022.

[25] A. B. Gumel, E. A. Iboi, C. N. Ngonghala, and G. A. Ngwa, "Toward achieving a vaccine-derived herd immunity threshold for COVID-19 in the US," *Frontiers in Public Health*, vol. 9, 2021.

[26] S. J. Brozak, B. Pant, S. Safdar, and A. B. Gumel, "Dynamics of COVID-19 pandemic in India and Pakistan: A metapopulation modelling approach," *Infectious Disease Modelling*, 2021.

[27] R. Hinch, W. J. Probert, A. Nurtay, M. Kendall, C. Wymant, M. Hall, K. Lythgoe, A. Bulas Cruz, L. Zhao, A. Stewart, *et al.*, "OpenABM-COVID-19—An agent-based model for non-pharmaceutical interventions against COVID-19 including contact tracing," *PLoS Computational Biology*, vol. 17, no. 7, p. e1009146, 2021.

[28] J. Almagor and S. Picascia, "Exploring the effectiveness of a COVID-19 contact tracing app using an agent-based model," *Scientific Reports*, vol. 10, no. 1, pp. 1–11, 2020.

[29] N. M. Ferguson, D. Laydon, G. Nedjati-Gilani, N. Imai, K. Ainslie, M. Baguelin, S. Bhatia, A. Boonyasiri, Z. Cucunubá, G. Cuomo-Dannenburg, *et al.*, "Impact of non-pharmaceutical interventions (NPIs) to reduce COVID-19 mortality and healthcare demand," *Imperial College*, 2020.

[30] C. C. Kerr, R. M. Stuart, D. Mistry, R. G. Abeysuriya, K. Rosenfeld, G. R. Hart, R. C. Núñez, J. A. Cohen, P. Selvaraj, B. Hagedorn, *et al.*, "Covasim: an agent-based model of COVID-19 dynamics and interventions," *PLOS Computational Biology*, vol. 17, no. 7, p. e1009149, 2021.

[31] N. Hoertel, M. Blachier, C. Blanco, M. Olfson, M. Massetti, M. S. Rico, F. Limosin, and H. Leleu, "A stochastic agent-based model of the SARS-CoV-2 epidemic in France," *Nature Medicine*, vol. 26, no. 9, pp. 1417–1421, 2020.

[32] A. Karaivanov, "A social network model of COVID-19," *Plos One*, vol. 15, no. 10, p. e0240878, 2020.

[33] N. Soures, D. Chambers, Z. Carmichael, A. Daram, D. P. Shah, K. Clark, L. Potter, and D. Kudithipudi, "Sirnet: Understanding social distancing measures with hybrid neural network model for COVID-19 infectious spread," *arXiv preprint arXiv:2004.10376*, 2020.

[34] L. Xue, S. Jing, J. C. Miller, W. Sun, H. Li, J. G. Estrada-Franco, J. M. Hyman, and H. Zhu, "A data-driven network model for the emerging COVID-19 epidemics in Wuhan, Toronto and Italy," *Mathematical Biosciences*, vol. 326, p. 108391, 2020.

[35] D. Calvetti, A. P. Hoover, J. Rose, and E. Somersalo, "Metapopulation network models for understanding, predicting, and managing the coronavirus disease COVID-19," *Frontiers in Physics*, vol. 8, p. 261, 2020.

[36] C.-J. Huang, Y.-H. Chen, Y. Ma, and P.-H. Kuo, "Multiple-input deep convolutional neural network model for COVID-19 forecasting in China," *MedRxiv*, 2020.

[37] I. Rahimi, F. Chen, and A. H. Gandomi, "A review on COVID-19 forecasting models," *Neural Computing and Applications*, pp. 1–11, 2021.

[38] Beoff Bennett, Karina Cuevas, "Why the COVID death rate in the U.S. is so much higher than other wealthy nations) dashboard." `https://www.pbs.org/newshour/show/why-the-covid-death-rate-in-the-u-s-is-so-much-higher-than-other-wealthy-nations`. Accessed February 02, 2024.

[39] Centers of Disease Control and Prevention, "COVID data tracker." `https://covid.cdc.gov/covid-data-tracker/#datatracker-home`. Accessed February 02, 2024.

[40] S. Flaxman, S. Mishra, A. Gandy, H. J. T. Unwin, T. A. Mellan, H. Coupland, C. Whittaker, H. Zhu, T. Berah, J. W. Eaton, *et al.*, "Estimating the effects of non-pharmaceutical interventions on COVID-19 in Europe," *Nature*, vol. 584, no. 7820, pp. 257–261, 2020.

[41] Y. Bo, C. Guo, C. Lin, Y. Zeng, H. B. Li, Y. Zhang, M. S. Hossain, J. W. Chan, D. W. Yeung, K. O. Kwok, *et al.*, "Effectiveness of non-pharmaceutical interventions on COVID-19 transmission in 190 countries from 23 January to 13

April 2020," *International Journal of Infectious Diseases*, vol. 102, pp. 247–253, 2021.

[42] L. A. Callender, M. Curran, S. M. Bates, M. Mairesse, J. Weigandt, and C. J. Betts, "The impact of pre-existing comorbidities and therapeutic interventions on COVID-19," *Frontiers in Immunology*, vol. 11, p. 1991, 2020.

[43] B. Wang, R. Li, Z. Lu, and Y. Huang, "Does comorbidity increase the risk of patients with COVID-19: evidence from meta-analysis," *Aging (Albany NY)*, vol. 12, no. 7, p. 6049, 2020.

[44] I. Djaharuddin, S. Munawwarah, A. Nurulita, M. Ilyas, N. A. Tabri, and N. Lihawa, "Comorbidities and mortality in COVID-19 patients," *Gaceta Sanitaria*, vol. 35, pp. S530–S532, 2021.

[45] A. Omame, N. Sene, I. Nometa, C. I. Nwakanma, E. U. Nwafor, N. O. Iheonu, and D. Okuonghae, "Analysis of COVID-19 and comorbidity co-infection model with optimal control," *Optimal Control Applications and Methods*, vol. 42, no. 6, pp. 1568–1590, 2021.

[46] A. Sanyaolu, C. Okorie, A. Marinkovic, R. Patidar, K. Younis, P. Desai, Z. Hosein, I. Padda, J. Mangat, and M. Altaf, "Comorbidity and its impact on patients with COVID-19," *SN Comprehensive Clinical Medicine*, vol. 2, no. 8, pp. 1069–1076, 2020.

[47] M. Freed, J. Cubanski, T. Neuman, J. Kates, and J. Michaud, "What share of people who have died of COVID-19 are 65 and older–and how does it vary by state? Kaiser Family Foundation." `https://www.kff.org/coronavirus-covid-19/issue-brief/what-share-of-people-who-have-`

died-of-covid-19-are-65-and-older-and-how-does-it-vary-by-state, 2021.

[48] T. Powell, E. Bellin, and A. R. Ehrlich, "Older adults and COVID-19: the most vulnerable, the hardest hit," *Hastings Center Report*, vol. 50, no. 3, pp. 61–63, 2020.

[49] E. Ing, Q. Xu, A. Salimi, and N. Torun, "Physician deaths from corona virus (COVID-19) disease," *Occupational Medicine*, vol. 70, no. 5, pp. 370–374, 2020.

[50] K. P. Iyengar, P. Ish, G. K. Upadhyaya, N. Malhotra, R. Vaishya, and V. K. Jain, "COVID-19 and mortality in doctors," *Diabetes & Metabolic Syndrome: Clinical Research & Reviews*, vol. 14, no. 6, pp. 1743–1746, 2020.

[51] M. Mutambudzi, C. Niedzwiedz, E. B. Macdonald, A. Leyland, F. Mair, J. Anderson, C. Celis-Morales, J. Cleland, J. Forbes, J. Gill, *et al.*, "Occupation and risk of severe COVID-19: prospective cohort study of 120075 UK Biobank participants," *Occupational and Environmental Medicine*, vol. 78, no. 5, pp. 307–314, 2021.

[52] Y.-H. Chen, M. Glymour, A. Riley, J. Balmes, K. Duchowny, R. Harrison, E. Matthay, and K. Bibbins-Domingo, "Excess mortality associated with the COVID-19 pandemic among Californians 18–65 years of age, by occupational sector and occupation: March through November 2020," *PLoS One*, vol. 16, no. 6, p. e0252454, 2021.

[53] Y.-H. Chen, A. R. Riley, K. A. Duchowny, H. E. Aschmann, R. Chen, M. V. Kiang, A. C. Mooney, A. C. Stokes, M. M. Glymour, and K. Bibbins-Domingo, "COVID-19 mortality and excess mortality among working-age residents in Cal-

ifornia, USA, by occupational sector: a longitudinal cohort analysis of mortality surveillance data," *The Lancet Public Health*, vol. 7, no. 9, pp. e744–e753, 2022.

[54] M. Matz, C. Allemani, M. van Tongeren, V. Nafilyan, S. Rhodes, K. van Veldhoven, L. Pembrey, M. P. Coleman, and N. Pearce, "Excess mortality among essential workers in england and wales during the COVID-19 pandemic," *Journal of Epidemiology and Community Health*, vol. 76, no. 7, pp. 660–666, 2022.

[55] M. H. Haischer, R. Beilfuss, M. R. Hart, L. Opielinski, D. Wrucke, G. Zirgaitis, T. D. Uhrich, and S. K. Hunter, "Who is wearing a mask? gender-, age-, and location-related differences during the COVID-19 pandemic," *PloS One*, vol. 15, no. 10, p. e0240785, 2020.

[56] S. R. Neely, C. Eldredge, R. Ersing, and C. Remington, "Vaccine hesitancy and exposure to misinformation: A survey analysis," *Journal of General Internal Medicine*, vol. 37, no. 1, pp. 179–187, 2022.

[57] K. Kricorian, R. Civen, and O. Equils, "COVID-19 vaccine hesitancy: Misinformation and perceptions of vaccine safety," *Human Vaccines & Immunotherapeutics*, vol. 18, no. 1, p. 1950504, 2022.

[58] R. Singh and R. Adhikari, "Age-structured impact of social distancing on the COVID-19 epidemic in India," *arXiv preprint arXiv:2003.12055*, 2020.

[59] Q. Richard, S. Alizon, M. Choisy, M. T. Sofonea, and R. Djidjou-Demasse, "Age-structured non-pharmaceutical interventions for optimal control of COVID-19 epidemic," *PLoS Computational Biology*, vol. 17, no. 3, p. e1008776, 2021.

[60] E. H. Elbasha and A. B. Gumel, "Vaccination and herd immunity thresholds in heterogeneous populations," *medRxiv*, 2021.

[61] B. Pant and A. Gumel, "Mathematical assessment of the roles of age heterogeneity and vaccination on the dynamics and control of SARS-CoV-2."

[62] J. Glasser, Z. Feng, A. Moylan, S. Del Valle, and C. Castillo-Chavez, "Mixing in age-structured population models of infectious diseases," *Mathematical Biosciences*, vol. 235, no. 1, pp. 1–7, 2012.

[63] C. for Disease Control and P. (CDC), "Requirement for proof of COVID-19 vaccination for air passengers," 2021.

[64] Centers for Disease Control and Prevention, "Frequently asked questions about COVID-19 vaccination." `https://www.cdc.gov/coronavirus/2019-ncov/vaccines/faq.html`, May 2022. Accessed Jun 13, 2022.

[65] V. Lakshmikantham, S. Leela, and A. A. Martynyuk, *Stability Analysis of Nonlinear Systems*. Springer, 1989.

[66] A. Gumel, C. C. McCluskey, and P. van den Driessche, "Mathematical study of a staged-progression HIV model with imperfect vaccine," *Bulletin of Mathematical Biology*, vol. 68, no. 8, pp. 2105–2128, 2006.

[67] H. W. Hethcote, "The mathematics of infectious diseases," *SIAM Review*, vol. 42, no. 4, pp. 599–653, 2000.

[68] G. Darroch, "The original coronavirus strain has almost disappeared in the US. One chart shows how variants took over.." `https://www.businessinsider.com/original-coronavirus-strain-`

replaced-by-variants-us-chart-2021-6, 2021. Accessed September 18, 2023.

[69] P. Paul, A. M. France, Y. Aoki, D. Batra, M. Biggerstaff, V. Dugan, S. Galloway, A. J. Hall, M. A. Johansson, R. J. Kondor, *et al.*, "Genomic surveillance for SARS-CoV-2 variants circulating in the United States, December 2020–May 2021," *Morbidity and Mortality Weekly Report*, vol. 70, no. 23, p. 846, 2021.

[70] A. S. Lauring, M. W. Tenforde, J. D. Chappell, M. Gaglani, A. A. Ginde, T. McNeal, S. Ghamande, D. J. Douin, H. K. Talbot, J. D. Casey, *et al.*, "Clinical severity of, and effectiveness of mRNA vaccines against, COVID-19 from Omicron, Delta, and Alpha SARS-CoV-2 variants in the United States: prospective observational study," *BMJ*, vol. 376, 2022.

[71] P. A. Christensen, R. J. Olsen, S. W. Long, R. Snehal, J. J. Davis, M. O. Saavedra, K. Reppond, M. N. Shyer, J. Cambric, R. Gadd, *et al.*, "Signals of significantly increased vaccine breakthrough, decreased hospitalization rates, and less severe disease in patients with coronavirus disease 2019 caused by the Omicron variant of severe acute respiratory syndrome coronavirus 2 in Houston, Texas," *The American Journal of Pathology*, vol. 192, no. 4, pp. 642–652, 2022.

[72] P. Cavazzoni, "Coronavirus (COVID-19) update: FDA limits use of certain monoclonal antibodies to treat COVID-19 due to the Omicron variant," *US Food and Drug Administration*, 2022.

[73] CSSE at Johns Hopkins University, "CSSE GIS and Data COVID-19." https://github.com/CSSEGISandData/COVID-19, 2020.

[74] B. Epstein and D. Lofquist, "US Census Bureau Today delivers state population totals for congressional apportionment. US Census Bureau."

https://www.census.gov/library/stories/2021/04/2020-census-data-release.html, 2021.

[75] Arias, Elizabeth and Tejada-Vera, Betzaida and Ahmad, Farida, "Provisional life expectancy estimates for January through June, 2020." https://www.cdc.gov/coronavirus/2019-ncov/hcp/planning-scenarios.html, Feb. 2020. Accessed May 20, 2021.

[76] E. A. Iboi, C. N. Ngonghala, and A. B. Gumel, "Will an imperfect vaccine curtail the COVID-19 pandemic in the U.S.?," *Infectious Disease Modelling*, vol. 5, pp. 510–524, Aug. 2020.

[77] Q. Ma, J. Liu, Q. Liu, L. Kang, R. Liu, W. Jing, Y. Wu, and M. Liu, "Global percentage of asymptomatic SARS-CoV-2 infections among the tested population and individuals with confirmed COVID-19 diagnosis: a systematic review and meta-analysis," *JAMA Network Open*, vol. 4, no. 12, pp. e2137257–e2137257, 2021.

[78] Centers for Disease Control and Prevention, "COVID-19 pandemic planning scenarios." https://www.cdc.gov/coronavirus/2019-ncov/hcp/planning-scenarios.html, Feb. 2020. Accessed May 20, 2021.

[79] N. M. Ferguson, D. Laydon, G. Nedjati-Gilani, N. Imai, K. Ainslie, M. Baguelin, S. Bhatia, A. Boonyasiri, Z. Cucunuba, G. Cuomo-Dannenburg, A. Dighe, I. Dorigatti, H. Fu, K. Gaythorpe, W. Green, A. Hamlet, W. Hinsley, L. C. Okell, S. van Elsland, H. Thompson, R. Verity, E. Volz, H. Wang, Y. Wang, P. G. Walker, C. Walters, P. Winskill, C. Whittaker, C. A. Donnelly, S. Riley, and A. C. Ghani, "Report 9: Impact of non-pharmaceutical interventions

(NPIs) to reduce COVID19 mortality and healthcare demand," tech. rep., Imperial College London, Mar. 2020.

[80] S. M. Kissler, C. Tedijanto, E. Goldstein, Y. H. Grad, and M. Lipsitch, "Projecting the transmission dynamics of SARS-CoV-2 through the postpandemic period," *Science*, vol. 368, pp. 860–868, May 2020. Publisher: American Association for the Advancement of Science Section: Report.

[81] NCIRD, "COVID-19 vaccination and case trends by age group, United States." `https://data.cdc.gov/Vaccinations/COVID-19-Vaccination-and-Case-Trends-by-Age-Group-/gxj9-t96f`, 2022.

[82] S. Nasreen, H. Chung, S. He, K. A. Brown, J. B. Gubbay, S. A. Buchan, D. B. Fell, P. C. Austin, K. L. Schwartz, M. E. Sundaram, *et al.*, "Effectiveness of COVID-19 vaccines against symptomatic SARS-CoV-2 infection and severe outcomes with variants of concern in Ontario," *Nature Microbiology*, vol. 7, no. 3, pp. 379–385, 2022.

[83] K. J. Bruxvoort, L. S. Sy, L. Qian, B. K. Ackerson, Y. Luo, G. S. Lee, Y. Tian, A. Florea, M. Aragones, J. E. Tubert, *et al.*, "Effectiveness of mRNA-1273 against Delta, Mu, and other emerging variants of SARS-CoV-2: test negative case-control study," *BMJ*, vol. 375, 2021.

[84] Y. Wu, L. Kang, Z. Guo, J. Liu, M. Liu, and W. Liang, "Incubation period of COVID-19 caused by unique SARS-CoV-2 strains: a systematic review and meta-analysis," *JAMA Network Open*, vol. 5, no. 8, pp. e2228008–e2228008, 2022.

[85] H. Xin, Y. Li, P. Wu, Z. Li, E. H. Lau, Y. Qin, L. Wang, B. J. Cowling, T. K.

Tsang, and Z. Li, "Estimating the latent period of coronavirus disease 2019 (COVID-19)," *Clinical Infectious Diseases*, vol. 74, no. 9, pp. 1678–1681, 2022.

[86] S. Zhao *et al.*, "Estimating the time interval between transmission generations when negative values occur in the serial interval data: using COVID-19 as an example," *Mathematical Biosciences and Engineering*, vol. 17, no. 4, pp. 3512–3519, 2020.

[87] A. D. Iuliano, J. M. Brunkard, T. K. Boehmer, E. Peterson, S. Adjei, A. M. Binder, S. Cobb, P. Graff, P. Hidalgo, M. J. Panaggio, *et al.*, "Trends in disease severity and health care utilization during the early Omicron variant period compared with previous SARS-CoV-2 high transmission periods United States, December 2020–January 2022," *Morbidity and Mortality Weekly Report*, vol. 71, no. 4, pp. 146–152, 2022.

[88] P. van den Driessche and J. Watmough, "Reproduction numbers and subthreshold endemic equilibria for compartmental models of disease transmission," *Mathematical Biosciences*, vol. 180, no. 1-2, pp. 29–48, 2002.

[89] O. Diekmann, J. A. P. Heesterbeek, and J. A. Metz, "On the definition and the computation of the basic reproduction ratio $\mathcal{R}_0$ in models for infectious diseases in heterogeneous populations," *Journal of Mathematical Biology*, vol. 28, no. 4, pp. 365–382, 1990.

[90] K. Katella, "Omicron, Delta, Alpha, and more: What to know about the coronavirus variants," *Yale Medicine, 28th February, available at: https://www. yalemedicine. org/news/covid-19-variants-of-concern-omicron (accessed 8th March, 2022)*, 2022.

[91] D. Duong, "Alpha, Beta, Delta, Gamma: What's important to know about SARS-CoV-2 variants of concern?," 2021.

[92] H. V. Huff and A. Singh, "Asymptomatic transmission during the coronavirus disease 2019 pandemic and implications for public health strategies," *Clinical Infectious Diseases*, vol. 71, no. 10, pp. 2752–2756, 2020.

[93] L. A. Nikolai, C. G. Meyer, P. G. Kremsner, and T. P. Velavan, "Asymptomatic SARS coronavirus 2 infection: Invisible yet invincible," *International Journal of Infectious Diseases*, vol. 100, pp. 112–116, 2020.

[94] C. N. Ngonghala, E. A. Iboi, and A. B. Gumel, "Could masks curtail the post-lockdown resurgence of COVID-19 in the US?," *Mathematical Biosciences*, vol. 329, p. 108452, 2020.

[95] J. Hale, *Ordinary Differential Equations*. New York: John Wiley and Sons, 1969.

[96] A. B. Gumel, "Causes of backward bifurcations in some epidemiological models," *Journal of Mathematical Analysis and Applications*, vol. 395, no. 1, pp. 355–365, 2012.

[97] H. W. Hethcote and H. R. Thieme, "Stability of the endemic equilibrium in epidemic models with subpopulations," *Mathematical Biosciences*, vol. 75, no. 2, pp. 205–227, 1985.

[98] H. R. Thieme, "Local stability in epidemic models for heterogeneous populations," in *Mathematics in Biology and Medicine*, pp. 185–189, Springer, 1985.

[99] L. Esteva, A. B. Gumel, and C. V. De LeóN, "Qualitative study of transmission

dynamics of drug-resistant malaria," *Mathematical and Computer Modelling*, vol. 50, no. 3-4, pp. 611–630, 2009.

[100] L. Esteva and C. Vargas, "Influence of vertical and mechanical transmission on the dynamics of dengue disease," *Mathematical Biosciences*, vol. 167, no. 1, pp. 51–64, 2000.

[101] R. M. Anderson and R. M. May, "Vaccination and herd immunity to infectious diseases," *Nature*, vol. 318, no. 6044, pp. 323–329, 1985.

[102] R. M. Anderson, "The concept of herd immunity and the design of community-based immunization programmes," *Vaccine*, vol. 10, no. 13, pp. 928–935, 1992.

[103] J. Khalife and D. VanGennep, "COVID-19 herd immunity in the absence of a vaccine: an irresponsible approach," *Epidemiology and Health*, vol. 43, 2021.

[104] J. Lopez Bernal, N. Andrews, C. Gower, E. Gallagher, R. Simmons, S. Thelwall, J. Stowe, E. Tessier, N. Groves, G. Dabrera, *et al.*, "Effectiveness of COVID-19 vaccines against the B. 1.617. 2 (Delta) variant," *New England Journal of Medicine*, vol. 385, no. 7, pp. 585–594, 2021.

[105] N. Andrews, J. Stowe, F. Kirsebom, S. Toffa, T. Rickeard, E. Gallagher, C. Gower, M. Kall, N. Groves, A.-M. O'Connell, *et al.*, "COVID-19 vaccine effectiveness against the Omicron (B. 1.1. 529) variant," *New England Journal of Medicine*, vol. 386, no. 16, pp. 1532–1546, 2022.

[106] S. Marino, I. B. Hogue, C. J. Ray, and D. E. Kirschner, "A methodology for performing global uncertainty and sensitivity analysis in systems biology," *Journal of Theoretical Biology*, vol. 254, no. 1, pp. 178–196, 2008.

[107] S. M. Blower and H. Dowlatabadi, "Sensitivity and uncertainty analysis of complex models of disease transmission: an HIV model, as an example," *International Statistical Review/Revue Internationale de Statistique*, pp. 229–243, 1994.

[108] R. G. McLeod, J. F. Brewster, A. B. Gumel, and A. Slonowsky, "Sensitivity and uncertainty analyses for a SARS model with time-varying inputs and outputs," *Mathematical Biosciences and Engineering*, vol. 3, no. 3, p. 527, 2006.

[109] S. Gao, P. Binod, C. W. Chukwu, T. Kwofie, S. Safdar, L. Newman, S. Choe, B. K. Datta, W. K. Attipoe, W. Zhang, *et al.*, "A mathematical model to assess the impact of testing and isolation compliance on the transmission of COVID-19," *Infectious Disease Modelling*, vol. 8, no. 2, pp. 427–444, 2023.

[110] B. Gomero, "Latin hypercube sampling and partial rank correlation coefficient analysis applied to an optimal control problem," *TRACE*, 2012.

[111] CDC, "Deaths by select demographic and geographic characteristics." `https://www.cdc.gov/nchs/nvss/vsrr/covid_weekly/index.htm`. Accessed September 04, 2023.

[112] CDC, "Laboratory-confirmed COVID-19-associated hospitalizations." `https://gis.cdc.gov/grasp/covidnet/covid19_5.html`. Accessed September 04, 2023.

[113] T. United States Census Bureau, "Age and Sex Composition in the United States: 2019." `https://www.census.gov/data/tables/2019/demo/age-and-sex/2019-age-sex-composition.html`, 20019. Accessed 12-Dec-2022.

[114] J. Bosman and S. Mervosh, "As virus surges, younger people account for

'disturbing' number of cases." https://www.nytimes.com/2020/06/25/us/coronavirus-cases-young-people.html, 2020. Accessed September 18, 2023.

[115] L. L. Maragakis, "Coronavirus and COVID-19: Younger adults are at risk, too." https://www.hopkinsmedicine.org/health/conditions-and-diseases/coronavirus/coronavirus-and-covid-19-younger-adults-are-at-risk-too, 2020. Accessed September 18, 2023.

[116] CDPH, "COVID-19 age, race and ethnicity data." https://www.cdph.ca.gov/Programs/CID/DCDC/Pages/COVID-19/Age-Race-Ethnicity.aspx. Accessed September 04, 2023.

[117] "Improving public health policy in Europe through modelling and economic evaluation of interventions for the control of infectious diseases." https://cordis.europa.eu/project/id/502084/reporting. Accessed September 06, 2023.

[118] J. Mossong, N. Hens, M. Jit, P. Beutels, K. Auranen, R. Mikolajczyk, M. Massari, S. Salmaso, G. S. Tomba, J. Wallinga, *et al.*, "Social contacts and mixing patterns relevant to the spread of infectious diseases," *PLoS medicine*, vol. 5, no. 3, p. e74, 2008.

[119] K. Prem, A. R. Cook, and M. Jit, "Projecting social contact matrices in 152 countries using contact surveys and demographic data," *PLoS Computational Biology*, vol. 13, no. 9, p. e1005697, 2017.

[120] A. Bergman, Y. Sella, P. Agre, and A. Casadevall, "Oscillations in US COVID-19 incidence and mortality data reflect diagnostic and reporting factors," *Msystems*, vol. 5, no. 4, pp. e00544–20, 2020.

[121] J. Hopkins, "Daily confirmed new cases (7-day moving average)." https://coronavirus.jhu.edu/data/new-cases. Accessed September 17, 2023.

[122] K. D. Kochanek, J. Xu, and E. Arias, "Mortality in the United States, 2019." https://www.cdc.gov/nchs/data/databriefs/db395-H.pdf.

[123] P. Sah, M. C. Fitzpatrick, C. F. Zimmer, E. Abdollahi, L. Juden-Kelly, S. M. Moghadas, B. H. Singer, and A. P. Galvani, "Asymptomatic SARS-CoV-2 infection: A systematic review and meta-analysis," *Proceedings of the National Academy of Sciences*, vol. 118, no. 34, p. e2109229118, 2021.

[124] C. Faes, S. Abrams, D. Van Beckhoven, G. Meyfroidt, E. Vlieghe, N. Hens, and B. C. G. on COVID-19 Hospital Surveillance, "Time between symptom onset, hospitalisation and recovery or death: statistical analysis of Belgian COVID-19 patients," *International Journal of Environmental Research and Public Health*, vol. 17, no. 20, p. 7560, 2020.

[125] W. B. Applegate and J. G. Ouslander, "COVID-19 presents high risk to older persons," *Journal of the American Geriatrics Society*, vol. 68, no. 4, p. 681, 2020.

[126] T. Britton, F. Ball, and P. Trapman, "A mathematical model reveals the influence of population heterogeneity on herd immunity to SARS-CoV-2," *Science*, vol. 369, no. 6505, pp. 846–849, 2020.

[127] F. Luo, R. Ghanei Gheshlagh, S. Dalvand, S. Saedmoucheshi, and Q. Li, "Systematic review and meta-analysis of fear of COVID-19," *Frontiers in Psychology*, vol. 12, p. 661078, 2021.

[128] K. M. Fitzpatrick, C. Harris, and G. Drawve, "Fear of COVID-19 and the mental health consequences in America.," *Psychological Trauma: Theory, Research, Practice, and Policy*, vol. 12, no. S1, p. S17, 2020.

[129] X. Liu, W.-T. Luo, Y. Li, C.-N. Li, Z.-S. Hong, H.-L. Chen, F. Xiao, and J.-Y. Xia, "Psychological status and behavior changes of the public during the COVID-19 epidemic in China," *Infectious Diseases of Poverty*, vol. 9, no. 03, pp. 20–30, 2020.

[130] D. K. Ahorsu, C.-Y. Lin, V. Imani, M. Saffari, M. D. Griffiths, and A. H. Pakpour, "The fear of COVID-19 scale: development and initial validation," *International Journal of Mental Health and Addiction*, pp. 1–9, 2020.

[131] J. Roozenbeek, C. R. Schneider, S. Dryhurst, J. Kerr, A. L. Freeman, G. Recchia, A. M. Van Der Bles, and S. Van Der Linden, "Susceptibility to misinformation about COVID-19 around the world," *Royal Society Open Science*, vol. 7, no. 10, p. 201199, 2020.

[132] J. Y. Cuan-Baltazar, M. J. Muñoz-Perez, C. Robledo-Vega, M. F. Pérez-Zepeda, and E. Soto-Vega, "Misinformation of COVID-19 on the internet: infodemiology study," *JMIR Public Health and Surveillance*, vol. 6, no. 2, p. e18444, 2020.

[133] N. Perra, D. Balcan, B. Gonçalves, and A. Vespignani, "Towards a characterization of behavior-disease models," *PloS one*, vol. 6, no. 8, p. e23084, 2011.

[134] I. Z. Kiss, J. Cassell, M. Recker, and P. L. Simon, "The impact of information transmission on epidemic outbreaks," *Mathematical Biosciences*, vol. 225, no. 1, pp. 1–10, 2010.

[135] M. M. Tanaka, J. Kumm, and M. W. Feldman, "Coevolution of pathogens

and cultural practices: a new look at behavioral heterogeneity in epidemics," *Theoretical Population Biology*, vol. 62, no. 2, pp. 111–119, 2002.

[136] S. Funk, E. Gilad, and V. A. Jansen, "Endemic disease, awareness, and local behavioural response," *Journal of Theoretical Biology*, vol. 264, no. 2, pp. 501–509, 2010.

[137] K. Yan, "Modeling the effect of human behavior on disease transmission," 2022.

[138] S. Del Valle, H. Hethcote, J. M. Hyman, and C. Castillo-Chavez, "Effects of behavioral changes in a smallpox attack model," *Mathematical Biosciences*, vol. 195, no. 2, pp. 228–251, 2005.

[139] A. G. Kummer, J. Zhang, M. Litvinova, A. Vespignani, H. Yu, and M. Ajelli, "Measuring the seasonality of human contact patterns and its implications for the spread of respiratory infectious diseases," *medRxiv*, pp. 2022–02, 2022.

[140] A. d'Onofrio, P. Manfredi, and E. Salinelli, "Vaccinating behaviour, information, and the dynamics of sir vaccine preventable diseases," *Theoretical Population Biology*, vol. 71, no. 3, pp. 301–317, 2007.

[141] P. Manfredi and A. D'Onofrio, *Modeling the interplay between human behavior and the spread of infectious diseases*. Springer Science & Business Media, 2013.

[142] F. C. Coelho and C. T. Codeço, "Dynamic modeling of vaccinating behavior as a function of individual beliefs," *PLoS Computational Biology*, vol. 5, no. 7, p. e1000425, 2009.

[143] J. de Mooij, P. Bhattacharya, D. Dell'Anna, M. Dastani, B. Logan, and S. Swarup, "A framework for modeling human behavior in large-scale agent-based epidemic simulations," *Simulation*, p. 00375497231184898, 2023.

[144] S. Y. D. Valle, S. M. Mniszewski, and J. M. Hyman, "Modeling the impact of behavior changes on the spread of pandemic influenza," *Modeling the interplay between human behavior and the spread of infectious diseases*, pp. 59–77, 2013.

[145] B. Espinoza, M. Marathe, S. Swarup, and M. Thakur, "Asymptomatic individuals can increase the final epidemic size under adaptive human behavior," *Scientific Reports*, vol. 11, no. 1, p. 19744, 2021.

[146] D. He, J. Dushoff, T. Day, J. Ma, and D. J. Earn, "Inferring the causes of the three waves of the 1918 influenza pandemic in England and Wales," *Proceedings of the Royal Society B: Biological Sciences*, vol. 280, no. 1766, p. 20131345, 2013.

[147] W. C. Roda, M. B. Varughese, D. Han, and M. Y. Li, "Why is it difficult to accurately predict the COVID-19 epidemic?," *Infectious Disease Modelling*, vol. 5, pp. 271–281, 2020.

[148] F. Sayers, "Why were Denmark's Covid models better than England's?." `https://unherd.com/thepost/why-were-denmarks-covid-models-better-than-englands/`. Accessed January 19, 2024.

[149] C. N. Ngonghala, H. B. Taboe, S. Safdar, and A. B. Gumel, "Unraveling the dynamics of the Omicron and Delta variants of the 2019 coronavirus in the presence of vaccination, mask usage, and antiviral treatment," *Applied Mathematical Modelling*, vol. 114, pp. 447–465, 2023.

[150] H. Howard and L. Andrews, "Another doomsday SAGE prediction that was wrong: Expert admits forecasting 6,000 Omicron deaths a day when it only reached 306 were wildly wrong because they failed to predict britons would change their behaviour." `https://www.dailymail.co.uk/news/article-10571661/SAGE-expert-says-wildly-wrong-Omicron-death-`

predictions-failed-account-behaviour-change.html. Accessed January 19, 2024.

[151] B. Pant, S. Safdar, M. Santillana, and A. Gumel, "Mathematical assessment of the role of human behavior changes on SARS-CoV-2 transmission dynamics," *medRxiv*, pp. 2024–02, 2024.

[152] V. S. Ivlev, "Experimental ecology of the feeding of fishes," *Yale University Press*, 1961.

[153] M. E. Bouton, "Why behavior change is difficult to sustain," *Preventive Medicine*, vol. 68, pp. 29–36, 2014.

[154] "COVID states project." https://lazerlab.shinyapps.io/Behaviors_During_COVID/. Accessed December 9, 2023.

[155] R. Li, S. Pei, B. Chen, Y. Song, T. Zhang, W. Yang, and J. Shaman, "Substantial undocumented infection facilitates the rapid dissemination of novel coronavirus (SARS-CoV-2)," *Science*, vol. 368, no. 6490, pp. 489–493, 2020.

[156] Y. Niu, J. Rui, Q. Wang, W. Zhang, Z. Chen, F. Xie, Z. Zhao, S. Lin, Y. Zhu, Y. Wang, *et al.*, "Containing the transmission of COVID-19: a modeling study in 160 countries," *Frontiers in Medicine*, vol. 8, p. 701836, 2021.

[157] R. Subramanian, Q. He, and M. Pascual, "Quantifying asymptomatic infection and transmission of COVID-19 in New York City using observed cases, serology, and testing capacity," *Proceedings of the National Academy of Sciences*, vol. 118, no. 9, p. e2019716118, 2021.

[158] S. M. Moghadas, M. C. Fitzpatrick, P. Sah, A. Pandey, A. Shoukat, B. H. Singer, and A. P. Galvani, "The implications of silent transmission for the control

of COVID-19 outbreaks," *Proceedings of the National Academy of Sciences*, vol. 117, no. 30, pp. 17513–17515, 2020.

[159] L. C. Tindale, J. E. Stockdale, M. Coombe, E. S. Garlock, W. Y. V. Lau, M. Saraswat, L. Zhang, D. Chen, J. Wallinga, and C. Colijn, "Evidence for transmission of COVID-19 prior to symptom onset," *Elife*, vol. 9, p. e57149, 2020.

[160] A. Mallela, J. Neumann, E. F. Miller, Y. Chen, R. G. Posner, Y. T. Lin, and W. S. Hlavacek, "Bayesian inference of state-level COVID-19 basic reproduction numbers across the United States," *Viruses*, vol. 14, no. 1, p. 157, 2022.

[161] J. Snow, *On the mode of communication of cholera*. John Churchill, 1849.

[162] T. H. Tulchinsky, "John Snow, cholera, the Broad Street pump; waterborne diseases then and now," *Case Studies in Public Health*, p. 77, 2018.

[163] J. D. Trask, J. R. Paul, *et al.*, "Periodic examination of sewage for the virus of poliomyelitis," *The Journal of Experimental Medicine*, vol. 75, no. 1, p. 1, 1942.

[164] J. R. Paul, J. D. Trask, and C. Culotta, "Poliomyelitic virus in sewage," *Science*, vol. 90, no. 2333, pp. 258–259, 1939.

[165] J. R. Paul, J. D. Trask, and S. Gard, "II. Poliomyelitic virus in urban sewage," *The Journal of Experimental Medicine*, vol. 71, no. 6, p. 765, 1940.

[166] Biobot Analytics, "Polio and the early history of wastewater epidemiology." `https://biobotanalytics.medium.com/polio-and-the-early-history-of-wastewater-epidemiology-8f39f984be9f`. Accessed December 7, 2023.

[167] W. Ahmed, S. L. Simpson, P. M. Bertsch, K. Bibby, A. Bivins, L. L. Blackall, S. Bofill-Mas, A. Bosch, J. Brandão, P. M. Choi, *et al.*, "Minimizing errors in RT-PCR detection and quantification of SARS-CoV-2 RNA for wastewater surveillance," *Science of the Total Environment*, vol. 805, p. 149877, 2022.

[168] S. L. Emery, D. D. Erdman, M. D. Bowen, B. R. Newton, J. M. Winchell, R. F. Meyer, S. Tong, B. T. Cook, B. P. Holloway, K. A. McCaustland, *et al.*, "Real-time reverse transcription–polymerase chain reaction assay for SARS-associated coronavirus," *Emerging infectious diseases*, vol. 10, no. 2, p. 311, 2004.

[169] Centers for Disease Control and Prevention, "National wastewater surveillance system (NWSS)." `https://www.cdc.gov/coronavirus/2019-ncov/cases-updates/wastewater-surveillance.html`. Accessed December 6, 2023.

[170] G. Li, P. Diggle, and M. Blangiardo, "Integrating wastewater and randomised prevalence survey data for national covid surveillance," *Scientific Reports*, vol. 14, no. 1, p. 5124, 2024.

[171] C. O'donnell, "Focus: Rapid COVID-19 tests increasingly scarce, pricey as demand from employers jumps." `https://www.reuters.com/business/healthcare-pharmaceuticals/rapid-covid-19-tests-increasingly-scarce-pricey-demand-employers-jumps-2021-10-05/`. Accessed Feburary 11, 2023.

[172] L. G. Ngwira, B. Sharma, K. B. Shrestha, S. Dahal, R. Tuladhar, G. Manthalu, B. Chilima, A. Ganizani, J. Rigby, O. Kanjerwa, *et al.*, "Cost of wastewater-based environmental surveillance for sars-cov-2: Evidence from pilot sites in

Blantyre, Malawi and Kathmandu, Nepal," *PLOS Global Public Health*, vol. 2, no. 12, p. e0001377, 2022.

[173] M. B. Diamond, A. Keshaviah, A. I. Bento, O. Conroy-Ben, E. M. Driver, K. B. Ensor, R. U. Halden, L. P. Hopkins, K. G. Kuhn, C. L. Moe, *et al.*, "Wastewater surveillance of pathogens can inform public health responses," *Nature Medicine*, vol. 28, no. 10, pp. 1992–1995, 2022.

[174] B.-K. Yoo, R. Iwamoto, U. Chung, T. Sasaki, and M. Kitajima, "Economic evaluation of wastewater surveillance combined with clinical covid-19 screening tests, japan," *Emerging Infectious Diseases*, vol. 29, no. 8, p. 1608, 2023.

[175] J. Peiser, "The University of Arizona says it caught a dorm's COVID-19 outbreak before it started. its secret weapon: Poop." `https://www.washingtonpost.com/nation/2020/08/28/arizona-coronavirus-wastewater-testing/`. Accessed December 7, 2023.

[176] J. Kaiser, "Poop tests stop covid-19 outbreak at university of arizona," *Science. June*, vol. 1, 2021.

[177] K. Mao, K. Zhang, W. Du, W. Ali, X. Feng, and H. Zhang, "The potential of wastewater-based epidemiology as surveillance and early warning of infectious disease outbreaks," *Current Opinion in Environmental Science & Health*, vol. 17, pp. 1–7, 2020.

[178] S. W. Olesen, M. Imakaev, and C. Duvallet, "Making waves: Defining the lead time of wastewater-based epidemiology for COVID-19," *Water Research*, vol. 202, p. 117433, 2021.

[179] E. Róka, B. Khayer, Z. Kis, L. B. Kovács, E. Schuler, N. Magyar, T. Málnási,

O. Oravecz, B. Pályi, T. Pándics, *et al.*, "Ahead of the second wave: Early warning for COVID-19 by wastewater surveillance in Hungary," *Science of the Total Environment*, vol. 786, p. 147398, 2021.

[180] A. Lastra, J. Botello, A. Pinilla, J. I. Urrutia, J. Canora, J. Sánchez, P. Fernández, F. J. Candel, A. Zapatero, M. Ortega, *et al.*, "SARS-CoV-2 detection in wastewater as an early warning indicator for COVID-19 pandemic. madrid region case study," *Environmental Research*, vol. 203, p. 111852, 2022.

[181] Y. Zhu, W. Oishi, C. Maruo, M. Saito, R. Chen, M. Kitajima, and D. Sano, "Early warning of COVID-19 via wastewater-based epidemiology: potential and bottlenecks," *Science of The Total Environment*, vol. 767, p. 145124, 2021.

[182] R. S. Fontenele, S. Kraberger, J. Hadfield, E. M. Driver, D. Bowes, L. A. Holland, T. O. Faleye, S. Adhikari, R. Kumar, R. Inchausti, *et al.*, "High-throughput sequencing of SARS-CoV-2 in wastewater provides insights into circulating variants," *Water Research*, vol. 205, p. 117710, 2021.

[183] S. Karthikeyan, J. I. Levy, P. De Hoff, G. Humphrey, A. Birmingham, K. Jepsen, S. Farmer, H. M. Tubb, T. Valles, C. E. Tribelhorn, *et al.*, "Wastewater sequencing reveals early cryptic SARS-CoV-2 variant transmission," *Nature*, vol. 609, no. 7925, pp. 101–108, 2022.

[184] R. C. Morfino, "Notes from the field: aircraft wastewater surveillance for early detection of SARS-CoV-2 variants—John F. Kennedy International Airport, New York City, August–September 2022," *MMWR. Morbidity and Mortality Weekly Report*, vol. 72, 2023.

[185] K. Farkas, R. Williams, N. Alex-Sanders, J. M. Grimsley, I. Pântea, M. J. Wade, N. Woodhall, and D. L. Jones, "Wastewater-based monitoring of SARS-CoV-2

at UK airports and its potential role in international public health surveillance," *PLOS global public health*, vol. 3, no. 1, p. e0001346, 2023.

[186] W. Ahmed, A. Bivins, S. L. Simpson, P. M. Bertsch, J. Ehret, I. Hosegood, S. S. Metcalfe, W. J. Smith, K. V. Thomas, J. Tynan, *et al.*, "Wastewater surveillance demonstrates high predictive value for COVID-19 infection on board repatriation flights to Australia," *Environment international*, vol. 158, p. 106938, 2022.

[187] M. C. Eisenberg, S. L. Robertson, and J. H. Tien, "Identifiability and estimation of multiple transmission pathways in cholera and waterborne disease," *Journal of Theoretical Biology*, vol. 324, pp. 84–102, 2013.

[188] Z. Shuai and P. Van den Driessche, "Global dynamics of cholera models with differential infectivity," *Mathematical biosciences*, vol. 234, no. 2, pp. 118–126, 2011.

[189] M. C. Eisenberg, Z. Shuai, J. H. Tien, and P. Van den Driessche, "A cholera model in a patchy environment with water and human movement," *Mathematical Biosciences*, vol. 246, no. 1, pp. 105–112, 2013.

[190] A. Mwasa and J. M. Tchuenche, "Mathematical analysis of a cholera model with public health interventions," *Biosystems*, vol. 105, no. 3, pp. 190–200, 2011.

[191] F. Brauer, Z. Shuai, and P. Van Den Driessche, "Dynamics of an age-of-infection cholera model," *Mathematical Biosciences & Engineering*, vol. 10, no. 5&6, pp. 1335–1349, 2013.

[192] A. F. Brouwer, J. N. Eisenberg, C. D. Pomeroy, L. M. Shulman, M. Hindiyeh, Y. Manor, I. Grotto, J. S. Koopman, and M. C. Eisenberg, "Epidemiology of

the silent polio outbreak in Rahat, Israel, based on modeling of environmental surveillance data," *Proceedings of the National Academy of Sciences*, vol. 115, no. 45, pp. E10625–E10633, 2018.

[193] E. Anis, E. Kopel, S. Singer, E. Kaliner, L. Moerman, J. Moran-Gilad, D. Sofer, Y. Manor, L. Shulman, E. Mendelson, *et al.*, "Insidious reintroduction of wild poliovirus into Israel, 2013," *Eurosurveillance*, vol. 18, no. 38, p. 20586, 2013.

[194] T. H. Tulchinsky, A. Ramlawi, Z. Abdeen, I. Grotto, and A. Flahault, "Polio lessons 2013: Israel, the West Bank, and Gaza," *The Lancet*, vol. 382, no. 9905, pp. 1611–1612, 2013.

[195] Centers for Disease Control and Prevention, "Vaccine-derived poliovirus." `https://www.cdc.gov/vaccines/vpd/polio/hcp/vaccine-derived-poliovirus-faq.html`. Accessed December 7, 2023.

[196] L. Roberts, "Israel's silent polio epidemic breaks all the rules," 2013.

[197] J. Moran-Gilad, E. Kaliner, M. Gdalevich, and I. Grotto, "Public health response to the silent reintroduction of wild poliovirus to Israel, 2013–2014," *Clinical Microbiology and Infection*, vol. 22, pp. S140–S145, 2016.

[198] X. Li, S. Zhang, S. Sherchan, G. Orive, U. Lertxundi, E. Haramoto, R. Honda, M. Kumar, S. Arora, M. Kitajima, *et al.*, "Correlation between SARS-CoV-2 RNA concentration in wastewater and COVID-19 cases in community: a systematic review and meta-analysis," *Journal of Hazardous Materials*, vol. 441, p. 129848, 2023.

[199] X. Pang, T. Gao, E. Ellehoj, Q. Li, Y. Qiu, R. Maal-Bared, C. Sikora, G. Tipples, M. Diggle, D. Hinshaw, *et al.*, "Wastewater-based surveillance is an ef-

fective tool for trending COVID-19 prevalence in communities: a study of 10 major communities for 17 months in Alberta," *ACS Es&t Water*, vol. 2, no. 11, pp. 2243–2254, 2022.

[200] J. Weidhaas, Z. T. Aanderud, D. K. Roper, J. VanDerslice, E. B. Gaddis, J. Ostermiller, K. Hoffman, R. Jamal, P. Heck, Y. Zhang, *et al.*, "Correlation of SARS-CoV-2 RNA in wastewater with COVID-19 disease burden in sewersheds," *Science of The Total Environment*, vol. 775, p. 145790, 2021.

[201] D. Polo, M. Quintela-Baluja, A. Corbishley, D. L. Jones, A. C. Singer, D. W. Graham, and J. L. Romalde, "Making waves: Wastewater-based epidemiology for COVID-19–approaches and challenges for surveillance and prediction," *Water Research*, vol. 186, p. 116404, 2020.

[202] A. Galani, R. Aalizadeh, M. Kostakis, A. Markou, N. Alygizakis, T. Lytras, P. G. Adamopoulos, J. Peccia, D. C. Thompson, A. Kontou, *et al.*, "SARS-CoV-2 wastewater surveillance data can predict hospitalizations and ICU admissions," *Science of The Total Environment*, vol. 804, p. 150151, 2022.

[203] F. Saguti, E. Magnil, L. Enache, M. P. Churqui, A. Johansson, D. Lumley, F. Davidsson, L. Dotevall, A. Mattsson, E. Trybala, *et al.*, "Surveillance of wastewater revealed peaks of SARS-CoV-2 preceding those of hospitalized patients with COVID-19," *Water Research*, vol. 189, p. 116620, 2021.

[204] X. Li, H. Liu, L. Gao, S. P. Sherchan, T. Zhou, S. J. Khan, M. C. Van Loosdrecht, and Q. Wang, "Wastewater-based epidemiology predicts COVID-19-induced weekly new hospital admissions in over 150 usa counties," *Nature Communications*, vol. 14, no. 1, p. 4548, 2023.

[205] J. S. Huisman, J. Scire, L. Caduff, X. Fernandez-Cassi, P. Ganesanandamoorthy, A. Kull, A. Scheidegger, E. Stachler, A. B. Boehm, B. Hughes, *et al.*, "Wastewater-based estimation of the effective reproductive number of SARS-CoV-2," *Environmental Health Perspectives*, vol. 130, no. 5, p. 057011, 2022.

[206] C. S. McMahan, S. Self, L. Rennert, C. Kalbaugh, D. Kriebel, D. Graves, C. Colby, J. A. Deaver, S. C. Popat, T. Karanfil, *et al.*, "COVID-19 wastewater epidemiology: a model to estimate infected populations," *The Lancet Planetary Health*, vol. 5, no. 12, pp. e874–e881, 2021.

[207] T. Phan, S. Brozak, B. Pell, A. Gitter, A. Xiao, K. D. Mena, Y. Kuang, and F. Wu, "A simple SEIR-V model to estimate COVID-19 prevalence and predict SARS-CoV-2 transmission using wastewater-based surveillance data," *Science of The Total Environment*, vol. 857, p. 159326, 2023.

[208] S. Nourbakhsh, A. Fazil, M. Li, C. S. Mangat, S. W. Peterson, J. Daigle, S. Langner, J. Shurgold, P. D'Aoust, R. Delatolla, *et al.*, "A wastewater-based epidemic model for SARS-CoV-2 with application to three Canadian cities," *Epidemics*, vol. 39, p. 100560, 2022.

[209] B. J. Silk, "COVID-19 surveillance after expiration of the public health emergency declaration—United States, May 11, 2023." `https://www.cdc.gov/mmwr/volumes/72/wr/mm7219e1.htm`, 2023. Accessed March 24, 2023.

[210] "CDC switching gears on Covid tracking." `https://www.nbcnews.com/health/health-news/cdc-stop-tracking-covid-levels-communities-rcna82059`. Accessed March 24, 2023.

[211] T. W. Russell, N. Golding, J. Hellewell, S. Abbott, L. Wright, C. A. Pearson, K. van Zandvoort, C. I. Jarvis, H. Gibbs, Y. Liu, *et al.*, "Reconstructing the

early global dynamics of under-ascertained covid-19 cases and infections," *BMC medicine*, vol. 18, no. 1, p. 332, 2020.

[212] F. Sheet, "The biden administration to begin distributing at-home, rapid covid-19 tests to americans for free." https://www.whitehouse.gov/briefing-room/statements-releases/2022/01/14/fact-sheet-the-biden-administration-to-begin-distributing-at-home-rapid-covid-19-tests-to-americans-for-free/, 2022.

[213] B. Rader, A. Gertz, A. D. Iuliano, M. Gilmer, L. Wronski, C. M. Astley, K. Sewalk, T. J. Varrelman, J. Cohen, R. Parikh, *et al.*, "Use of at-home COVID-19 tests—United States, August 23, 2021–March 12, 2022," 2022.

[214] "Mathematical assessment of wastewater-based epidemiology to predict SARS-CoV-2 cases and hospitalizations in pmiami-dade county."

[215] Y. Guo, Y. Liu, S. Gao, X. Zhou, M. Sivakumar, and G. Jiang, "Effects of temperature and water types on the decay of coronavirus: a review," *Water*, vol. 15, no. 6, p. 1051, 2023.

[216] C. McCall, Z. N. Fang, D. Li, A. J. Czubai, A. Juan, Z. W. LaTurner, K. Ensor, L. Hopkins, P. B. Bedient, and L. B. Stadler, "Modeling sars-cov-2 rna degradation in small and large sewersheds," *Environmental Science: Water Research & Technology*, vol. 8, no. 2, pp. 290–300, 2022.

[217] W. O. Kermack and A. G. McKendrick, "A contribution to the mathematical theory of epidemics," *Proceedings of the royal society of london. Series A, Containing papers of a mathematical and physical character*, vol. 115, no. 772, pp. 700–721, 1927.

[218] Biobot Analytics, "COVID-19 wastewater monitoring by county and U.S. territory." https://biobot.io/data/.

[219] Miami Dade County, "Public health dashboard." https://www.miamidade.gov/information/library/2023-01-30-covid-dashboard.pdf. Accessed March 1, 2024.

[220] The New York Times, "Quickfacts Miami-Dade County, Florida." https://www.census.gov/quickfacts/fact/table/miamidadecountyflorida/POP060210.

[221] R. Wölfel, V. M. Corman, W. Guggemos, M. Seilmaier, S. Zange, M. A. Müller, D. Niemeyer, T. C. Jones, P. Vollmar, C. Rothe, *et al.*, "Virological assessment of hospitalized patients with COVID-2019," *Nature*, vol. 581, no. 7809, pp. 465–469, 2020.

[222] S. K. Greene, A. Levin-Rector, N. T. Kyaw, E. Luoma, H. Amin, E. McGibbon, R. W. Mathes, and S. D. Ahuja, "Comparative hospitalization risk for SARS-CoV-2 Omicron and Delta variant infections, by variant predominance periods and patient-level sequencing results, New York City, August 2021–January 2022," *Influenza and Other Respiratory Viruses*, vol. 17, no. 1, p. e13062, 2023.

[223] Metro Water Recovery, "The cycle of wastewater." https://metrowaterrecovery.com/transforming-wastewater/the-cycle-of-wastewater/. Accessed March 10, 2024.

[224] A. Harris and M. Herald, "Miami-dade dumps sewage into the ocean: Overhaul will reduce the foul flow." https://phys.org/news/2024-02-miami-dade-dumps-sewage-ocean.html. Accessed March 3, 2024.

[225] Miami-Dade County, "All you need to know about your miami-dade water and sewer department." https://www.miamidade.gov/water/library/brochures/about-water-sewer-department.pdf. Accessed March 3, 2024.

[226] The New York Times, "Tracking coronavirus in Maimi-dade County, fla.: Latest map and case count." https://www.nytimes.com/interactive/2021/us/miami-dade-florida-covid-cases.html.

[227] N. Menachemi, B. E. Dixon, K. K. Wools-Kaloustian, C. T. Yiannoutsos, and P. K. Halverson, "How many SARS-CoV-2–infected people require hospitalization? using random sample testing to better inform preparedness efforts," *Journal of Public Health Management and Practice*, vol. 27, no. 3, pp. 246–250, 2021.

[228] Miami-Dade County, "Miami-dade county - florida's most populous county." http://edr.state.fl.us/content/area-profiles/county/miamidade.pdf. Accessed March 11, 2024.

[229] C. Rose, A. Parker, B. Jefferson, and E. Cartmell, "The characterization of feces and urine: a review of the literature to inform advanced treatment technology," *Critical reviews in environmental science and technology*, vol. 45, no. 17, pp. 1827–1879, 2015.

[230] CBC, "Is My Poop Normal? Here's the Scoop." https://www.cbc.ca/natureofthings/features/is-my-poop-normal-heres-the-scoop.

[231] Citi-Data, "Miami-Dade County, Florida (FL)." https://www.city-data.com/county/Miami-Dade_County-FL.html.

[232] T. Hoffmann and J. Alsing, "Faecal shedding models for SARS-CoV-2 RNA

among hospitalised patients and implications for wastewater-based epidemiology," *Journal of the Royal Statistical Society Series C: Applied Statistics*, vol. 72, no. 2, pp. 330–345, 2023.

[233] D. Cuicchi, T. Lazzarotto, and G. Poggioli, "Fecal-oral transmission of SARS-CoV-2: review of laboratory-confirmed virus in gastrointestinal system," *International Journal of Colorectal Disease*, vol. 36, pp. 437–444, 2021.

[234] Miami-Dade County, "Miami-dade county at-a-glance." `https://www.miamidade.gov/information/library/at-a-glance.pdf`. Accessed March 7, 2024.

[235] Florida Department of State, "Quick facts." `https://dos.fl.gov/florida-facts/quick-facts/`. Accessed March 7, 2024.

[236] M. Mancuso, S. E. Eikenberry, and A. B. Gumel, "Will vaccine-derived protective immunity curtail COVID-19 variants in the US?," *Infectious Disease Modelling*, vol. 6, pp. 1110–1134, 2021.

[237] O. J. Peter, H. S. Panigoro, A. Abidemi, M. M. Ojo, and F. A. Oguntolu, "Mathematical model of COVID-19 pandemic with double dose vaccination," *Acta Biotheoretica*, vol. 71, no. 2, p. 9, 2023.

[238] S. Marino, I. B. Hogue, C. J. Ray, and D. E. Kirschner, "A methodology for performing global uncertainty and sensitivity analysis in systems biology," *Journal of Theoretical Biology*, vol. 254, no. 1, pp. 178–196, 2008.

[239] NIH, "NIH clinical trial shows Remdesivir accelerates recovery from advanced COVID-19." `https://www.nih.gov/news-events/news-releases/nih-`

clinical-trial-shows-remdesivir-accelerates-recovery-advanced-covid-19, Apr. 2020. Accessed August 28, 2023.

[240] Covid Act Now, "Miami-Dade County, FL." https://covidactnow.org/us/florida-fl/county/miami_dade_county/?s=49353680. Accessed March 7, 2024.

[241] K. Hayes, "COVID-19 infection rates in many areas likely 10 times higher than official case counts, CDC study finds." https://www.fox7austin.com/news/covid-19-infection-rates-in-many-areas-likely-10-times-higher-than-official-case-counts-cdc-study-finds.

[242] S. L. Wu, A. N. Mertens, Y. S. Crider, A. Nguyen, N. N. Pokpongkiat, S. Djajadi, A. Seth, M. S. Hsiang, J. M. Colford Jr, A. Reingold, *et al.*, "Substantial underestimation of SARS-CoV-2 infection in the United States," *Nature communications*, vol. 11, no. 1, p. 4507, 2020.

[243] A. Natarajan, S. Zlitni, E. F. Brooks, S. E. Vance, A. Dahlen, H. Hedlin, R. M. Park, A. Han, D. T. Schmidtke, R. Verma, *et al.*, "Gastrointestinal symptoms and fecal shedding of SARS-CoV-2 RNA suggest prolonged gastrointestinal infection," *Med*, vol. 3, no. 6, pp. 371–387, 2022.

[244] R. Rubin, "SARS-CoV-2 RNA can persist in stool months after respiratory tract clears virus," *JAMA*, vol. 327, no. 22, pp. 2175–2176, 2022.

[245] The Nobel Prize, "Kary b. mullis facts." https://www.nobelprize.org/prizes/chemistry/1993/mullis/facts. Accessed April 13, 2024.

[246] K. Mullis, F. Faloona, S. Scharf, R. Saiki, G. Horn, and H. Erlich, "Specific enzymatic amplification of dna in vitro: the polymerase chain reaction," 1986.

[247] C. Chen, G. Kaur, A. Adiga, B. Espinoza, S. Venkatramanan, A. Warren, B. Lewis, J. Crow, R. Singh, A. Lorentz, *et al.*, "Wastewater-based epidemiology for covid-19 surveillance: A survey," *arXiv preprint arXiv:2403.15291*, 2024.

[248] D. T. Hill, M. A. Alazawi, E. J. Moran, L. J. Bennett, I. Bradley, M. B. Collins, C. J. Gobler, H. Green, T. Z. Insaf, B. Kmush, *et al.*, "Wastewater surveillance provides 10-days forecasting of COVID-19 hospitalizations superior to cases and test positivity: A prediction study," *Infectious disease modelling*, vol. 8, no. 4, pp. 1138–1150, 2023.

[249] M. A. Safi and A. B. Gumel, "Global asymptotic dynamics of a model for quarantine and isolation," *Discrete Contin. Dyn. Syst. Ser. B*, vol. 14, no. 1, pp. 209–231, 2010.

[250] H. I. Freedman and J.-H. So, "Global stability and persistence of simple food chains," *Mathematical Biosciences*, vol. 76, no. 1, pp. 69–86, 1985.

[251] A. B. Gumel, "Global dynamics of a two-strain avian influenza model," *International Journal of Computer Mathematics*, vol. 86, no. 1, pp. 85–108, 2009.

[252] H. Guo and M. Y. Li, "Global dynamics of a staged progression model for infectious diseases," *Mathematical Biosciences & Engineering*, vol. 3, no. 3, p. 513, 2006.